# Doppler coherence imaging of ion flows and temperatures in the MAGPIE helicon plasma

Romana Louise Lester

A thesis submitted for the degree of
Doctor of Philosophy
of the Australian National University

December 2018


Australian
National
University

# Declaration

This thesis is an account of research undertaken between February 2012 and December 2018 at The Department of Physics, Faculty of Science, The Australian National University, Canberra, Australia.

Except where acknowledged in the customary manner, the material presented in this thesis is, to the best of my knowledge, original and has not been submitted in whole or part for a degree in any university.

Romana Lester
Dec, 2018

# Abstract

This work presents the development details of a snapshot coherence imaging system designed to measure the brightness, flows and temperatures of argon ions in the MAGnetised Plasma Interaction Experiment (MAGPIE), a helicon plasma with expected ion temperatures of $\sim$ 1 eV and subsonic ion flows $<$ 1000 m/s. Coherence imaging uses various multiplexing techniques to capture Doppler information from the 488 nm ion spectral line and encoded this in the phase and contrast of an interferogram. Taking into account line-of-sight effects, demodulation of the interferogram yields a 2D spatial map of the ion temperatures and flows. For MAGPIE plasma conditions, large interferometric delays ($> 10^4$ waves) are necessary to resolve the Doppler features. Passive stabilisation and an automated online calibration system was used to manage thermally-induced phase drifts in the thick birefringent delay plates required to produce the large delays. The design features of this device are presented here.

Various contamination effects and sources of error that affect the interpretation of the interferogram have been examined. Contamination from secondary spectral lines were found to cause modulations in the contrast and phase. The coherence-length of the air-cooled argon ion laser calibration source was found to be comparable with the Doppler effect for the cold core plasma, and this precluded detailed measurements of the ion distribution function. Inversion methods were used to examine line-integration effects. For this study the brightness and contrast projections were inverted to give radial profiles of the local emissivity and ion temperature while vector tomography of the azimuthal flow was achieved through reconstruction of the vorticity and also via a cosine weight term.

Measurements are presented of the ion brightness, flows and temperatures of the MAGPIE argon plasma for 'standard' discharge conditions (3 mTorr gas pressure, forward power of 1 kW and a 0.08 T peak magnetic field in a magnetic pinch configuration). Spatial scans taken longitudinally along the chamber show that the peak brightness occurs in the high magnetic field region and the radial profile is centrally peaked with secondary wing-like features. There are high ion temperatures near the source and also in the plasma edge (0.8–1.0 eV) which suggest a dual ion heating mechanism. The azimuthal ion flows are largest in the magnetic pinch region reaching speeds of 400 m/s and decrease to near zero in the near-antenna region. The axial flows show a flow stagnation near the position of the maximum magnetic pinch. Flow measurements were confirmed using a Mach probe. Measurements of the brightness, ion temperature and flow are also presented over a range of magnetic field and pressure conditions.

The purpose of this work has been to demonstrate the capability of this technique for measuring low temperature ion dynamics in helicon devices by reporting on ion temperatures and flows that are presently only accessible by standard diagnostics such as probes, spec-

trometers and laser induced fluorescence - each of which have numerous limitations. This thesis reports on a rich set of results and demonstrates that, with careful consideration to instrument design, coherence imaging can be extended to the study of ion features in cold plasmas. The developments reported in this thesis open opportunities for ion-dynamics measurements in laboratory-based plasmas across a range research areas.

# Acknowledgments

My sincere thanks goes to my PhD supervisor Professor John Howard for taking me on as a student, challenging me with new ideas and skills, and, for his never ending insight into plasma physics. I am also profoundly grateful to my co-supervisors Dr Cormac Corr and Dr Clive Michael for their support, guidance and encouragement throughout this project.

I thank also Mr Michael Blacksell, Dr Fenton Glass, and Professor Boyd Blackwell for the skills they have taught me and the technical conversations we have had. Your combined knowledge is incredible and has made a huge contribution to the development of my laboratory skills and general understanding of plasma systems and diagnostics. I would also like to say a personal thank you to Mr Mark Gwynneth for all the time that he spent modifying various holders and mounts for my optical system so that we could reach the stability and precision required for these measurements. Thanks also to Dr Juan Caneses and Dr Cameron Samuell for your friendship, training and giving me the confidence to use MAGPIE. A huge thanks also goes to Dr Alex Thorman, for his friendship and for some excellent conversations.

I would also like to extend my gratitude to Uyen, Lan, Luda and Karen for their unfailing support. Also, to my fellow PhD students Matt, Stuart, Jesse, Sam, Gavin, Kate, Amelia and friends in the research school thank you for your friendship and for sharing this experience with me.

To my dearest friends Alison, Roisin, Tara and Tess. Words cannot amount to the gratitude I feel. Thank you for maintaining the life balance, for your patience and for your unfaltering support and words of encouragement.

I would not have followed this path without the support and encouragement from my parents. Mum and Dad - thank you for inspiring me to make the most out of my schooling, encouraging me to follow science and for your support along the way.

Finally, to my wonderful husband Quan - thank you for standing by me all the way, for being my anchor, a listener, a voice of reason, for making me laugh and for giving me the support to make the most of this experience.

# Contents

# Table of Symbols

The following table lists the relevant symbols used within this thesis.

| Symbol | Description |
|---|---|
| $A_p$ | area of probe tip |
| $A(t)$ | amplitude of u(t), a complex scalar electric field |
| $\boldsymbol{A}$ | vector potential |
| $\alpha$ | angle on incidence |
| $B$ | birefringence |
| $\mathbf{B}$ | magnetic field |
| $\beta$ | angle of refracted ray |
| $\beta_H$ | the Hall parameter |
| c | optical axis |
| $c$ | speed of light |
| $c_S$ | sound speed |
| $\chi$ | axial viewing angle |
| D | Deuterium - hydrogen isotope |
| $D$ | distance from the final lens to the mid-plane |
| $d$ | lateral displacement between the ordinary and extraordinary ray |
| $\delta$ | angle between the optical axis and the plane of incidence (Veiras model) |
| $\delta_\phi$ | phase difference between two spectral lines |
| $\mathbf{E}$ | electric field |
| $\mathbf{E_H}$ | Hall field |
| $E$ | energy |
| $e$ | electric charge |
| $e(\xi, \boldsymbol{r}; \hat{\boldsymbol{l}})$ | line-integrated spectral line-shape |
| $\epsilon_T$ | thermal coefficient |
| $\epsilon_T^{EXP}$ | experimentally determined thermal coefficient |
| $\epsilon_\phi$ | small phase distortion |
| $\epsilon(\boldsymbol{r})$ | emissivity (local emission radiance) |
| $\eta_{ef}$ | optical efficiency |
| $\eta$ | mean phase term |
| $f$ | focal length |
| f | local reconstructed quantity of the Radon transform |
| F($j$) | discrete form of f over $j$ radial shells |
| $\mathbf{F}$ | matrix notation for F($j$) |
| $\check{\text{f}}$ | 1D projection quantity of the Radon transform |
| $\check{\text{F}}(i)$ | discrete form of $\check{\text{f}}$ over $i$ impact parameters |
| $\check{\mathbf{F}}$ | matrix notation for $\check{\text{F}}(i)$ |
| $\mathcal{F}$ | Fourier transform |

| | |
|---|---|
| $f_i(\boldsymbol{r}, \boldsymbol{V})$ | ion velocity distribution function |
| $g$ | grating groove period |
| $g_J$ | Lande g factor |
| $g(\xi, \boldsymbol{r}; \hat{\boldsymbol{l}})$ | local spectral lineshape |
| $G(\phi, \boldsymbol{r}; \hat{\boldsymbol{l}})$ | local spectral coherence (Fourier transform of $g(\xi, \boldsymbol{r}; \hat{\boldsymbol{l}})$) |
| $\gamma$ | ratio describing the optical wave dispersion through dual crystal plates |
| $\gamma(\phi; \hat{\boldsymbol{l}})$ | the line-integrated complex coherence |
| $h$ | the Planck constant |
| He | Helium |
| $I_0$ | spectrally-integrated and line-integrated irradiance of the plasma (brightness) |
| $I_{Cal}$ | calibration brightness |
| $I(\xi)$ | spectral distribution of the irradiance |
| $\mathfrak{I}$ | imaginary part |
| $\mathbb{I}$ | current |
| $\mathbb{I}_{\mathrm{D}}$ | downstream current |
| $\mathbb{I}_{\mathrm{U}}$ | upstream current |
| $\mathbb{I}_{\mathrm{e,sat}}$ | electron saturation current |
| $\mathbb{I}_{\mathrm{i,sat}}$ | ion saturation current |
| $\mathcal{J}$ | total angular momentum quantum number |
| $K_{DC}, K^+, K^-$ | carrier frequencies |
| $k_0$ | wavenumber |
| $k_{\mathrm{M}}$ | Mach probe calibration constant |
| $k_B$ | the Boltzmann constant |
| $\kappa$ | optical dispersion coefficient |
| $\kappa_T$ | optical dispersion coefficient for cell with multiple materials |
| $L$ | length |
| $\mathcal{L}$ | orbital angular momentum quantum number |
| $\boldsymbol{l}$ | line-of-sight |
| $\hat{\boldsymbol{l}}$ | unit vector along the line-of-sight |
| $\lambda$ | wavelength |
| $\lambda_0$ | central wavelength |
| $\Delta\lambda$ | spectral resolution |
| $\lambda_{De}$ | Debye length |
| $\lambda_{mfp}$ | mean-free-path |
| $m$ | mode number |
| $m_e$ | mass of an electron |
| $m_i$ | mass of an ion |
| $m_S$ | species mass |
| M | Mach number |
| $M$ | (dimension) number of projections |
| $\mathcal{M}$ | Magnetic quantum number |
| $\mu$ | magnetic moment |
| $\mu_B$ | Bohr Magneton |
| $n$ | refractive index |
| n | neutron |
| $N$ | (dimension) number of radial shells |
| $n_{\mathrm{E}}$ | extraordinary refractive index |

| | |
|---|---|
| $n_{\mathrm{O}}$ | ordinary refractive index |
| $n_{eff}$ | effective refractive index of the imaging filter |
| $n_e$ | electron density |
| $n_i$ | ion density |
| $\nu$ | frequency |
| $\nu_{i,n}$ | ion-neutral collision frequency |
| $\nu_0$ | central frequency |
| $\Delta\nu$ | frequency spread |
| $\omega_c$ | cyclotron frequency (subscript $i$ indicates the ion cyclotron frequency). |
| $\Omega$ | vorticity |
| $p$ | impact parameter |
| P | pressure |
| $\varphi$ | polar angle describing the line-of-sight |
| $\varphi_p$ | impact angle |
| $\phi$ | interferometric phase delay coordinate |
| $\phi_0$ | interferometric phase delay at the central frequency |
| $\phi_D$ | Doppler phase |
| $\phi_{DC}$ | DC component of the phase |
| $\hat{\phi}_0$ | group phase delay |
| $\Phi$ | potential |
| $\psi$ | angle describing the line-of-sight vector in the (x,y) direction |
| $q$ | species charge |
| $r_L$ | Lamour radius |
| $R$ | ratio of intensities |
| $R_p$ | probe tip radius |
| $R_{power}$ | resolving power |
| $\mathcal{R}$ | Radon transform |
| $\Re$ | real part |
| $S_{\pm}$ | interferometric signal ($\pm$ sign corresponds to the transmitted and reflected components, respectively) |
| $\mathcal{S}$ | Spin angular momentum quantum number |
| $\sigma$ | standard deviation |
| $\Sigma$ | a rectangular diagonal matrix with dimensions $N \times M$ which contain singular values of $\boldsymbol{W}$ |
| $t$ | time |
| T | Tritium - hydrogen isotope |
| $T_C$ | characteristic (instrumental) temperature |
| $T_e$ | electron temperature |
| $T_i$ | ion temperature |
| $T_S$ | species temperature |
| $\tau$ | time delay coordinate |
| $\theta'$ | polar angle in the rotated cylindrical co-ordinate system describing the plasma |
| $\vartheta$ | angle between the optical axis and the crystal interface (Veiras model) |
| $\Theta$ | angle between the line-of-sight and the azimuthal flow component |
| $\boldsymbol{U_M}$ | unitary matrix of dimension $M \times M$ in SVD |
| $\boldsymbol{U_N}$ | unitary matrix of dimension $N \times N$ in SVD |
| $u(t)$ | complex scalar electric field |

| | |
|---|---|
| $\boldsymbol{V}$ | flow velocity (units m/s) with components $(V_r, V_\theta, V_z)$ in cylindrical coordinates and also $(V_\parallel, V_\perp)$ which are parallel and perpendicular to the magnetic field $\mathbf{B}$. Additional subscript $i$ indicates ion flow. |
| $\mathbf{V}$ | emissivity-weighted flow velocity $\mathbf{V} = \epsilon(\boldsymbol{r})\boldsymbol{V}$ with components $(\mathrm{V}_r, \mathrm{V}_\theta, \mathrm{V}_z)$ in cylindrical coordinates. |
| $\boldsymbol{v}$ | normalised flow velocity $\boldsymbol{v} = \boldsymbol{V}/c$ (dimensionless) with components $(v_r, v_\theta, v_z)$ in in cylindrical coordinates. |
| $\mathbf{v}$ | normalised and emissivity-weighted flow velocity |
| $\boldsymbol{V}_C$ | characteristic velocity |
| $V_{th}$ | thermal speed (subscript $i$ indicates the ion thermal speed) |
| $v_{th}$ | normalised thermal velocity $(V_{th}/c)$ |
| $V_{msr}$ | measured velocity component |
| $\boldsymbol{v}_D$ | normalised drift velocity. $v_D = \boldsymbol{v}_D \cdot \hat{\boldsymbol{l}}$ is used for the drift component along the line-of-sight |
| $\mathbb{V}$ | voltage |
| $\mathbb{V}_\mathrm{f}$ | floating potential |
| $\mathbb{V}_\mathrm{P}$ | plasma potential |
| $W(i,j)$ | weight function |
| $\boldsymbol{W}$ | matrix notation for $W(i,j)$ |
| $\xi$ | normalised frequency |
| $\xi_{th}$ | normalised thermal frequency |
| $\zeta$ | interferometric fringe contrast |
| $\zeta_D$ | Doppler fringe contrast |
| $\zeta_0$ | Instrumental fringe contrast |

A list of other useful symbols are described below.

| Symbol | Description |
|---|---|
| $\boldsymbol{x}$ | position vector describing the plasma with coordinates $(x, y, z)$ |
| $\boldsymbol{r}$ | position vector describing the plasma with coordinates $(r, \theta, z)$ |
| $i, j, n, k, s, \ell$ | index values |
| $^{\mathbf{2}s+\mathbf{1}}\boldsymbol{L}_{\boldsymbol{J}}$ | term symbol |

# Introduction

Plasma is the fourth state of matter and makes up 99% of the visible universe [1]. The breakdown of gas into the plasma state can occur through the presence of strong electric fields which acts to accelerate electrons leading to collisions and the ionisation of the gas molecules. Space phenomena including the solar wind and the solar corona [2–4], and terrestrial phenomena such as the Earth's plasmasphere, lightning, the aurora and Saint Elmo's fire [5–8] are all examples of naturally occurring plasmas.

Early investigations into plasmas included whistler waves which were heard over radio broadcasts during the second world war. Whistlers were identified as electromagnetic plasma waves propagating in the Earth's ionosphere and were first studied by Helliwell [9]. Current investigations into plasmas range from fundamental research into space and atmospheric plasma phenomena to novel commercial applications such as plasma etching for the manufacture of microelectronic and optoelectronic devices [10] and the development of specialised plasma driven devices such as laser-plasma accelerators [11] and plasma thrusters [12]. There is particular interest also from a materials science perspective where materials exposed to plasma can result in etching or deposition of thin films which can have particular electrical or structural properties. This is particularly important in the development of biomaterials including those used in bone tissue replacement or for materials interacting directly with the nervous system [13].

Of course, another key area of research is the pursuit of fusion energy, which, using plasma technology can allow the fusion process to be recreated on a terrestrial scale. Harnessing such a reaction offers exciting potential as a sustainable world energy source [14].

## 1.1 The fusion reaction

Nuclear fusion, is the process when two or more atomic nuclei are combined together to produce a heavier atomic nuclei and a release of energy. In the sun, the p-p fusion chain (where hydrogen isotopes are converted to helium) is the dominant fusion reaction responsible for the suns glow and heat. In these reactions, two positively charged protons are pushed together, overcoming the coulomb repulsion force, so that the nuclei fuse together to form an $\alpha$ particle ($^4$He) and a release of energy. The Suns high temperature (plus gravity which causes immense pressure resulting in a further increase in the suns

core temperature) provides enough energy that the sun is able to lose 5 million tonnes of its mass every second to radiation through this reaction. There is more than 1 million times more energy released in the fusion reaction compared with conventional chemical reactions. For example, 1 kg of fusion fuel is equivalent to the energy output of burning $\sim 4100$ tonnes of oil or $\sim 6600$ tonnes of coal. On top of this, the fusion reaction has very little waste and does not have any $CO_2$ emissions, making it an ideal candidate to replace conventional coal fueled power stations.

There are however challenges in recreating the fusion reaction on a terrestrial scale. Without the aid of the suns gravity, the temperature required to ignite the fusion reaction is on the order of 100 million degrees. This is around $5 - 10$ times hotter than the core of the Sun. Fortunately, the fusion reaction occurs in the plasma state and because plasmas consist of charged particles, they are responsive to electric and magnetic fields. This aids in the confinement of the fusion process.

The fusion reaction that is most suitable for power generation is,

$$\mathrm{D} + \mathrm{T} \rightarrow {}^{4}\mathrm{He}\ (3.5\ \mathrm{MeV}) + \mathrm{n}\ (14.1\ \mathrm{MeV}) \tag{1.1}$$

Here, D is deuterium, an isotope of hydrogen that is found in heavy water and T is tritium, another hydrogen isotope which, although doesn't occur naturally on Earth, can be created from lithium - an alkali metal which can be extracted from seawater and many kinds of naturally occurring rocks. The neutron released, n, carries 80% of the energy and as it is uncharged it will not be affected by any electric or magnetic confinement fields. This neutron can be trapped in a blanket of lithium to breed more tritium and heat a water reservoir for standard steam-turbine energy conversion.

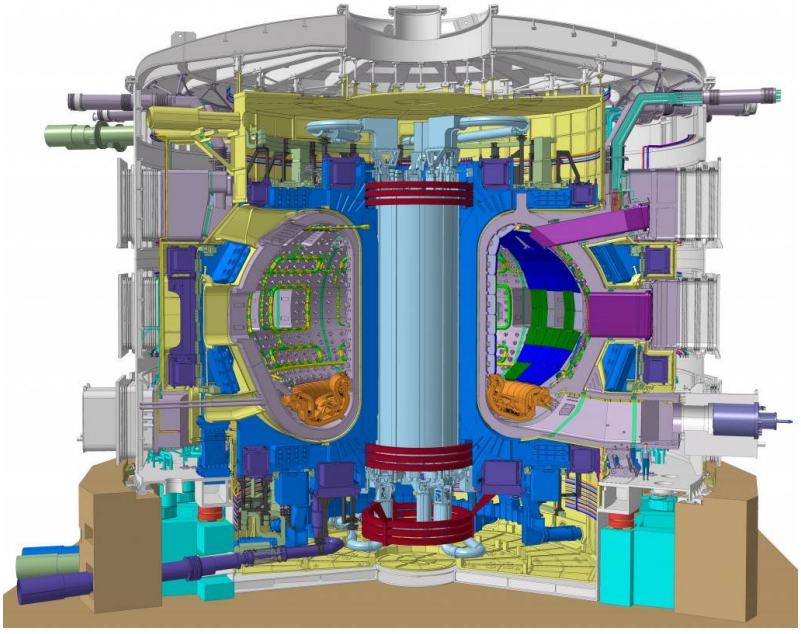

**Figure 1.1**: Diagram of the ITER tokamak. This image has been reproduced from [15].

Tokamaks are magnetic fusion devices designed to contain the fusion reaction. The ITER reactor will be the largest tokamak in the world and is scheduled to hold its first plasma in 2025. A diagram of the ITER tokamak is shown in figure 1.1. ITERs mission is to produce 10 times the amount of output energy compared to the input energy and produce a deuterium-tritium reaction that is sustainable through internal heating. This device will demonstrate the integration of fusion technologies and test engineering performance and new components required for functional reactors [16].

The design of ITER relies heavily on the discoveries from other tokamak devices currently in operation. The Joint European Torus (JET) [17] in UK is currently the largest tokamak in operation and provides research into plasma processes and scaling laws for reactor size devices as well as investigating various heating techniques such as RF heating and neutral beam injection. The JET tokamak is currently the only tokamak licensed to hold deuterium-tritium plasmas and as such is key in investigating alpha-particle production and plasma confinement for fusion fuel.

## 1.2 Divertor research

In order to maintain a stable confined fusion plasma, particle exhaust must be removed from the bulk of the reactor. This is controlled by an area called the divertor which is located at the base of the tokamak vessel (see the orange components in figure 1.1). Outside the last closed flux surface, in the scrape off layer, the magnetic field lines are open and channel fusion waste out of the plasma volume and onto the divertor plates. This means that this component of the reactor needs to endure high heat flux ($\sim 10$ MW/m$^2$) [18]. A design of the ITER tokamak divertor is shown in figure 1.2. The ITER divertor is water cooled to remove the heat and is fitted with tungsten plates which has the highest melting point of all metals and therefore can best tolerate large particle and heat flux, minimising sputtering erosion and radiation effects from escaping neutrons. For working reactors the divertor will be responsible for removing $\sim 15\%$ of the total thermal power from the fusion reaction and the design of the divertor will be paramount in maximising the efficiency of the power conversion from the fusion reaction into a viable power source [18]. As such, research into various materials and divertor geometry is an active area of research.

The MAGnetised Plasma Interaction Experiment (MAGPIE) at the Australian National University is a linear helicon plasma device capable of recreating the conditions found in the divertor region of tokamaks [19]. This device is used to study plasma-materials interactions for characterising materials suitable for use in high plasma bombardment areas. It is also suitable for studying fundamental plasma behaviour such as instabilities and various wave phenomena.

Factors such as plasma flow, temperature and density are key in understanding the plasma behavior around the divertor. Additionally, gas flow rate, contamination from impurities, power coupling and chamber geometry have all been shown to effect the equilibrium properties (density, flow, temperature, ionization) of a plasma. Deviation from thermodynamic equilibrium can also drive instabilities which can disrupt the plasma stability [20]. As such, understanding the connection between these factors and plasma behavior is particularly

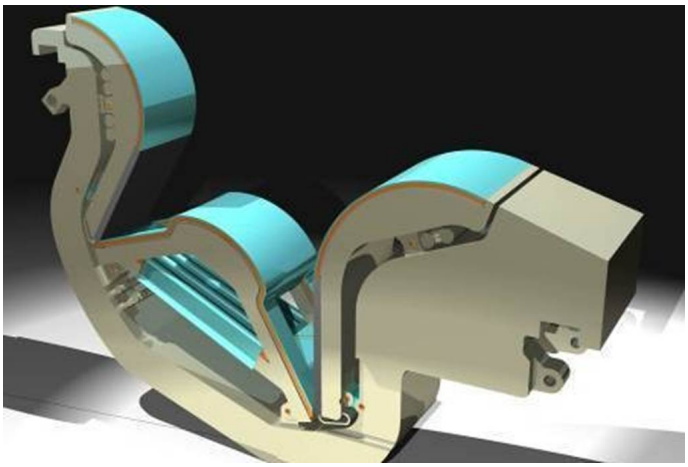

**Figure 1.2:** Diagram of the divertor region in a tokamak. This image has been reproduced from [15].

important when designing plasma systems. Research undertaken in smaller helicon devices such as MAGPIE offers the flexibility to characterise plasma behaviour over various gas types, fill pressures, magnetic field configurations and power coupling without the complicated chamber geometry and magnetic field structures, multiple heating sources, mode transitions and high operating costs associated with large fusion-related devices.

## 1.3 A brief introduction to helicon plasmas

Helicon plasmas are usually contained in linear chambers and radially confined using an axial magnetic field. Input power is coupled to the plasma though an antenna supporting a right-hand-polarised radio frequency wave and operates between the ion- and electron-cyclotron frequencies. The helicon antenna used on the MAGPIE chamber is shown in figure 1.3.

Helicon plasma devices are known to exhibit three modes of operation [21]. At low power, a plasma is generated at or below atmospheric pressures by a simple pair of electrodes is called a capacitively coupled plasma (E-mode). The potential difference between the electrodes and the small mean free path of the electrons allows for collisions within the gas resulting in a breakdown into plasma state.

The inductive mode (H-mode) operates at intermediate powers. An inductive plasma is a created using a time varying electric current which when passed through the antenna results in time varying magnetic field. In turn this induces an electric field within the gas resulting in a plasma.

The third (high power, W-mode) is the helicon mode, where the plasma is created by the propagation and absorption of electromagnetic waves within the gas. The primary mechanism of excitation is electron Landau damping, where the group velocity of the helicon wave is slightly faster than the velocity of the electrons causing energy transfer

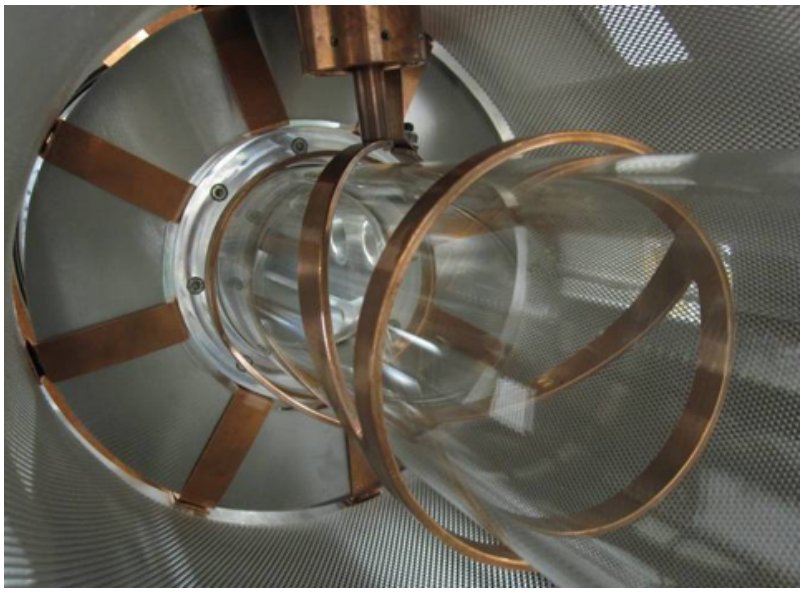

**Figure 1.3:** Antenna for the MAGnetised Plasma Interaction Experiment (MAGPIE). Photo provided through the courtesy of Dr Cormac Corr.

from the wave to the plasma [22]. Transition between the modes depends on the skin depth of the antenna RF field [23]. Helicon plasmas are known for their intense core brightness in the high power mode and have been found to produce high density plasmas ($10^{18}$ m$^3$) compared with those of the inductive ($10^{16}$ m$^3$) and capacitive ($10^{17}$ m$^3$) types operating at the similar power conditions with varying magnetic field [24, 25].

A particular area of interest for fusion research (and plasma studies in general) is ion behavior within confinement devices. Ions play an important role in plasma transport, driving (and mitigating) instabilities and in plasma heating. However, fully characterising ion behavior is an on-going area of investigation. Some of the key developments in experimental ion studies are now summarised. In general many of the experiments cited here have been performed using argon as the fill gas. Argon is an inert gas and generally has only a simple excitation pathway which makes results simpler to interpret compared with gases such as hydrogen.

The Hot HELIcon eXperiment (HELIX) and the Large Experiment on Instabilities and Anisotropies (LEIA) at the West Virgina University in the USA are two (connected) plasma devices which are driven by a helicon antenna and able to generate high beta fully magnetised plasmas. The HELIX-LEIA device has been instrumental in characterising anisotropic ion heating between the temperature components parallel and perpendicular to the magnetic field. In the works of Scime [26] and Kline [27, 28] the perpendicular ion temperature was found to increase 10 times that of the parallel component and the perpendicular ion temperature was linearly dependent on the magnetic field. These temperature studies showed that the perpendicular ion temperatures were peaked and correlated with the lower hybrid frequency and this lead to the understanding that heating of the perpendicular ion temperature was a result of ion Landau damping which occurs due to a resonance between the slow component of the helicon wave (known as the Trivelpiece-Gould mode) and the lower hybrid frequency [29]. This causal relationship was later

experimentally demonstrated [30].

The HELIX device has also been used measure axial ions flows in argon plasma along the magnetic field on the order of the thermal speed [28]. In this same study, measurements of the azimuthal flow showed that the core of the plasma exhibits bulk rotation while the edge region is sheared and could excite various plasma instabilities. Studies in argon have shown that ions also flow radially outward ($\sim 400$ m/s at the edge of the discharge) [31]. Flows studied over pressure and into expanding magnetic field regions have revealed a dual ion-population exists, where a fast group of ions were accelerated out of the high magnetic field region at velocities at super-sonic speeds through the slow (subsonic) background population [32]. Later work in this area has presented measurements of a bi-modal ion velocity distribution function (IVDF) in this expansion region. The results also show significant temperature anisotropy in the fast ion population [33]. The acceleration of multiple ions populations was later observed in the diverging magnetic field region and was found to be accompanied by multiple spontaneous current-free double layers [34].

The Controlled Shear De-correlation eXperiment (CSDX) at the University of California in Sandiago USA is another a linear helicon driven plasma which runs at the same operating conditions as found in the scrape-off layer of tokamaks. Research using this device has contributed significantly to the knowledge of the drift wave - zonal flow interaction. Drift wave instabilities arise in the presence of density or ion temperature gradients and can drive poloidally and toroidally sheared flows in tokamaks. They are also believed to be responsible for loss of particles and energy in magnetically confined toroidal plasmas. Sheared azimuthal flows, rotating in the electron diamagnetic drift direction, have been measured on CSDX and experiments have shown a reversal in the azimuthal flow at large radii for maximum magnetic field strengths [35]. Measurement of broad-band electrostatic potential fluctuations in the range of $3-4$ kHz and $25-35$ kHz have been shown to have peak amplitude at the same location as the flow shear, and are consistent with resistive drift waves [36, 37]. Studies have indicated that the end-plate boundary conditions (insulating vs conducting) play a role in the levels of drift wave saturation and this in turn affects the azimuthal sheared flow [38]. The ion temperature was observed to be centrally peaked and increased with magnetic field which was indicative of reduced heat transport [38].

The Versatile Instrument for studies on Nonlinearity, Electromagnetism, Turbulence and Applications (VINETA) at the Max Planck Institute for Plasma Physics in Berlin is a collisional helicon plasma device deployed for studying plasma waves and instabilities under various pressure regimes. Studies on this device have also confirmed low-frequency fluctuations which have been identified as drift waves along with $\mathbf{E} \times \mathbf{B}$ rotational flows in the ion diamagnetic direction [39].

There is a cross-over between devices such as HELIX and CSDX and those such as the Variable Specific Impulse Mgnetoplasma Rocket (VASMR) and the Magnetic Nozzle eXperiment (MNX) which use helicon plasmas to focus on plasma flow and confinement properties for plasma thruster performance. As such, the devices mentioned here not only have applications to the fusion community, but can also deliver insights into other areas of research such as thruster development, space plasma phenomena and plasma materials processing, where high density helicon sources have also found to have important roles.

## 1.4 Diagnostics for plasma studies

Understanding plasma behavior relies on diagnostics ranging from simple probe measurements to highly sophisticated multichannel time-resolved systems able to measure spatially and dynamically resolved plasma features.

Probe measurements are usually cheap and fast to employ, and, depending on the application, can often deliver high temporal resolution when studying dynamic features. A variety of probe designs allow access to information including, but not limited to, the electron temperature, density, plasma and floating potentials, electron and ion saturation currents and the electron energy distribution function. Probes are used to study both equilibrium plasmas as well as dynamical features such as sheath formation, turbulence and plasma instabilities. The spatial resolution, however, is often limited to the reproducibility of the plasma and chamber accessibility. The interpretation of probe results is also difficult and is often left to the discretion of the theoretical model employed and can be affected dramatically by the interaction of the probe and the plasma.

Spectrometers and interferometers are non-perturbative diagnostics which measure features of the plasma light. Spectral features such as wavelength and intensity are unique to each plasma and can be measured to identify fundamental plasma properties. For instance, the prominence of particular spectral lines is determined by the dominant atomic interactions and plasma species composition. Fluctuations in the emission light can be measured to identify plasma-wave phenomena and, asymmetries in the intensity profile can be used to identify spatial features such as wakes from streaming particles. Brightness is also linked to plasma density and electron temperature. Spectral line broadening and shifting (through Zeeman and Stark effects) can be measured to determine the plasma ion temperature and flows and, internal magnetic and electric field structures. These instruments are limited by light throughput and so measurements of fast dynamic plasma features can be challenging. Also, post analysis of raw data is required in these measurements (such as demodulation, interpretation of line-integration effects and/or calibration using black and uniform light sources) in order to accurately extract the measurement.

Laser Induced Fluorescence is a diagnostic technique used to excite electronic transitions in species (such as neutrals or ionised particles) within the plasma using a laser tuned to the transition frequency. The excited species will decay releasing photons which are captured by a detector, positioned at a right angle to the laser beam leading to spatially well-resolved measurements. Transition energies between energy levels are usually quite unique to a particle species and so by tuning the laser to the correct wavelength, a single transition can be excited, making this technique highly selective in the species it investigates. To date, many of the measurements of IVDF such as anisotropic temperatures, edge peaked temperatures sheared flows and IVDFs have been achieved using LIF. Unfortunately LIF is an expensive technique and as such is not always available for standard laboratory studies.

The benefits and disadvantages of each of these techniques for measuring the ion velocity distribution function in helicon plasmas are summarised in 1.4 (coherence imaging is included here for comparison).

| Diagnostic | Advantages | Disadvantages |
|---|---|---|
| **Probes** | • Relatively inexpensive and can be built using standard laboratory materials<br>• High temporal resolution – good for studying dynamic features<br>• directly delivers information about the local plasma (don't need to consider line integration) | • Usually single point measurement (requires many measurements to study a spatial region and/or IVDF)<br>• Usually requires prior knowledge about the plasma or a model to interpret data<br>• Can perturb and interact with the plasma making results difficult to interpret<br>• Can experience instrumental degradation due to plasma exposure |
| **Spectrometers** | • Allows for 2D measurements where 1 dimension captures spatial details<br>• Non-perturbative<br>• Directly measures the spectral scene | • Low light throughput (limits spectral resolution)<br>• Only 1 spatial channel as other channel is reserved for spectral information<br>• Delivers line-integrated measurements and will need to be tomographically inverted in order to infer local plasma features |
| **Interferometers** | • High light throughput<br>• Allows for 2D measurements where both dimensions capture spatial details<br>• Non-perturbative | • Sensitive to vibrational noise which limits resolution in the visible frequencies<br>• Requires demodulation and calibration against a known source<br>• Generally require multiple measurements over varied interferometric delay to determine details about the IVDF |
| **Laser Induced Fluorescence (LIF)** | • High spatial accuracy – directly delivers information about the local plasma (don't need to consider line integration)<br>• Delivers direct measurements of the IVDF<br>• Uniquely selective of the plasma species for consideration | • Expensive and therefore not always available for standard laboratory studies<br>• Usually requires multiple measurements to study a spatial region |
| **Snapshot Coherence Imaging** | • High light throughput<br>• Allows for 2D measurements where both dimensions capture spatial details<br>• IVDF details can be captured in a single measurement<br>• Can be used for studies of dynamic plasma features<br>• Inexpensive compared to LIF systems and can be built using laboratory materials<br>• Non-perturbative | • Requires demodulation and calibration against a known source<br>• Requires careful consideration to thermal stability and contamination (to be discussed in following chapters)<br>• Delivers line-integrated measurements will need to be tomographically inverted in order to understand local plasma |

**Figure 1.4:** Summary of the advantages and disadvantages of various diagnostic tools for measuring the IVDF in helicon plasmas.

## 1.5 Motivation for this work

Over recent years, an interferometer for Doppler imaging has been developed at the Australia National University [40–44]. These instruments have been coined 'snapshot systems' because they are able to capture, in a single image, a 2D spatial map of plasma spectral features. These instruments have successfully been deployed to study spectral effects on fusion focused devices [45–47] however the opportunity arises now to apply these sophisticated systems to study plasma features on a cooler laboratory plasma. The potential ease of access to plasma spectral information along with the low cost mean that these systems could be a valuable new diagnostic tool for studies on linear devices aiding fusion studies and also non-fusion plasma research centers. The delivery of simultaneous and highly resolved spatial scans of Doppler features along with the ability to discern non-Maxwellian properties of the ion velocity distribution function will be especially valuable in fields such as divertor research.

The focus of this work is therefore to adapt the current design of the snapshot coherence imaging system so that it is suitable for low temperature plasma studies. The imaging system here is designed to fit the argon plasma conditions of MAGPIE and is deployed to study the equilibrium brightness, ion temperatures and flows accessed through the emission intensity and the Doppler broadening and shifting of the spectral line. The low temperatures ($\sim 1$ eV) and slow ion velocities ($< 1000$ m/s) expected in MAGPIE require high resolving power which, in turn, require additional features, such as thermal stability and on-line calibration, to the current systems designed for fusion plasmas. These features along with operation and performance details are addressed in this work. The brightness, ion temperature, azimuthal and axial flow is then surveyed across a range of gas pressures and magnetic field configurations. For validity, the flow results of coherence imaging are compared to those acquired using a Mach probe. A key aspect of this work is also to assess the effects of line-integration for measurements of inhomogeneous plasmas. This is examined using tomographic reconstruction techniques.

This study will demonstrate that coherence imaging can deliver a rich set of measurements of Doppler features in linear plasma devices. Measurements of the ion brightness, temperature and flows are taken of an equilibrium helicon plasma across a variety of plasma conditions. These measurements will be compared to those reported in other linear devices to demonstrate the capabilities of this diagnostic as a new tool for low temperature ion studies.

Chapter 2

# Spectroscopic and probe diagnostics on MAGPIE

Plasma spectral emission is caused by the excitation of ions and neutrals following collisions with other particles in the plasma. These emissions contain a wealth of information about the plasmas natural state including density and composition of the plasma, electron and ion temperatures, particle flows and the presence of electric and magnetic fields. Spectroscopic instruments are well known techniques of determining such features from spectral light. These techniques are labeled as non-perturbing as they generally do not disrupt the natural state of the emission source and as such these techniques are widely used in plasma research. Coherence imaging is a type of spectroscopic technique that is based on interferometry and is able to capture a 2D image of the plasma spectral features. The first half of this chapter introduces the relevent theory behind spectroscopic measurments in plasmas.

Mach probes are a common diagnostic tools for measuring ion flows in plasmas. In this study, a Mach probe is used to validate the flow results delivered by the coherence imaging system. The background theory for probe measurements in plasmas is presented in the second half of this chapter.

## 2.1 Spectroscopic diagnostics in plasmas

This work uses coherence imaging to measure the Doppler shift and broadening of spectral lines to determine the ion temperature and flow in a cold plasma. This section reviews the development of the coherence imaging system as well as the principles behind this technique and the theory of Doppler measurements.

### 2.1.1 The Doppler effect

Spectroscopic instruments measure light in either the spectral or temporal domains. In the spectral domain, light is broken into a spectrum of its fundamental frequency components and described by frequency coordinate $\nu$. Such information is accessible using spectroscopy

or laser techniques such as Laser Induced Fluroescence (LIF). In the temporal domain, the light is a correlation of radiation fields (a complex quantity called the coherence) and is considered according to the time delay coordinate $\tau$ between these fields [48] which can be measured using interferometry.

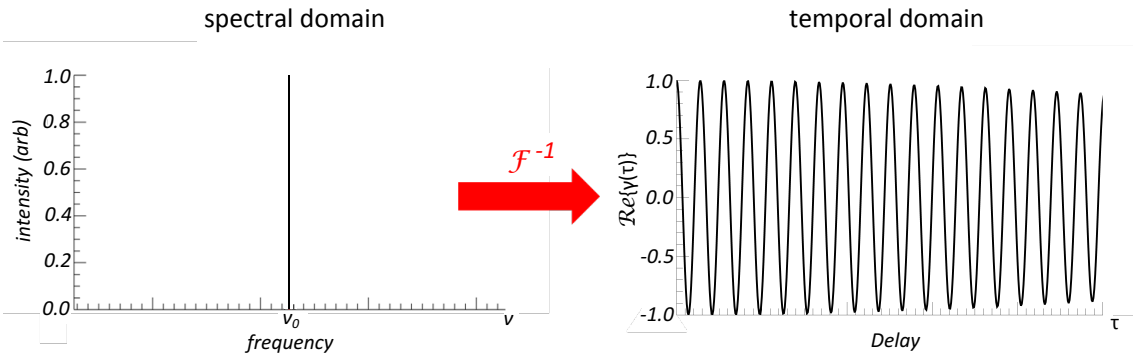


**Figure 2.1:** Left) the power spectrum showing spectral line of a monochromatic emission at emission frequency $\nu_0$. Right) The inverse fourier transform of the power spectrum is the complex coherence, the real part of which is plotted as a function of delay.

The two domains are connected via the Fourier transform as illustrated in figure 2.1. Shown here, a coherent light source, such as a laser, emits monochromatic light (single frequency). In the spectral domain (left plot in figure 2.1) this source approximates a delta-function, while in the temporal domain (right plot in figure 2.1) the coherence oscillates with delay due to the interference between the radiation fields.

The Doppler shift in frequency due to motion of the source, $\nu$, assuming the emitting species are moving much slower than the speed of light, (which is generally the case for radiating ions), is given by the non-relativistic Doppler shift formula,

$$\nu = \nu_0 \left( 1 - \frac{\boldsymbol{V} \cdot \hat{\boldsymbol{l}}}{c} \right) \tag{2.1}$$

Where $\nu_0$ is the central (stationary) emission frequency and $\boldsymbol{V} \cdot \hat{\boldsymbol{l}}$ is the speed of the source (in the direction of view $\hat{\boldsymbol{l}}$). A shift in the emission line away from the central emission frequency results in a shift in the phase, $\phi_D = 2\pi\Delta\nu\tau$, of the coherence in the temporal domain (see figure 2.2).

The emission Doppler broadening is a statistical effect caused by the thermal motion of the hot particles. The width of the distribution is determined by the source temperature. To illustrate this, model emission lines are compared for cold and hot plasma sources and are shown in figure 2.3. The cold source (black) emits exactly at the frequency $\nu_0$ and therefore has a long coherence length in the temporal domain. The hotter source (yellow) emits at a spread of frequencies around the central frequency and these off-centre frequencies result in phase mixing at higher delays, degrading the coherence in the time domain. By measuring the amplitude 'envelope' in the coherence, it is possible to determine the Doppler broadening, and hence the source temperature.

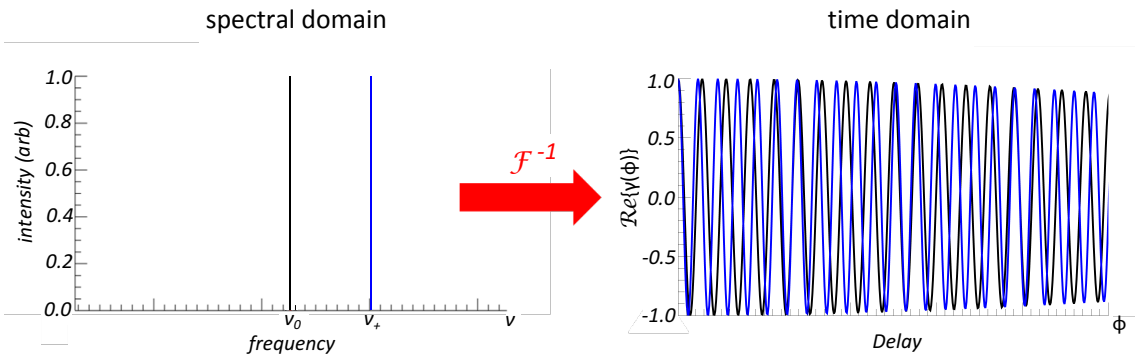


**Figure 2.2:** Left) the spectral lines for a monochromatic light source (black) which has had the frequency 'blue-shifted' (blue) due to movement of the source towards the observer. Right) the coherence plots for the the unshifted (black) and blue-shifted (blue) sources. There is a phase shift between the two coherence plots. due to the change in frequency.

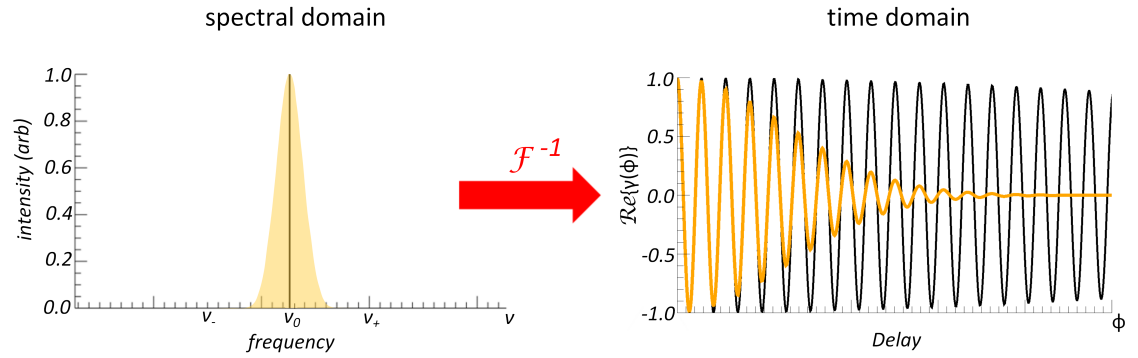


**Figure 2.3:** Left) the emission line of a cold coherent source (black) and the Doppler-broadened emission line for a hot quasi-monochromatic source (yellow), is shown. Right) the coherence from the cold source (black) has a near-constant amplitude while the signal generated by the quasi-monochromatic 'hot' source (yellow) has a rapid decrease in the signal amplitude with delay.

In general, the Doppler broadening is determined by measuring the standard deviation $\sigma$ of the line shape. This can be related to the temperature of the species, $T_S$, using the relationship

$$\sigma = \sqrt{\frac{k_B T_S}{m_S c^2}} \nu_0 \tag{2.2}$$

where $\nu_0$ is the central emission frequency, $m_S$ is the mass of the radiating species and $k_B$ is Boltzmann's constant.

### 2.1.2 Spectroscopy

Optical spectrometers are instruments designed to study light by dispersing the emission into its wavelength components. The main components of a Czerny-Turner spectrometer

are shown in figure 2.4. The basic operation of a spectrometer is is to sample the light source though a narrow slit which illuminates a diffraction grating. The light rays hitting the diffraction grating are collimated. The grating splits the components of light into a spectrum of wavelength components which are then relayed onto a screen for viewing. The resolution is determined by the entrant slit width [49] and grating groove period, $g$ through

$$\sin\alpha + \sin\beta = m\lambda/g \tag{2.3}$$

where $m$ is the mode number, $\lambda$ is the wavelength and $\alpha$ and $\beta$ are angles between the normal vector of the diffraction grating and the incident ray and refracted ray, respectively.

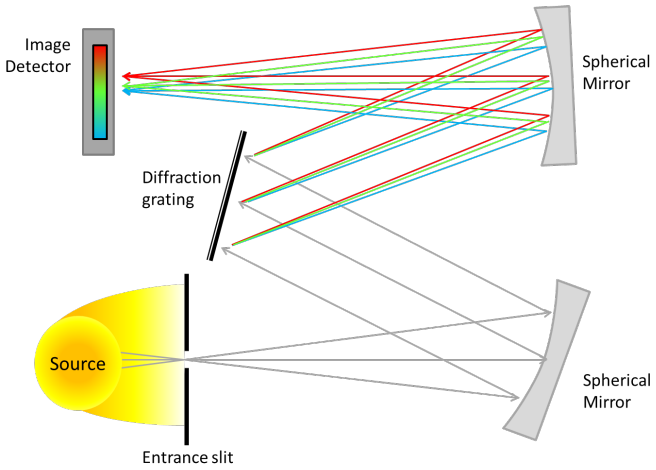


**Figure 2.4:** Operational components of a Czerny-Turner spectrometer. Light from a source enters through a narrow entrant slit and is collimated by a spherical mirror which directs the light onto a diffraction grating. The grating splits the light, transmitting the wavelength components at different angles. These are then focused by a secondary spherical mirror onto an imaging detector.

This type of spectrometer offers the possibility to directly study spectral line shifts and broadening due to the Dopper, Zeeman or other effects. Coupled with a 2D detector array such as a CCD screen, spectrometers use one dimension to encode the spectrum while reserving the other dimension for a spatial scan.

For a plasma moving at velocity $\boldsymbol{V}\cdot\hat{\boldsymbol{l}}$, the resolving power required to detect the Doppler shift in the spectral line is given by $R_{power} = \lambda/\Delta\lambda = c/\boldsymbol{V}\cdot\hat{\boldsymbol{l}}$, where $c$ is the speed of light and $\Delta\lambda$ is the spectral resolution. Considering the expected parameters for the MAGPIE plasma in this study: for argon ions moving at 1000 m/s the required resolving power will be $3\times10^5$. For measurements of such features in the visible wavelength range (350 to 600 nm m/s), the required spectral resolution needs to be on the order of $\Delta\lambda \approx 10^{-3}$ nm.

Standard spectrometers operate with slit widths between 5 $\mu$m and 200 $\mu$m and have typical spectral widths on the order of $< 0.1$ nm. This is therefore not small enough to resolve plasma Doppler spectral features for the MAGPIE plasma when measuring emission in the visible wavelengths. In order to achieve the necessary resolution, a spectrometer would require very a narrow slit-width resulting in extremely low light-throughput.

### 2.1.3 Interferometry of quasi-monochromatic light

Interferometers are devices which cause two or more waves of light to interfere. Interferometers used in plasma studies include, but are not limited to, mechanical interferometers of the Michelson-Morley, Mach-Zehnder and Fabry-Periot [49] type which require movable components and rely on a spatial variation between branches of the device to introduce the delay between the orthogonally polarised components of the light.

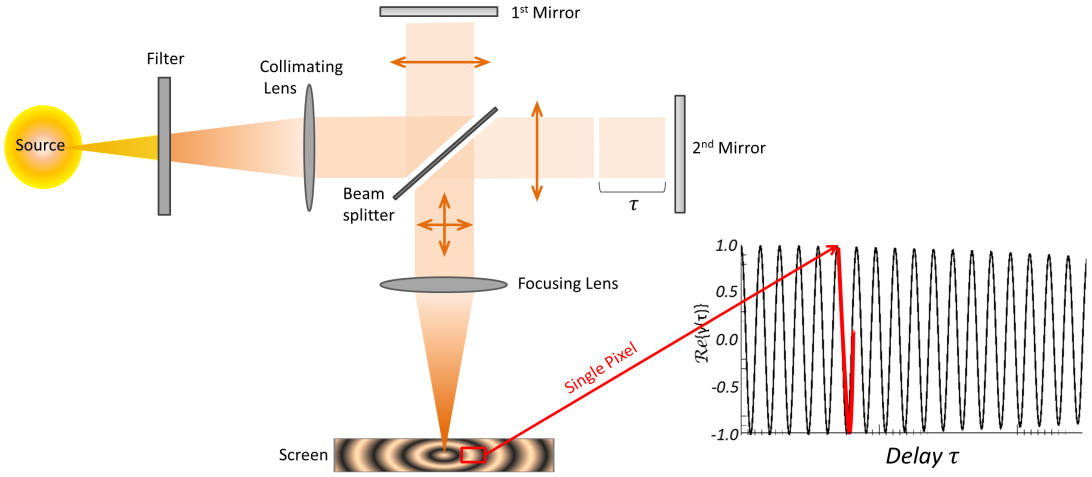


**Figure 2.5:** Standard components of a polarising Michelson-Morley interferometer, showing how light is channeled through the instrument and combined onto the screen to form interference fringes. By following the light emission of a single pixel as the delay $\tau$ is increased will give the contrast and phase associated with the coherence.

A Michelson-Morley interferometer is shown in figure 2.5. Quasi-monochromatic light is selected from a light source using a filter and is then passed through a beam splitter so that each of the components are transmitted along one arm of the instrument. The components are reflected by a mirror and recombined at the beam splitter. The light is focused by a lens onto a screen. When the lengths of the arms are equal the light recombines in phase. When the length of one of the arms is extended, there is a time delay, $\tau$, introduced between the two orthogonal components. The components now interfere on recombination causing the intensity image on the screen to split into a series of light and dark circular fringes. The circular fringes are caused by slight difference in $\tau$ due to angular effects from the dispersion of the light through the lens.

Features such as shifts and broadening of the spectral line are related to changes in the phase and contrast (envelope) of the coherence and can be determined using a Michelson-Morley type interferometer using the plasma emission as the source. A standard set-delay interferometer is able to sample the coherence at the fixed delay. Interferometers which scan the coherence by varying the delay between the emission components are called Fourier transform interferometers.

The following discussion on the interferometer for measuring spectral shifts and broadening is based on established theory presented in [48] and [42]. The interferometric signal for a

given pixel on the screen at delay $\phi = 2\pi\nu\tau$, is given by

$$S_{\pm}(\phi) = \frac{I_0}{2}\big(1 \pm \Re[\tilde{\gamma}(\phi)]\big) \tag{2.4}$$

where $I_0$ is the spectrally integrated irradiance of the incident beam (the amount of light collected by the interferometer over all wavelengths) and $\tilde{\gamma}(\phi)$ is the phase dependent complex-coherence. The $\pm$ indicates the transmitted and reflected signal components, respectively.

For an incident field $u(t)$, the spectrally integrated irradiance and the complex coherence are defined as $I_0 = \langle uu^* \rangle$ and $\tilde{\gamma}(\phi) = \langle u(t)u^*(t+\tau)\rangle / I_0$ respectively. The brackets denote the time average.

The Wiener-Khinchine theorem states if $u(t)$ has a Fourier transform given by $U(\nu)$, then its autocorrelation function $\langle u(t)u^*(t+\tau)\rangle$ will have the Fourier transform, $|U(\nu)|^2$, which is equal to the power spectrum of the radiation i.e.

$$\tilde{\gamma}(\tau) = \frac{1}{I_0}\int_{-\infty}^{\infty} |U(\nu)|^2 \exp(i2\pi\nu\tau)\, d\nu \tag{2.5}$$

The power spectrum $I(\nu) = |U(\nu)|^2$ of the emission field $u(t)$ describes the intensity contributed from each of the different frequencies in the frequency spread $\Delta\nu$ present in the emission.

Considering a quasi-monochromatic light source, where the spectral line has a central frequency $\nu_0$ and has a small spread, $\Delta\nu << \nu_0$, the complex scalar electric field may be written as an analytic signal

$$u(t) = A(t)\exp(i2\pi\nu_0 t) \tag{2.6}$$

Where the amplitude, $A(t)$, varies slowly with respect to the complex phasor.

For the snapshot polarisation interferometers used in this work, the emission must pass through birefringent optics which can result in optical dispersion effects. The time delay is therefore a function of frequency $\tau(\nu)$ and the phase $\phi = 2\pi\nu\tau(\nu)$ can be approximated as a first order Taylor series expansion

$$\phi = 2\pi\left(\nu_0\tau_0 + \left(\tau_0 + \nu_0\frac{d\tau}{d\nu}\right)(\nu - \nu_0)\right) = \phi_0 + \kappa\phi_0\xi \tag{2.7}$$

where $\tau_0 = \tau(\nu_0)$. The phase delay at the central frequency is $\phi_0 = 2\pi\nu_0\tau_0$ and $\xi = (\nu - \nu_0)/\nu$ is a normalised frequency difference coordinate. The constant $\kappa$ describes the

optical dispersion in the delay

$$\kappa = \left(1 + \frac{\nu_0}{\tau_0}\frac{d\tau}{d\nu}\right) \tag{2.8}$$

Allowing for dispersion and changing the variable of integration the complex coherence may be rewritten as

$$\tilde{\gamma}(\phi_0) = \frac{\exp(i\phi_0)}{I_0}\int_{-\infty}^{\infty} I(\xi)\exp(i\hat{\phi}_0\xi)\ d\xi \tag{2.9}$$

$$= \gamma(\phi_0)\exp(i\phi_0) \tag{2.10}$$

where $\hat{\phi}_0 = \kappa\phi_0$ is the group delay and

$$\gamma(\phi_0) = \frac{1}{I_0}\int_{-\infty}^{\infty} I(\xi)\exp(i\hat{\phi}_0\xi)\ d\xi \tag{2.11}$$

The term $I(\xi)$ is the spectral distribution of the irradiance. It is convenient to separate the complex coherence into an amplitude and a complex phasor as each quantity can independently be related to the contrast and phase of the interferogram. This is shown by substituting equation 2.10 into equation 2.4 so that the interferometric signal for a quasi-monochromatic light source is given as

$$S_{\pm}(\hat{\phi}_0) = \frac{I_0}{2}\left(1 \pm \Re[\gamma(\phi_0)\exp(i\phi_0)]\right) \tag{2.12}$$

This derivation shows the connection between the interferogram generated by an interferometer and the coherence in the temporal domain. For the case of the Doppler effect, spectral shifts and broadening of the spectral line in the spectral domain will be observed as shifts in the phase and contrast of the interferometric fringe pattern measured by an interferometer.

An interferometer coupled to a photo detector array or camera can provide even greater spatial resolution (1D or 2D) compared to spectrometers and they are not limited by light throughput which in theory, makes them a powerful diagnostic tool for spectral measurements of plasmas. In practice however, mechanical interferometers such as the Michelson-Morley interferometer are rarely used for measuring spectral broadening or shifts in plasmas as these effects are usually very small and therefore such systems require very precise alignment and stability of the optical components in order to detect the resulting changes in the coherence. For measurements using short wavelengths, such as the visible region, vibrational noise becomes the major limitation, scaling as $1/\lambda^2$ [49]. For this reason many interferometers operate in the 100 $\mu$m $-$2000 $\mu$m wavelengths [49].

Typically, plasma features which are difficult to obtain using spectroscopic or interferometric methods, are instead measured using electronic probes or laser techniques, such as

laser induced fluorescence (LIF) or laser absorption.

### 2.1.4 The development of coherence imaging

In recent years, solid-state interferometric systems based on birefringent crystals have been developed at the Australian National University for use in the imaging of simple spectral scenes. These systems replicate the functionality of a mechanically scanned interferometer by exploiting the birefringent and electro-optic properties of optical crystals.

Birefringence is a difference in refractive indices along optical axes of a crystal plate which results in a delay between the orthogonally polarised components of the transmitted light (this will be discussed in more detail in section 3.1). The optical delay between the polarisation components is determined by the material of the crystal and the thickness of the crystal. Some birefringent crystals also exhibit electro-optic properties.

Snapshot coherence imaging systems are based on the standard polarising interferometer, shown in figure 2.6. The interferometer operates by collecting quasi-monochromatic emission light and selecting linear polarisation through an initial polarising optic. The emission passes through a waveplate (see details in section 3.2) where a net phase delay is introduced between the components polarised parallel and perpendicular to the principal axis (opical axis) of the crystal. The components are then recombined through a final polariser and the spectral line of interest is isolated using a narrow bandwidth filter. The lens focuses the interference fringes onto a screen (such as a photodetector or CCD) for viewing. The optical configuration of the polarisation interferometer, is shown in figure 2.6. The fringe pattern can be decoded to obtain useful information about sufficiently simple spectral scenes.

In order to obtain Doppler information the contrast, phase and intensity must be measured (see equation 2.26). As the polarisation interferometer only makes a single measurement of the coherence (fixed delay) it cannot deliver enough information to retrieve these three unknown features. Therefore, in order to measure spectral information the signal must be modulated or scanned across the interferometric delay. One way to achieve this is by modulating the interferometric delay with time. For mechanical interferometers this may be achieved by making measurements while extending the length of one of the interferometer arms. For polarisation-based systems, electro-optic crystals can be used. Pockels cells are voltage controlled waveplates where the birefringence of the crystal varies with the applied electric field. Devices such as MOSS (Modulated Optical Solid-State) or ToMOSS (Tomographic Modulated Optical Solid-State) interferometers employ such strategies [40]. These devices were the forerunner to snapshot coherence imaging systems.

The MOSS system (shown in figure 2.7 a) operates similar to the standard polarisation interferometer. The horizontal polarisation component is selected by the first beam splitter polarising cube. The birefringent optic is orientated with the optical axis at 45° to the horizintal axis. The polarised component is then split into two polarisation components parallel and perpendicular to the optical axis of the electro-optic (E-O) birefringent crystal. The birefringent property causes a delay between these components which is varied by

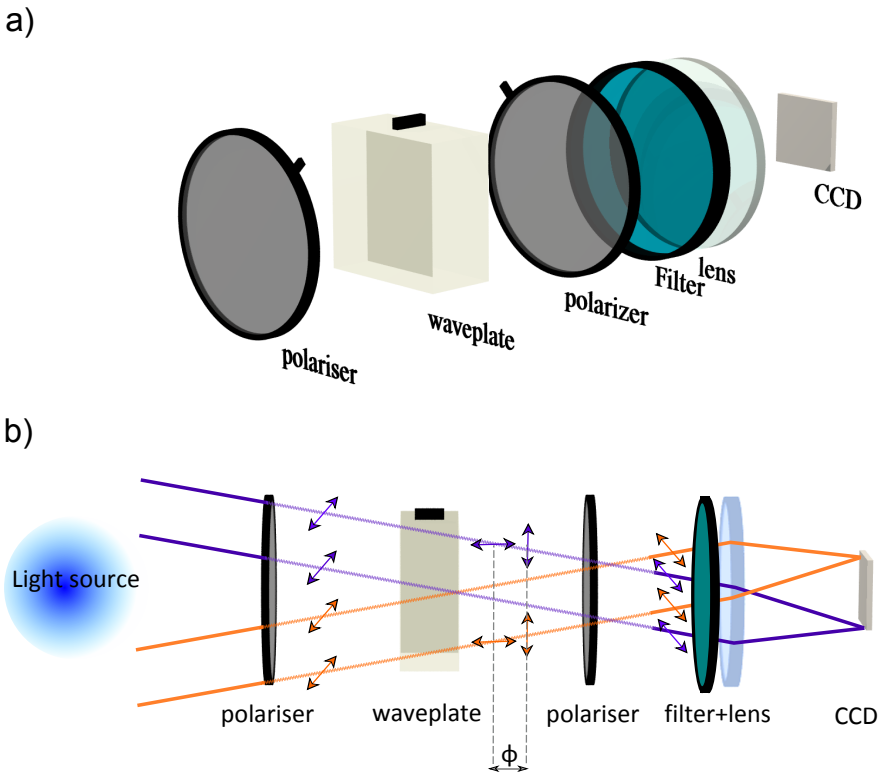


**Figure 2.6:** (a) Optical setup for a fixed delay polarisation interferometer. (b) Ray diagram showing the functionality of the interferometer, depicting the polarisation state and waveplate delay at different angles of incidence.

applying a voltage across the crystal. The components are then recombined through the second polarsing cube and focused onto a detector array. The output from the detector is a sample of the coherence, selected over the delay range provided by the applied voltage (see figure 2.7 b). The coherence envelope (amplitude) is determined by the temperature of the plasma and therefore higher temperatures cause a more rapid decay of the envelope with delay. The phase will vary depending on the flow of the plasma.

By sweeping the delay the coherence is sampled for each pixel. These systems can either be single-channel where the emission light is collected through the system by a single photomultiplier tube, or they can be multi-channel where a series of fiber optics can be coupled into the MOSS system using angular multiplexing allowing features from a range of views to be measured [40].

The multi-channel ability, along with high light throughput and stability of the MOSS systems offered significant advantages over standard spectrometers and interferometers and as such are able to achieve the resolution required for plasma spectral studies. The voltage modulation operates at frequencies between 0 and 50 MHz [40], giving these instruments the added advantage of high temporal resolution.

A phase-stepped coherence imaging spectrometer, adapted from the MOSS system by coupling to a CCD and using an additional birefringent plates, was used to study the Doppler features of the $He_{II}$ 468 nm transition line on the WEGA stellarator [50]. In

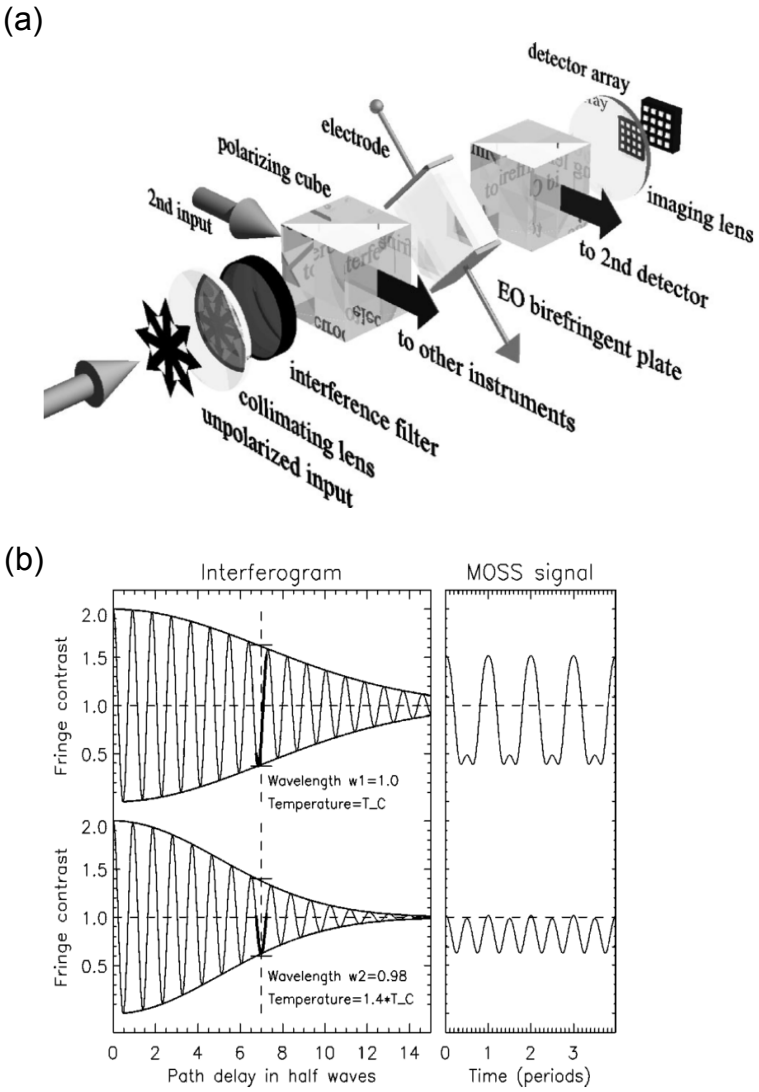


**Figure 2.7:** (a) Instrumental components of the Modulated Optical Solid State (MOSS) system. (b) sample of the signal obtained from MOSS at two different temperatures. This figure was supplied courtesy of Professor John Howard. Additional details can be found at [40].

this system the voltage of the electro-optic crystal was varied in synchronisation with the camera exposure so that a sequence of 2D images of the plasma, over-laid with a fringe pattern, were obtained. The stepped voltage resulted in the phase of the fringe pattern shifting by $\pi/2$ radians between each image.

Snapshot coherence imaging is a technique which evolved from the MOSS and phase-stepped systems and allows for 2D time-resolved plasma imaging without the need to apply the voltage modulation. Like the polarisation interferometer and MOSS systems, the snapshot systems exploit the birefringent property of uniaxial crystals to cause a phase delay between the orthogonal polarisation components. The voltage modulation is however replaced by another 'static' birefringent optic crystal called a shearing plate. This plate adds an additional phase shear, replacing the need to manually sample delay and encoding the coherence directly into the measured interferometric fringe pattern. The functionality

of the shearing plate is described in more detail in chapter 3.3.

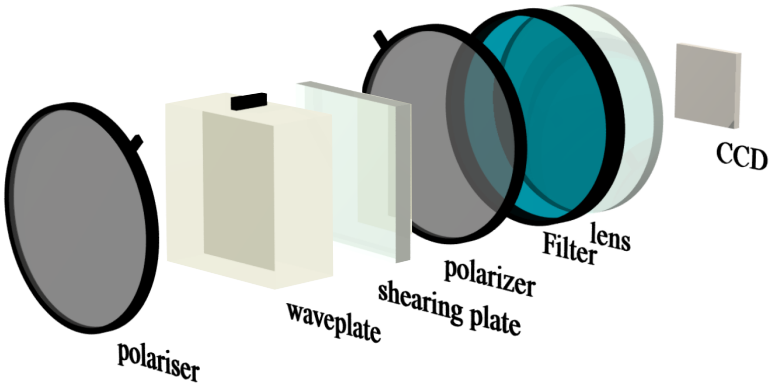


**Figure 2.8**: Instrumental components of the snapshot coherence imaging system.

The use of the static optic allows a 2D spatial snapshot of the coherence to be obtained in a single image, without the complexity of encoding the coherence in a time modulation. The acquisition speed for snapshot systems is only limited by the brightness of the plasma and the frame-rate of the camera. For a good signal-to-noise ratio (SNR) the exposure time is typically on the order of milliseconds and therefore suitable for dynamical plasma studies. Intensified cameras, which employ an inbuilt gain and phase-locking, can be used in conjunction with the coherence imaging systems to study coherent plasma wave phenomena up to the MHz range.

Coherence imaging has been successfully deployed to measure Doppler spectral features on fusion focused experiments [43–45, 47, 51, 52]. Work to investigate internal magnetic and electric fields through the Zeeman and Motional Stark spectral effects using coherence imaging has also been undertaken on the K-STAR, DIII-D, ASDEX-U and TEXTOR fusion experiments [53–56].

### 2.1.5 Theory of Doppler coherence imaging measurements

Coherence imaging measures emission light from plasmas and generates a fringe pattern which contains features of the spectral coherence. The discussion so far has been fairly basic assuming a Maxwellian velocity distribution of particles and a homogeneous-plasma ignoring effects such as line integration. The following discussion provides a more complete theory of coherence imaging measurements for a general plasma source.

### 2.1.6 Ion velocity distribution function

In this section we study how the Doppler spectral line-shape is related to the inhomogenious ion velocity distribution function, $f_i(\boldsymbol{r}, \boldsymbol{V})$. This is a six dimensional quantity which describes the number of particles in a plasma species at position $(x, y, z)$ with the velocity $(V_x, V_y, V_z)$. It may also extend to seven dimensions to include variation in time, $t$.

An arbitrary ion velocity distribution function (IVDF) when considered at a single position in the plasma, is a 3D quantity and can be depicted as volume in velocity space as shown in left image of figure 2.9. The color indicates the value of the IVDF and the velocity coordinates are normalised such that $\boldsymbol{v} = \boldsymbol{V}/c$. For a cold stationary plasma the distribution function would be a delta function centered at $\boldsymbol{v} = (0, 0, 0)$. A hot moving plasma will have the distribution shifted in the direction of the particle flow, and the spread will be determined by the thermal energy carried by the particles.

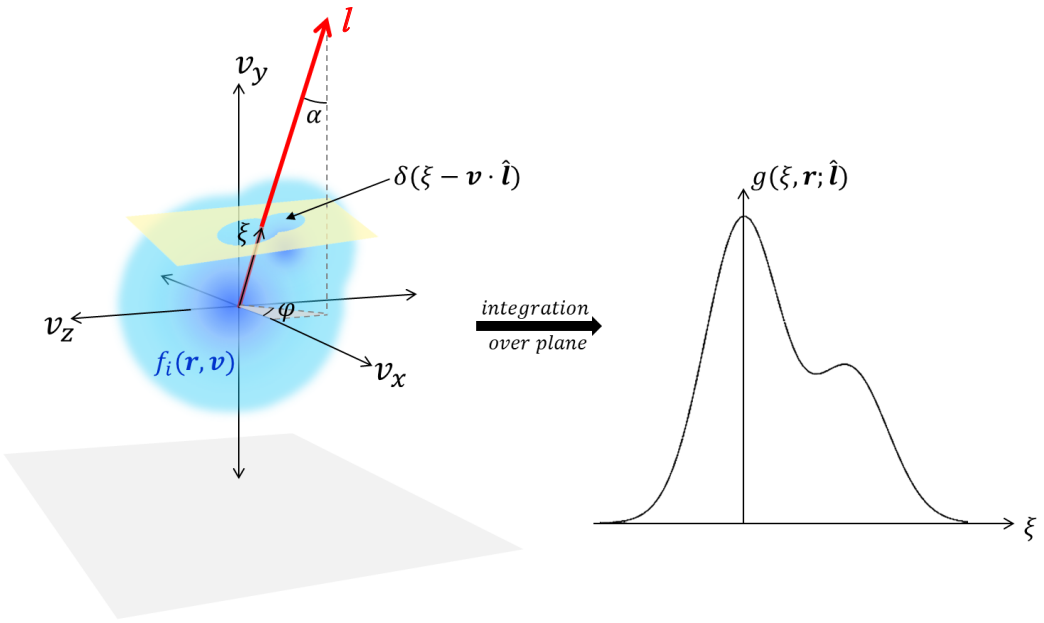


**Figure 2.9:** Left) A Non-Maxwellian IVDF at position $\boldsymbol{r}$ within the plasma. The blue represents the value of the IVDF in velocity space. The line (red) denoted $\boldsymbol{l}$ is the direction of view defined by the angles $\alpha$ and $\varphi$. The length $\xi$ is the coordinate along the viewing chord. Right) the line shape $g(\xi, \boldsymbol{r}; \hat{\boldsymbol{l}})$ is the plane-integrated IVDF at coordinate $\xi$ as defined in Equation 2.13.

In this model the direction of observation is shown by the line $\boldsymbol{l}$ (described by the unit vector $\hat{\boldsymbol{l}}$) which is defined by the angle of incidence $\alpha$ and azimuthal angle $\varphi$. The Doppler features of the measured spectral line are determined from the contribution of the intensity-weighted velocities in the direction of the line of observation.

The spectral lineshape for the line $\boldsymbol{l}$ at position $\boldsymbol{r}$ can be called $g(\xi, \boldsymbol{r}; \hat{\boldsymbol{l}})$ where the coordinate $\xi$ is the normalized frequency coordinate already described in equation 2.7. The values of $g(\xi, \boldsymbol{r}; \hat{\boldsymbol{l}})$ at frequency coordinate $\xi$ are determined by summing over the values of the IVDF which have a velocity component parallel to $\hat{\boldsymbol{l}}$ that is equal to the coordinate $\xi$, see fig 2.9. This 3D Radon transform (integral over planes) is discussed further in chapter 6. Mathematically, this is written as,

$$g(\xi, \boldsymbol{r}; \hat{\boldsymbol{l}}) = \int f_i(\boldsymbol{r}, \boldsymbol{v}) \delta(\xi - \boldsymbol{v}\cdot\hat{\boldsymbol{l}})\, d\boldsymbol{v} \tag{2.13}$$

The line-shape $g(\xi, \boldsymbol{r}; \hat{\boldsymbol{l}})$ is local as it depends on the position vector $\mathbf{r} = (x, y, z)$ in the

plasma.

A state of thermal equilibrium means the distribution function for a species is homogeneous (no $\boldsymbol{r}$ dependence), isotropic (independent of the direction of $\boldsymbol{v}$) and is time invariant [57]. The Maxwell-Boltzmann distribution function is often used to describe the velocity distribution function of a plasma in thermal equilibrium, where the standard deviation is related to the temperature.

A plasma in local thermal equilibrium (LTE) can also be described by a Maxwell-Boltzmann distribution but relaxes the homogeneity condition so that the temperature and drift may change spatially depending on external parameters such as magnetic fields or sources. For this condition to hold, the plasma density must be high enough that collisional processes dominate radiative processes so that radiative losses (thermal and other) do not significantly disrupt the local thermal equilibrium [57]. The drifting local thermal equilibrium model is employed as a simple starting point in understanding radiative processes or modeling distribution functions in plasmas. The following discussion has been addressed in the works of Howard [42, 58].

Considering the case where the plasma is drifting in local thermal equilibrium, the IVDF is Maxwellian and can be written in the form,

$$f_i(\boldsymbol{r}, \boldsymbol{v}) = \left(\pi v_{th}^2\right)^{-\frac{3}{2}} \exp - \left(\frac{\boldsymbol{v} - \boldsymbol{v_D}}{v_{th}}\right)^2 \tag{2.14}$$

where the normalised thermal velocity is

$$v_{th}^2 = \frac{k_B T_S}{mc^2} \tag{2.15}$$

and $T_S(\boldsymbol{r})$ is the species temperature. The velocity drift, $\boldsymbol{v_D}$, and the thermal velocity have been normalised to $c$.

Substituting the distribution function into the equation 2.13, the spectral line-shape becomes

$$g(\xi, \boldsymbol{r}; \hat{\boldsymbol{l}}) = \left(\pi v_{th}^2\right)^{-\frac{1}{2}} \exp - \left(\frac{\xi - \boldsymbol{v_D} \cdot \hat{\boldsymbol{l}}}{v_{th}}\right)^2 \tag{2.16}$$

where

$$\xi = \frac{\nu - \nu_0}{\nu_0} = \boldsymbol{v_D} \cdot \hat{\boldsymbol{l}} \tag{2.17}$$

From the Doppler shift formula (equation 2.1). The Fourier transform of the line-shape gives the local complex coherence (compare with equation 2.11),

$$\begin{aligned} G(\phi_0, \boldsymbol{r}; \hat{\boldsymbol{l}}) &= \int_{-\infty}^{\infty} g(\xi, \boldsymbol{r}; \hat{\boldsymbol{l}}) \ \exp(i\hat{\phi}_0 \xi) \ d\xi \\ &= \left(\pi v_{th}^2\right)^{-\frac{1}{2}} \int_{-\infty}^{\infty} \exp - \left( \frac{\xi - \boldsymbol{v_D} \cdot \hat{\boldsymbol{l}}}{v_{th}} \right)^2 \ \exp(i\hat{\phi}_0 \xi) \ d\xi \\ &= \exp i\hat{\phi}_0 \boldsymbol{v_D} \cdot \hat{\boldsymbol{l}} \ G_0(\phi_0, \boldsymbol{r}; \hat{\boldsymbol{l}}) \end{aligned} \tag{2.18}$$

where $G_0$ is the Fourier transform of the Gaussian lineshape

$$G_0(\phi_0, \boldsymbol{r}; \hat{\boldsymbol{l}}) = \exp - \frac{\hat{\phi}_0^2 \xi_{th}^2}{4} \tag{2.19}$$

and where $\hat{\phi}_0$ is the phase delay set by the interferometer. This is distinct to the complex coherence $\tilde{\gamma}(\phi_0)$ (as presented in section 2.1.3) which is weighted by the local intensity and subject to line integration effects. The connection between $G(\phi_0, \boldsymbol{r}; \hat{\boldsymbol{l}})$ and $\tilde{\gamma}(\phi_0)$ is discussed in section 2.1.7.

It is convenient to introduce the characteristic temperature of the instrument $T_C$ (set by the delay $\hat{\phi}_0$),

$$\frac{1}{2} m_S V_C^2 = k_B T_C \quad \text{where} \quad V_C = \frac{2c}{\hat{\phi}_0} \tag{2.20}$$

The expression for the Gaussian lineshape can be re-written as,

$$G_0(\phi_0, \boldsymbol{r}; \hat{\boldsymbol{l}}) = \ \exp - \frac{T_S}{T_C} \tag{2.21}$$

Plasmas can be inhomogeneous in both space and velocity having multiple features such as fast moving beams or contain both hot and cold species. The velocity distribution functions for such plasmas are non-Maxwellian and therefore the emission line shapes for such plasmas are not expected to be Gaussian.

Figure 2.10 compares the spectral line shapes and associated coherence for the case of (a) a Maxwellian, and (b) a non-Maxwellian IVDF. For a Maxwellian IVDF, the contrast and phase are given by known expressions shown in figure 2.10 (these are derived later in section 4.3.7). As $T_C$ is a function of $\hat{\phi}_0$, it is clear that the ion temperature $T_S$ and the flow $v_D$ (equivilent to $\boldsymbol{v_D} \cdot \hat{\boldsymbol{l}}$) can be calculated from measurements of the coherence at an appropriately chosen delay.

For non-Gaussian spectral lineshapes the complex coherence is not a known function of $\phi_0$.

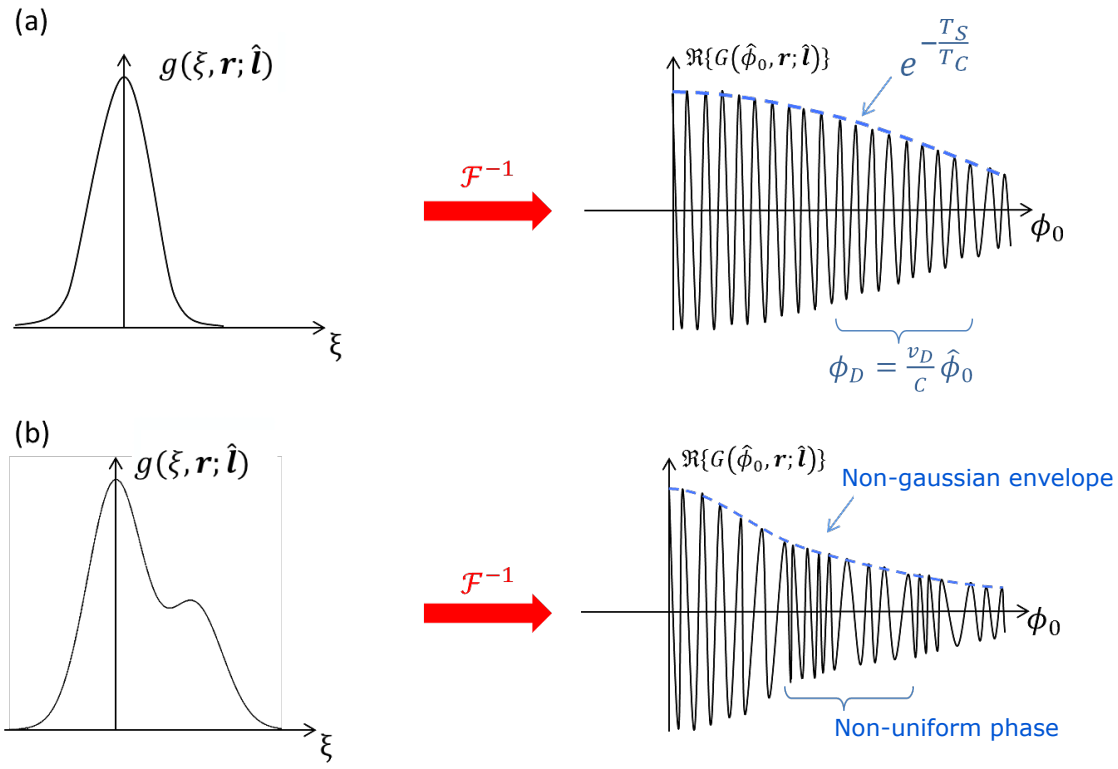


**Figure 2.10:** Spectral line shape and corresponding real component of the coherence for (a) a Maxwellian and (b) a Non-Maxwellian distribution function.

An example of a spectral line and the corresponding coherence in the temporal domain for a non-Maxwellian plasma is shown in 2.10 (b). In this case, a single measurement of the coherence is not enough to return information about the IVDF. However measurements at multiple $\phi_0$ coordinates can help us sample the coherence and therefore identify the shape of the coherence envelope and phase. In theory, tomography on the 3D Radon transform can then deliver the velocity distribution function.

The MAGPIE IVDF has not previously been determined for the plasma conditions examined in this study. Non-Maxwellian IVDFs have been reported in other helicon devices operating at similar conditions [32, 33, 59] and so it is important to consider the extended theory for the non-Maxwellian case.

### 2.1.7 Line-integrated measurements

The discussion so far has only considered the measurement of the line-shape at a single point within a plasma. For applications such as spectral imaging of charge exchange emission from neutral beams in fusion devices where the beam appears as a thin plane of emission light or for applications where the plasma is assumed to be homogeneous - this discussion sufficient. However, in this work the inhomogeneous plasma radiates within a bulk volume and measurements of the emission light will be a summation of the light directed along the line-of-sight. This is depicted in figure 2.11 where the image plane is

a detector, and the line $\boldsymbol{l}$ is the line-of-sight passing through the plasma volume from a pixel.

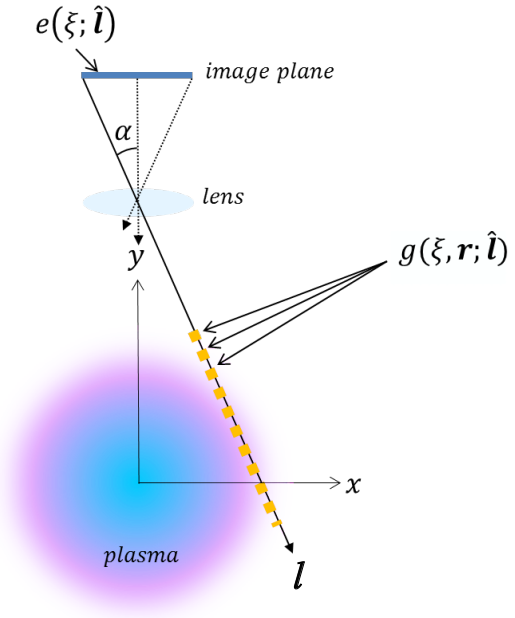


$$e(\xi;\hat{\boldsymbol{l}}) = \frac{1}{I_0}\int_L \epsilon(\boldsymbol{r}) g(\xi,\boldsymbol{r};\hat{\boldsymbol{l}})\, dl$$

**Figure 2.11:** Diagram of the line-of-sight $\boldsymbol{l}$ and its view of the plasma from the detector (image plane) through a simple lens system. The measured lineshape $e(\xi;\hat{\boldsymbol{l}})$ is the integration of the local lineshape $g(\boldsymbol{r},\xi;\hat{\boldsymbol{l}})$ along the line-of-sight.

If the local emission radiance at position $\boldsymbol{r}$ is denoted, $\epsilon(\boldsymbol{r})$ and proportional to the zeroth moment of the velocity distribution function

$$\epsilon(\boldsymbol{r}) \propto \int f_i(\boldsymbol{r},\boldsymbol{v})\, d\boldsymbol{v} \tag{2.22}$$

The measured line-integrated radiance, $I_0$, at a pixel on the detector is a sum of the local radiance at each position along the line-of-sight,

$$I_0 = \int_{\mathrm{L}} \epsilon(\boldsymbol{r})\, dl \tag{2.23}$$

This transformation assumes that the plasma is optically thin such that any photon emitted in the bulk plasma will not be reabsorbed and that the emission is isotropic. The normalised spectral line-shape denoted, $e(\xi;\hat{\boldsymbol{l}})$, is a sum over the local line-shape at each point viewed by the line-of-sight and weighted by the local radiance,

$$e(\xi;\hat{\boldsymbol{l}}) = \frac{1}{I_0}\int_{\mathrm{L}} \epsilon(\boldsymbol{r}) g(\xi,\boldsymbol{r};\hat{\boldsymbol{l}})\ dl \tag{2.24}$$

and the associated coherence is given as

$$\gamma(\phi_0;\hat{\boldsymbol{l}}) = \frac{1}{I_0}\int_{\mathrm{L}} \epsilon(\boldsymbol{r})\ G(\phi_0,\boldsymbol{r};\hat{\boldsymbol{l}})\ dl \tag{2.25}$$

Line-integration effects can often be ignored in cylindrical geometry if the radiance is peaked centrally, as contributions from the center of the plasma volume dominate the contributions from the edge region. In general, however, line-integration effects cannot be ignored and tomographic inversion is required to unwrap the local quantities.

In the case of LTE, the interferogram for a simple Doppler shift and broadening can be written as

$$S_{\pm}(\phi) = \frac{I_0}{2}\Big(1 \pm \zeta_D \cos\left(\phi_0 + \phi_D\right)\Big) \tag{2.26}$$

where $\phi_D$ is a additional phase term capturing information about the plasma flows and the ion temperature is encoded in the contrast term $\zeta_D$. The advantage of the LTE approximation is that the lineshape is known to be Gaussian and the phase is known to increase uniformly with delay and hence the temperature and drift velocity of the plasma can be determined in a single measurement at an appropriately chosen delay.

Substituting equations 2.18, 2.19 into 2.25, the expressions for the line-integrated phase and contrast can be derived.

$$\zeta_D = |\gamma| = \frac{1}{I_0}\int_{\mathrm{L}} \epsilon(\boldsymbol{r}) \exp -\frac{T_S(\boldsymbol{r})}{T_C}\ dl \tag{2.27}$$

and to first order

$$\phi_D = \arctan\frac{\Im(\gamma)}{\Re(\gamma)} = \frac{\hat{\phi}_0}{I_0\zeta}\int_{\mathrm{L}} \epsilon(\boldsymbol{r}) \exp -\frac{T_S(\boldsymbol{r})}{T_C}\ \boldsymbol{v_D}\cdot\hat{\boldsymbol{l}}\ dl \tag{2.28}$$

This expression has been determined by applying the small angle approximation, assuming $\hat{\phi}_0 \boldsymbol{v_D}\cdot\hat{\boldsymbol{l}} << 1$. For small $\hat{\phi}_0$ values the change in the contrast will be small and hence measurements will be highly sensitive to noise errors. For large changes in $\hat{\phi}_0$ the contrast will drop towards zero, and again noise errors become significant. An ideal system therefore selects $\hat{\phi}_0$ such that $T_C \approx T_S$. The measured contrast will therefore have decreased to $e^{-1} \approx 37\%$ of its intial value.

The above derivation gives the expressions for the phase and contrast for the standard

case where $v_D <<< v_{th}$. For these conditions the phase and contrast are shown to be independent of each other.

This result shows that simple interferometry gives well defined information regarding the ion temperature and flow which can be accessed using tomographic techniques. For this work, the interferometric data is initially evaluated by ignoring line-integration effects, however, the effects of the line-integration and reconstruction of the local quantities are later considered in detail in chapter 6.

## 2.2 Mach probe design for MAGPIE

This section presents the design elements of a Mach probe which is used in this work to validate the direction and magnitude of the flows in MAGPIE.

### 2.2.1 Introduction to probes

The Langmuir probe is the simplest type of electric probe diagnostic used in plasma measurements and is a good starting point when discussing probe measurements. In its basic form, the Langmuir probe consists of a single metal tip with swept bias and is used to measure the electron temperature and density of a plasma. A common probe I/V characteristic is shown in figure 2.12 which demonstrates the relationship between the applied bias voltage and the current measured by the probe.

When a probe is suspended within a plasma and there is no applied bias voltage, the difference in particle mass will cause electrons to hit the probe tip more frequently than ions. This will cause a sheath to form around the metallic tip so that quasi-neutrality in bulk of the plasma is maintained. In this state, the probe sits at the floating potential $\mathbb{V}_\mathrm{f}$ and no current is drawn. When the bias voltage, $\mathbb{V}$ is lower than the floating potential, electrons will be repelled away from the probe tip and ions will be collected. At large negative voltages, the current drawn by the tip is purely due to the collection of ions. The I/V characteristic shows that the ion current at large negative voltages becomes saturated and no longer increases with bias voltage. At this point, electric shielding around the probe tip limits further ions from being collected and the current drawn by the probe tip is called the ion saturation current, $\mathbb{I}_\mathrm{i,sat}$. The plasma potential $\mathbb{V}_\mathrm{p}$ is indicated by the knee in the I/V characteristic. Beyond this, at large positive voltages, the probe tip only attracts electrons (ions are repelled). As bias voltage increases, the sheath thickens in order to shield the tip from further electron collection putting an upper limit on the current drawn by the probe. This current limit is called the electron saturation current, $\mathbb{I}_\mathrm{e,sat}$ [60].

The transition region between $\mathbb{V}_\mathrm{f}$ and $\mathbb{V}_\mathrm{P}$, for Maxwellian electrons follows

$$\mathbb{I} = \mathbb{I}_{\mathrm{e,sat}} \exp\left(e\frac{\mathbb{V} - \mathbb{V}_{\mathrm{P}}}{k_B T_e}\right) \tag{2.29}$$

and the electron saturation is given by

$$\mathbb{I}_{\mathrm{e,sat}} = e n_e A_p \left(\frac{k_B T_e}{2\pi m_e}\right)^{\frac{1}{2}} \tag{2.30}$$

where $k_B$ is the Boltzmann constant, $A_p$ the probe tip area, $m_e$ is the electron mass and $e$ is the electronic change. For a cylindrical probe tip the exposed area is given by $A_p = 2\pi R_p L$ where $R_p$ and $L$ are the tip radius and length respectively. From these equations, the I/V characteristic can be used to determine the electron temperature $T_e$ and the electron density $n_e$.

The expected ion saturation current, $\mathbb{I}_{\mathrm{i,sat}}$, drawn by the probe is derived from the ion sheath current from Bohms formula and is given as [61, 62]

$$\mathbb{I}_{\mathrm{i,sat}} = 0.605 A_p n e \left(\frac{k_B T_e}{m_i}\right)^{\frac{1}{2}} \tag{2.31}$$

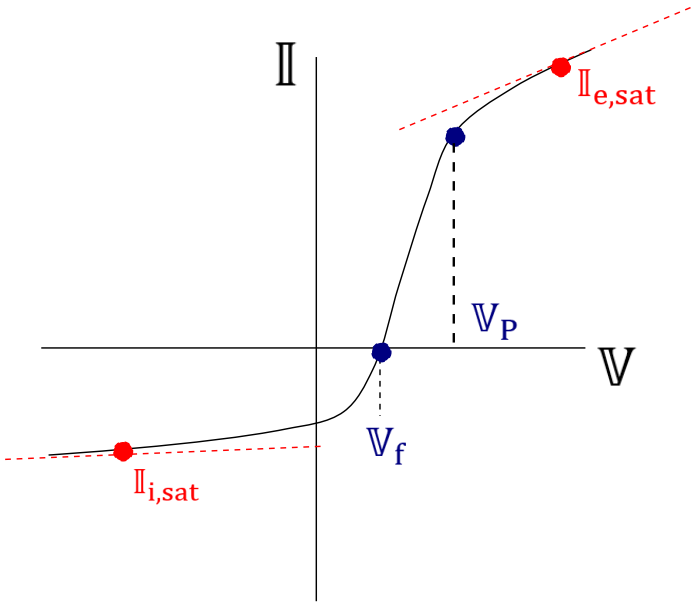


**Figure 2.12:** I/V characteristic of a standard Langmuir probe. Here $\mathbb{I}$ is the current measured by the probe and $\mathbb{V}$ is the applied bias voltage. $\mathbb{V}_{\mathrm{f}}$ is the floating potential. $\mathbb{V}_{\mathrm{P}}$ is the plasma potential and $\mathbb{I}_{\mathrm{i,sat}}$ and $\mathbb{I}_{\mathrm{e,sat}}$ are the ion and electron saturation currents respectively.

where $n$ is the plasma density and $m_i$ is the ion mass.

This theory works well when the plasma is assumed to be Maxwellian and the probe is not considered to significantly perturb the plasma. However, probe theory becomes more complicated by the presence of magnetic fields and collisionality. Such effect are addressed in the following section.

### 2.2.2 The Mach probe

Mach probes are common diagnostic tools employed to measure ion flows in plasmas [62]. They have been used in fusion studies to investigate fluctuations and turbulence in the ion drift velocity in the scrape-off layer, to characterise the toroidal and sheared $\mathbf{E} \times \mathbf{B}$ flows, and, to study the effect on the ion flow due to instabilities such as the interchange instability and ELMs (Edge-Localized Modes) [62–66]. Mach probes also have wide applications in cooler laboratory-scale plasmas, and have been used to characterise flows in divertor simulation experiments [67], propulsion systems to quantify plasma thrust [68] and to measure turbulent driven sheared flow in CSDX [37]. Mach probes are simple to use, however often results can be difficult to interpret and probe measurements are not well suited for large spatial and parameter scans as data is usually only obtained through single-point measurements. A summary of the current Mach probe theory can be found in the review article by Chung [62].

A Mach probe consists of two identical probe tips separated by an insulating barrier. The tips are biased negatively so that electrons are repelled from the tip and the ion saturation current is measured. The barrier between the tips provides the directionality to the measurement. The basic assumption is that the upstream probe tip, which is exposed to the flow, will capture more ions than the down stream tip, and hence there will be an observed difference in the ion saturation current measured at each tip.

The ratio of the currents is related to the Mach number, M, via

$$\exp(k_{\mathrm{M}}\mathrm{M}) = \left(\frac{\mathbb{I}_{\mathrm{U}}}{\mathbb{I}_{\mathrm{D}}}\right) \tag{2.32}$$

where $\mathbb{I}_{\mathrm{U}}$ is the current measured from the upstream tip and $\mathbb{I}_{\mathrm{D}}$ is the current measured from the downstream tip and $k_{\mathrm{M}}$ is a calibration constant which is determined by the model employed. The Mach number here is a ratio of the ion velocity, $V_i$ to the ion sound speed, $c_S$

$$\mathrm{M} = \frac{V_i}{c_S} \tag{2.33}$$

The ion sound speed is determined by the electron temperature and ion mass, $m_i$, and is

given by

$$c_S = \left( \frac{k_B T_e}{m_i} \right)^{\frac{1}{2}} \tag{2.34}$$

Difficulty arises in Mach probe measurements when choosing the calibration constant $k_{\mathrm{M}}$. This has been addressed extensively in theoretical models [69–73] and requires prior knowledge of the effects of magnetisation on the rate of ion collection. The magnetisation is determined by the ratio of the probe tip dimensions, $R_p$, to the Lamour radius,

$$r_L = \frac{V_\perp}{\omega_c} = \frac{m_s V_\perp}{|q|\mathrm{B}} \tag{2.35}$$

where, $\omega_c = |q|\mathrm{B}/m$ is the cyclotron frequency, and, $q$ and $m$ are the charge and mass of the particle, respectively. Probes are considered under two conditions, the magnetised and unmagnetised case, which is determined by the ratio of the probe tip radius to the Lamour radius. There are many models used to determine the calibration constant $k_{\mathrm{M}}$ and each have a narrow range of validity. Hence great care must be taken in selecting the model suitable for the plasma and probe conditions under consideration [62].

Strongly magnetised plasmas are characterised by $R_p >> r_L$, where the dimensions of the probe tip are far greater than the Lamour radius and the electron and ion temperatures are taken to be equal, $T_i/T_e \sim 1$. Such conditions can be found in plasmas with small species mass (such as hydrogen) exposed to strong external magnetic fields. Fusion relevant experiments where the fuel is light mass and the magnetic field is often $1 - 3.5$ Tesla is a good example of a strongly magnetised plasma. For this case, the quasi-neutral presheath around the probe is elongated by the magnetic field and hence the ion collection is dominated by flow parallel to the magnetic field. When the probe tip is parallel to the field, it collects ions from cross-field diffusive effects and therefore the currents generated by the perpendicular flows are much weaker than the currents from flows parallel to the field. Under such conditions the model of the plasma presheath becomes one dimensional and the shape of the probe tip collection area is unimportant [70]. The theoretical model for the strongly magnetised case is well established and the choice of calibration factor $k_{\mathrm{M}} \sim 1.64$ has been verified through experiments [70, 71].

Unmagnetised plasmas are characterised by $r_L >> R_p$, and $T_i << T_e$. In this case, the sheath is expected to be small and the probe collection area is usually taken to be equal to the tip area. However, the calibration factor in unmagnetised plasmas is tricky to determine. Investigation of this first began in the works by Al'pert (1965) and Laframboise (1966) in who considered a sphere in a stationary collisionless plasma [71]. Their models were based on kinetic theory and relied upon conservation of angular momentum for simplifications. Laframboise found that providing $T_i/T_e << 0.1$ and $R_p/\lambda_{De} > 1$ then the effects of a finite probe potential penetrating into the plasma could be neglected [69]. However, for the case where the probe is exposed to a background plasma drift, the symmetry breaks and conservation of angular momentum is no longer able to simplify the problem. Following this, a one dimensional model was presented by Hudis and Lisky (1970) which attempted to explain the physics for a probe in a drifting unmagnetised plasma.

This model was widely accepted until the problem was re-evaluated by Hutchinson in 2002 [71].

Hutchinson found that the Hudis and Lindsky model did not consider the 3−dimensional geometry of the probe tip and suggested that there was no reason for the calibration factor to be independent of the shape of the probe [71]. The theoretical model presented by Hutchinson [71] was based on a spherical probe tip collection area and was developed using a PIC (particle-in-cell) code and delivers a $k_{\mathrm{M}} \sim 1.34$ for the case where $T_i/T_e < 3$ eV and negligible Debye length. Hutchinson also examined the effects of finite and large Debye length as well particle velocity and that both these parameters caused non-trivial effects to the current ratio and calibration constant $k_{\mathrm{M}}$ [72].

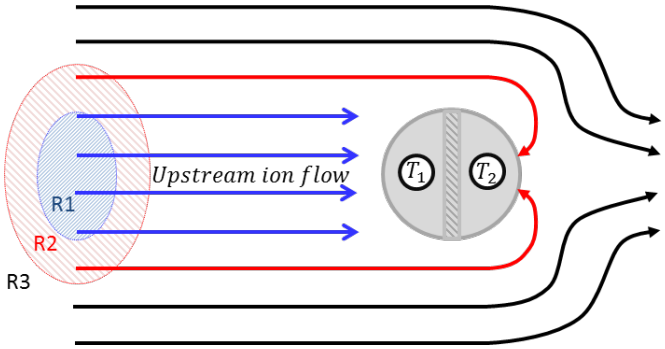


**Figure 2.13:** Model presented by Hutchinson [71] of the ion collection by a Mach probe in an unmagnetised plasma.

Hutchinson's model proposed that the ions flowing towards the probe could be separated into three distinct regions, shown in figure 2.13. The ions flowing in the inner region (denoted, $R1$, and shown in blue) would be collected by the upstream probe. The ions flowing from the central region (denoted, $R2$, and shown in red) would pass unperturbed by the upstream probe but be deflected by the sheath of the downstream probe where they would be collected. Ions outside these two regions (region $R3$) would pass by the probe unperturbed. For the case where the Debye length is negligible or the ion velocity was high, ions would either be collected by the upstream probe tip or they would pass by the tip unperturbed. In this case, the sheath of tip 2 is too small or the ions are flowing too fast to be deflected into the collection area of the downstream tip and the ratio of the upstream to downstream current ratio is high. Increasing the Debye length or the probe bias, or, in the case of smaller ion velocities, the ions contained in the central region will feel the potential of the downstream probe tip. This will result in higher ion densities around the downstream probe tip and is such cases the ion current ratio between the tips would be very small or could in some instance flip. Current ratio reversal has been experimentally demonstrated [74]. In the case where the Debye length is larger than the probe dimensions then the plasma behavior is lost and the ions will behave as individual particles. This demonstrates that Mach probe measurements in unmagnetised plasmas is only valid for a small range of parameters. It was found however, despite the complex physics presented by Hutchinson, the Hudis and Linski model was still valid in very slow drift motion with very low ion temperatures [62].

The interpretation of Mach probe measurements are further complicated by the effects

of collisions which have been known to decrease the measured ion currents and atomic processes such as impurities generated from plasma-surface interactions with the probe tip. Sensitivity to the ion temperature can also change the calibration constant [62]. For many Mach probe measurements, secondary calibration data taken using Laser Induced Fluorescence (LIF) or electrostatic probes (measuring the plasma potential which is approximately the average of the plasma potential measured from the upstream and downstream tips) is often required to confirm the Mach probe results. An error of $\sim 20\%$ is common in Mach probe measurements [62].

It should also be noted, that Mach probes can be made in a variety of geometries such as the rotating directional probe, the visco-Mach probe, perpendicular Mach probe and the Gundestrup probe. For these cases more complicated theories apply and the exponential relation between the Mach number and the ratio become a angular dependent. This work has opted for a simple two tip Mach probe design due to the simple construction and well established theoretical model.

Chapter 3

# Coherence imaging using polarisation interferometry

The standard coherence imaging system has already been introduced in section 2.1.4 (see figure 2.8). These systems use birefringent crystals to provide the fixed and sheared interferometric delay components necessary for the Doppler studies undertaken in this work. This chapter will discuss the function and performance of each of the optical components used in the construction of the snapshot coherence imaging system.

## 3.1 Optical birefringence

Birefringence is a quality used to describe materials which exhibit an anisotropy in the refractive index according to the polarisation and propagation direction of the incident beam. The refractive index, $n$, is a dimensionless number which quantifies the speed of light as it passes through a material.

$$n = c/v \tag{3.1}$$

where $c$ is the speed of light in vacuum ($n = 1$) and $v$ is the velocity of light through the material. The optical axis of an anisotropic crystal is the direction in which the propagation speed of a ray of light passing through the crystal is independent of polarisation. Uniaxial crystals have two different refractive index values corresponding to propagation parallel or orthogonal to the optical axis. Biaxial crystals have three refractive index values and two optical axes. The optical components for the instrument described in this work employs uniaxial crystals and hence this will be the focus of this discussion.

The index ellipsoid describes the orientation and magnitude of the refractive indices for light propagation in a birefringent crystal (see figure 3.1). For a uniaxial crystal the axis, c, is the optical axis of the crystal and the other axes are chosen with arbitrary orientation in the plane orthogonal to c. The polarisation component perpendicular to the crystal optical axis, (a polarisation vector which lies within the blue plane in figure 3.1), called the ordinary ray, will refract through the optic according to Snell's law with ordinary

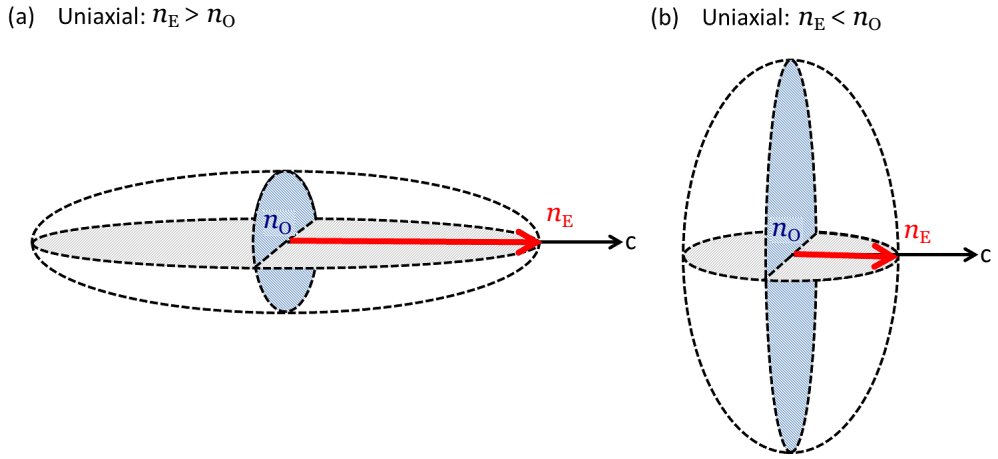


**Figure 3.1**: Index ellipsoid for a positive (a) and negative (b) uniaxial crystal.

refractive index $n_O$. Light propagating in the direction of the optical axis (along the red vector in 3.1) will see the extraordinary refractive index $n_E$. For a uniaxial crystal, the birefringence is given by

$$B = n_E - n_O \tag{3.2}$$

Uniaxial crystals can exhibit either positive or negative birefringence depending on whether $n_E > n_O$ or vice versa, as shown for the two cases in figure 3.1. The birefringence of a material can change with temperature or wavelength [75–78]. The temperature dependence of birefringent materials is discussed later in section 4.3.1. The phase delay between the extraordinary and ordinary rays depends on the thickness of the crystal, $L$, the wavelength, $\lambda$, and the direction of the incident beam relative to the index ellipsoid.

The angle dependent formula for the phase difference between the ordinary and extraordinary rays is provided by Veiras [79],

$$\phi_0(\alpha,\delta,\vartheta) = -\frac{2\pi L}{\lambda_0}\left( (n_O^2 - n^2\sin^2\alpha)^{\frac{1}{2}} + \frac{n(n_O^2-n_E^2)\sin\vartheta\cos\vartheta\cos\delta\sin\alpha}{n_E^2\sin^2\vartheta + n_O^2\cos^2\vartheta} - \frac{n_O\{n_E^2(n_E^2\sin^2\vartheta + n_O^2\cos^2\vartheta) - \left[n_E^2 - (n_E^2-n_O^2)\cos^2\vartheta\sin^2\delta\right]n^2\sin^2\alpha\}^{\frac{1}{2}}}{n_E^2\sin^2\vartheta + n_O^2\cos^2\vartheta}\right) \tag{3.3}$$

The negative sign has been introduced here so that the phase, $\phi_0$, corresponds to the phase difference in the E and O ray in line with the definition of the birefringence. The subscript, 0, indicates that this phase is instrumental. The refractive index of the medium outside the crystal is usually taken as $n \approx 1.0$ (for air). The ordinary and extraordinary refractive indices are commonly available in literature for a range of materials. The angle

terms are best described using a diagram as shown in figure 3.2. The incident ray (red arrow) is defined in terms of the incident angle, $\alpha$, which is the angle between the incident ray and the vector normal to the crystal interface. The plane of incidence is outlined in red.

The coordinate system is chosen so that $(x, y)$ span the crystal interface, and $z$ points in the direction normal to the interface. The vector c points in the direction of the optical axis and is determined by the two angles: $\delta$ which subtends the optical axis and the plane of incidence, and $\vartheta$ which subtends the optical axis and the crystal interface. The thickness of the plate in the direction of transmission is given by $L$.

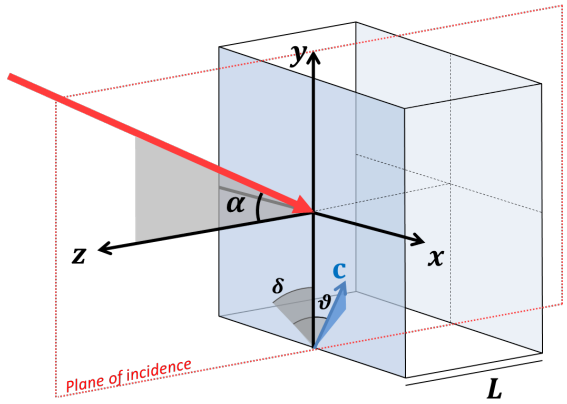


**Figure 3.2:** Geometry of a uniaxial crystal as defined by Veiras in his analytical model [79]. The incident light (red) is defined by the angle $\alpha$ on the plane of incidence. The optical axis is c. The angles $\delta$ and $\vartheta$ describe the position of the optical axis with respect to the plane of incidence and the crystal interface, respectively. The thickness of the crystal is given by $L$.

The Veiras formula has been implemented in this work to calculate the phase map for various optical components. This aids in the discussion regarding the operation of these components and allows numerical simulation of the expected interferogram for individual plates as well as combined optical systems. The accuracy of the formula has been confirmed by comparing the interferogram produced by real uniaxial birefringent crystals (with known orientation) with the interferogram produced by taking the cosine of the phase calculated using Veiras formula. This is shown as part of the discussion in the following two sections which describe the main optical components required in coherence imaging.

## 3.2 The waveplate

The waveplate or retarder plate is a uniaxial birefringent crystal, cut such that the principal (optical) axis lies parallel to the entrant and exit surfaces of the crystal [80]. The components of the impinging light which have perpendicular and parallel polarisation to the optical axis direction will experience an offset in phase due to the anisotropy of the refractive indices. The function of the waveplate is shown in figure 3.3 for a ray directed normal to the entrant plane. The extraordinary components, polarised parallel to the

optical axis, are depicted by the green arrows and the ordinary components, polarised orthogonal to the optical axis, are vectors oriented normal to the page and depicted as the red dots. As the ray passes through the optic, the components separate in phase in the direction of the ray propagation. The resulting phase offset is determined by the crystal refractive indices, wavelength of the incident light and the plate thickness.

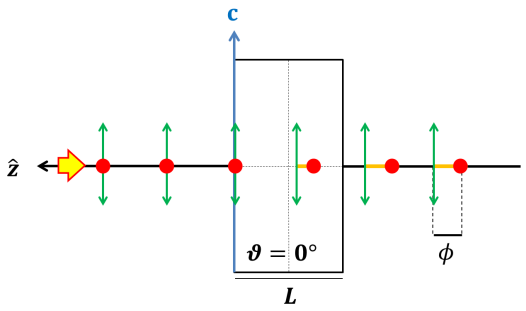


**Figure 3.3:** Transmission of light at normal incidence through a waveplate showing the delay in path length between the polarization components perpendicular (red) and parallel (green) to the optical axis.

Waveplates can be cut so that they change the phase by a large number of waves (referred to here as delay plates or retarders), or, they can shift the phase by only a portion of a single wave. The latter types of plates are designed to delay the phase by either $\pi/2$ or $\pi$ and are known as quarter and half-waveplates respectively [80]. Half-wave plates, delay the phase by a half-wave and hence result in the polarisation of the wave being flipped about the axes. A quarter waveplate shifts the phase by a quarter-wave and can change the polarisation from linear to circular. These particular plates can be useful in techniques such as field widening which will be discussed in section 3.4.

Substituting $\vartheta = 0$ into Veiras formula, the phase of the waveplate is given by,

$$\phi_0(\alpha,\delta) = \frac{2\pi L}{\lambda_0}\left((n_{\mathrm{O}}^2 - \sin^2\alpha)^{\frac{1}{2}} - \frac{1}{n_{\mathrm{O}}^2}\left[n_{\mathrm{E}}^2 n_{\mathrm{O}}^2 - (n_{\mathrm{E}}^2 - n_{\mathrm{O}}^2)\sin^2\delta\sin^2\alpha\right]^{\frac{1}{2}}\right) \tag{3.4}$$

Considering only the on-axis ray ($\alpha = 0$), the on-axis phase shift between the E and O ray simplifies to,

$$\phi_0 = \frac{2\pi LB}{\lambda_0} \tag{3.5}$$

which is well documented in literature [41, 42, 46, 48].

The interferogram for a 20 mm $\alpha$-barium borate plate was imaged at 488 nm using a 75 mm focal length lens attached to a $1392 \times 1040$ pixel CCD (square pixel width of 6.45 $\mu$m). The plate was placed between crossed polarisers and rotated around the $z$ axis so that the optical axis was 45° to the polariser axes. The interferogram measured is shown in figure 3.4 a).

For comparison, the interferogram was also calculated using equation 3.4. The focal length and pixel offset values in the model were adjusted manually to obtain the best fit with the measured pattern. A difference of 1.5 mm in focal length, a 0.5° rotation of the viewing angle and an offset of 80 and 25 pixels were required in the $i$ and $j$ pixel directions, respectively, to obtain the best fit between measurement and model (see figure 3.4 b).

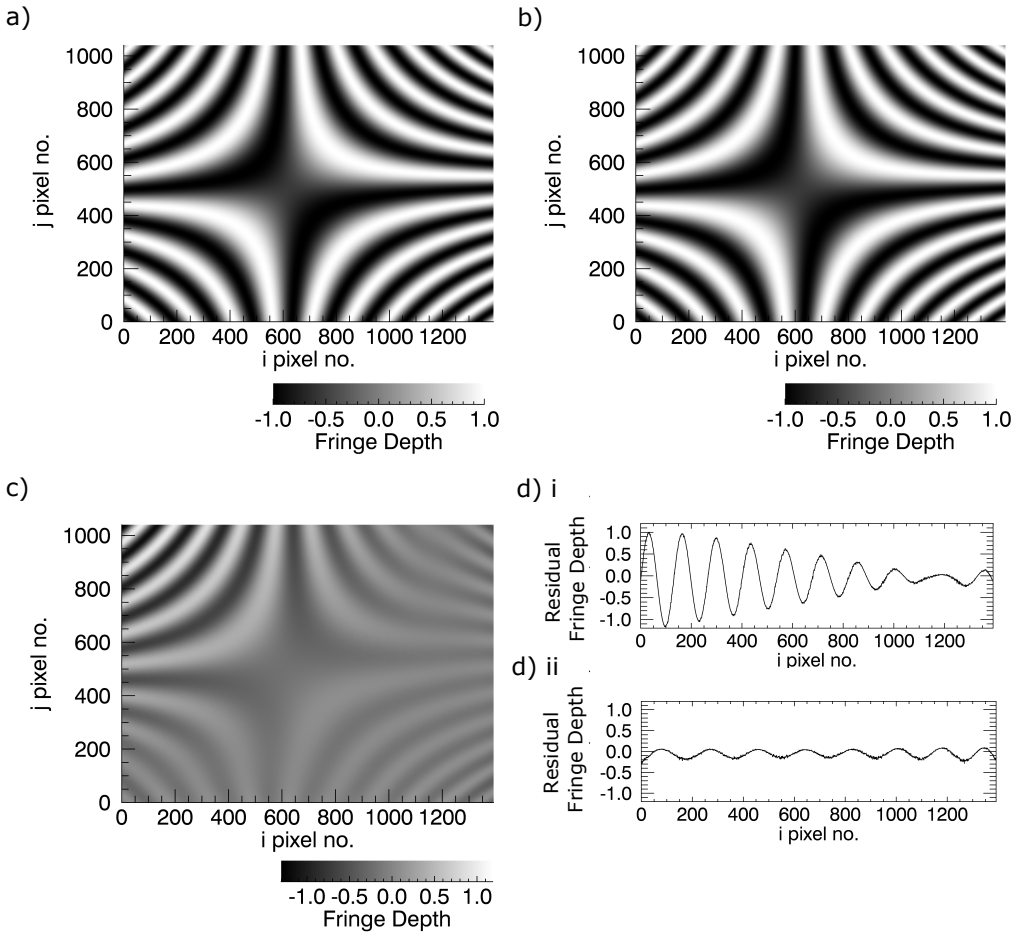


**Figure 3.4:** Interferometric fringe pattern from a 20 mm $\alpha$-barium borate waveplate obtained from (a) a computer model using Verias formula and (b) a waveplate placed between crossed polarisers for the same uniaxial plate orientation. Image (c) shows the residual difference between (a) and (b). Plots (d) i. and (d) ii. are cross sections of (c) at $j = 1000$ and $j = 100$, respectively.

The difference image shown in figure (c), reveals a good fit across the image except in the upper left quadrant. Minor deviations between the model and the measurement are most likely due misalignment between the optic and lens and/or to imperfections in the crystal such slight changes in the thickness and orientation of the optic. The localised 'bad fit' in the upper left quadrant is due to a decrease in the fringe contrast on the periphery of the measurement image. On inspection it is clear that the model still accurately predicts the position of the fringes in this region.

The 2D phase profile for a waveplate is a saddle surface. The phase surfaces are shown for two plate thicknesses (20 mm and 80 mm crystal thicknesses of $\alpha$-barium borate at a wavelength of 488 nm) in figure 3.5 a i) and b i). These two examples were chosen as 20

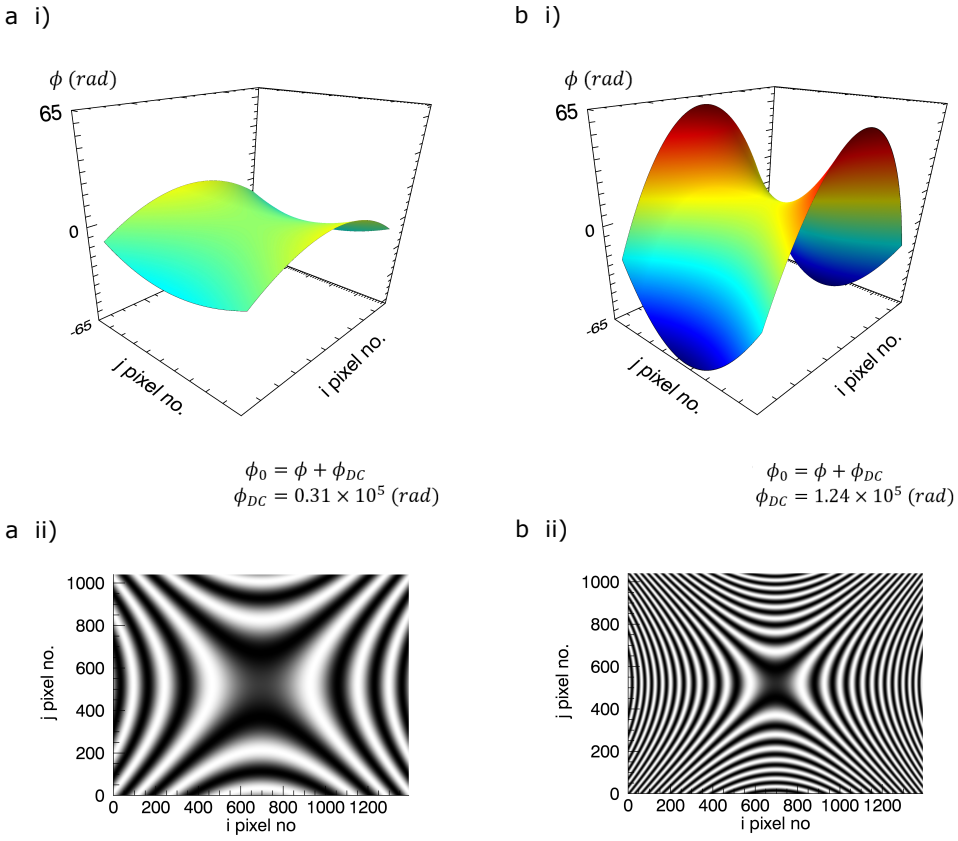


**Figure 3.5:** (i) The phase surface and (ii) the interferometric fringe pattern is shown for a $\alpha$-barium borate waveplate of length (a) a 20 mm and (b) an 80 mm.

mm plates are readily available in the laboratory and are the standard delay plates used to construct the snapshot imaging system for this work. An 80 mm thickness of delay plate is considered as this is the reference length of delay used for instruments in this work.

The crystals modeled in these figures have been rotated around the $z$ axis by 45° (compared with the waveplate shown in figure 3.4) and the DC offset has been subtracted for each of these saddles so that the magnitude of the surface variation can be compared. The DC offset is indicated as the value for $\phi_{DC}$. The saddle surface is dependent on the polar angle, $\delta$ and is therefore governed by the $\sin^2 \delta$ term in equation 3.4. This term scales as $L/n_O$ and become more pronounced at larger interferometric delays (large crystal thickness $L$). This results in more densely packed hyperbolic fringes for thicker crystals as can be seen by comparing figure 3.5 a ii) and b ii).

## 3.3 The shearing plate

The shearing plate is used to tilt the phase saddle so that the associated fringes appeared straight and uniform (not hyperbolic). The spatial heterodyne fringes encode the local coherence in the carrier without the need to scan the delay. The approximately straight and parallel fringes allow for straightforward numerical demodulation processes. The simplest

type of shearing plate is the displacer plate, show in figure 3.6 a). It is a uniaxial crystal cut so that the optical axis is oriented at an angle $\vartheta \neq 0$ to the crystal interface. Standard displacer plates are manufactured to maximise path difference between the ordinary and extraordinary rays and therefore have $\vartheta \sim 45°$. At normal incidence, the ordinary ray transverses the crystal with no angular displacement. The extraordinary ray refracts at an angle determined by both the ordinary and extraordinary refractive indices. The difference in refraction angles results in a spatial separation, $d$, between the components on passage through the crystal plate. This separation is in the same direction as the projection of the optical axis onto the crystal interface. As well as displacement there is a significant phase difference between the E and O ray due to their separate paths through the crystal.

A second common type of shearing plate is the Savart plate, shown in figure 3.6 b). This is a compound plate created from two displacer plates separated by a 90° rotation about the $z$ axis [80]. The resulting ray displacement is diagonal and the average phase shift in this case is small because the the E and O rays switch their identities when passing from the first plate to the second.

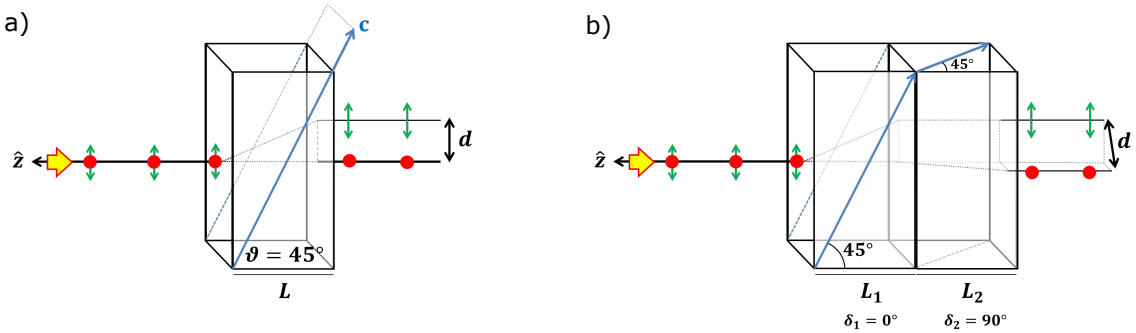


**Figure 3.6:** Transmission of light at normal incidence through (a) a displacer plate and (b) a Savart plate. The orientation of the optical axis c causes a spatial separation between the polarisation components parallel (green) and perpendicular (red) to the optical axis.

The difference in phase for the displacer plate can be derived from the Veiras formula (equation 3.3) by setting $\vartheta = 45°$

$$\phi_0 = \frac{2\pi L}{\lambda_0}\Big((n_{\mathrm{O}}^2 - \sin^2\alpha)^{\frac{1}{2}} + \frac{(n_{\mathrm{O}}^2 - n_{\mathrm{E}}^2)}{(n_{\mathrm{O}}^2 + n_{\mathrm{E}}^2)}\cos\delta\sin\alpha - \frac{2n_{\mathrm{O}}}{(n_{\mathrm{E}}^2 + n_{\mathrm{O}}^2)}\{n_{\mathrm{E}}^2(n_{\mathrm{E}}^2 + n_{\mathrm{O}}^2) - 4n_{\mathrm{E}}^2\sin^2\alpha - (n_{\mathrm{E}}^2 - n_{\mathrm{O}}^2\sin^2\delta\sin^2\alpha)\}^{\frac{1}{2}}\Big) \tag{3.6}$$

For small incident angles the expression reduces to

$$\phi_0 = \frac{2\pi L}{\lambda_0}\left(\frac{1}{b} - \left(\frac{2}{a^2 + b^2}\right)^{-\frac{1}{2}} + \frac{(a^2 - b^2)}{(a^2 + b^2)}\cos\delta\sin\alpha\right) \tag{3.7}$$

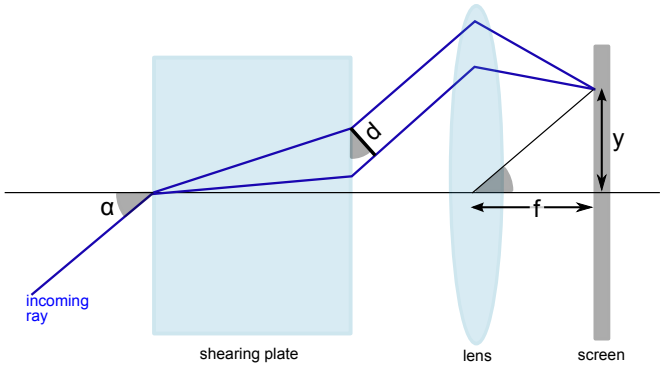


**Figure 3.7**: The ray diagram for a shearing plate when viewed through a lens.

where the refractive index values are captured in the terms $a = 1/n_{\mathrm{E}}$ and $b = 1/n_{\mathrm{O}}$. This expression is the same as that given by the works of Francon [80].

The lateral displacement between the ordinary and the extraordinary ray, $d$, at normal incidence is also given by Francon [80]

$$d = \frac{(a^2 - b^2)\sin(2\vartheta)}{(a^2 + b^2) - (a^2 - b^2)\cos(2\vartheta)} L \tag{3.8}$$

and for the displacer plate with $\vartheta = 45°$ we obtain

$$d = \frac{(a^2 - b^2)}{(a^2 + b^2)} L \tag{3.9}$$

The phase of the Savart plate can be calculated using Veiras formula by adding the phase shifts for the two individual plates with the $\delta$ values changed by 90° to obtain [46]

$$\phi_0 = \frac{2\pi L}{\lambda_0} \left( \frac{(a^2 - b^2)}{(a^2 + b^2)} (\cos\delta + \sin\delta) \sin\alpha \right) \tag{3.10}$$

As $\delta = 45°$, then $\cos\delta + \sin\delta = \sqrt{2}$. The ray displacement for the Savart plate is therefore just $\sqrt{2}d$ where $d$ is calculated from equation 3.9 using the thickness of the combined plates.

When viewed through a lens (see figure 3.7) the phase of the shearing plate can be written in terms of the height in the image plane, $y$, and the focal length of the lens, $f$ and $\tan\alpha = y/f$. The expression for the phase simplifies to

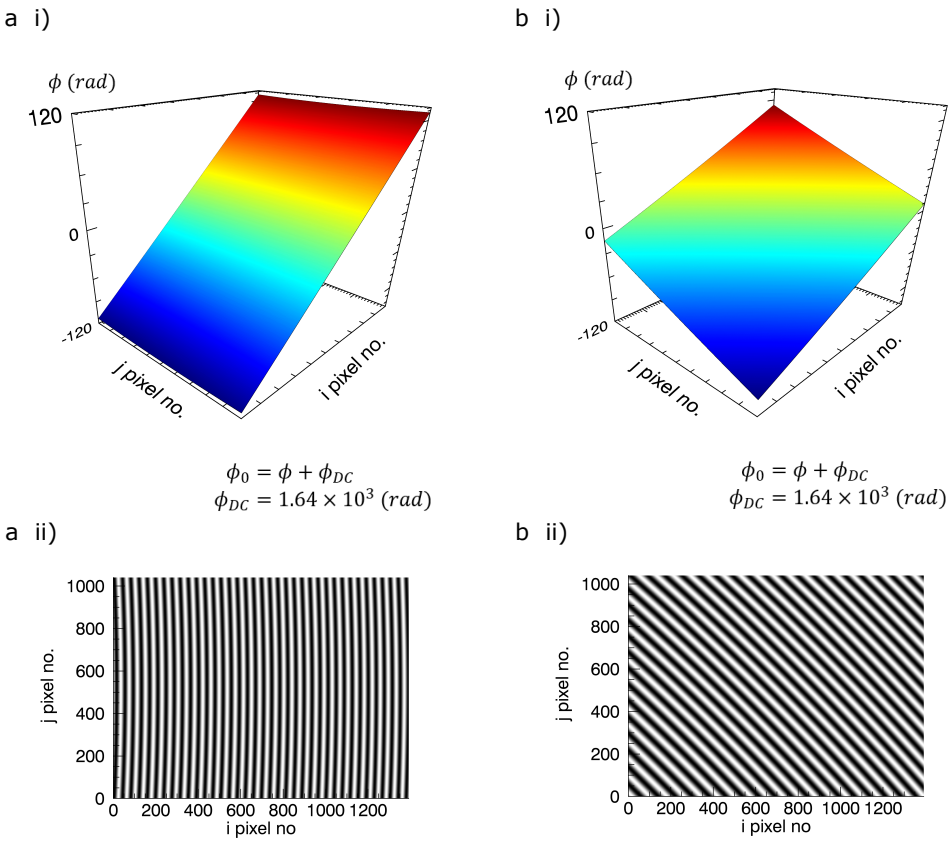


**Figure 3.8:** (i) The phase surface and (ii) the interferometric fringe pattern is shown for (a) a 2 mm thick displacer plate ($\alpha$-BBO) and (b) a 2 mm (combined thickness) Savart plate ($\alpha$-BBO)

$$\begin{aligned} \phi_0 &= \frac{2\pi}{\lambda_0}\frac{d}{f}y \\ &= k_0 y \end{aligned} \tag{3.11}$$

where $k_0 = 2\pi d/\lambda_0 f$ is the wave number.

The phase profile for a displacer plate is a ramp across the image plane. We calculate this for a 2 mm displacer plate. As previous modeling, we assume a 488 nm light source, a $1392 \times 1040$ (6.45 $\mu$m square pixel width) CCD screen, and a 75 mm focal length imaging lens. The modeled displacer plate phase is shown in figure 3.8 a i) and the resulting interferogram consists of near straight fringes shown in figure 3.8 a ii).

The phase profile for a Savart plate is also a ramp of amplitude $\sqrt{2}$ smaller than the displacer phase. However, the phase for the Savart plate is 45° rotated compared with the displacer phase and results in a diagonal fringe pattern. The phase and interferogram shown in figures 3.8 b i) and b ii), respectively, have been calculated for a Savart plate constructed from two 1 mm displacer plates with optical axis crossed.

## 3.4 Field widening

Standard coherence imaging systems employed for high temperature studies can be constructed using small waveplate thicknesses and standard shearing plates, such as displacer plates or a Savart plate. For these systems it is fairly easy to generate a near straight fringe field as the variation in the saddle phase surface of the waveplates is small in comparison to the phase ramp of the shearing plate. In these systems the shearing plate dominates the phase surface and straight fringes can be easily achieved.

However, for the low temperature measurements described in this work, achieving straight uniform interference patterns is not as simple. The large interferometric delays needed in low temperature measurements require large thicknesses of waveplate. The phase surface from an 80 mm $\alpha-$BBO waveplate with a 2 mm $\alpha-$BBO displacer plate is shown in figure 3.9 a). The resulting phase profile has large variations across the saddle surface on the same order of magnitude as the phase ramp produced by the shearing plate. The contributions from the waveplate cause significant distortions in the resulting interferogram, shown in figure 3.9 b).

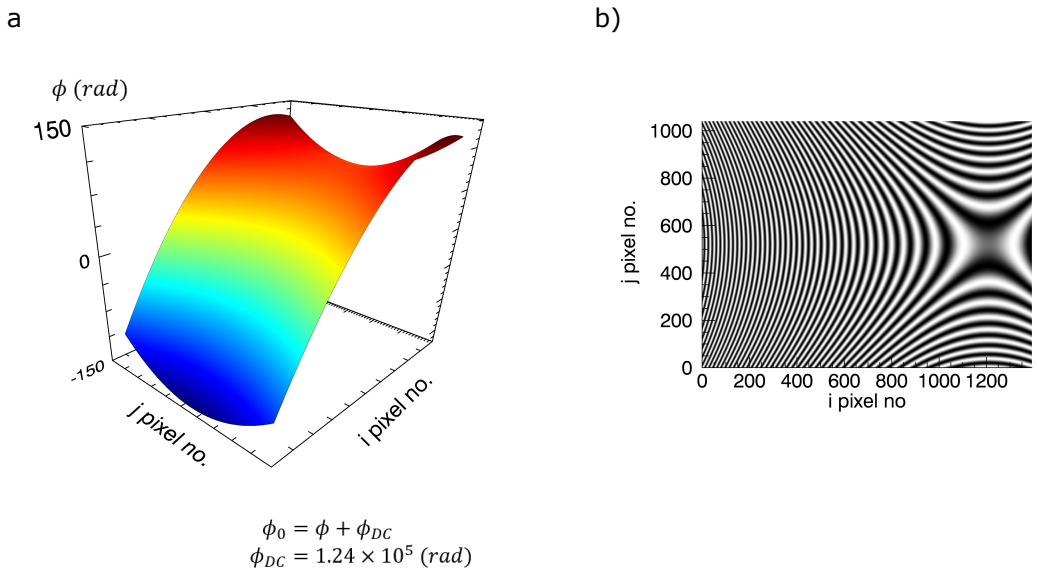


**Figure 3.9:** (a) The phase surface and (b) the interferometric signal produced by a coherence imaging system with large wave-plate thickness. This model uses a 2 mm displacer plate and 80 mm of $\alpha$-BBO waveplate which is similar to the standard requirements for coherence imaging on MAGPIE. The dense 'skewed' interferometric fringe pattern can be reproduced with the same optical components in the laboratory.

In order to correct these distortions, field-widening strategies must be employed. A common method for correcting for fringe distortions is to introduce a half-waveplate to the standard snapshot system [48] (see figure 2.8). The main delay waveplates are split and positioned in equal thicknesses either side of the half-waveplate. these two sections are oriented so their optical axis are crossed (90° plate rotation) and the half-waveplate is inserted and oriented at 45° to the axis of the delay plates.

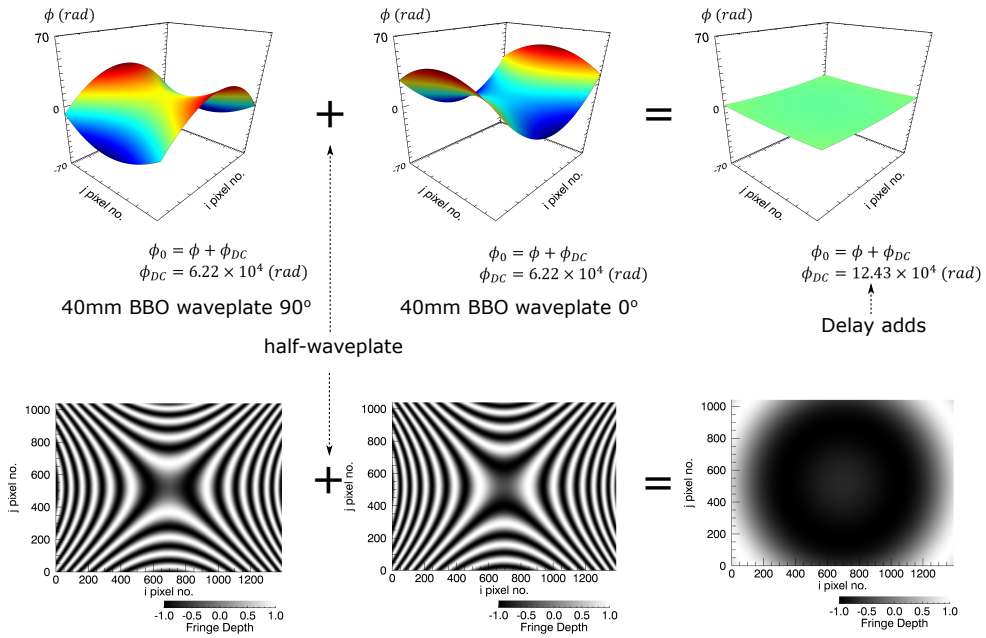


**Figure 3.10:** The phase surface for two waveplates orietated with optical axes at 90°. The plus symbolizes a half waveplate. In this field-widened configuration the net delay of the waveplates add maintaining the required delay offset, while the phase surface flattens. This removes the distortions in the interferogram shown in figure 3.9.

The phase surfaces for each plate are shown in figure 3.10. Without the intervening half-waveplate, the DC phase for each of the two plates will cancel each other and there will be no net DC phase. The intervening half-waveplate flips the polarisation of the ordinary and extraordinary rays so that the delay from each plate continues to add. The saddle phase surface is opposite for each plate and hence the combination of the two plates approximately flattens the phase. A standard shearing plate added to the field widened phase will now dominate the features of phase surface and near-straight fringes can be achieved.

The addition of the half-waveplate presents the opportunity to use an alternative shearing component called the modified Savart plate. This optic can achieve a straighter fringe pattern than a standard Savart plate of the same thickness.

## 3.5 The modified Savart plate

The field widened or modified Savart plate is constructed from two displacer plates of equal thickness with opposing optical axes and an intervening half-waveplate at 45° as shown in figure 3.11.

The half-waveplate flattens the displacer phase profile to correct for the fringe curvature which is manifested at larger plate thicknesses. Without the half-waveplate the phase of the two displacer plates will cancel. Instead, the half-waveplate flips the ordinary and

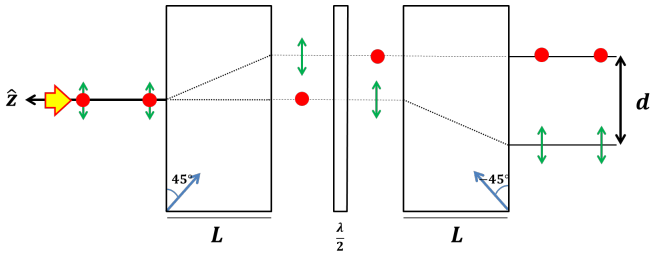


**Figure 3.11:** Transmission of the parallel (green) and perpendicular (red) polarisation components of a light ray (yellow arrow) at normal incidence through a modified Savart plate. The blue arrow indicates the orientation of the optical axes. There is a spatial separation between the two components indicated by 'd'.

extraordinary axis so that the spatial separation between the two beams is double that of a single displacer, and $\sqrt{2}$ larger than a standard Savart plate.

## 3.6 Snapshot coherence imaging

The simplest coherence imaging system is constructed from the combination of these delay and shearing plates as shown in figure 3.12 a). The ray path in figure b) shows how each component affects the polarisation state.

The thickness of the shearing plate is usually chosen according to the desired density of interferometric fringes. The higher the fringe frequency in the image, the greater the spatial resolution of the measurement. The Nyquist sampling criterion requires the sampling rate to be equal or greater than twice the signal frequency [81]. In theory, this means a fringe could be sampled over a range of only a few pixels. In practice, high interferometric fringe-frequencies cause the instrumental fringe contrast to deteriorate due a number of effects including the finite optical system resolution, birefringent plate inhomogeneities and averaging over the pixels leading to a consequent loss of dynamic range for temperature measurements. A carrier period of 10 pixels or more per fringe has been found to be an acceptable compromise between spatial resolution and dynamic range for this study.

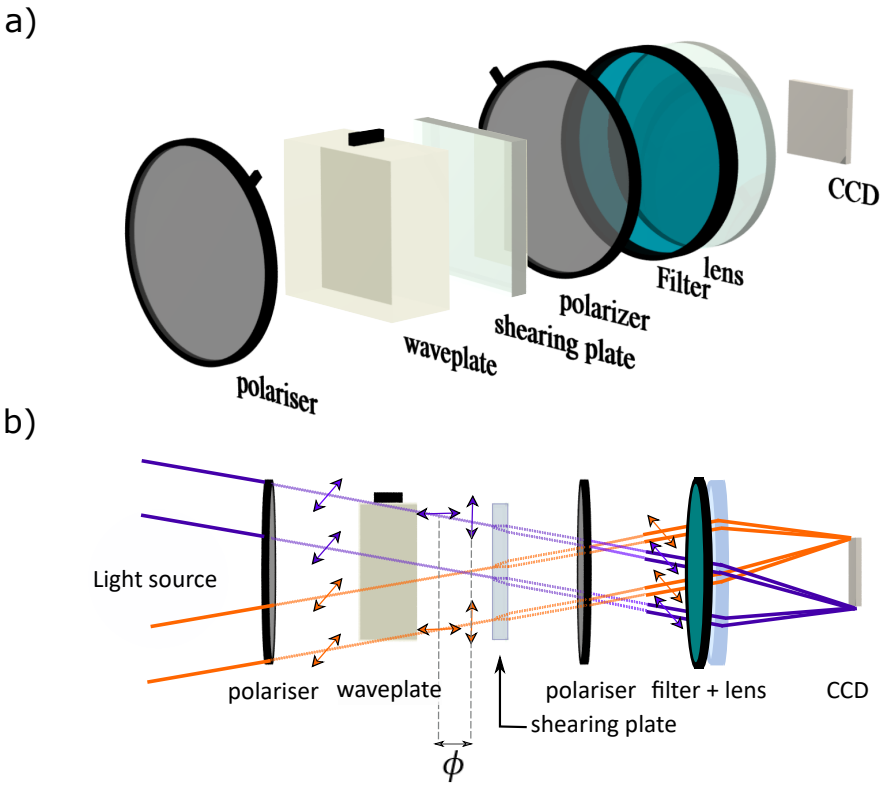


**Figure 3.12:** (a) Optical setup for a standard snapshot coherence imaging system. (b) diagram showing ray path through the optical system and depicts the wave polarisation state, the delay between the polarisation components due to the waveplate, and, the spatial separation of the polarisation components due to the shearing optic. This is shown for different ray incident angles.

Chapter 4

# System design for MAGPIE

This chapter introduces the experimental setup and design considerations for coherence imaging, spectroscopy and Mach probe measurements on the MAGPIE linear plasma device. The details of the MAGPIE device are presented followed by the optical design considerations for the coherence imaging system and the operational details of the measurement. The details of the Mach probe design and calibration are also included here.

## 4.1 The Magnetised Plasma Interaction Experiment

The MAGnetised Plasma Interaction Experiment (MAGPIE) is a linear helicon plasma chamber commissioned as part of the Australian Plasma Fusion Research Facility at the Australian National University. The device has been constructed to produce similar plasma conditions as observed in the divertor region in fusion devices with the fundamental purpose of investigating the surface interactions between the high density helicon plasma and target samples under consideration for the divertor wall material. One of the current research studies on the device examine the production of negative ions in hydrogen for the formation of negative ion beams for applications in fusion heating as well as examination into the properties of ammonia plasma as a boundary gas to trap heat entering the divertor region.

The setup of the MAGPIE solenoidal coils allows controlled variability in the axial magnetic field. This along with the simple linear geometry appeals to the study of fundamental plasma physics including energy transfer between the plasma and helicon wave, and, plasma chemistry and force balance of the equilibrium plasma. The large parameter space (magnetic field, pressure, power variation, geometry and fill gas) as well easy viewing access makes MAGPIE the ideal candidate for coherence imaging in order to characterise the physics underpinning ion flows and temperatures in helicon sources.

A schematic of MAGPIE is shown in figure 4.1. The plasma is contained within a cylindrical column, 1.7 m in length and 10 cm in diameter. The column is divided into two sections. The source section consists of a 1 m Pyrex tube and accommodates the heating antenna. The target chamber (aptly named as this is where the sample targets are placed for material studies) is a 0.68 cm stainless steel vessel equipped with interchangeable

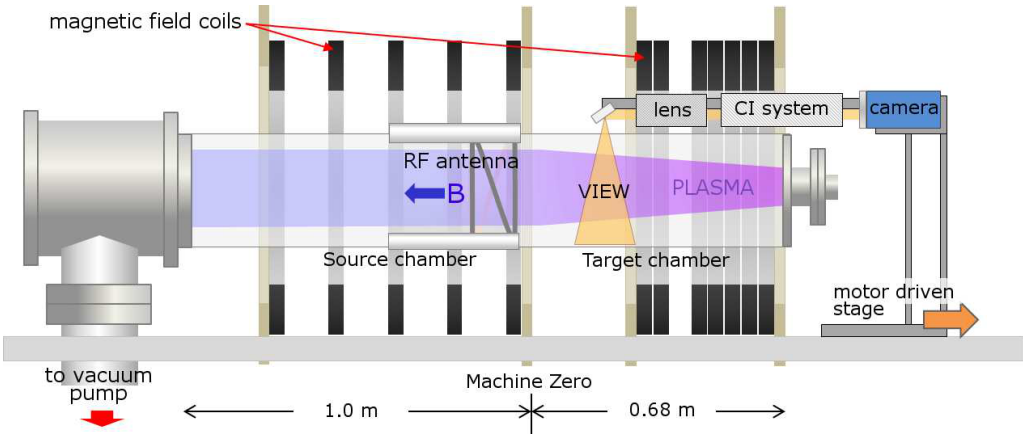


**Figure 4.1:** Diagram of the MAGPIE plasma chamber showing the placement of the coherence imaging system.

widows, blanking plates and entrant ports to allow for flexible diagnostic access.

Base pressures of $10^{-6}$ Torr are achieved using a two-pump (turbonuclear pump and rotary pump) system located at the exit port of the source chamber. The gas enters via a butterfly valve located at the end plate of the target region. The gas flow is regulated by a flow meter and is generally set to provide pressures within the $1 - 10$ mTorr range. A three-gauge (convectron→baratron→ion gauge) system is required to monitor the pressure in MAGPIE which ranges from atmospheric pressure ($7.6 \times 10^2$ Torr) to base pressure ($\sim 10^{-6}$ Torr). The discharge gases include argon, hydrogen and helium.

The plasma is confined by an axial magnetic field produced by solenoidal coils ($\sim$ 30 cm diameter) each positioned co-axially with the cylindrical vessel. Each coil contains 13.5 windings and are internally water-cooled. There are 12 coils in total, 5 are positioned at 16 cm intervals along the source region and another 5 are packed together with 1 cm spacing in the target region to produce a magnetically pinched plasma. The final 2 coils are also positioned with 1 cm spacing along the target chamber, with a 5 cm gap between the set of 5 target coils. These coils are usually inactive and have only been employed for studies requiring a magnetic nozzle configuration. The magnetic field is directed away from the target region towards the source (see figure 4.1).

The mirror and source coils are powered independently by separate 1000 A (20 V) variable DC power supplies. The maximum achievable magnetic field is $\sim 0.19$ Tesla in the target region and 0.09 Tesla in the source. The magnetic field along the axis of MAGPIE for maximum field strength configuration is shown by the black solid curve in figure 4.2. In practice, the coils are usually operated with a maximum current of 800 A as higher currents cause the coils to heat too rapidly and limit measurement time to less than 1 minute, before an interlock system shuts off the system to allow for coil cooling. The reference magnetic field configuration for this work was taken as 400 A in the target coils (0.08 Tesla) and 50 A in the source coils ($\sim 0.005$ Tesla). The on axis magnetic field field profile for the reference configuration is shown by the red dashed plot in figure 4.2.

The plasma is generated using an RF (Nagoya type III) left-handed helicon antenna with a

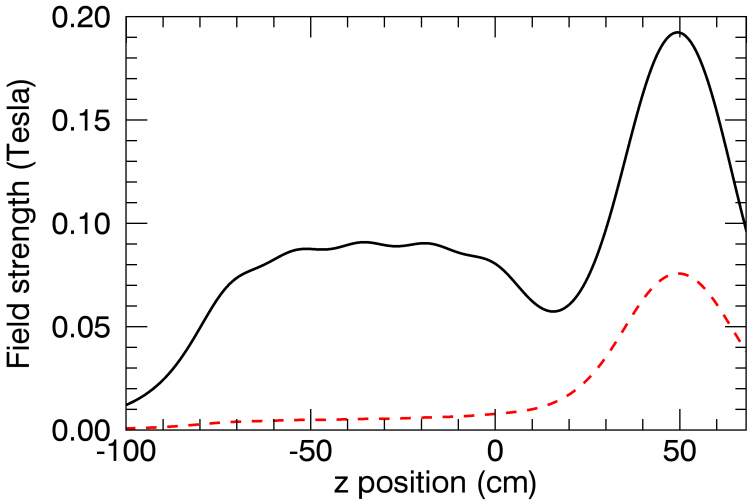


**Figure 4.2:** On axis magnetic field for maximum magnetic field operation (black) and the standard magnetic field operation (red).

180° twist, which launches $m = +1$ polarised waves towards the target chamber (opposite to the direction of the magnetic field). A 13.5 mHz signal (from a Rohde and Schwartz SM300 9kHz-3GHz signal generator) is passed to an ENI 150 W broadband amplifier. This drives the 5 kW Alpha DC amplifier. The power is coupled to the plasma via a 2× variable-capacitor matching network. The forward and reflected power are monitored using an Alpha $A4520$ $(2-30$ MHz) power meter with the plasma operating in continuous mode [19]. In the high power (1 kW) helicon mode, the visible emission in argon discharges is dominated by a distinctive 'blue core' of ion emission. To facilitate the study of argon ion behavior in the helicon mode, the plasma is operated at forward powers $> 800$ W.

Ion density profiles with central maximum density of $5.5 \times 10^{18}$ m$^3$ and radial peaked electron temperatures of 4 eV, measured using an RF compensated probe, have been reported for the 1 kW argon helicon mode in MAGPIE. The magnitude and phase of the axial wavefield has also been measured using an RF magnetic probe [19]. Measurements of the electron energy probability function (EEPF) as well as ion density and electron temperature have also been reported for MAGPIE in the argon inductive mode ($\sim$ 200W) [82].

## 4.2 Spectral measurements on MAGPIE

The spectral lines for argon plasma in MAGPIE were measured (for this work) using a Czerny-Turner spectrometer setup. Measurements of the spectral emission profile were an important preliminary step in this work in order to determine the dominant spectral lines and the likelihood of contamination from neighboring lines.

Figure 4.3 (i) shows a wavelength scan of the argon spectrum for light acquired at $\sim 20$ cm axially (radially central) along the chamber. The spectrum was measured using the USB

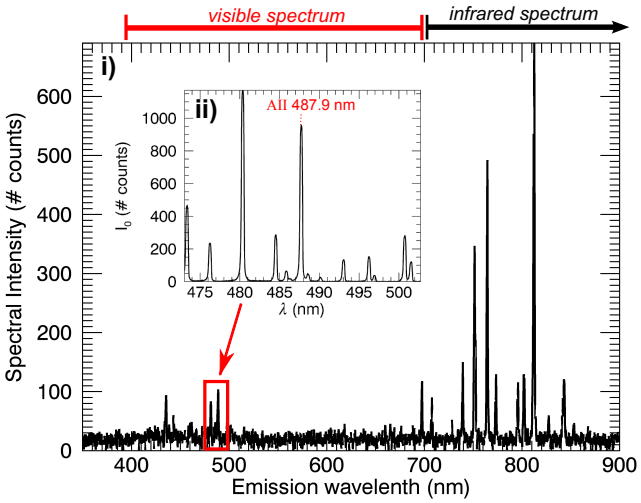


**Figure 4.3:** Spectrum of the argon plasma in MAGPIE showing neutral lines in the infra-red and strong ion lines around $400 - 500$ nm.

HR400 Ocean Optics spectrometer with $\sim 2$ nm resolution. Light was coupled into the spectrometer using an optic fiber fitted with a small lens. The spectral scan shows a large collection of spectral lines in the infrared wavelengths. These are mostly Ar I neutral lines [83]. This work is concerned with the measurement of the argon ion Ar II 487.9 nm line. A snapshot of the spectrum in the vicinity of the 487.9 nm line was obtained using the IsoPlane-SCT 320 spectrometer coupled to a PI-max 4, $1024 \times 1024$ pixel CCD. Slit widths of $200 - 150$ $\mu$m were used to achieve resolutions between $0.4 - 0.6$ nm. The high resolution spectrum is shown in insert, (ii), and was taken over the $473 - 503$ nm wavelength range. The spectral lines in this range are dominated by argon ion lines, Ar II. The spectrum shows the 487.9 nm line is strong and fairly isolated from other lines and therefore a good candidate for coherence imaging. A small secondary line at 486.5 nm also exists and may not be excluded by the passband of the imaging filter. The contamination effects from neighboring lines will be discussed in a later chapter. The 487.9 nm line was selected over the strong 480.6 nm line as an argon ion gas laser with wavelength 488 nm was readily available to use as the calibration source.

Coherence imaging relies on Doppler broadening to measure the ion temperature. It is expected that the ion temperature in MAGPIE will be between 0.1 eV and 1 eV following reports from similar helicon sources [29]. This correspond to an expected Doppler broadening of $\Delta\lambda = 0.8 - 2.5$ pm (equation 2.2). The presence of the large magnetic field in MAGPIE means that the Zeeman effect is expected to have a small but measurable effect on the coherence imaging result. This will now be discussed.

### 4.2.1 The Zeeman effect

A magnetic field applied to an emitting source is observed to cause the central emission frequency to split into multiple polarised components. This effect arises due to the interaction of the emitting particles magnetic moment, $\mu$ and the external magnetic field, $\mathbf{B}$,

where the interaction potential is given by [84]

$$\Delta E = -\boldsymbol{\mu} \cdot \mathbf{B} \tag{4.1}$$

This is known as the Zeeman effect, where the degree of energy splitting is determined by the strength of the external magnetic field and also on the atomic structure of the emitting particle. The fine spitting of these lines causes a perceived broadening of the central line width which, if on the same order as Doppler broadening, can be interpreted as an elevation in temperature.

Electrons orbiting an atom can be thought of as a current loop and therefore have an associated magnetic moment given by the Bohr magneton

$$\mu_B = \frac{eh}{2\pi m_e} \tag{4.2}$$

which is a constant equal to $\mu_B = 9.274009 \times 10^{-24}$ J T$^{-1}$. Here $e$ is the electronic charge, $h$ is the Planck constant and $m_e$ is the mass of an electron. A multi-electron atom is also described using quantum numbers, $\mathcal{L}, \mathcal{S}, \mathcal{J}, \mathcal{M}$, and is dependent on the microstates of the electrons. For weak magnetic fields the $\mathcal{L}$ and $\mathcal{S}$ quantum numbers are well defined and are treated using the L-S (Russel-Saunders) coupling scheme where the total angular momentum quantum number is given by the values

$$\mathcal{J} = \mathcal{L} + \mathcal{S}, \mathcal{L} + \mathcal{S} - 1, \ldots, |\mathcal{L} - \mathcal{S}| \tag{4.3}$$

and the magnetic quantum number is determined by $\mathcal{M} = \mathcal{J},\ \mathcal{J} - 1,\ \ldots,\ 0, \ldots,\ -\mathcal{J}$.

The 488 nm emission line observed in MAGPIE corresponds to the transition [83]

$$3s^2 3p^4(^3P)4s\ \boldsymbol{^2P_{\frac{3}{2}}} \rightarrow 3s^2 3p^4(^3P)4p\ \boldsymbol{^2D^{\circ}_{\frac{5}{2}}} \tag{4.4}$$

Where term symbol (in bold) is written in the form $\boldsymbol{^{2s+1}L_J}$.

For an multi-electron system, the magnetic moment is formed from both the contributions from orbiting electrons and also the intrinsic magnetism associated with the nucleus and the electron. The angular momentum quantum number, $\mathcal{M}$, forms a set of degenerate energy states which become differentiable in the presence of a magnetic field. A single emission line will therefore be split into $2\mathcal{J} + 1$ new lines, each shifted in energy from the central line. In weak magnetic fields the shift in energy is given by [84, 85]

$$\Delta E = \mathcal{M}\ g_J\ \mu_B\ \mathrm{B} \tag{4.5}$$

where $g_J$ is the Lande g factor defined as

$$g_J = 1 + \frac{\mathcal{J}(\mathcal{J}+1) + \mathcal{S}(\mathcal{S}+1) - \mathcal{L}(\mathcal{L}+1)}{2\mathcal{J}(\mathcal{J}+1)} \tag{4.6}$$

Considering the 488 nm transition: the presence of a magnetic field will cause the initial $^2\boldsymbol{P}_{\frac{3}{2}}$ state to separate into four distinct energy levels and the final state, $^2\boldsymbol{D}^{\circ}_{\frac{5}{2}}$, will separate into six distinct energy levels. Each level is distinguished by the magnetic quantum number $\mathcal{M}$ and Lande factor. The expected energy states for the 488 nm transition in a 0.2 Tesla magnetic field are shown in figure 4.4.

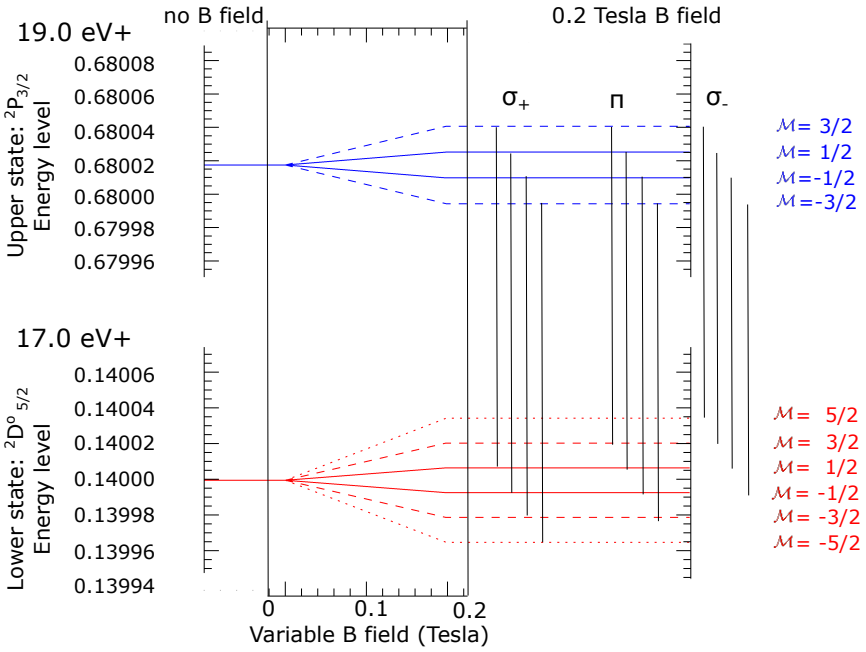


**Figure 4.4**: Zeeman splitting levels for the 488 nm argon transition.

The unshifted energy states observed at times when there is no magnetic field are indicated by the far left red and blue lines. When a magnetic field is applied, the degeneracy of the energy levels are lifted and each level is uniquely described by its own magnetic angular momentum quantum number, $\mathcal{M}$. Transitions will only occur between energy levels which satisfy: $\Delta\mathcal{M} = 0$ or $\Delta\mathcal{M} = 1$. The allowed transitions are indicated by the vertical lines on the right hand side.

These $\Delta\mathcal{M}$ transitions are uniquely polarised so that when viewed orthogonally to the magnetic field the $\pi$ components ($\Delta\mathcal{M} = 0$) are linearly polarised parallel to the field while the $\sigma_+$ and $\sigma_-$ components ($\Delta\mathcal{M} = \pm 1$) are linear polarised perpendicular to the field. When viewed along the magnetic field, the $\sigma_+$ and $\sigma_-$ components are circularly polarised and the $\pi$ components have no magnitude. The intensity of the $\pi$ components combined is equal to the total combined intensity of both the $\sigma_+$ and $\sigma_-$ components so that the total output, from any viewing direction, is net unpolarised.

The relative intensities for the Zeeman components have been given in [86]. For components viewed transverse to the magnetic field, as is the case for MAGPIE, the relative intensities are summarised in the table 4.1.

| transition | $I_\pi$ | $I_\sigma(\mathcal{M} \to \mathcal{M}-1)$ | $I_\sigma(\mathcal{M} \to \mathcal{M}+1)$ |
|---|---|---|---|
| $\mathcal{J} \to \mathcal{J}$ | $\mathcal{M}^2$ | $\frac{1}{4}(\mathcal{J}+\mathcal{M})(\mathcal{J}+1-\mathcal{M})$ | $\frac{1}{4}(\mathcal{J}-\mathcal{M})(\mathcal{J}+1+\mathcal{M})$ |
| $\mathcal{J} \to (\mathcal{J}-1)$ | $\mathcal{J}^2-\mathcal{M}^2$ | $\frac{1}{4}(\mathcal{J}+\mathcal{M})(\mathcal{J}-1+\mathcal{M})$ | $\frac{1}{4}(\mathcal{J}-\mathcal{M})(\mathcal{J}-1-\mathcal{M})$ |
| $\mathcal{J} \to (\mathcal{J}+1)$ | $(\mathcal{J}+1)^2-\mathcal{M}^2$ | $\frac{1}{4}(\mathcal{J}+1-\mathcal{M})(\mathcal{J}-\mathcal{M}+2)$ | $\frac{1}{4}(\mathcal{J}+1+\mathcal{M})(\mathcal{J}+\mathcal{M}+2)$ |

**Table 4.1:** The relative intensities of the Zeeman components for the case of transverse observation.

The change in frequency of the lines is related to the energy through equation $E = h\nu$. The change in wavelength can therefore be determined remembering that $\Delta\lambda/\lambda_0 = \Delta\nu/\nu_0$. Each emission line is also Doppler broadened with temperature $T_S$ and can be written as a Gaussian described by equation 2.16. The total lineshape for an emission affected by the Zeeman and Doppler effects is just the weighted sum of each Doppler broadened Zeeman component.

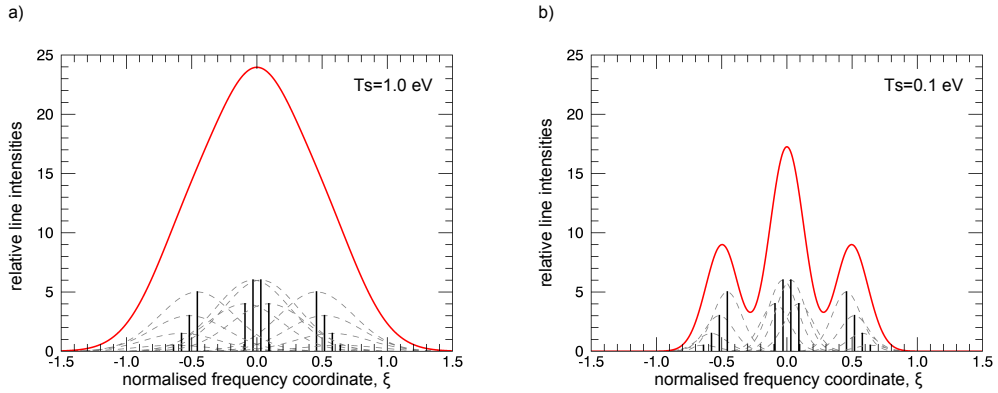


**Figure 4.5:** With an applied magnetic field the degeneracy of the energy levels is lifted revealing multiple spectral lines. These are shown for the 488 nm argon transition considering a magnetic field of 0.2 Tesla (black vertical lines). The grey dashed outline indicates the Doppler broadened lineshape for each of these components assuming an ion temperature of in case (a) 1.0 eV and (b) 0.1 eV. The red lineshape is the total lineshape calculated from the weighted sum of each of the components.

The Zeeman components for the 488 nm argon transition are modeled assuming a magnetic field of 0.2 Telsa and ion temperatures of 1.0 eV and 0.1 eV shown in figure 4.5 (a) and (b) respectively. The black vertical lines represent the central frequency of each Zeeman component, with height scaled by the relative intensities given in table 4.1. The grey dashed lines indicate the Doppler broadened lineshape for each Zeeman component and the thick red line indicates the total lineshape produced from the sum of the lineshapes. The frequency coordinate used here is the normalised frequency given in equation 2.16.

For the high temperature case (1.0 eV shown in figure (a)) the Doppler broadening is large so that the total line-shape appears near Gaussian. For the lower temperature (0.1 eV shown in figure (b)) the Doppler broadening is small and so the $\sigma$ components create wings at the edges of the lineshape.

The coherence for each Zeeman component can be calculated analytically from equation 2.25. Due to the nature of the Fourier transform, the coherence from each individual component can simply be added to give a total coherence. Taking the absolute value of the coherence delivers the expected contrast, $\zeta$, assuming there are no line integration effects.

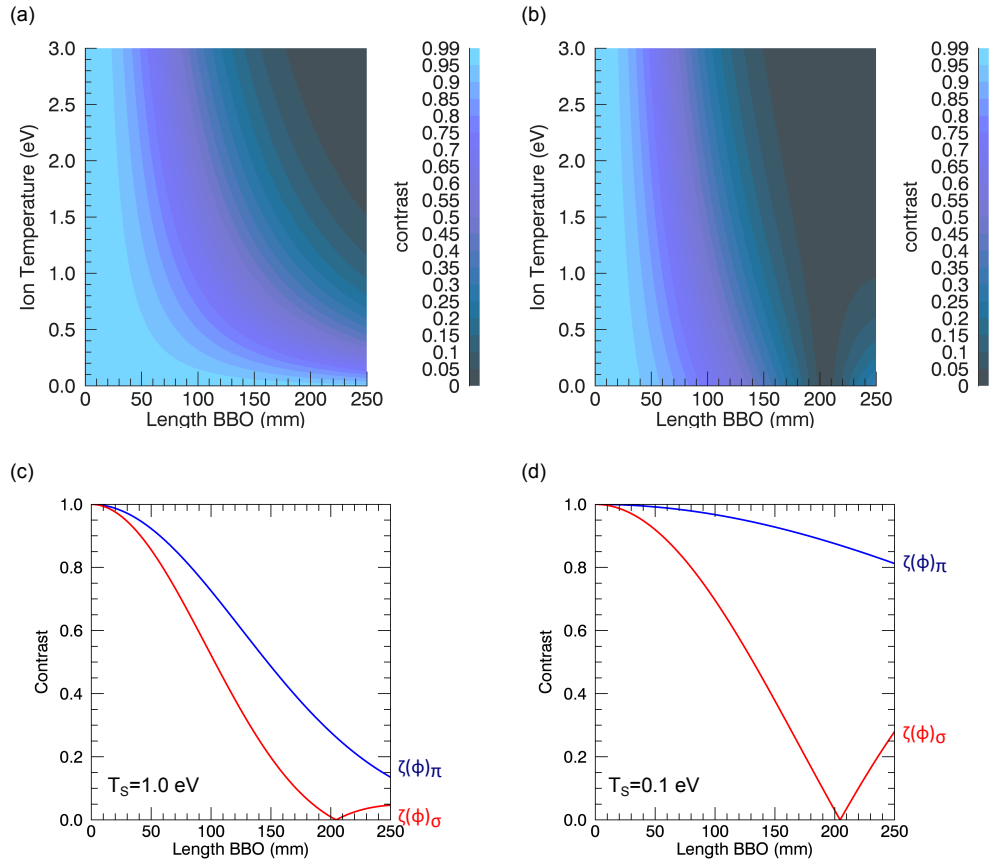


**Figure 4.6:** Contrast, $\zeta$, maps of (a) $\pi$ component and (b) combined $\sigma$ components, plotted for ion temperature and instrumental delay for the 488 nm transition, assuming a magnetic field of 0.2 Tesla. Cross-sections of (a) and (b) are plotted in (c) and (d) for constant ion temperatures of 1.0 eV and 0.1 eV, respectively. The blue plots indicate the $\pi$ contribution (indicated by the subscript $\pi$) the red plots are the combined $\sigma$ contributions (indicated by subscript $\sigma$).

The expected contrast for a 0.2 Tesla magnetic field is shown as a function of species temperature and instrumental delay in figures 4.6 where figure (a) is the contrast for the $\pi$ component, labeled $\zeta_\pi$, and (b) is the contrast for the combined $\sigma$ components, labeled $\zeta_\sigma$. Cross sections of figures (a) and (b) taken at temperature values of 1.0 eV and 0.1 eV are shown in figures (c) and (d). The blue plots are the cross-sections of $\zeta_\pi$ and the red plots are cross sections of $\zeta_\sigma$.

The 0.2 Tesla magnetic field condition is the maximum achievable magnetic field for this study. In general, most measurements in this study are related to the reference magnetic field condition, with the on axis magnitude plotted in figure 4.2. This reference condition has a maximum magnetic field of only 0.075 Tesla and therefore the effect of Zeeman splitting is substantially reduced. The contrast for the $\pi$ and $\sigma$ components along with the contrast averaged for the two components are plotted in figures 4.7, for ion temperatures

of 1.0 eV (a) and 0.1 eV (b).

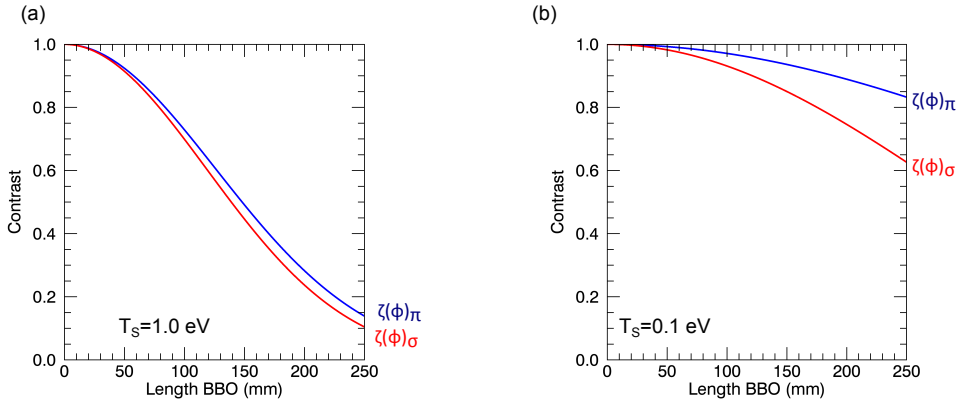


**Figure 4.7:** Contrast, $\zeta(\phi)$ expected at (a) $T_S = 1.0$ eV and (b) $T_S = 0.1$ eV with an applied magnetic field of 0.075 Tesla. Blue and red plots are the calculated contrast for the $\pi$ and combined-$\sigma$ components respectively.

It can therefore be concluded that spectral broadening is only likely to be significant at the highest magnetic field conditions, or at very low temperatures. To test the manifestation of the Zeeman effect experimentally, an additional vertical polariser was placed at the front of the imaging system to eliminate the Zeeman sigma components which can, due to their slight wavelength shift away from the central wavelength, cause a decrease in the measured fringe contrast. In order to confirm that the Zeeman effect does not contribute to a measurable elevation in temperature, a second measurement was then made with the additional polariser orientated horizontally so that the $\pi$ component was excluded and only $\sigma$ components were detected. Comparing the two measurements ($\pi$ only and $\sigma$ only) there was no marked change in the measured contrast, confirming that Zeeman spectral effects were insignificant at the reference conditions compared with the Doppler spectral broadening.

## 4.3 Doppler coherence imaging on MAGPIE

Doppler coherence imaging for fusion experiments generally rely on the assumption that the plasma is in a state of local thermal equilibrium. This allows for simplifications when interpreting the phase and contrast to determine plasma flow and temperature. For studies on cooler laboratory plasmas this is not necessarily true. Therefore the coherence measurement in this study must be treated carefully. The following section discusses the requirements for coherence imaging on low-temperature laboratory plasmas.

Radiating species in the edge and core of high temperature plasmas ($T_e \sim T_i \sim 10$ keV) such as those found in fusion experiments exhibit significant Doppler broadening and only require a small amount of interferometric delay (1000 waves, low resolving power) in order to observe Doppler effects. For small crystal thicknesses ($< 5$ mm) the coherence imaging systems employed for fusion plasmas are usually quite compact and robust and do not suffer significantly from thermal drifts and other instrumental challenges associated with

the long delay ($> 10^4$ waves, 100 mm plate thickness) imaging system required for the study of cold and heavy (A = 40) ion species.

Large interferometric delays presents challenges for low temperature measurements, as birefringent material exhibits high sensitivity to temperature and the large lengths of birefringent crystal required in this study led to thermal stability issues for the interferometric phase. The clear solution would be to mount the entire system in a temperature regulated oven, however, due to the space restrictions in the location of the imaging system a custom built oven was not practical. Instead this study focused on building a compound system using birefringent plates with different thermal properties to passively compensate the thermal drifts. This work will be discussed in section 4.3.1. Large interferometric delays also result in significant curving of the shearing fringes. Field-widening techniques were therefore required to maintain the regularity of the interferometric fringe pattern.

### 4.3.1 Selection of birefringent materials

There are many options when choosing the birefringent crystal components for the design of these systems. In this study, yttrium orthovanadate ($YVO_4$), lithium niobate ($LiNbO_3$), calcite ($CaCO_3$) and $\alpha-$barium borate ($\alpha-$BBO) were considered as they all exhibit high birefringence and are commonly available through optical suppliers. Table 4.2 lists these materials with their birefringence ($n_E - n_O$) values.

| Crystal | Birefringence | $n_O$ | $n_E$ | Ref. |
|---|---|---|---|---|
| $YVO_4$ | 0.24 | 2.035 | 2.278 | [87] |
| $LiNbO_3$ | -0.09 | 2.349 | 2.256 | [75] |
| $CaC0_3$ | -0.18 | 1.667 | 1.488 | [78] |
| $\alpha-$BBO | -0.12 | 1.679 | 1.559 | [76] |

**Table 4.2:** The Birefringence along with the refractive index values are listed for the materials considered in this study.

Using the birefringence of a given material, it is possible to calculate the expected contrast or characteristic temperature for various crystal lengths and species using equations 3.5 and 2.20. This has been calculated for the materials considered and is shown in figure 4.8. These plots can be used to determine the amount of a crystal required for measurements at a given species temperature, $T_S$. For high resolution of the temperature a delay was chosen so that the contrast is $1/e$. At this condition $T_S \approx T_C$. These plots show that $YVO_4$ is the best candidate for low temperature plasma measurements as it exhibits the highest birefringence and hence only $\sim 60$ mm of crystal is required for measurements of a 1 eV plasma (considering the ion temperature). It is also, however, important to consider the other material properties such as available aperture, cost, thermal properties and so on.

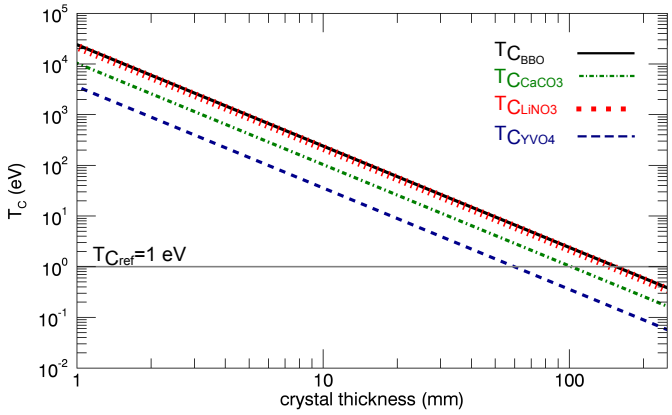


**Figure 4.8:** Characteristic temperature plotted against crystal length (mm) for four different birefringent materials: $\alpha$-BBO (black solid line), $CaCO_3$ (green dash-dot line), $LiNbO_3$ (red dotted line) and $YVO_4$ (blue dash line). The grey reference line indicates a characteristic temperature of 1 eV indicating the required crystal thickness for a plasma temperature at the same temperature (for where $\zeta \sim 1/e$, $T_S \approx T_C$).

### Temperature dependence and passive stabilisation

Birefringent crystals are highly sensitive to changes in temperature. Not only can the temperature cause the crystals to expand and contract, but the temperature dependence of the refractive indices can change the birefringence of the crystal. This can produce a significant thermal drift in the interferometric phase and contaminate absolute flow measurements. As the shearing plate is usually only millimetres thick, the following study focuses on remediating the thermal phase drifts associated with large waveplate thicknesses ($\sim$ 100 mm). Moreover, a modified Savart plate is employed to create the phase shear so that this shearing optic is already compensated to first order against thermal drifts.

The on axis phase of a waveplate is given by equation 3.5. The birefringence $B$ is the difference in the ordinary and extraordinary refractive indices and these are dependent on the temperature of the crystal and the wavelength. The refractive indices for a material are approximated by the Sellmeier equations, which take the form

$$n_{\mathrm{O}}(\lambda,T)^2 = a_{\mathrm{O},0} + b_{\mathrm{O},0}T^2 + \frac{a_{\mathrm{O},1} + b_{\mathrm{O},1}T^2}{\lambda^2 - \left(a_{\mathrm{O},2} + b_{\mathrm{O},2}T^2\right)^2} + a_{\mathrm{O},3}\lambda^2$$
$$n_{\mathrm{E}}(\lambda,T)^2 = a_{\mathrm{E},0} + b_{\mathrm{E},0}T^2 + \frac{a_{\mathrm{E},1} + b_{\mathrm{E},1}T^2}{\lambda^2 - \left(a_{\mathrm{E},2} + b_{\mathrm{E},2}T^2\right)^2} + a_{\mathrm{E},3}\lambda^2 \qquad (4.7)$$

where the constants $a_{\mathrm{O}}, b_{\mathrm{O}}, a_{\mathrm{E}}$ and $b_{\mathrm{E}}$ have been determined empirically for many materials and are documented in the literature. The constants $b_{\mathrm{O}}$ and $b_{\mathrm{E}}$ are associated with the $T^2$ temperature dependence and can be significant for materials such as lithium niobate. The refractive indices have been calculated for each of the materials considered and are

quoted in table 4.3. For Sellmeier equation details, see appendix A.

The thermal dependence of a waveplate delay, $\phi_0 = 2\pi LB/\lambda$, is given by

$$\epsilon_T = \frac{1}{\phi_0}\frac{d\phi_0}{dT} = \left(\frac{1}{L}\frac{dL}{dT} + \frac{1}{B}\frac{dB}{dT}\right) \tag{4.8}$$

The thermal expansion coefficient, $(1/L)\ dL/dT$, and the thermo-optic coefficients $dn_O/dT$ and $dn_E/dT$ given in 4.3 are determined empirically and are usually available in literature. Uniaxial crystals are hexagonal or tetragonal lattice crystal systems with two main cell dimensions, a and c. The optical axis of uniaxial crystals correspond to the c-crystolographic axis (principal axis). For a waveplate, the direction of transmission is orthogonal to the optical axis and hence the thermal expansion coefficients were cited for the a-crystolographic axis direction.

| Crystal | $n_O$ | $n_E$ | $\frac{1}{L}\frac{dL}{dT}(K^{-1})$ | $\frac{dn_O}{dT}(K^{-1})$ | $\frac{dn_E}{dT}(K^{-1})$ | $\epsilon_T \times 10^{-6}$ | Ref. |
|---|---|---|---|---|---|---|---|
| $YVO_4$ | 2.035 | 2.278 | $2.0 \times 10^{-6}$ | $15.6 \times 10^{-6}$ | $9.5 \times 10^{-6}$ | $-13.79$ | [77, 87] |
| $LiNbO_3$ | 2.349 | 2.256 | $14.8 \times 10^{-6}$ | $3.5 \times 10^{-6}$ | $40.7 \times 10^{-6}$ | $-386.22$ | [75, 88, 89] |
| $CaC0_3$ | 1.667 | 1.488 | $-3.7 \times 10^{-6}$ | $3.0 \times 10^{-6}$ | $13.0 \times 10^{-6}$ | $-50.80$ | [78, 90] |
| $\alpha-BBO$ | 1.679 | 1.559 | $4.0 \times 10^{-6}$ | $-16.6 \times 10^{-6}$ | $-9.3 \times 10^{-6}$ | $-56.47$ | [76] |

**Table 4.3:** The thermal and optical properties are listed for the materials considered in this study. $n_O$ and $n_E$ are the ordinary and extraordinary refractive indices $(1/L)\ dL/dT$ is the thermal expansion coeficient, and $dn_O/dT$ and $dn_E/dT$ are the ordinary and extraordinary thermo-optic coefficients.

The thermal values have been quoted from relevant works for the wavelengths closest to 488 nm and temperatures nearest 25° C. Where multiple (different) values have been quoted in literature, the most recent published results have been taken. It should be noted that there are, in some cases, significant differences between the values quoted from different sources for some of these materials. In the case of lithium niobate, values here are quoted for congruent melt crystals as this is the most common form of lithium niobate in optical applications due to the high optical quality, uniform birefringence and growth length of up to 50 mm [75, 89]. The calcite thermo-optic coefficients have not been widely documented in journal literature and many values quoted on the data-sheets of crystal manufacturers have been incorrectly labeled and not referenced. The above values were quoted from [90], which was taken as the most reliable source.

For each material under consideration, the thermal expansion coefficients, thermo-optic coefficients and $\epsilon_T$ are listed in table 4.3. Note that all the values for $\epsilon_T$ are negative.

In order to build a temperature stable imaging system, the temperature induced phase-change for the total system must be equal to zero,

$$\begin{aligned}\left(\frac{d\phi}{dT}\right)_T &= \left(\frac{d\phi}{dT}\right)_a \pm \left(\frac{d\phi}{dT}\right)_b \pm \ ... \\ &= 0\end{aligned} \tag{4.9}$$

where the subscripts $a, b...$ designate the material type and the $\pm$ indicates whether the temperature-induced phase adds or subtracts according to the relative orientation of the crystal axes. A two material combination was considered for this work. The first material provides the main interferometric delay and ideally should have high birefringence and low thermal sensitivity. The second material which is used to compensate the phase drift of the first material should have a high thermal sensitivity and low birefringence. It is clear from the values in table 4.3 that lithium niobate is very sensitive to temperature changes and hence is an good choice as the compensating material.

Setting the total phase change to zero in equation 4.9 and substituting the expression given in 4.8, a ratio between the lengths of the materials for thermal compensation is found

$$\frac{L_b}{L_a} = \pm\frac{B_a\epsilon_{T_a}}{B_b\epsilon_{T_b}} \tag{4.10}$$

The above ratio is calculated for yttrium othvanadate, calcite and $\alpha$-barium borate using lithium niobate as the compensation material. It is also useful to calculate the characteristic temperature for these combined systems to show the achievable temperature sensitivity. The delay for the combined system is given by

$$\phi_T = \phi_a \pm \phi_b \tag{4.11}$$

where the $\pm$ term is chosen whether the delay of the compensating plate is adding or subtracting from the main delay plates. The total delay will be dependent on the optical dispersion effects of each of the materials.

Given that

$$\frac{\Delta\phi}{\kappa\phi} = \frac{\Delta\lambda}{\lambda} \tag{4.12}$$

and

$$\Delta\phi_T = \Delta\phi_a \pm \Delta\phi_b \tag{4.13}$$

then

$$\Delta\phi_T = \frac{\Delta\lambda}{\lambda}\kappa_T\phi_T \tag{4.14}$$

$$= \frac{\Delta\lambda}{\lambda}\kappa_a\phi_a \pm \frac{\Delta\lambda}{\lambda}\kappa_b\phi_b \tag{4.15}$$

Rearranging in terms of $\kappa_T$ and using equation 4.11

$$\kappa_T = \frac{\kappa_a\phi_a \pm \kappa_b\phi_b}{\phi_a \pm \phi_b} \tag{4.16}$$

This can written in terms of the thickness and birefringence of each material using the definition 3.5. We can define the ratio

$$\gamma = \frac{L_aB_a}{L_aB_a \pm L_bB_b} \tag{4.17}$$

and so the dispersion coefficient for the combined system simplifies to

$$\kappa_T = \gamma\kappa_a + (1-\gamma)\kappa_b \tag{4.18}$$

The total phase of the composite system, including optical dispersion effects, $\hat{\phi}_T$ is required to calculate the instrumental temperature using equation 2.20. It should be noted that using the definition in equation 4.16, the total phase is simply

$$\hat{\phi}_T = \kappa_T\phi_T$$

$$= \kappa_a\phi_a \pm \kappa_b\phi_b \tag{4.19}$$

Figure 4.9 shows the instrumental temperature plotted against the length of the main delay crystal for each of the three possible compensated systems considered. Values of $T_C = 1$ eV are indicated by the red line, and the ratios for the length of the main delay material compensated with lithium niobate (equation 4.10) are shown in the top right corner.

The plot in 4.9 suggests that the $YVO_4$:$LiNBO_3$ compound system is the best choice as it is able to achieve the desired characteristic temperature for shorter lengths of crystal. The high compensation ratio (10.72) of the $YVO_4$:$LiNBO_3$ system implies that only a small amount of the lithum niobate is required to compensate the thermal drifts of the yttirum othovanadate. An second advantage is that the birefringence values for yttrium othovanadate is opposite in sign to that of lithium niobate (indicated by $*$ in the ratio values in figure 4.9) which means that the crystals are oriented with orthogonal optical

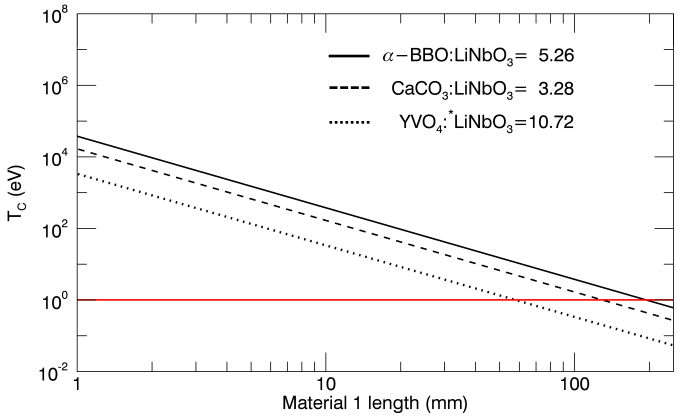


**Figure 4.9:** Log-log plot of the instrumental temperature $T_C$ achieved using composite systems with $\alpha$-BBO (solid line), $CaCO_3$ (dashed line) and $YVO_4$ (dotted line) as the material providing the main interferometric delay (material 1) and $LiNBO_3$ (material 2) used to thermally stabilise the system. The ratio of the main crystal to $LiNBO_3$ are listed in the top right corner. The $*$ label indicates the birefringence of the plates are opposite so that the delay contribution from each plate add to the net delay. For other materials the delay contributions for each plate will subtract. The red line indicates the expected temperature of the MAGPIE plasma and the intersection of the plots with this value gives the required length of material 1.

axes for cancellation of the thermal effects, but the opposite birefringence values cause the main delay to add.

In spite of its high birefringence yttrium othovanadate is not a feasible option because of practical limitations on the available crystal aperture, which, is not sufficient for our imaging requirements ($\geq$ 20 mm plates diameter). For this reason, yttrium othovanadate was not a suitable choice despite its excellent material properties.

Considering the theoretical curves for calcite and $\alpha$-barium borate; calcite appears to be the better choice because its higher birefringence means the required characteristic temperature can be reached with shorter crystal lengths. Calcite is however a fragile and deliquescent material and requires extra care when handling while $\alpha$-barium borate has the advantage that it is more thermally stable, and requires a smaller amount of lithium niobate to compensate thermal effects (see higher ratio in figure 4.9). Because of its favourable material properties and low cost, $\alpha$-barium borate is the preferred material for producing the large delays in the compound system.

The ratios for the crystals used in this system are determined experimentally and discussed in the next section.

### Experimentally determined temperature sensitivity of the interferometric phase

Measurements of the temperature sensitivity for each material is required to confirm the ratio derived in the previous section for the $\alpha-$BBO:$LiNbO_3$ system and to demonstrate

the effectiveness of this technique.

A simple coherence imaging system was constructed, consisting of a waveplate and a 4 mm $\alpha-$BBO displacer plate sandwiched between two crossed polarisers (See the configuration given in figure 3.12). A 20 mm $\alpha-$BBO and a 5 mm $LiNbO_3$ waveplate were investigated, both orientated with optical axes vertical. Each plate was mounted (separately) in a temperature controlled oven. A thermo-couple was inserted into the chamber to record the temperature of the oven. The system was illuminated by a hydrogen spectral lamp fitted with a 488 nm filter so that the 486 nm spectral line was isolated. The lamp light was projected into an integration sphere to create a diffuse source. The interference pattern was focused by a 70 mm c-mount lens connected to the $696 \times 696$ pixel PCO-sensicam camera. A photograph of the experiment is shown in figure 4.10 (a) and the resulting interferogram shown for 5 mm $LiNbO_3$ is shown in (b).

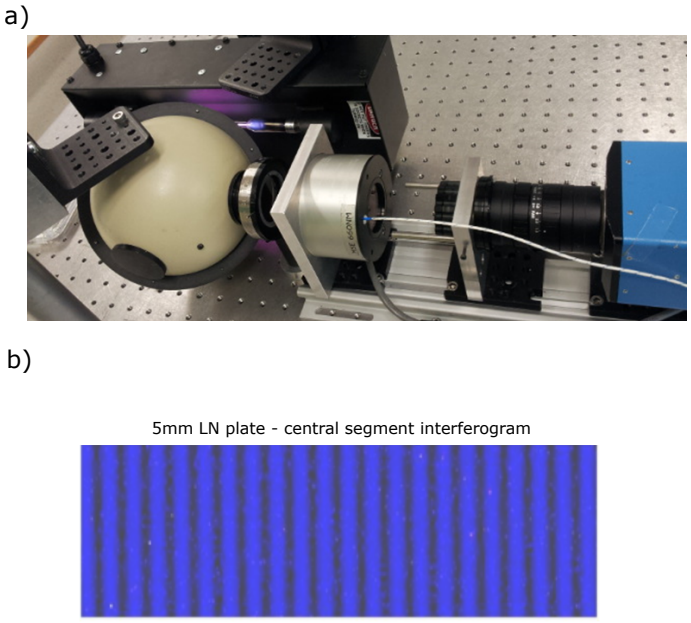


**Figure 4.10:** (a) photograph of the experimental set up used to acquire the temperature sensitivity measurements. Light from a spectral lamp (left-behind) is channeled into (from left to right-foreground) the integration sphere, through a polarising optic and then through the waveplate mounted in the oven. A 4 mm $\alpha$-BBO displacer plate, second polarising optic, spectral filter and a 75 mm focal length lens separate the oven and the CCD (far right). The white wire is the chord of the thermal couple mounted inside the oven and connected to the digital meter. Figure (b) is the central segment of an interferogram for a 5 mm $LiNbO_3$ plate, showing the uniformity of the fringes.

Initially, the oven was switched on and left for 35 minutes to reach its set temperature (30° C). The camera was then activated and images of the interferogram were taken once every 10 seconds for 100 minutes to track the movement of the interference fringes with oven temperature. After 10 minutes into the recording session (with the oven temperature sitting at 30° C) the oven temperature was increased to 35° C. The system was then left for 45 minutes to reach equilibrium again. After this period, the oven temperature was increased to 40° C and once again left for 45 minutes. The high frequency recording (1 shot every 10 seconds) was required to resolve the rapid change in the phase when

the oven temperature was increased. The 45 minute interval, left between temperature increases, was to ensure that equilibrium between the plate and oven temperature had been reached and to explore possible over-drifts. The exposure time for each shot was set to 1.5 seconds. The oven temperature was recorded manually from the digital thermocouple meter. Readings were taken every minute in the final 5 minute period (equilibrium period) before the temperature increase.

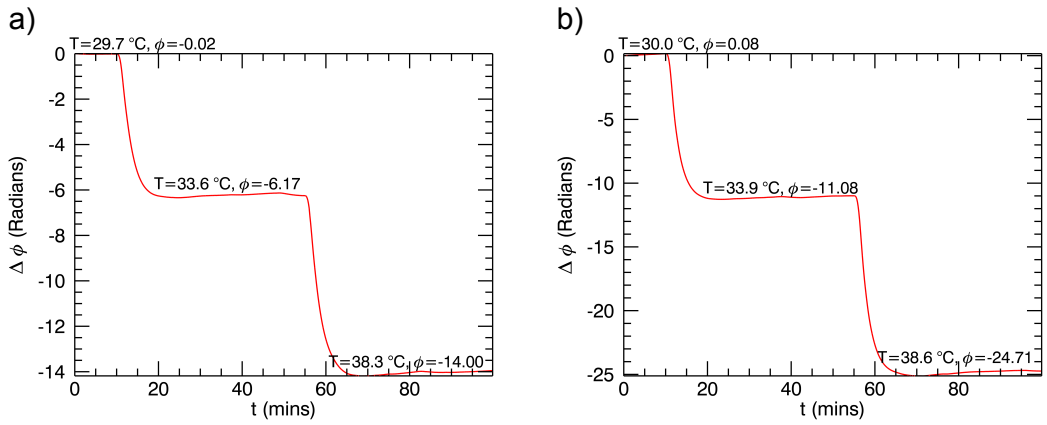


**Figure 4.11:** a) Temperature induced phase drift at $\lambda = 468$nm of (a) 20mm $\alpha$-BBO and b) 5 mm $LiNbO_3$. Both plates have been orientated so the optical axis is vertically aligned.

For each image, the central segment of the interferogram was selected for analysis (as shown in figure 4.10 (b)) as the fringes were near vertical in this region. At the edges of the image the fringes are slightly curved due to the single displacer plate used as the shearing optic. The image was demodulated using the standard demodulation process (discussed in section 4.3.7). The initial phase image (taken at time, $t = 0$), was subtracted from the phase image at each time step to give a difference in phase. Each of these images was then averaged to give a value for the phase difference with time. This is plotted for both the $\alpha-$BBO and $LiNbO_3$ plates in figure 4.11. The equilibrium temperature and average phase are annotated for the equilibrium periods.

Using this data, the thermal phase drift for $\alpha-$BBO and $LiNbO_3$ were determined as

$$\frac{d\phi}{dT}_{\alpha-BBO} = 0.081 \pm 0.003 \text{ rad/°C mm} \tag{4.20}$$

$$\frac{d\phi}{dT}_{LiNbO_3} = 0.572 \pm 0.03 \text{ rad/°C mm} \tag{4.21}$$

with corresponding thermal coefficients

$$\epsilon^{EXP}_{T,\alpha-BBO} = -52.4 \times 10^{-6} \pm 19.4 \times 10^{-6} \text{ 1/°C} \tag{4.22}$$

$$\epsilon^{EXP}_{T,LiNbO_3} = -493 \times 10^{-6} \pm 25.9 \times 10^{-6} \text{ 1/°C} \tag{4.23}$$

indicating a compensation ratio of $7.1 \pm 0.4$.

The experimentally measured thermal phase drift for $\alpha$-BBO agrees within error to the values quoted from literature, however, the experimentally measured thermal coefficient for $LiNbO_3$ is much higher than the value quoted in literature, (see values in table 4.3). There is significant variability in the lithium niobate thermal coefficients quoted in literature [91] which is attributed to the crystal composition. Hence the difference between the experimentally measured ratio and that derived through theory is not surprising. The larger value for $LiNbO_3$ correspondingly causes the compensation ratio to be higher than the theoretical value (compare with the ratio in figure 4.9).

To test the effectiveness of thermal stabilisation using a compound wave-plate, a 20 mm $\alpha-$BBO waveplate and a 3 mm $LiNbO_3$ plate were placed in an oven with optical axes crossed. The phase was tracked (over a a 25 minute period) and the oven temperature was increased (after 5 minutes) by $\sim 3^\circ$ C. The same measurement was then repeated using the single 20 mm $\alpha-$BBO plate. A 488 nm argon laser was used as the light source for these measurements. Figure 4.12 a) show the recorded phase drift for each measurement, tracked over the central ($200 \times 100$ pixel) image region.

The phase for the single $\alpha-$BBO plate has a negative drift of $\sim 6$ (rad) (shown by the red plot) while the phase of the compensated system (shown by the blue plot) has a positive phase drift of $\sim 0.5$ (rad). The oven temperature was tracked during the measurement using a digital thermocouple and the data is shown in the lower figure of 4.12 where the red plot is the temperature data taken during the single-plate measurement and the blue plot is the data taken during the compound-plate measurement. The difference values quoted on the phase and temperature plots was calculated by averaging the data over the first and last 5 minutes of the measurement to find the initial and final values and then taking the difference.

Using the reported oven temperature change, it is possible to calculate (using the values given in 4.20 and 4.21) the expected phase drift for each measurement. For a single $\alpha$-BBO plate a 3.7 $^\circ$ C change in temperature is estimated to produce a phase change of $-5.9$ (rad). This agrees well with the single plate measurement. The compensated system (20 mm $\alpha$-barium borate and 3 mm lithium niobate-oriented with optical axis crossed) is estimated to produce a phase shift of $+0.32$ (rad) for a 3.4 $^\circ$ C change in temperature. The phase change is slightly positive as there is more lithium niobate provided than required to compensate the 20 mm $\alpha-$barium borate plate. Hence, the additional thickness of the lithium niobate causes the phase to drift in the positive direction.

If the phase is plotted against the oven temperature then in theory the graph should be linear with gradient given as $\Delta\phi/\Delta T$. On investigation it is clear that this is not the case for this measurement. The phase in the crystal appears to lag the change in temperature. This is particularly obvious when comparing the phase and temperature of the uncompensated $\alpha$-barium borate plate (red plot) in figure 4.12. The temperature change is initiated at $t = 5$ minutes. The phase does not begin to change until $t = 6$ minutes. The temperature also reaches equilibrium at around $t = 9$ minutes while the phase does not reach equilibrium until $t \sim 15$ minutes. The lag is due to the coupling efficiency of the heat source, insulation of the oven and other effects that determine the

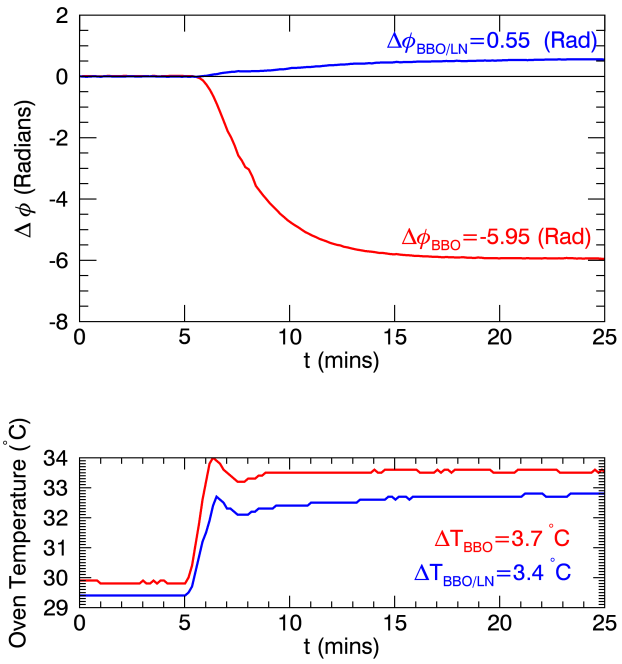


**Figure 4.12:** Top diagram: phase change in Radians for (red) single 20 mm $\alpha$-BBO plate and (blue) thermally-stabilised compound plate constructed from a single 20 mm $\alpha$-BBO and a 3 mm $LiNbO_3$ with optical axes crossed. The average phase values (taken over the time period 15-25 minutes) are annotated for each plot. Bottom diagram: recorded oven temperature values with time for (red) the single plate and (blue) the thermally stabilised compound plate. The average temperatures (taken over the time period 15-25 minutes) are annotated.

systems equilibration.

The phase was also inspected across the entire image plane, for each oven measurement. Both plates exhibited non-uniform phase changes as the temperature of the oven rapidly increased, but became nominally flat again once the system reached thermal equilibrium. The single $\alpha-$BBO plate showed the lower plate region decreased in phase more rapidly than the upper plate region and had a maximum phase difference $\sim$ 0.2 (rad). it took $\sim$ 3 minutes (from when the oven temperature was increased) for the phase to equalise across the image plane. The compensated system showed a diagonal phase ramp with maximum variation of 0.4 (rad), and took $>$ 10 minutes for the phase disturbance to flatten across the image. The compensated system is expected to be more susceptible to non-uniform phase changes as each plate component will respond independently to the change in temperature.

The results presented in figure 4.12 confirm that passive stabilization of the phase using secondary birefringent optics can provide far greater phase stability than a system constructed from a single material. As such this technique is employed to stabilise the measurements for measurements on MAGPIE. It has been found experimentally that suitable online calibration of the instrument properties taken within a short time of the plasma measurement is required to obtain accurate results.

### 4.3.2 System design for MAGPIE measurements

This work focuses on argon ion flow and temperature measurements in the MAGPIE linear plasma device. Current LIF measurements of the argon ion temperature in other linear helicon plasma devices report, $T_S < 1$ eV, ion temperatures and flow measurements recorded using LIF and RFEA techniques have reported subsonic ion flows, $V_D < 1000$ m/s [29,31,92]. With these estimates in mind, we require $\phi_0 \approx 10^5$ radians using $\phi_D/\kappa\phi_0 = V_D/c$ which corresponds to delay plates on the order of $\sim 100$ mm. The construction of the imaging system for low temperature measurements is shown in figure 4.13.

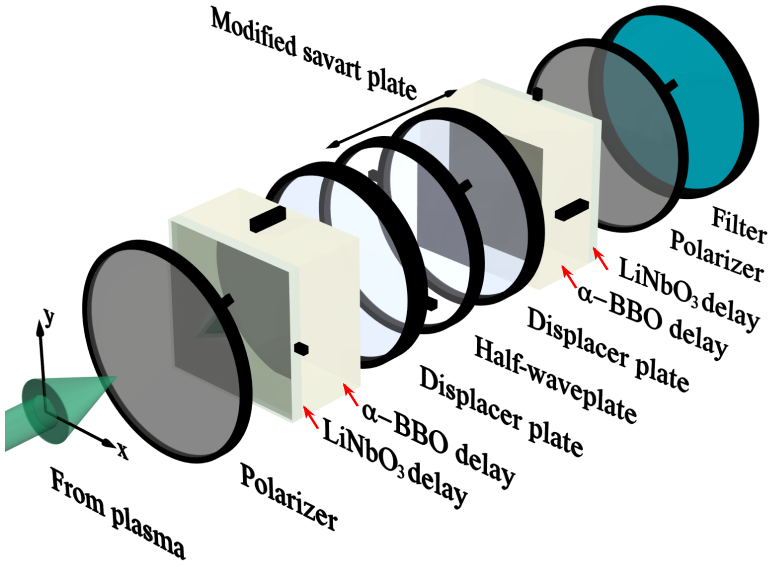


**Figure 4.13:** The full optical construction of a coherence imaging system for measurements for MAGPIE. This system utilised compound waveplates ($\alpha$-BBO/$LiNbO_3$) for thermal stabilisation, field-widening and a modified savart plate as the shearing optic.

A waveplate ratio of $8:1$ ($\alpha-$BBO with $LiNbO_3$) is used to compensate the thermal phase drifts. The compensating lithium niobate waveplates are orientated $90°$ around the $z$ axis to the $\alpha-$barium borate waveplates. The thickness of the $\alpha-$barium borate waveplates must be larger than 75 mm to achieve the required resolution taking into account the deduction of the phase contribution from the compensating lithium niobate wave plates. A systems built using $\alpha-$barium borate lengths of more than 150 mm, is in theory more ideal however these systems become susceptible to very low instrumental contrast due to small imperfections and misalignments in the optics contributing to contamination or blurring of the fringe pattern.

A modified Savart plate constructed from anti-parallel displacer plates either side of an intervening half wave plate, is used as the shearing component for field widening. This is shown as the central component in figure 4.13. The system is symmetric but $90°$ rotated around the half waveplate allow for field widening.

### 4.3.3 Instrumental setup

The coherence imaging system is mounted on a retractable arm which glides in the available space between the top window of the target chamber and the magnetic coils. The tip of the arm is fitted with a mirror oriented at 45° to the vertical so that the plasma light (collected vertically through the top window) is reflected by the mirror and transmitted horizontally along the arm through a series of lenses and the coherence imaging system components. The optical axis of the system sits 150 mm above the plasma mid-plane. A pixelfly USB 1392 × 1040 CCD (with 6.45 $\mu$m pixel width) is mounted at the end of the arm and is used to capture the final image, as depicted in figure 4.1. The operation of the camera, exposure sequences, plasma initiation and moterised-stage is controlled using a LABVIEW program as discussed in the section 4.3.6. The MAGPIE coherence imaging system uses a 3-lens system to relay the plasma emission through the instrument and onto the CCD. The lenses were of C-mount design in order to keep the system compact so that it would fit in the restricted space.

The optical setup is shown in figure 4.14. The first 17 mm focal length objective lens produces an intermedial real image and the two remaining 75 mm focal length lenses, which are focused at infinity, collimate the light as it traverses the imaging system and produce sharp interference fringes on the CCD. The first objective lens is adjusted to bring the plasma mid-plane into focus on a plane coincident with the focal plane of the first 75 mm lens. The approximate system magnification is $\sim \times 11$ which is the the ratio of the object diameter (180 mm) and the first image distance ($\sim$ 17 mm) so that the rectangular image of the CCD (approx. $6.7 \times 9$ mm) in the plasma mid-plane spans a radial and axial

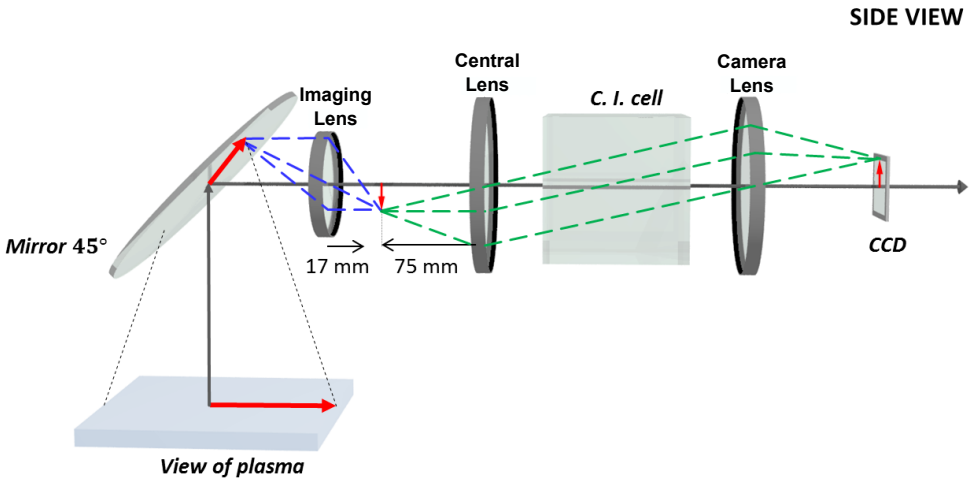


**Figure 4.14:** POVray generated image of the 3-lens system consisting of an imaging lens (lens 1) which focuses the plasma light as shown by the blue rays, and the telecentric lenses consisting of a central lens (lens 2) and camera lens (lens 3) which together ensure the light rays are collimated through the coherence imaging system. This is shown by the green rays. The camera lens is also responsible for the focus of the interferometric fringe pattern onto the CCD.

distance of dimension $75 \times 100$ mm.

A model of the diagnostic set-up has been generated using Zemax OpticStudio software. The ray trace model through the diagnostic system, using correct dimensions, is shown in figure 4.15. Three points are chosen at the plasma midplane. The blue point is taken at the center of view and the red and green points are chosen at the extreme edges of view. The rays are traced from these points through the imaging system. The model shows that the rays are collimated as they pass through the coherence imaging cell and that the edge of the cell acts as an optical stop, only allowing a small range of angles to pass through the system. The necessary separation of the collimating lens and the finite aperture of the crystal therefore give rise to significant vignetting losses. One way of minimising the effects of vignetting is to decrease the aperture diameter of the final camera lens. For a given pixel this also reduces the range of angles through the crystal plates and can improve the instrumental fringe contrast.

It was found that a final f-number of $f/4$ delivers a good compromise between light throughput, fringe contrast and reduced vignetting.

### 4.3.4 Image quality

A 50 mm image-quality interference filter along with large aperture ($\sim 40$ mm) birefringent elements with broadband ($400 - 700$ nm) anti-reflection coatings was used to suppress the appearance of Newtons rings due to multiple reflections within a given element. These spurious rings can contaminate the extracted contrast and phase, as shown in figure 4.16 (a). These images were taken using a a calibration sphere as a light source, illuminated by a 488 nm argon laser.

Hyperbolic features contaminating the fringes were also observed due to angular errors in the rotational alignment of the main delay plates. These contamination features are shown for the contrast in image 4.16 (b). These features compound with crystal length and hence become a significant issue for low-temperature specific coherence imaging instruments. Elimination of these patterns require very careful and slight adjustments of the orientation of the main delay plates.

The combined effects of these two contaminating fringe features are shown in an image of the contrast, see figure 4.17 (a). A system corrected for these effects shows a substantially clearer and more uniform brightness, see figure 4.17 (b).

### 4.3.5 Calibration setup

Calibration is essential in order to interpret the phase, contrast and brightness measurements obtained using the coherence imaging system. The calibration image should represent an ideal coherent and diffuse light source. The phase and contrast difference between the measurement and the calibration shot is therefore assumed to be a direct consequence of the Doppler shift and broadening of the plasma emission.

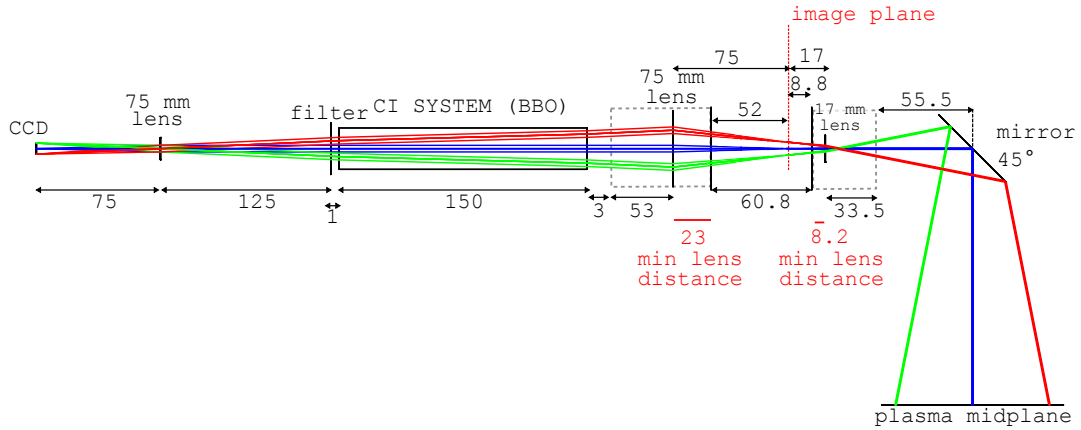


**Figure 4.15:** Zemax model showing a ray trace through the coherence imaging diagnostic set-up. Lengths are quoted in mm.

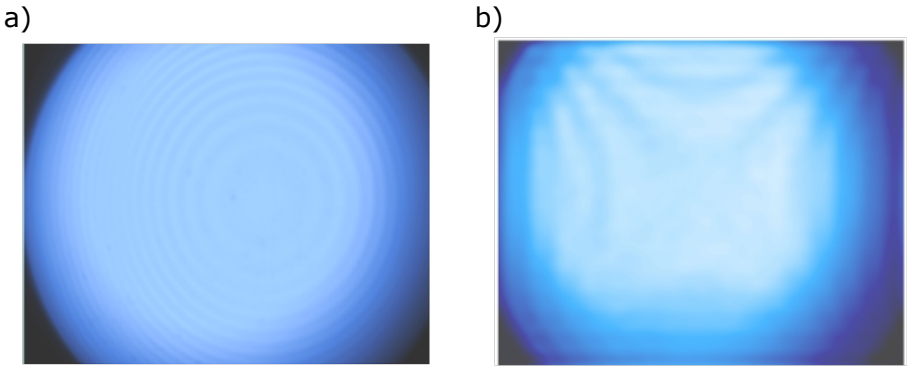


**Figure 4.16:** The measured contrast extracted from the interferometric signal is shown for (a) a standard delay plate with shearing plate system and with 20 mm $\alpha$-BBO marginally out of alignment, and, (b) a displacer plate with a faulty anti-reflection coating generating newtons rings.

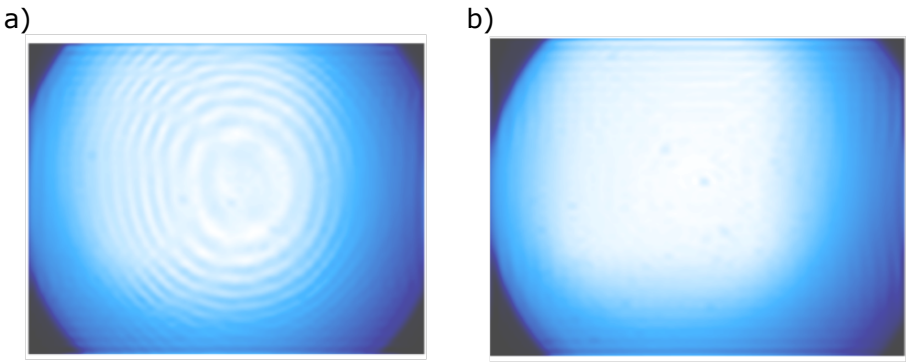


**Figure 4.17:** The measured contrast extracted from the interferometric signal of a standard coherence imaging system which (a) has not been corrected for minor misalignment problems and faulty reflection coatings and shows the contamination before correction, and, (b) has been corrected-the brightness is fairly smooth and uncontaminated.

A National Laser Company $450 - 515$ nm argon ion laser (160 mW maximum output power) was employed as the calibration source. The 488 nm line was selected using a diffraction grating. These measurements were made using the IsoPlane spectrometer with 200 $\mu$m and 120 $\mu$m slit widths respectively.

The initial measurements were made using a static calibration source which was created by coupling the light from the argon ion laser (via optical fiber) into a calibration sphere so that the output light was uniformly diffuse. The uniformity of the light from the sphere allowed vignetting effects to be captured in the calibration image and removed from the final plasma measurements. The calibration shot was obtained when the optical arm (see figure 4.1) was fully retracted so that the mirror was removed from view of the plasma chamber. The integration sphere was mounted so that it could be rotated into the view of the mirror. For this setup the calibration image was obtained prior to the set of plasma measurements.

Unexpected ramps in the phase and contrast observed in initial plasma measurements were discovered to be due to non-uniform heating and movement-induced stress in the birefringent crystals. This prompted the construction of an on-line calibration system which was designed remedy these stability issues.

The design for the online calibration system is shown in figure 4.18 (a).

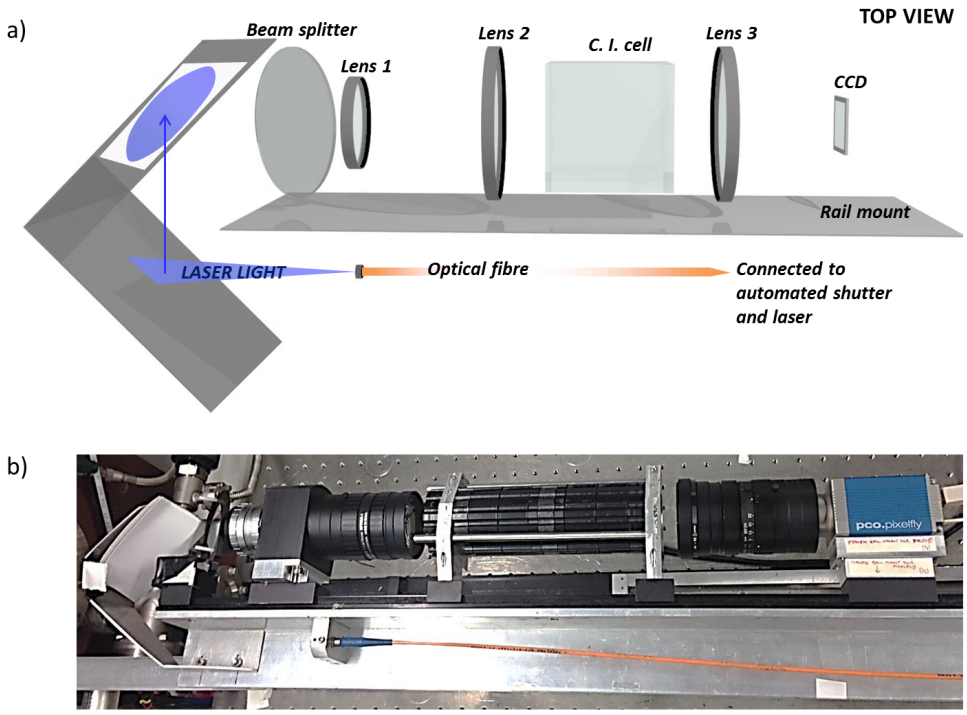


**Figure 4.18:** Set-up of the coherence imaging system with the on-line calibration system. (a) POVray diagram showing the path of the laser light into the coherence imaging system and (b) a photograph looking down onto the calibration system.

An optic fiber carrying the light from the laser was attached to the rail on the counter-side of the rail mount. This projected the laser light onto a reflective plate which allowed the light to be transmitted around the edge of the rail and then projected onto a sheet of card acting as a diffuser. The beam of light diverged with distance, so that the light projected onto the card acted to fill the field of view of the camera lens. The mirror was replaced by a beam splitter allowing light to be obtained either from the calibration direction or the plasma direction. The source of the light was controlled using an automated shutter system. A photograph of the entire set up is shown in figure 4.18 (b).

The intensity map generated by this on-line calibration design was significantly non-uniform compared with the integration sphere. The intensity profiles of the integration sphere and the on-line calibration are shown in figure 4.19 a) and b) respectively.

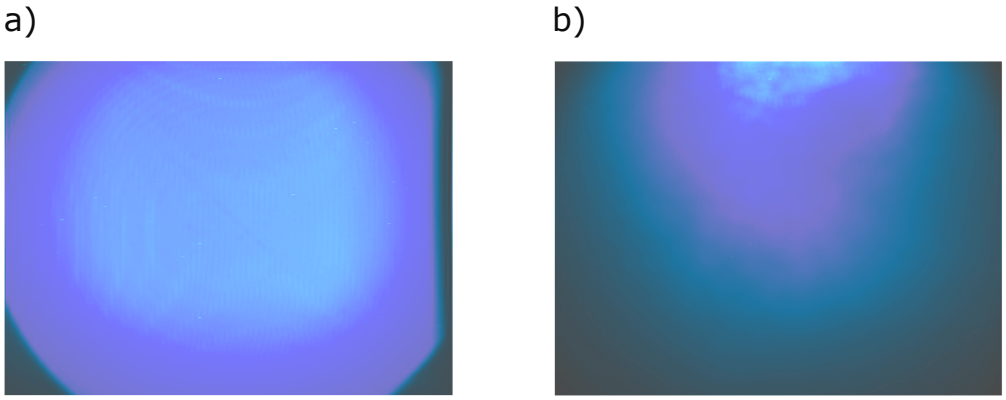


**Figure 4.19:** Intensity profiles of (a) the integration sphere and (b) the on-line calibration system imaged by the pixelfly USB CCD.

The non-uniformity of the on-line calibration brightness meant in was unsuitable to correct for vignetting effects. Therefore it was still important to take a calibration using the integration sphere prior to the measurement to correct for this effect. The bright intensity spot at the top of the image, figure 4.19 b), also suggested the new calibration may not fill the same range of angles as the plasma measurement images. Such effects can have consequences on the measured contrast and phase.

By subtracting the phase or contrast measurement from measurements made with the calibration sphere (placed below the beam splitter in place of the plasma) the on-line system could be tested. The expected result was a flat image and any observed features would indicate that the on-line calibration system captured information differently to the integration sphere calibration.

The phase and contrast comparison between the sphere and the online calibrations was performed for a range of imaging system construction lengths (25 mm $\rightarrow$ 160 mm $\alpha-$BBO lengths). In all the comparisons, the contrast difference was flat and near equal to 1.0 indicating the online calibration system performed equally well in determining the contrast when compared with the integration sphere, despite the non-uniform brightness profile. The phase comparison also appeared flat, suggesting there were no significant differences in the phase measurements. Any deviations from this was explained by experimental

factors.

The importance of immediate calibration prior to each plasma measurement was confirmed by tracking the phase and contrast obtained by the on-line calibration system during a measurement scan along the MAGPIE chamber with no plasma or magnetic field active. The phase and contrast of the on-line calibration at each scan position (taken 40 mm apart) was compared with the on-line calibration taken at the initial position ($z = 550$ mm). This was tracked over 6 repeat measurements, and was used to quantify any systematic variations in the phase and contrast induced by temperature or stresses to the optical system.

Over the period of the scan, hyperbolic distortions (from residual patterns generated by the wave plates) became prominent, distorting both the contrast and phase. The growth of the patterns show that the system stability deteriorates with scan time, and hence confirms the necessity for the on-line calibration system.

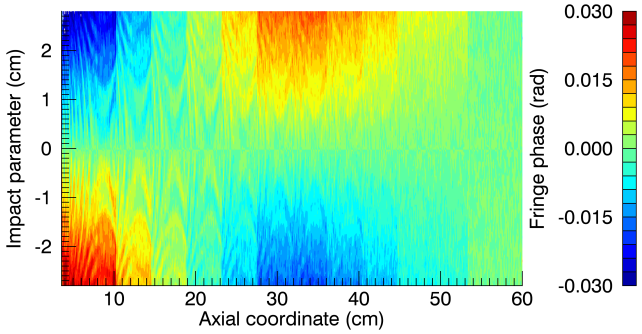


**Figure 4.20:** The coherence imaging system undergoes slight torsional movement as the system is physically relocated along the rail. This induces stress across the birefringent plates resulting in phase disturbances. This phase disturbance is non-uniform along the chamber as different locations of the system feel different torsional movement.

Apart from the hyperbolic distortions, the contrast remains fairly constant over the scan. There are however non-trivial reproducible changes in the phase, which without on-line calibration manifest as false flows of $\approx 100$ m/s. The systematic appearance and reproducibility of these phase variations in the radial direction, was interpreted in initial results as a reversal in the azimuthal flow. Optimisation of measurement acquisition time and employing the on-line calibration system have since caused these features to disappear. The azimuthal flow variation calculated from the heat and stress induced phase is shown in figure 4.20. This is purely an instrumental effect, which are removed from measurements by the on-line calibration system.

### 4.3.6 Software setup

The coherence imaging measurements on MAGPIE require precise timing of the camera, laser shutter, plasma pulse, movement of the motorised stage and saving of data into the MDSplus database. Such requirements are best handled using automated software.

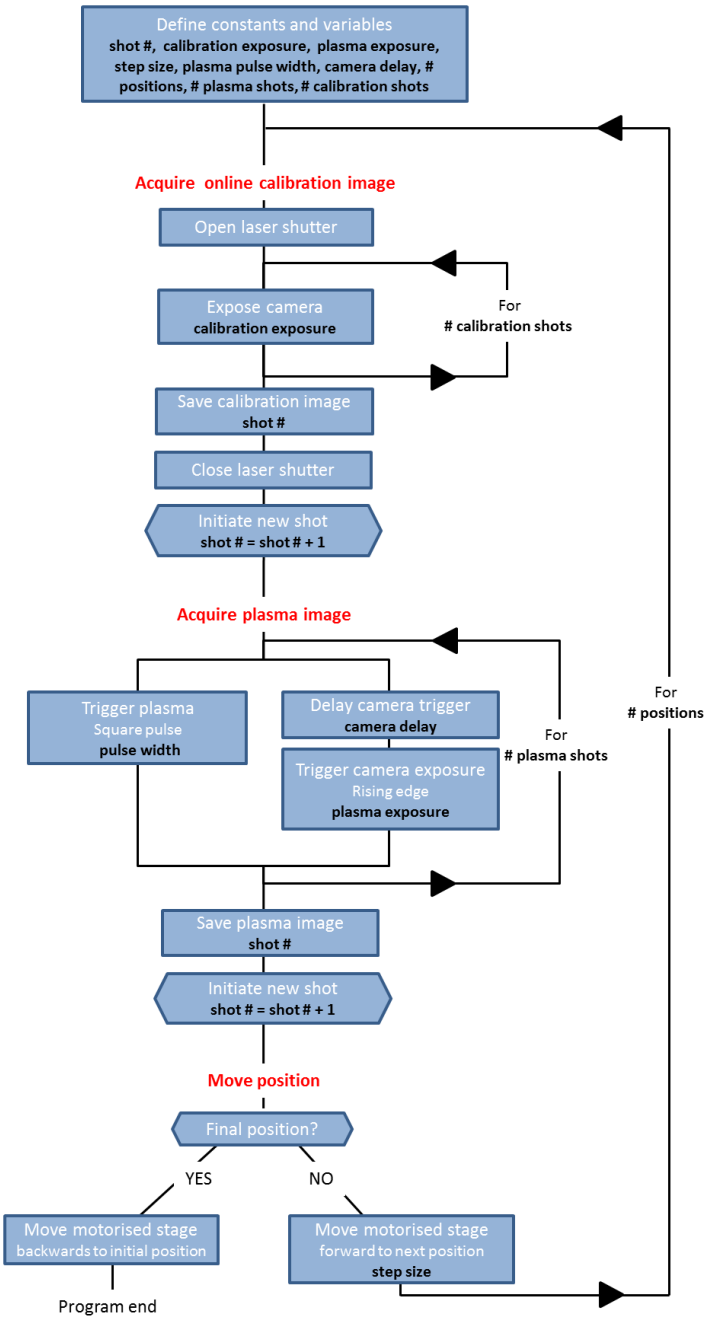


**Figure 4.21:** Flow chart showing the operation of the LABVIEW program in order to aquire coherence imaging measurements on MAGPIE.

A LABVIEW program was written to control the measurement process. The flow chart of the program is shown in figure 4.21. The program presented in this work calls upon already-available LABVIEW modules which control each of the individual elements and combines these processes into a master program designed for the coherence imaging measurements.

The program initiates by defining all the required constants, such as the exposure time for the calibration shot and the plasma shot, the pulse width of the plasma discharge and the stage position. The input parameters are shown in figure 4.22 which is a screen shot of the LABVIEW control panel for the program.

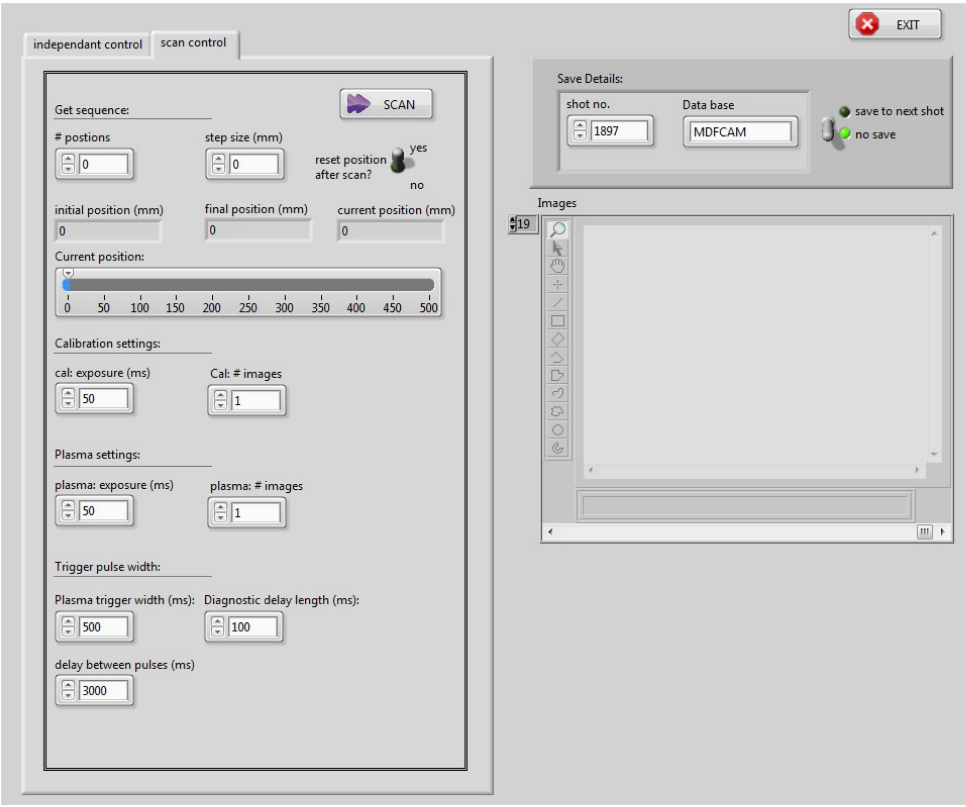


**Figure 4.22:** screen shot of the LABVIEW control panel for coherence imaging measurements on MAGPIE.

Once a scan is initiated, the argon laser shutter is opened and a preselected number of calibration images of fixed exposure are acquired (typically $\sim 5$ images) and saved to the MDSplus database. The shutter is then closed and the plasma measurement commences. A periodic gate is provided to the RF signal generator synchronised with the trigger for the camera exposure. A low duty cycle is preferred ($< 10\%$) so that heating of the plasma chamber is kept to a minimum. The camera exposure can be delayed (with respect to the plasma pulse) to allow the plasma evolution to be studied. The shots are then saved to the MDSplus database and the stepper motor translates the system to the next axial position. The program terminates once the measurement at the final position has been acquired. At termination the stepper motor is returned to its start position. The program also allows for operation in other modes which facilitate single image shots (for calibration shots using the integration sphere or black shots) and continuous operation for live image focusing.

### 4.3.7 Image analysis

A plasma image (taken at 48 cm axially along the chamber) and a raw calibration image using the integration sphere is shown in figure 4.23. Only a central section has been shown so that the interferometric fringe pattern can be clearly discerned.

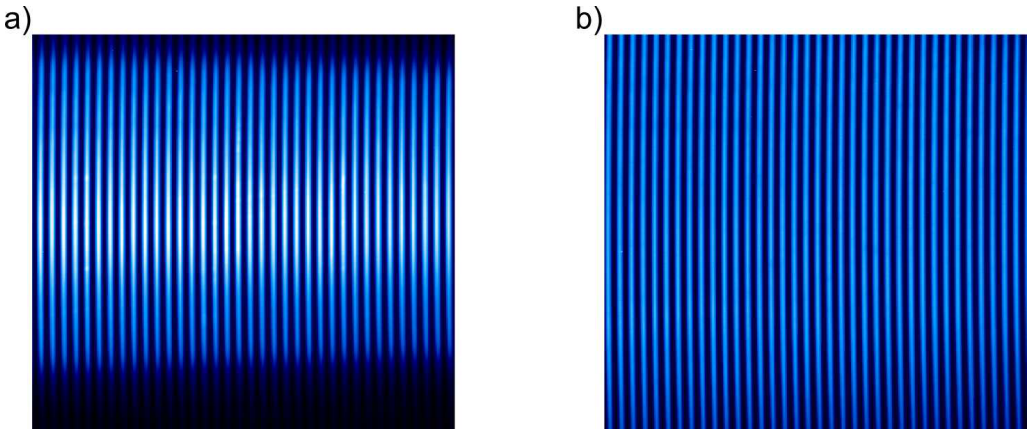


**Figure 4.23:** Central segment for; (a) plasma measurement and (b) calibration measurement. The interferometric fringe pattern is clearly visible for each measurement. The background brightness in (a) shows the brightness profile of the plasma column and for (b) shows the uniform brightness profile obtained using the calibration sphere.

To commence analysis, the dark image is subtracted from both the raw plasma and calibration images to remove the background level.

The measurement $S$, can be written mathematically as

$$S = \frac{I}{2}\left\{1 + \zeta\left(\frac{\exp -i\phi + \exp i\phi}{2}\right)\right\} \tag{4.24}$$

where $\zeta$ and $\phi$ are the contrast and phase of the interferogram. The phase, $\phi$ is the sum of the instrumental phase at the laser wavelength, $\phi_0$, and the Doppler shift of spectral line, $\phi_D$ while the contrast, $\zeta$, is the product of the instrumental and Doppler contrasts $\zeta_0$ and $\zeta_D$, respectively. The brightness, $I$, is proportional to the product of the source radiance and its optical efficiency, $\eta_{ef}$, that describes the instruments light transmission which is determined by illuminating the system with a spatially uniform light source that fills the optical field of view.

Taking the 2D Fast Fourier Transform of the measured interferogram, equation 4.24, the frequency components can be isolated. The Fourier space for a calibration image is shown in figure 4.24 a). The image has been scaled to $\log \mathcal{F}\{S\}$.

There are two main features shown in figure 4.24 a). A peak at the center of the image captures the DC features of the image while the positive and negative frequency peaks $(K^+, K^-)$ are called carrier peaks and are the frequency of the interferometric fringe pattern. The DC and carrier peaks are plotted (at normal scale) in 4.24 b). These have

been taken from the central horizontal region and averaged over 20 rows, as indicated by the dotted square region in figure a). The $k_i$ frequency coordinates have been normalised to the Nyquist frequency.

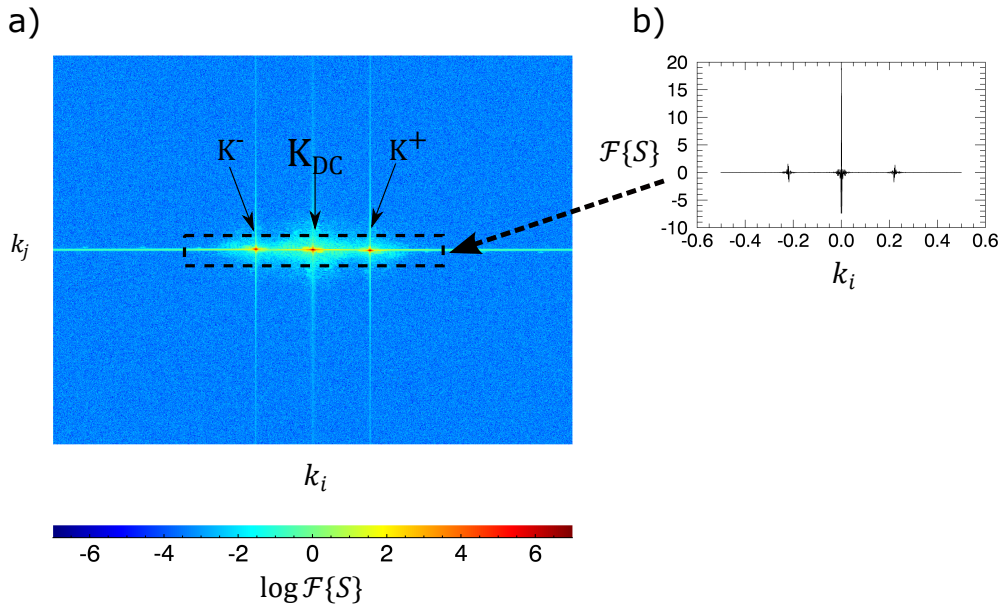


**Figure 4.24:** (a) The 2D Fourier transform of the spatial interferometric fringe pattern showing three predominant frequencies (in $k$-space). The central frequency is the $K_{DC}$ at $k_i = k_j = 0$ and captures the brightness distribution of the image. The interferometric fringe pattern is captured in the $(K^+, K^-)$ peaks. (b) average over $k_j$ showing the relative magnitudes of each of the frequencies.

A filter is used in the Fourier plane to isolate the DC peak and the carriers. A window filter which truncates the horizontal dimension but spans the entire vertical dimension is the preferred type of filter as this maintains the spatial resolution in the vertical dimension. This is equivalent to taking the Fourier transform of each individual horizontal row in the image. The horizontal width of the filter must be large enough to capture the features of the carrier but not so large that it picks up contributions from the DC peak.

The measured brightness term, $I/2$, can be determined by isolating the DC peak. By taking the ratio of the measured plasma brightness (denoted by subscript 0) and the measured calibration brightness (denoted by subscript *cal*) the efficiency factor can be removed. As the calibration is ideally uniform, this can be normalised ($I_{cal} \sim 1$) to return only the plasma brightness

$$\frac{\eta_{ef} I_0}{\eta_{ef} I_{cal}} \sim I_0 \tag{4.25}$$

An example of the extracted plasma brightness, is shown in figure 4.25, for a plasma shot taken at 47.8 cm along the plasma chamber.

The plasma is localised along the axis of the plasma chamber and lies horizontally along the center of the image. The artifact which appears as a vertical stripe slightly right of

the image center is due to reflections from the base plate of the chamber. The rounded edges of the image appear as the calibration shot has not completely filled the field of view and the dark edge on the RHS of the image is due to an optical component in the imaging system stopping the light. This feature was corrected with slight realignment of the optical lenses. Results of the measurement are discussed in the following chapter.

The phase and contrast can also be found by isolating one of the carrier peaks in the Fourier domain. The interferogram produced with only a single carrier frequency (and no DC component), $S_1$, is written as

$$S_1 = \frac{I}{4}\left(\zeta \exp -i\phi\right) \tag{4.26}$$

Taking the absolute value of this will return the contrast $\zeta$ and calculating the arctangent will return $\phi$ (assuming $\phi << 1$). These quantities can be extracted for measurements of both the plasma and the calibration source. As the calibration measurement purely contains information regarding the instrumental phase and contrast it can therefore be used to extract the $\phi_D$ and $\zeta_D$ components from the plasma measurement.

An example of the extracted contrast and phase (due to the Doppler broadening and shift) is shown in figure 4.26, for a plasma shot taken at 47.8 cm along the plasma chamber.

It is possible, assuming LTE conditions, that the ion temperature and flow can then be inferred from these quantities using equations 2.27 and 2.28. Ignoring line integration effects these quantities then simplify to

$$\zeta_D = \exp\left(-\frac{T_S(\boldsymbol{r})}{T_C}\right) \tag{4.27}$$

and

$$\phi_D = \hat{\phi_0}\ \boldsymbol{v_D} \cdot \hat{\boldsymbol{l}} \tag{4.28}$$

This would be a first approximation on the ion flows and temperatures in MAGPIE, however as the ion velocity distribution function for the argon MAGPIE plasma is not yet characterised there may be non-Maxwellian features present. This is considered in section 5.3.

It should also be noted, the drifting flows in MAGPIE, are expected to be on the order of the thermal velocity and therefore, $v_D \sim v_{th}$. Under these conditions in the LTE assumption, it is possible for second order terms to contaminate the phase and contrast so that they are not uniquely determined. This case is evaluated in appendix B. An interesting outcome of the $v_D \sim v_{th}$ condition is that radial flow information can manifest as second order terms in the contrast. Information regarding the radially diffusive flows

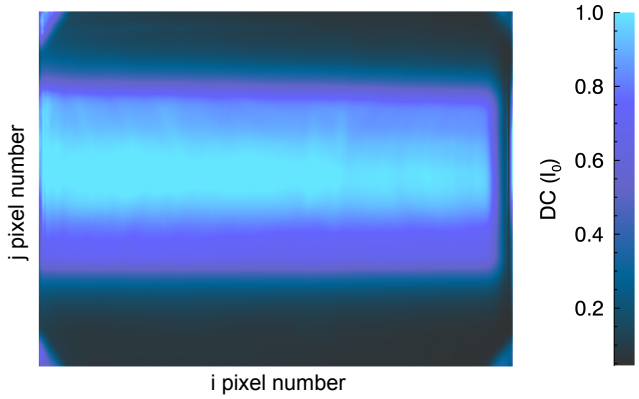


**Figure 4.25:** Extracted plasma brightness image (DC) for a plasma shot taken at $z = 47.8$ cm. The $(i, j)$ coordinates represent pixels in the image captured on the CCD. They can be related to the $(z, r)$ coordinates describing the plasma geometry, respectively (where $r = \sqrt{y^2 + x^2}$ and ignoring line integration effects the image can be considered as a snapshot of the plasma at the mid-plane and hence $r = x$).

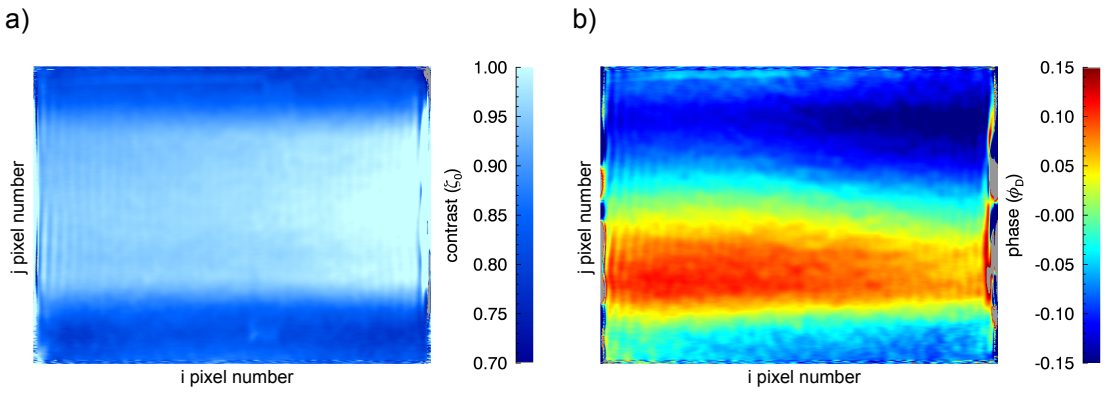


**Figure 4.26:** (a) the extracted contrast and (b) the extracted phase for a plasma shot taken at $z = 47.8$ cm. The $(i, j)$ coordinates are the same as those given in figure 4.25.

have so far be invisible for coherence imaging measurements. It is concluded that the results presented in 2.27 and 2.28 are still valid in this study as long as there are no significant radial diffusive flows.

Chapter 6 will address the validity of ignoring line integration effects and will use tomography to unwrap the temperature and flows with respect to radius. Section 5.3 will use coherence imaging to examine whether the results point to a non-Maxwellian IVDF.

This work focuses on a single fringe carrier to encode the Doppler information, however multi-carrier systems have been employed in hot temperature fusion studies to encode different polarisation information (such as Zeeman or Motional Stark splitting information) across multiple carriers in a single measurement image. For horizontal fringes, the frequency carrier (see image 4.24) lies along the horizontal axis. Systems with multiple overlapping fringe patterns at different orientations will have carrier peaks positioned at various on-axis and off axis locations. Such techniques could be employed as a future instrument to measure the Doppler information at several interferometric delays.

### 4.3.8 Extraction of the axial and azimuthal flow components

The MAGPIE system is described in terms of a cylindrical coordinate system as shown in figure 4.27. The angles $(\chi, \psi)$ describe the line-of-sight vector $\hat{\boldsymbol{l}}$ in the $(x, y)$ and $(y, z)$ directions where

$$\boldsymbol{l} = l_x\ \hat{\boldsymbol{x}} - l_y\ \hat{\boldsymbol{y}} + l_z\ \hat{\boldsymbol{z}} \tag{4.29}$$

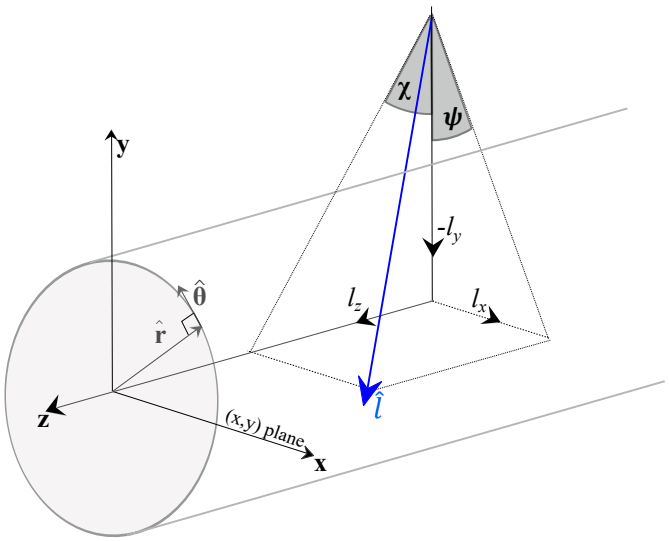


**Figure 4.27:** Viewing geometry of the MAGPIE plasma showing the viewing angles $(\chi, \psi)$ which describe the viewing line $\hat{\boldsymbol{l}}$. The $(x, y, z)$ axis describe the standard Cartesian co-ordinate system, while the co-ordinate $(r, \theta, z)$ describe a cylindrical coordinate system.

and defining $D$ as the distance between the focal point and the mid-plane (along the $\hat{\boldsymbol{y}}$ axis)

$$\begin{aligned} l_x &= |\boldsymbol{l_x}| = D\tan\psi \sim D\psi \\ l_y &= |\boldsymbol{l_y}| = D \\ l_z &= |\boldsymbol{l_z}| = D\tan\chi \sim D\chi \\ l &= |\boldsymbol{l}| = D(1+\chi^2+\psi^2)^{1/2} \sim D \end{aligned} \tag{4.30}$$

The flow in MAGPIE can be written as the emissivity weighted vector field $\mathbf{V} = \epsilon(\boldsymbol{r})\boldsymbol{V}$ where $\boldsymbol{V}$ is the velocity vector and $\epsilon(\boldsymbol{r})$ is the local emissivity. The measured phase is proportional to the line-integrated velocity

$$\phi \propto \int_{\mathrm{L}} \mathbf{V}\cdot\hat{\boldsymbol{l}}\; dl \tag{4.31}$$

The flow can be written in cylindrical coordinates as

$$V(r,z) = V_r(r,z)\;\hat{\boldsymbol{r}} + (\boldsymbol{\nabla}\Phi\times\hat{\mathbf{B}})\;\hat{\boldsymbol{\theta}} + V_z(r,z)\;\hat{\boldsymbol{z}} \tag{4.32}$$

where $V_r(r,z)$ and $V_z(r,z)$ are the radial and azimuthal flow components, and the azimuthal flow $V_\theta(r,z)$ is a drift driven by a potential $\boldsymbol{\nabla}\Phi$ and magnetic field $\mathbf{B}$. Due to the cylindrical symmetry, $\boldsymbol{\nabla}\Phi = (\partial\Phi_r/\partial r, 0, \partial\Phi_z/\partial z)$ and $\mathbf{B} = (\mathrm{B}_r, 0, \mathrm{B}_z)$. Therefore

$$V_\theta = \nabla\Phi_r\mathrm{B}_z - \nabla\Phi_z\mathrm{B}_r \tag{4.33}$$

Transforming the line-of-sight vector into the cylindrical coordinate system, the unit vector $\hat{\boldsymbol{l}}$ is

$$\hat{\boldsymbol{l}} = (\psi\cos\theta - \sin\theta)\;\hat{\boldsymbol{r}} - (\psi\sin\theta + \cos\theta)\;\hat{\boldsymbol{\theta}} + \chi\;\hat{\boldsymbol{z}} \tag{4.34}$$

The viewing angles $\chi$ and $\psi$ are small and therefore various allowances can be made to simplify the view. At $\chi \neq 0$ the plasma cross-section becomes elliptical, elongated in $\hat{\boldsymbol{y}}$. For small $\chi$ this effect is ignored so that the plasma does not change in the axial direction in the plane of integration. The angle $\psi$ is related to the polar angle $\theta$ as shown in figure 4.28. By rotating the $(x,y)$ coordinate system by $\psi$ the polar angle becomes $\theta' = \theta - \psi$ and the angle between the line-of-view and the $\boldsymbol{y'}$ axis is zero.

The equation for $\hat{\boldsymbol{l}}$ in the rotated system becomes

$$\hat{\boldsymbol{l}} = -\sin(\theta-\psi)\;\hat{\boldsymbol{r}} - \cos(\theta-\psi)\;\hat{\boldsymbol{\theta}} + \chi\;\hat{\boldsymbol{z}} \tag{4.35}$$

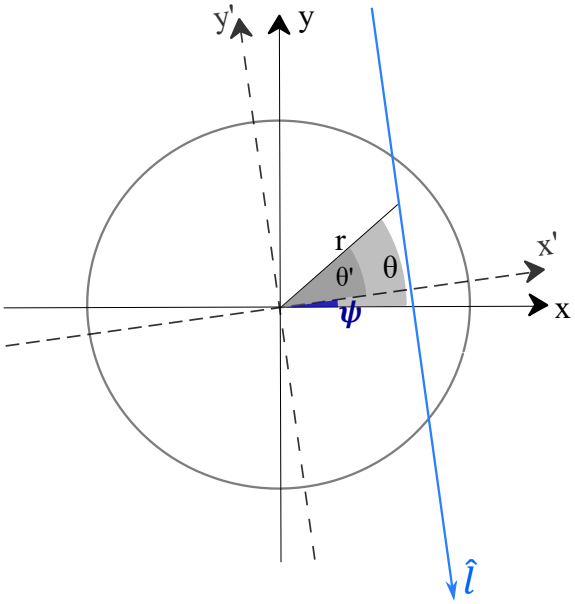


**Figure 4.28:** Orientation of the line-of-sight with respect to the plasma cross section taken in the $(x, y)$ plane. The diagram shows that by rotating the axes by $\psi$ the line-of-sight becomes parallel to the $y'$ axis.

Using 4.35 and 4.32 the measured phase becomes

$$\begin{aligned}\phi &\propto -\int_{\mathrm{L}} \mathrm{V}_r \sin(\theta - \psi)\, dl - \int_{\mathrm{L}} \mathrm{V}_\theta \cos(\theta - \psi)\, dl + \chi \int_{\mathrm{L}} \mathrm{V}_z\, dl \\ &\propto -\int_{\mathrm{L}} \mathrm{V}_\theta \cos\theta'\, dy' + \chi \int_{\mathrm{L}} \mathrm{V}_z\, dy' \end{aligned} \tag{4.36}$$

The radial flow term disappears in the line integral as $\sin\theta'$ is anti-symmetric over the $x'$ axis. This equation shows that the measurements of the flows contain an axial component (symmetric over the central axis as no $\theta$ dependence) and an azimuthal component (anti-symmetric over the central axis due to the $\cos\theta$ term). The axial flow is scaled by $\chi$ and therefore cannot be seen when the line-of-sight is contained within the $(x, y)$ plane. The direction of the azimuthal flow is determined by the magnetic field (see 4.33).

For the phase given in figure 4.26 b), the symmetric and anti-symmetric components have been calculated and are shown in figure 4.29 a) and b) respectively. For these images the plasma coordinates have been indicated. From these phase quantities the Doppler shifted azimuthal and axial flows can be determined.

Difficulty arises in this analysis in choosing the center axis of the image in which to perform the symmetry. In an ideal case the plasma is perfectly radially symmetric and therefore the axis of symmetry is apparent in the brightness profile. For the MAGPIE data (as discussed in the following chapter) the discharge appears asymmetric and the axis of symmetry is not immediately apparent. The axis was chosen according to the center of mass (first moment) of the radial brightness profile. The position of symmetry was also extracted from the phase measurements by subtracting a linear ramp along the axial image direction. The remaining phase image corresponds to the antisymmetric phase

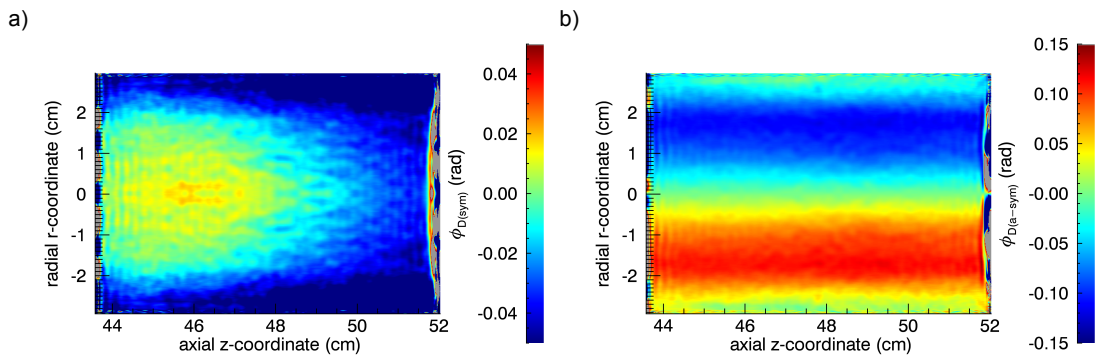


**Figure 4.29:** (a) symmetric and (b) antisymmetric phase components extracted from the total phase shown in figure 4.26 (b).

component with the position of the axis of symmetry apparent. The position of the axis of symmetry found using this method was in close agreement to the position found using the center of mass of the brightness.

As radial components are not detected in the phase measurement, there should be a zero phase measured at the center pixel for the viewing chord normal to the plasma. Instead, there is a DC offset in the phase measurements (on the order of 0.3 (rad)) which is constant across all the measurements. There is also a curvature in the symmetric component of the phase in the high magnetic field region (see figure 4.29 (a)).

It is likely that this offset and curvature is an instrumental effect arising from either a small shift in the spectral line between the plasma and the calibration or perhaps an effect of the imaging filter where the filter window shifts in wavelength for large incident angles. The investigation of the imaging filter and calibration laser are discussed in the following chapter. For these results, the phase has been scaled so that the phase measurement at the central pixel is zero.

## 4.4 Mach Probe design for MAGPIE

A in-house Mach probe was made to benchmark the flows for MAGPIE. The following section presents the design details and considerations for the Mach probe used to measure ion flows in MAGPIE.

### 4.4.1 Mach probe - design

Careful consideration of the plasma conditions was required in designing a Mach probe for MAGPIE so that results could be interpreted using a valid model. The probe tips needed to be electrically conducting, highly heat resistant and have minimal sputtering

so degrading material does not contaminate the plasma. Tungsten wire with 0.2 mm diameter ($R_p = 0.1$ mm) and Molybdenum wire with 1.0 mm diameter ($R_p = 0.5$ mm) were two such materials readily available in the laboratory. Both were considered in this study.

Temperature studies in other helicon devices, have reported that the ion temperature significantly lower than the electron temperature $T_i << T_e$ [27, 35]. The ratio $R_p/r_L$ has been calculated using the MAGPIE magnetic field geometry along the machine axis taken at the reference condition (see the plot in figure 4.2). The ion temperature has been taken as constant 0.05 eV along the central axis which is the lower temperature limit found from preliminary studies in this work. We consider here the lower temperature limit as this will give the maximum value of $r_L$. This allows us to test the condition $R_p << r_L$ required for the unmagnetised case.

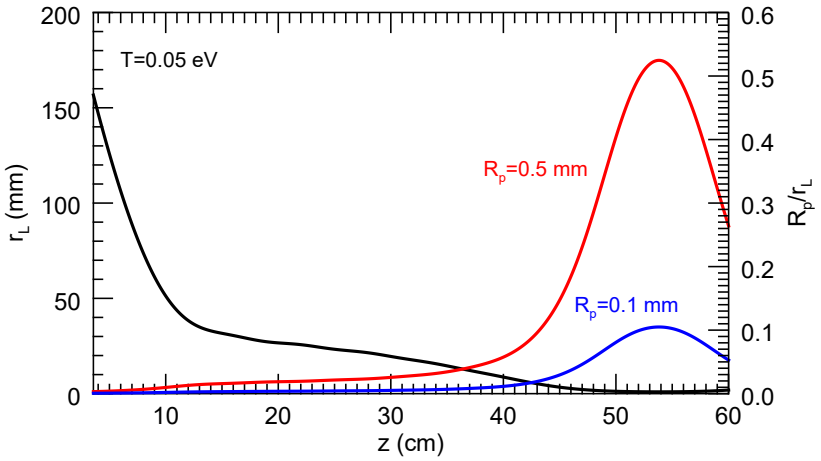


**Figure 4.30:** The Lamour radius (black) calculated along the axis of MAGPIE for 0.1 eV ion temperature and the reference magnetic field condition. The corresponding ratio $R_p/r_L$ is plotted for tips of radius 0.5 mm (red) and 0.1 mm (blue).

The Lamour radius and the corresponding ratio $R_p/r_L$ is plotted in figure 4.30 for both the 0.5 mm radius and the 0.1 mm radius probe tips. it is clear that for the plasma closest to the antenna (source) region the ratio is $R_p/r_L << 1$ while in the target region the ratio increases due to the high magnetic field. As the ratio is always less than 1 the unmagnetised plasma conditions were applied to the Mach probe measurements.

Table 4.4 summarises the expected plasma conditions for Mach probe measurements in MAGPIE. The sound speed has been calculated from equation 2.34 assuming an electron temperature of 4 eV [82]. The lower and upper values for the tip radius and tip area have been given for the two thicknesses of wire considered, and, the Debye length has been calculated using values of the electron density ($n_e = 8.0 \times 10^{18}$ m$^{-3}$) and electron temperature ($T_e = 4$ eV), obtained for the conditions examined in this work (See figure 5.3 in the following chapter). The calculated Debye length is over an order of magnitude smaller than the tip dimensions ($\lambda_{De} \sim 0.01 R_p$) and hence the measurements should not be complicated by ion-collection by the downstream tip identified by Hutchinson. For this

reason a calibration constant of $k_{\mathrm{M}} = 1.34$ was chosen, which is the value reported by Hutchinson [71] for plasmas at these conditions.

| | |
|---|---|
| $R_p$ | $0.1, 0.5$ mm |
| $L$ | 10 mm |
| $\lambda_{De}$ | $\sim 5$ $\mu$m |
| $\mathbb{I}_{\mathrm{i,sat}}$ | $\sim 30$ mA |
| $\mathbb{V}_{\mathrm{bias}}$ | $-60$ V |
| $c_S$ | 3100 m/s |
| $V_{th}$ | 800 m/s |

**Table 4.4:** A list of the values for the probe tip parameters: $R_p$ is the probe tip radius, $L$ is the probe tip length reported for the thin- (left) and thick- (right) tipped probe. The expected plasma parameters also given where $\lambda_{De}$ is the debye length, $\mathbb{I}_{\mathrm{i,sat}}$ is the ion saturation current, $\mathbb{V}_{\mathrm{bias}}$ is the bias voltage, $c_S$ is the sound speed and $V_{th}$ is the ion thermal speed.

The probe tip for a Mach probe built using Molybdenum wire (0.5 mm radius) is shown in 4.31 (a). The tip area is partly shielded by the ceramic casing and hence the collection area is reduced. The Mach probe was designed to access the plasma through the rear entrant port of MAGPIE (the end-plate closest to the target region) depicted in figure 4.31 (b). This allowed measurement collection along the length of the chamber.

For azimuthal flow measurements, the probe shaft was straight and the tips were orientated at a right-angle to the radial vector. The probe for this measurement was positioned at a radial distance of 2.5 cm from the machine axis, in line with the location of peak azimuthal flows for the reference position. For axial flow measurements, a shaft with a 'dogleg' (90° bend) near the probe tip was used so that the each tip pointed towards the source and mirror regions, respectively. The probe was positioned along the machine axis (radial distance of 0 mm).

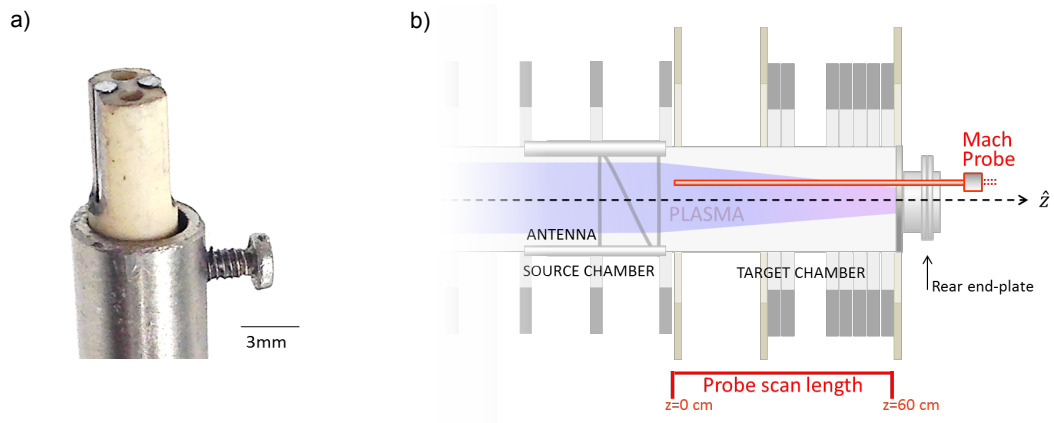


**Figure 4.31:** (a) photograph of the thick-tipped Mach probe (b) position of the Mach probe within the MAGPIE chamber.

The shaft and internal conducting wires of the probe were held at vacuum through a hermetic seal before connecting to an external battery source supplying the voltage. Six 9 V batteries were connected in series to provide the negative bias voltage for each tip. The batteries were connected through a two directional switch so that the polarity of the bias could be reversed (positive bias) to draw high electron currents to enable tip cleaning. The

voltage from each tip was measured over a resistor using a Digitized Acquisition (DAQ) box controlled by LABVIEW. The size of the resistor was chosen so that the measured signal was around $1-2$ V, but did not exceed 5 V which was the upper limit of the DAQ system. LABVIEW controlled the plasma pulse width and provided a trigger for the data collection.

The Mach numbers expected in MAGPIE are very low M $\leq 0.1$, and hence small differences in the tip sensitivity can result in large differences in the calculated ratio. A bias voltage of $-60$ V was selected as a safe upper limit on the voltage available within this experiment. It is important to keep the bias high enough that the ion saturation current is measured but also low enough to avoid arcing and unwanted sheath expansion.

### 4.4.2 Mach probe - data analysis and calibration

A typical ion saturation curve for each tip (red plot: tip 1, blue plot: tip 2) is shown in figure 4.32. The raw current data has been smoothed by a 4-pixel window to remove the effects of noise and the standard deviation between the repeat plasma pulses was calculated at $\sim 10\%$. There is clear disturbance in the plasma at initiation, which accompanies dramatic bursts in the emission brightness. The severity of this instability is effected by the power matching conditions. The first 60 m/s of the signal is excluded from these measurements to ensure plasma equilibrium is reached. In order to evaluate the reproducibility between measurements, the standard deviation was calculated from multiple flow scans (at the same plasma and probe conditions) to estimate the measurement error. This standard deviation has been used to determine the error bars for all flow measurements.

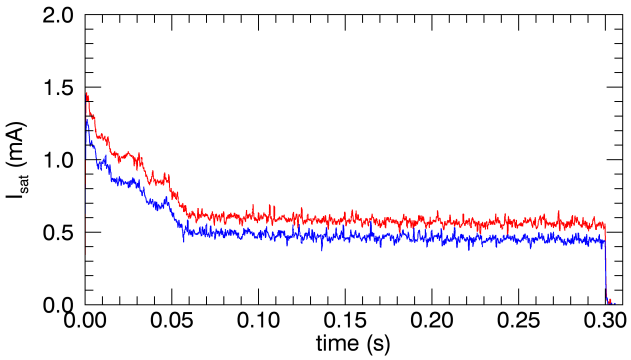


**Figure 4.32:** A typical ion saturation profile obtained for tip 1 (red) and tip 2 (blue) over time at a single axial position along MAGPIE.

There is a clear difference in magnitude between the current profiles measured by each tip. This can naively be interpreted as the effect due to plasma flow. On 180° rotation of the probe it was expected that the currents would switch as the upstream tip would always read a higher current compared to the downstream tip. This was not observed and suggested that the sensitivity of the tips were not equal. Such issues have been reported elsewhere in literature [74] and prompted calibration of the probe tips. A measurement of the ion current was taken at a given probe orientation. the probe was then rotated 180° so that the tips faced the opposite direction and were effectively exposed to the same

plasma conditions as the initial measurement. It was found that there was a scaling factor of 0.8 required in order to balance the tip sensitivity for the thick (0.5 mm radius) probe and a scaling factor of 1.3 was required for the thin (0.1 mm radius) probe. These scaling factors were then applied to all further probe measurements.

The difference in tip sensitivity is believed to be due to the probe tip collection area. This can be due to differences in construction such as the the tip length and alignment but also from a sputtering layer that can build up and add to the collection area. The latter issue was addressed by applying a strong positive bias so that electron bombardment would clean the tips.

The larger scaling factor for the thin probe tip is expected as the tips were suspended in the ceramic casing and not flush up against the walls on the cavity. The head of the thin tipped probe is depicted in figure (a) in 4.33 where the probe tips are shown in grey and the white cylindrical casing represents the ceramic insulation providing a barrier between the tips. The estimated collection angle is depicted by the blue cone and a misaligned tip along with the associated collection angle is shown in red. This shows that for the construction of the thin tips small misalignment can lead to large collection angle errors. This can be compared to (b) which depicts the thick tipped probe head. Here the tips are flush against the ceramic casing and the collection area for each tip is wider and the set-mounting of the tip makes it less likely to have collection angle errors.

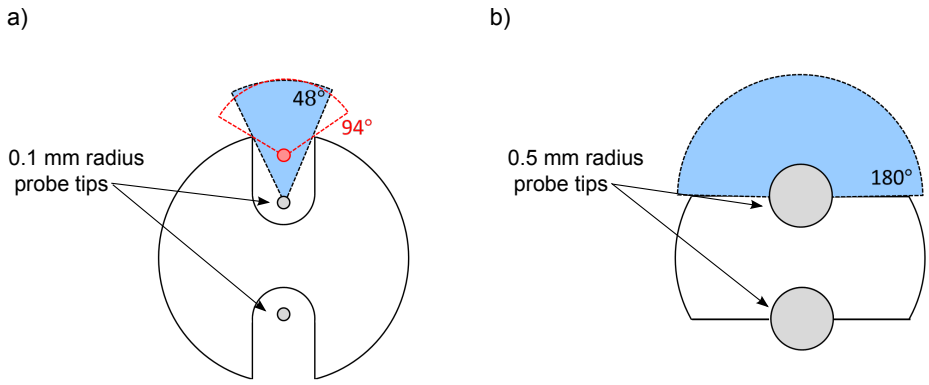


**Figure 4.33:** Diagram depicting the probe head and expected collection angles (shown by the blue cone) for (a) the thin-tipped probe and (b) the thick-tipped probe. The red outline in (a) shows the effects on the collection angle if the tip was misaligned.

It is important to compare the probe measurements for the thin and think tips before any insights can be drawn regarding the flows. For this, probe measurements were made of the azimuthal flows (at a radial position of 2.5 cm) using both the thin and thick tips. These measurements were taken over a scan in the axial direction and are shown in figure 4.34. It is possible that there is an error ($\pm 10$ mm) in the radial positioning of the probe, as the shaft was observed to curve when viewed from above. The azimuthal flows measured using coherence imaging are also presented (shown in figure 4.34 plotted in red) and has been averaged over 20 rows radially and reduced in the axial direction to 40 data points using a rebin function.

Figure 4.34 shows that the thick probe tip agrees (within error) with the flows obtained

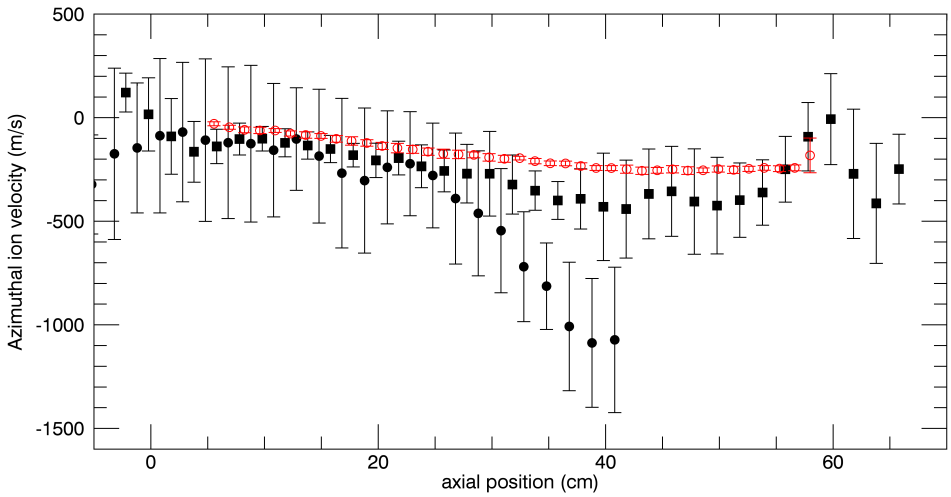


**Figure 4.34:** Probe measurements of the azimuthal flows along $z$ (with radial coordinate of 2.5 cm) using the thick tip (■) and thin tip (●). Azimuthal flow data obtained using the coherence imaging system at the same position is shown in red (○).)

using coherence imaging. We see however, that the thin probe significantly over-estimated the flows in the target region ($z > 30$ mm). This over-estimation is most likely due to an effect called shadowing which has been well documented in Mach probes [22, 67, 93, 94].

Gosselin [95] has shown that probe shadowing occurs for two reasons. Firstly the probe shaft can cause a geometric shadow leading to a reduced ion density in the region near the downstream tip. Secondly, ion neutral collisions cause the presheath to shorten below the natural width to the order of the ion-neutral mean free path. A lower ion density at the downstream tip and lower potential will cause a decrease in the expected ion saturation current, $\mathbb{I}_{\mathrm{D}}$. Hence the ratio of the measured upstream and downstream currents will be increased.

The ion saturation current measured by the upstream tip is determined by both the thermal motion of the ions as well as the flowing ions collected directed toward the tip. In the case of the geometric barrier, the downstream tip (shadowed by the barrier) will need to pull ions within the probe collection angle from the flow in order to measure a current. In the unmagnetised case, the ions have a gyro-radius bigger than the probe tip dimensions and so can cross the magnetic field to be attracted to the tip. The electrons, on the other hand, are usually highly magnetised (electron gyro-radius smaller than the tip dimensions) due to the much lighter mass. The electrons are therefore confined to the magnetic field lines and will obey the Boltzmann relation. Therefore quasi-neutrality will balance the decreased ion charge near the downstream tip resulting in a decreased tip potential. This effect is expected to be more prominent in probes with a narrow collection angle as there is less area for the downstream probe to collect the flowing ions and hence the decrease in the downstream tip potential is expected to be more severe [67].

In the work by Kado and Shikama on the MAP-II linear divertor simulator, the Mach

number was measured using a standard Mach probe (with large collection angle $\sim 100^\circ$ for each tip) and a directional Langmuir probe (DLP) with small collection angle ($\sim 20^\circ$) [67, 94]. The DLP delivered ion velocities far higher than expected (on the order of the sound speed or higher) while the data obtained with the Mach probe agreed with the spectroscopic data taken. The overestimation of the ion flow data acquired by the DLP was attributed to the shadowing effect [67]. Gosselin [95, 96] have since investigated this effect using a Mach probe in CSDX and developed a correction term based on the ratio of upstream to downstream densities where the perturbed downstream density was calculated using an advection-diffusion model. This worked showed that the wake near the downstream tip increased with magnetic field.

With this in mind, an adjustment factor of 0.45 was found to scale the thin tip measurements so that they are in line with the measurements taken using the thick tip which are expected to have a smaller degree of shadowing due to the large collection angle.

Chapter 5

# Coherence imaging of the MAGPIE argon plasma: single condition study

Coherence imaging measurements of the argon ion emission brightness, flow and temperature at the reference condition in MAGPIE are presented here. These measurements are termed 'apparent' as they assume that line-integration effects can be ignored. This assumption is addressed in chapter 6. Measurements are also considered over a series of interferometric delays to investigate the properties of the velocity distribution function. The results are interpreted, taking into account contamination effects such as stray reflections and secondary spectral lines.

## 5.1 Results: Reference condition study

This section presents coherence imaging projections of the brightness, ion temperature and plasma flow at the standard configuration of 3 mT pressure, 1 kW delivered power and peak magnetic field values of $\sim 0.005$ Telsa in the near-source region and 0.08 Tesla in the magnetic-pinch region (see reference magnetic field in figure 4.2). Repeat measurements were made at this condition (6 times) over the course of several months to characterise the extent of error due to plasma and chamber variations. The results presented in this section are an average of these measurements and the error bars have been calculated from the standard deviation of the acquired data.

### 5.1.1 Argon ion emission brightness

A normalised image of the plasma emission brightness at a single position, taken at 35.8 cm along the machine axis is shown in figure 5.1 (a). The dotted contour lines represent the levels of constant magnetic field strength. The axes are the axial $z$ coordinate and the impact parameter, which is approximately the radial coordinate (see definition in section 6.1).

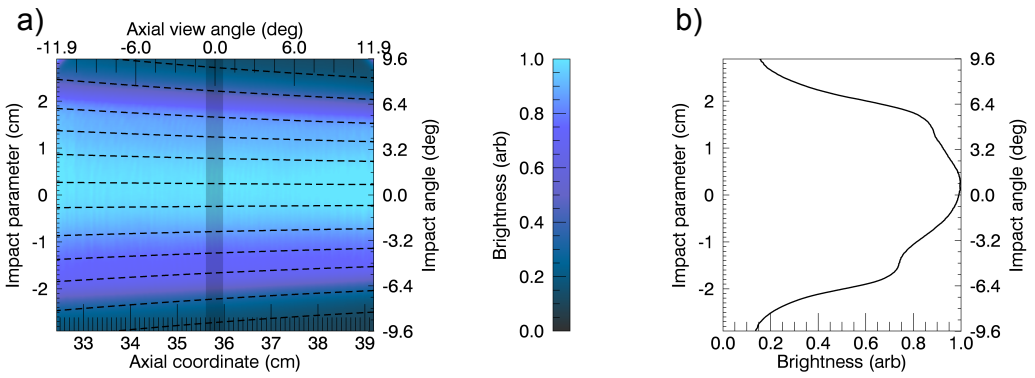


**Figure 5.1:** (a) Brightness image of the argon ion light normalised to the peak value where the axes are the axial $z$ coordinate and the impact parameter $p$ and the additional axes label the axial ($\chi$) and impact angles ($\psi$), respectively. The black contour lines represent contours of the magnetic field. The shaded segment in the center of the image is 10 columns wide and represents the region averaged in the $z$ direction to give the cross section of the brightness shown in (b).

The additional axes located at the top and right of the image indicate the axial and radial viewing angles of the imaging system. The shaded area covers the central 10 columns of the image. This region has been averaged in the axial direction to produce the radial cross section of the plasma brightness shown in figure 5.1 (b). Error bars have not been added onto the brightness profile as the magnitude of the brightness was observed to fluctuate with the matching conditions of the plasma. Ignoring the overall magnitude variation, the shape of the brightness profile showed little variation.

The snapshot (figure 5.1 (a)) shows the plasma is centrally bright and that the brightness contours conform well with the contours of the magnetic field. The cross-section plot shown in figure (b) reveals wing like features at $p \sim 2$ cm which appear to match the MAGPIE electron temperature profile (See figure 5.3). These secondary peaks show slight asymmetry and persist along the entire length of the chamber following the contours of the magnetic field (See figure 5.2 (a)). This radial asymmetry is attributed to the potential difference across the loop-like helicon antenna.

A full axial scan of the ion emission brightness at the reference condition is shown in figure 5.2. Individual images at each position have been acquired and then patched together to generate the axial scan. The brightness shows a clear compression of the plasma column in the high magnetic field region peaking on axis at 45 cm which is well away from the antenna.

Measurements of the density and electron temperature have been measured using a double probe along the axis ($p = 0$ cm, see figure 5.3 (a)) and radially (at $z = 11$ cm, see figure 5.3 (b)) for the same plasma conditions. These probe measurements have been provided courtesy of Dr Juan Caneses. Comparing the emission profile on-axis with the density and electron temperature, it is evident that the peak in the brightness profile corresponds to the same position as a peak in the density. Downstream density peaking is explained by a pressure balance described in [57] where in the case that the electron temperature, $T_e$, decays monotonically along the axis the density must rise to keep the pressure constant.

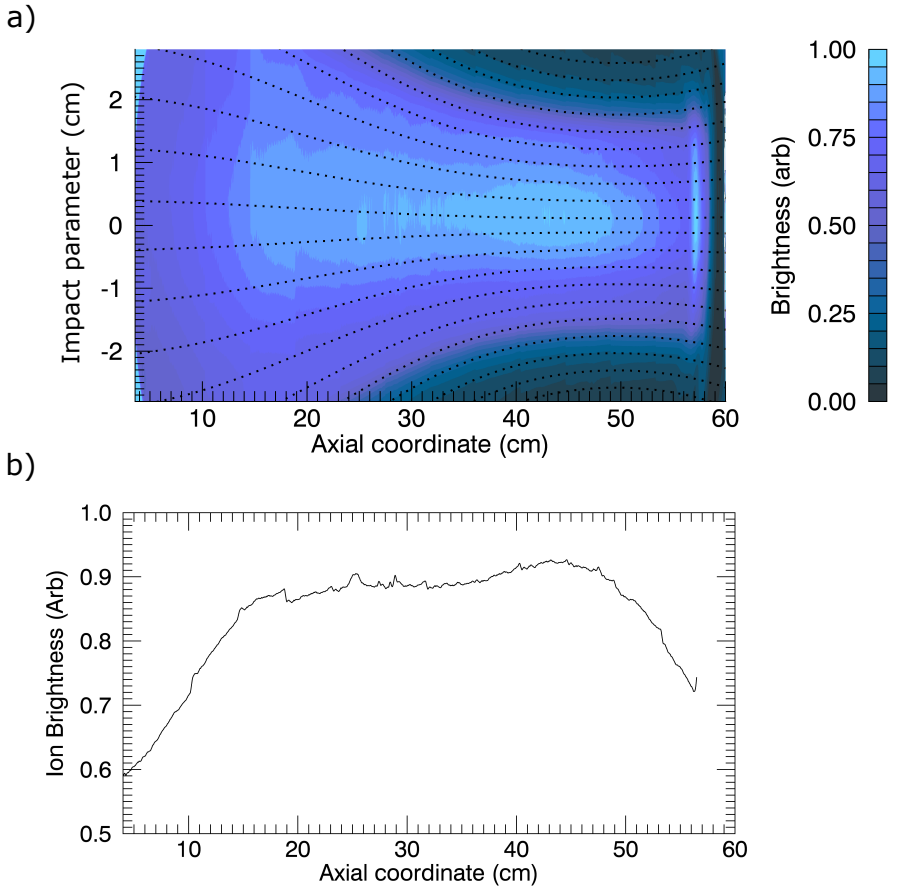


**Figure 5.2:** (a) shows a scan of the normalised plasma emission brightness and (b) is a plot of the normalised emission brightness along the axis, taken at the reference condition.

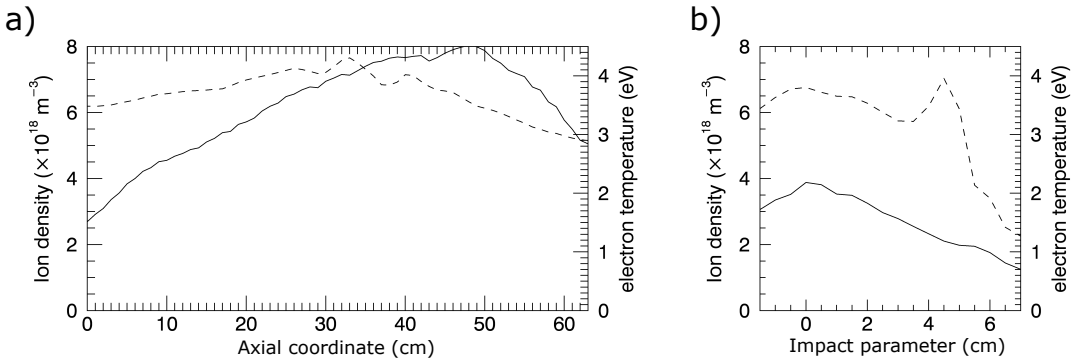


**Figure 5.3:** shows the density (solid) and electron temperature (dashed) for scans in the (a) axial ($p = 0$ cm) and (b) radial ($z = 11$ cm) directions taken using a double probe, for a plasma at the reference condition.

### 5.1.2 Argon ion temperature

The contrast measured for the 488 nm argon ion emission at axial position 35.8 cm is shown in figure 5.4 (a). Ignoring line-integration effects and using equation 4.27 the ion temperature was estimated and is shown in figure 5.4 (b). Again, a central section (10 pixels wide), shown by the shaded area in figures (a) and (b), is averaged over columns to produce radial cross-sections of the contrast and ion temperature shown in figures (c) and (d) respectively.

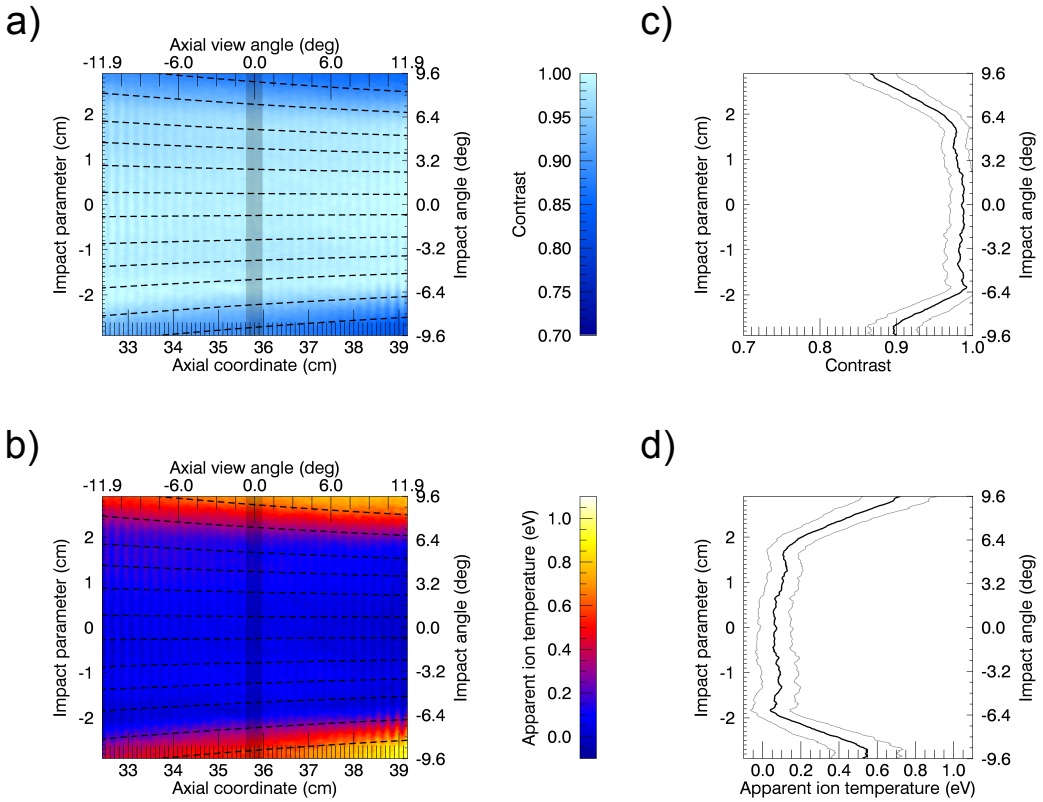


**Figure 5.4:** shows the (a) contrast and (b) apparent ion temperature, measured at the reference condition where the axes are the axial $z$ coordinate and impact parameter $p$ and the additional axes label the axial ($\chi$) and impact angles ($\psi$), respectively. The black contour lines represent contours of the magnetic field. The shaded segment in the center of the image is 10 columns wide and represents the region averaged in the $z$ direction to give the cross section of (a) and (b) shown in (c) and (d), respectively.

The measured ion temperature is centrally flat and cold with ion temperatures recorded as $< 0.1$ eV. The images also suggest ion heating at the edges of the plasma ($> 2$ cm) where the ion temperature is recorded to peak at $0.8 - 1.0$ eV. It has been shown that second order perturbations to in the ion temperature can be indicative of radial flow (see appendix B). Such flows would broaden the spectral line especially near the axis where radial components will be largest. For a line-of-sight orthogonal to the central axis and ignoring line-integration effects the second order flow contribution to the contrast is proportional to $-\phi_0^2 v_r^2/2$ (where $v_r$ is the radial flow velocity normalised by $c$). Radial flows of 500 m/s would therefore result in a contrast perturbation of only $\sim 0.02$ (ion temperature $\sim 0.1$ eV) which is on the threshold of error for these measurements. This

means that only very large radial flows (> 500 m/s) will be observed as elevated core ion temperatures.

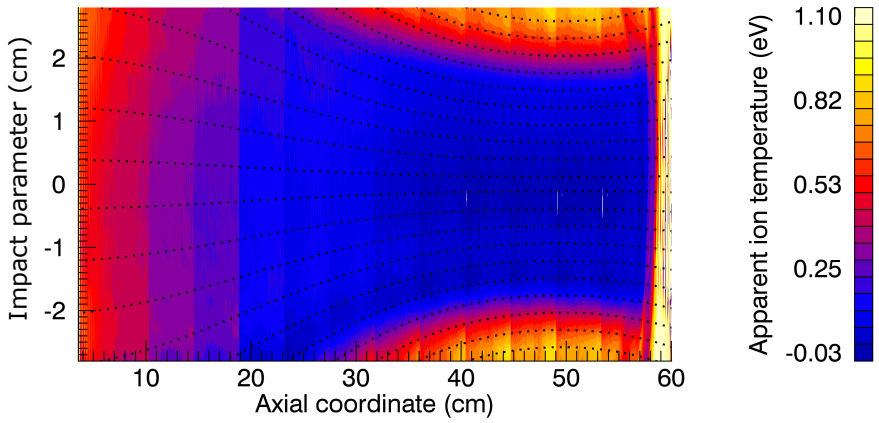


**Figure 5.5**: Scan of the ion temperature at the reference condition in MAGPIE.

Edged-peaked ion temperature profiles in helicon plasmas have previously been reported by Kline for measurements in HELIX [29] using laser induced fluorescence techniques. The high-edge temperatures have been attributed to a resonance between the Trivelpiece-Gould mode and the lower hybrid frequency. Parameter scans are presented in a following chapter to explore this in more detail. A full temperature scan along the length of the MAGPIE chamber is presented in figure 5.5. The edge peaked profile follows the contours of the magnetic field along the full length of the chamber. There is also an observed increase in the ion temperature near the antenna region. The core ion temperatures in the high magnetic field region are very low compared with the near-source and edge temperatures and considerable care is required to obtain meaningful measurements. We must also take care that other effects such as spectral contamination and stray reflections are not artificially elevating the measured edge-temperature. Such issues are addressed later is this chapter.

### 5.1.3 Argon ion flows

The average phase measured at axial position 35.8 cm is shown in figure 5.6 (a). A central section (10 pixels wide), shown by the shaded area in figure (a), is averaged over columns to produce the cross-section shown in figure (d).

The phase can be separated into symmetric and asymmetric components due to the cylindrical symmetry of MAGPIE (see discussion in section 4.3.7) to allow the rotational and axial components of the flow to be separated. These are shown in figures 5.6 (b) and (c) respectively, with corresponding cross sections shown in figures (e) and (f). The radially symmetric artifact in the axial flow component is unexpected and it is unlikely that this is a real feature of the plasma flow due to the unnatural form of the phase shift (shift to the blue either side of the machine axis and increasing radially). This would naively suggest a bulk flow of ions vertically from the base of the chamber to the viewing plate which breaks

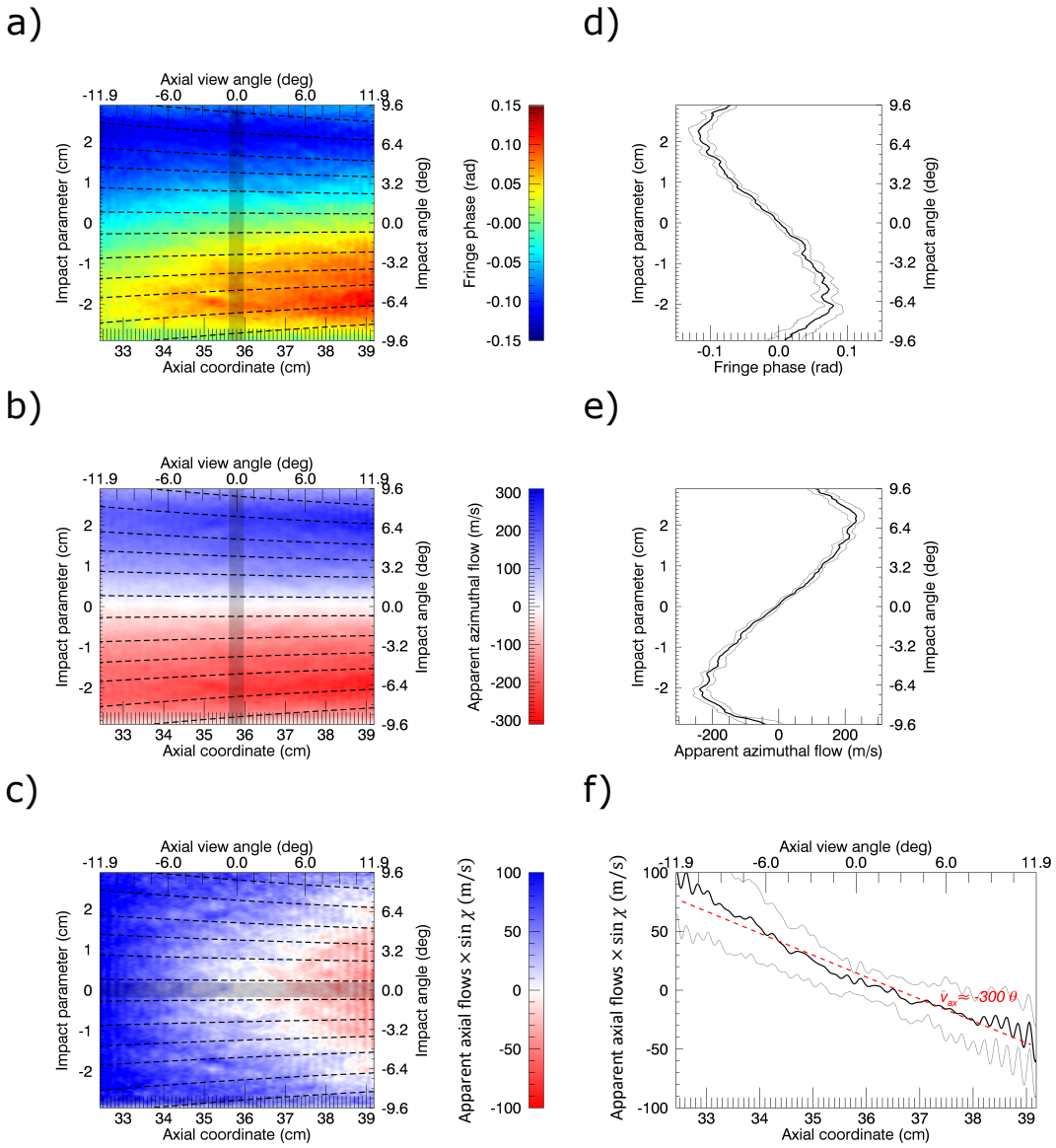


**Figure 5.6:** (a) Phase image, (b) apparent azimuthal flow and (c) apparent axial flow $\times \sin\chi$ for the reference condition where the axis are the axial $z$ and impact parameter $p$ plasma coordinates and the additional axes label the axial ($\chi$) and impact angles ($\psi$), respectively. The black contour lines represent levels of constant magnetic flux. The shaded segment in (a), (b) and (c) at the center of the image is 10 columns wide and represents the region averaged to give the cross section shown in (d), (e) and (f), respectively.

the azimuthal symmetry requirement. Instead, this phase shift is likely to be caused by some kind of contamination effect or unaccounted for instrumental effect. Unfortunately the origin of this artifact has not been determined.

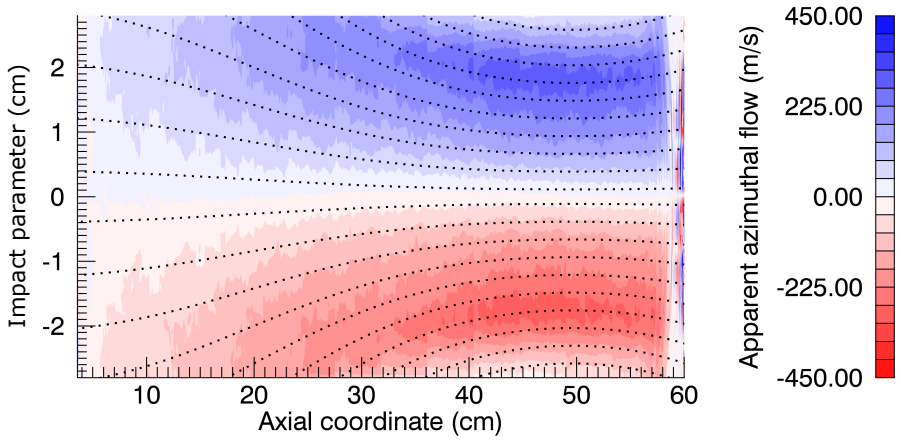


**Figure 5.7**: Scan of the azimuthal flow in MAGPIE at the reference condition.

The rotational flow shown in figures 5.6 (b) and (e) shows rigid body rotation of the plasma up to a radial distance of 2 cm with velocities reaching 200 m/s. This is far lower than both the sound speed and thermal speed of the ions which were calculated as 3100 m/s and 800 m/s, respectively. For radii greater than 2 cm the flows are sheared and decrease to 0 m/s at 3 cm. The transition between the rigid body rotation and the sheared flow region corresponds to the same radial position where the ion temperature starts to elevate.

Figure 5.7 shows the rotational flows along the length of the MAGPIE chamber. The flows are greatest in the high magnetic field region and conform with the magnetic lines of force. The flows in the near-source region are small. The direction of the flows are confirmed in a later chapter using the Mach probe.

Sheared sub-sonic rotational flows have been reported in other helicon plasmas, most notably in the HELIX device [28,31], CSDX device [37,97,98] and VINETA [39] which all share similar operating parameters to MAGPIE. In each of these devices, the bulk rigid body rotation has been attributed to an $\mathbf{E} \times \mathbf{B}$ drift, which has been reported to flow in either the electron or ion diamagnetic directions. All of these devices also report flow shear at large radii and propose this is due to the presence of turbulent drift waves, either driven by a radial gradient in the density or the ion temperature. Drift waves are often observed as coherent modal structures usually between the frequency range of $5 - 50$ kHz are referred to as a universal instability as they affect all magnetically confined plasmas and are largely responsible for plasma transport across the magnetic field [99].

Kilohertz range ($\sim$ 20 - 40 kHz) modal structures observed in MAGPIE using measurements of brightness fluctuations in argon obtained using a 16 channel photo-multiplier tube suggest that such instabilities may exist in MAGPIE and could contribute to the shear observed in the azimuthal flow. Further investigations of this modal behavior using a gated fast imaging coherence imaging camera [100] have revealed a coherent $m = 1$ mode rotating structure. However, there has been no study of turbulent light fluctuations at

larger radii or over a survey of plasma conditions. It has been suggested by Kline [28] that the rigid body rotation next to the sheared layer is also expected to result in Kelvin Helmholtz instabilities, which occur at the interface between two fluids flowing at different velocities.

The apparent axial flow component shown in figure 5.6 (c) is proportional to $\sin\chi$, as only components parallel to the line-of-sight are measured. By assuming that the variation in the flow is small along the axis, it is possible to fit an axial linear-ramp to the measured apparent axial flows to deduce the mean axial flow. The axial flow components measured, $V_{msr}$ are related to the true axial flow, $V_z$, though the axial viewing angle, $\chi$

$$\begin{aligned} V_{msr} &= V_z \ \sin\chi \\ &\approx V_z \ \chi \end{aligned} \tag{5.1}$$

The mean (apparent) axial flow is obtained from the gradient of the straight line fit against viewing angle as shown in figure 5.6 (d). The variation of the apparent axial flows along the chamber is shown in figure 5.8.

The red error bars have been calculated for measurements made in the same experimental set and characterise the error expected in measurements taken over consecutive scans. The black error bars reflect the standard deviation calculated over axial flow measurements repeated over several months and capture variations in the instrumental build and chamber properties. In general the profile of the flows was relatively similar as indicated by the smaller error bars between $10 - 50$ cm. These axial scan results suggest there is a large acceleration of plasma (flows $0 - 600$ m/s) from the throat of the magnetic pinch ($z = 45$ cm) towards the end-plate of the target chamber. There is also a steady flow ($-200$ m/s with little acceleration) away from the high magnetic field region into the near-source region. Interestingly, the zero point for the axial flows is located at $\sim 45$ cm which corresponds to the peak in brightness and also the peak in density shown in plots 5.2 and 5.3 suggesting that this location is where the helicon wave is absorbed and the particles are ionised. The decrease of ion speed into the high magnetic field region also suggests conservation of ion flux. The acceleration of ions out of the magnetic pinch towards the end-plate may therefore also be a consequence of magnetic field expansion. Axial ion acceleration through regions of expanding magnetic fields have been reported in HELIX-LEIA [32].

Flow reversal downstream of the antenna has previously been reported in [101] for a hydrogen plasma in MAGPIE. For that study, an axial flow reversal was reported closer to the antenna at $z = 13$ cm and ions were found to flow away from that point, i.e. into the antenna and into the magnetic pinch. The flow reversal for that study was attributed to a parallel electron pressure gradient. Theoretical modeling for the hydrogen plasma [102] suggest there is a strong axial flow dependence on the gradient of the electron temperature. The direction and magnitude of the MAGPIE argon flows are examined using a Mach probe and the results are presented in chapter 7.

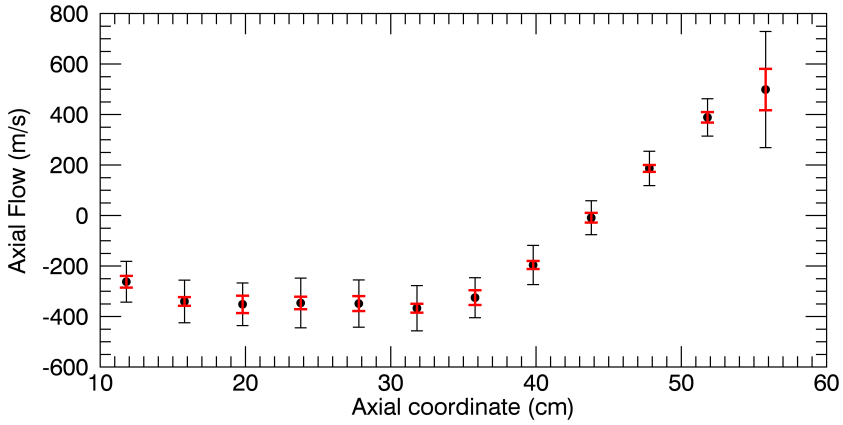


**Figure 5.8:** Axial flow measured along the machine axis at the reference condition. The red error bars indicate the standard deviation between measurements taken during the same experimental set. The black error bars indicate the standard deviation between measurements taken at the same plasma conditions and imaging system specification but for experiments made over the course of a few months, capturing variations in the instrumental build and chamber properties.

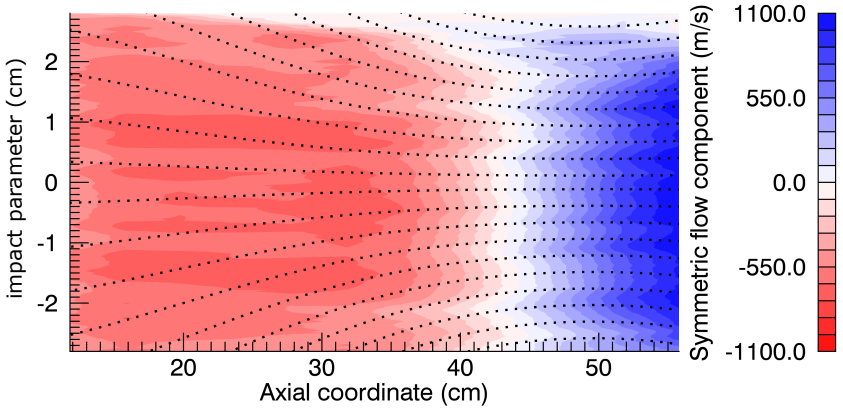


**Figure 5.9:** A 2D scan of the axial flow in MAGPIE at the reference condition. The blue and red colours correspond to positive and negative flows, respectively (the flow direction is determined later using a Mach probe).

The spatial scan of the axial flows in MAGPIE (with impact parameter $p$ and axial coordinate $z$) is shown in figure 5.9 (a). Here the axial flows are flat and positive in the high magnetic field region and reduce to zero at the edges of the plasma. Near the source, the axial flows are also flat with negative flows. The bumpy artifacts appear to be a product of the averaging process and are not considered features of the true flow.

## 5.2 Contamination effects

Apparent 'negative' temperatures have been measured in the high magnetic field region. These features are likely caused by instrumental or spectral effects contaminating the measurements. In this section the effects of reflections within the chamber or within the optical system are evaluated along with angular shifts in the filter spectral passband and the effect of contaminating spectral lines.

### 5.2.1 Spectral line contamination

Zeeman splitting of the spectral line has been shown in in section 4.2.1 to be small compared with the Doppler effects for the 487.9 nm measurements on MAGPIE (at peak field of 0.08 T) and is only expected to affect the results at high magnetic fields. Even in the high magnetic field case, an initial vertical polariser was used during all measurements to remove contamination from $\sigma$ components.

Near-neighbor spectral lines can also be a source of contamination. The spectrum near the 487.9 nm spectral line for the argon discharge was measured at four spatial locations and at pressures of 3 mT and 10 mT using the IsoPlane spectrometer (see description in section 4.2). The raw spectral data is shown by the black plots in figure 5.10 and the red overlay indicates the spectral data selected by the filter. This has not been corrected for angular shifts in the filter passband - such effects are considered in section 5.2.3. The gain factor on the spectrometer is specified.

In order to evaluate the extent of the contamination, the cumulative area under the spectrum was calculated for each measurement. For this analysis, the spectrum transmitted by the filter (red overlay in figure 5.10) has been considered. The area curves are shown in figure 5.11 where the wavelength of each spectral line has been indicated. The values of the area curve are indicated for the flat region following each spectral line. Using these values, the ratio of the secondary line to the primary 487.9 nm line has been calculated to give the percentage contamination. The 3 mT edge measurements show that the spectrum goes negative (resulting in a decrease in area) for wavelengths above 488.9 nm. This arises due to noise is the signal pushed negative with the subtraction of the black baseline measurement.

This data shows that the 486.5 nm spectral line has $\sim 8\%$ contribution in the centre of the near-source region for the 3 mT case and up-to an $\sim 11\%$ contribution in both the centre and edge of the high magnetic field region for the 10 mT case. The 488.9 nm spectral line

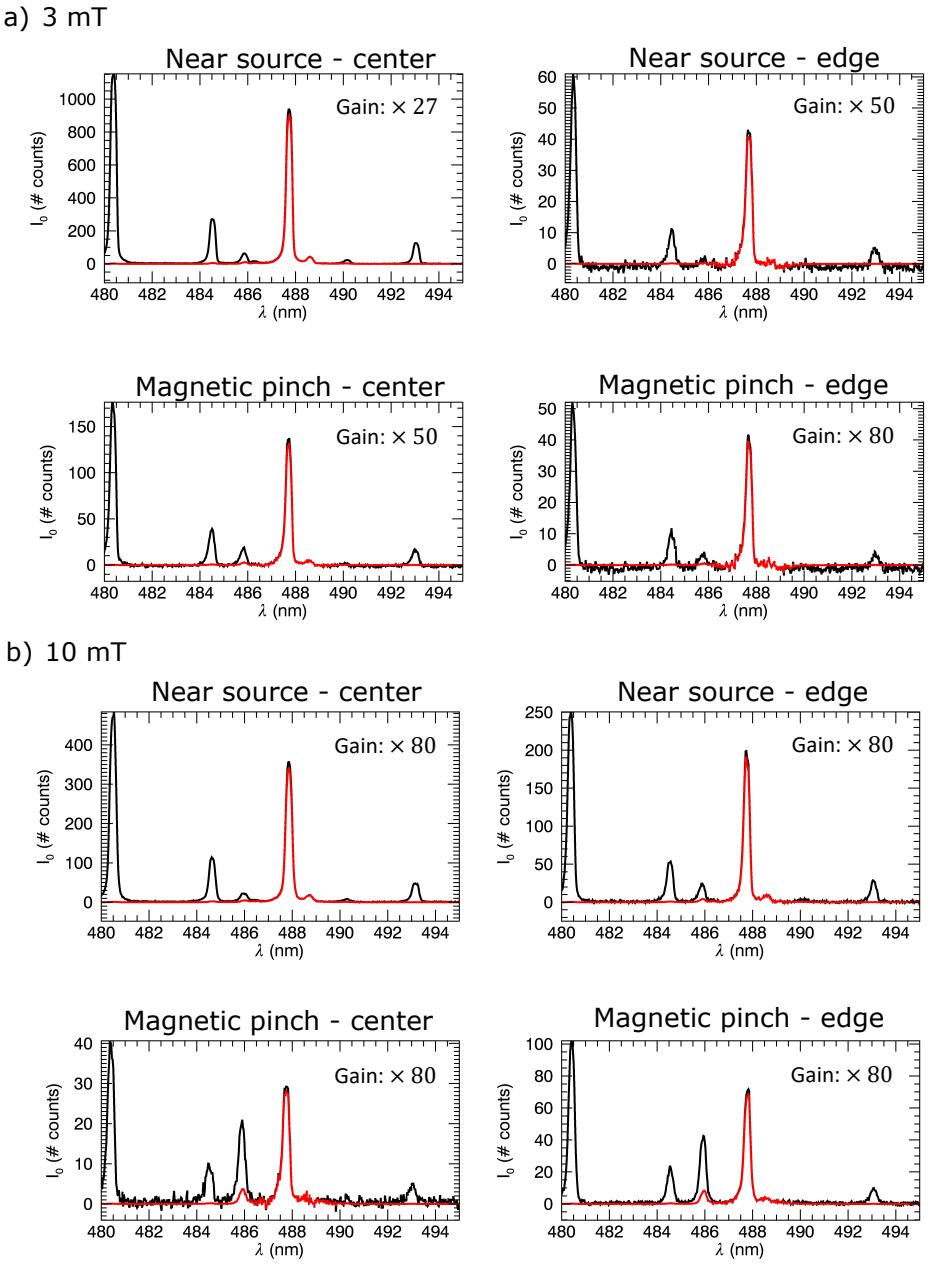


**Figure 5.10:** Spectral measurements at (a) 3 mT and (b) 10 mT for positions in the near-source and high magnetic field regions on axis and at the radial edge of the discharge.

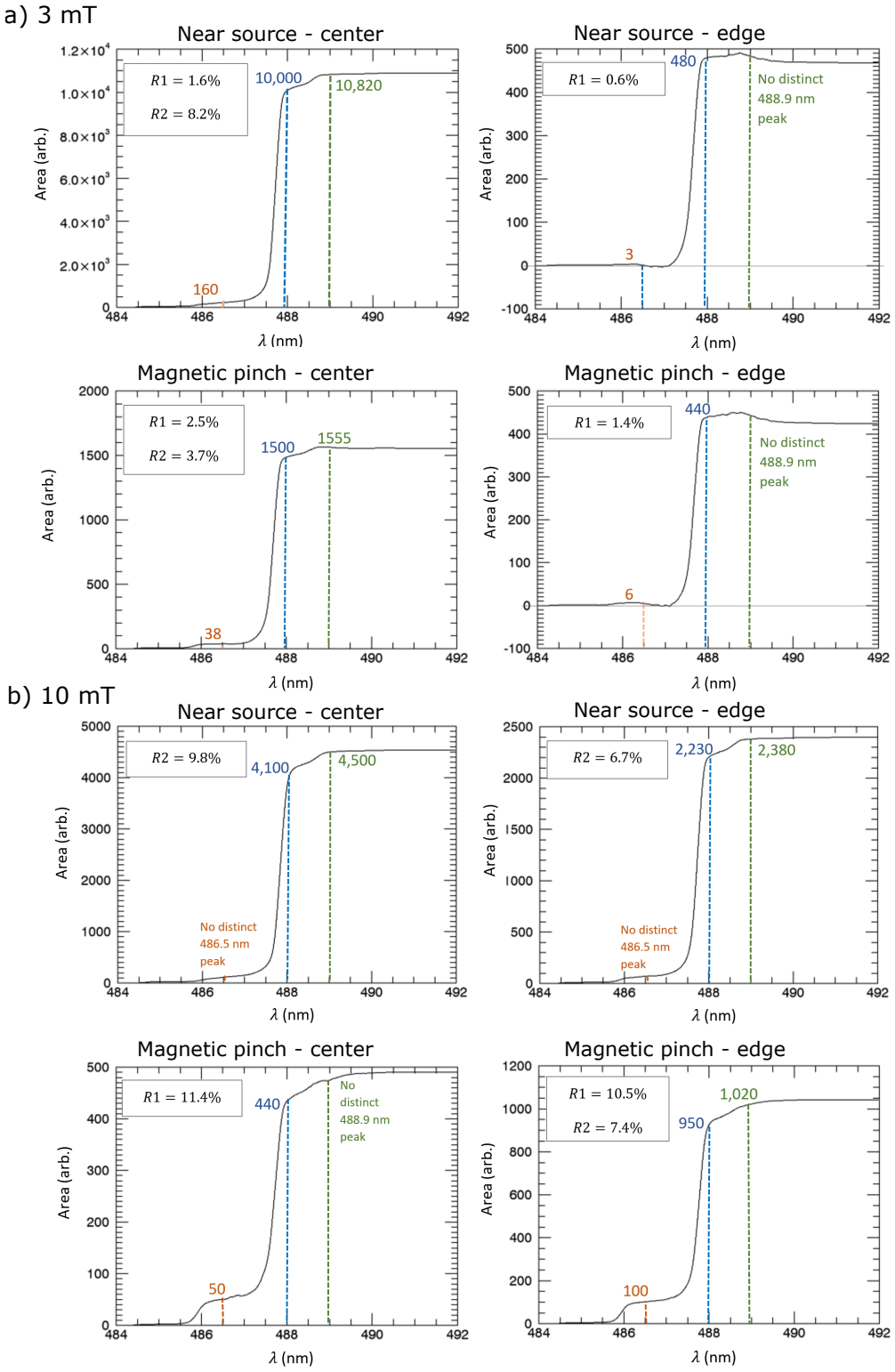


**Figure 5.11:** Area under the spectrum taken at (a) 3 mT and (b) 10 mT for positions in the near-source and high magnetic field regions - on axis (centre) and at the radial edge (edge) of the discharge. The orange, blue and green dotted lines indicate the positions of the 486.5 nm, 487.9 nm and 488.9 nm spectral lines, respectively. The corresponding labels indicate the value of the area curve in the near-flat region near the spectral line. The ratio $R1$ is the area value for 486.5 nm line divided by the area value of the 487.9 nm line. The ratio $R2$ is the area value difference between the 488.9 nm line and the 487.9 nm line divided by the area value of the 487.9 nm line.

is also apparent, with up-to a 3% contribution in the centre region for the 3 mT case, and $\sim$ 10% contribution in the near-source centre for the 10 mT case. As the contributions from secondary lines are non-negligible, it is important to determine what effect this has on the coherence-imaging data.

Coherence imaging measurements with respect to multiple spectra lines has been previously considered by Howard [42] for the $H_\beta$ and $D_\beta$ spectral lines in the H1 Heliac which considered much higher ion temperatures and smaller interferometric delays ($\sim$ few thousand waves) as compared with the conditions in MAGPIE. Here, the effects of a secondary spectral line are considered for the MAGPIE imaging system. The effects of a third line are not addressed.

The interferometric signal due to two spectral lines, $S_T$, is the sum of the individual signals, $S_1$ and $S_2$. The interferometric signal for the total signal is therefore,

$$\begin{aligned} S_T &= S_1 + S_2 \\ &= I_1(1 + \zeta_1 \cos\phi_1) + I_2(1 + \zeta_2 \cos\phi_2) \\ &= (I_1 + I_2) + (I_1\zeta_1 + I_2\zeta_2)\cos\phi_0 \cos\delta_\phi + (I_1\zeta_1 - I_2\zeta_2)\sin\phi_0 \sin\delta_\phi \end{aligned} \tag{5.2}$$

Where the normalisation factor has been ignored and the mean phase is is calculated as $\phi_0 = (\phi_1 + \phi_2)/2$ and the difference in phase is given by $\delta_\phi = (\phi_1 - \phi_2)/2$. In this model the parameters $\phi, \zeta$ and $I$ are specified for each spectral line. It is assumed that the spectral lines are generated from the same species and are therefore effected by the same electron temperature, ion temperature and species drift velocity.

If we assume that the new interferogram takes the form

$$S_T = I_0(1 + \zeta \cos(\phi + \eta)) \tag{5.3}$$

Where $\eta$ is the mean phase, $\zeta$ is the effective contrast taking into account multiple spectral lines and $I_0 = I_1 + I_2$ the combined brightness of both lines. The two quadratures can be written as

$$I_0\zeta \cos\eta = (I_1\zeta_1 + I_2\zeta_2)\cos\delta_\phi \tag{5.4}$$

and

$$I_0\zeta \sin\eta = (I_1\zeta_1 - I_2\zeta_2)\sin\delta_\phi, \tag{5.5}$$

where

$$\zeta = \frac{\left((I_1\zeta_1)^2 + 2I_1\zeta_1 I_2\zeta_2\cos(2\delta_\phi) + (I_2\zeta_2)^2\right)^{\frac{1}{2}}}{(I_1 + I_2)} \tag{5.6}$$

and the mean phase is given by

$$\tan\eta = \frac{I_1\zeta_1 - I_2\zeta_2}{I_1\zeta_1 + I_2\zeta_2}\tan\delta_\phi \tag{5.7}$$

Setting $R = I_2/I_1$ and noting that for a small contaminating line $R^2 << 1$, and assuming $\zeta_1 \approx \zeta_2 \equiv \zeta_0$ then these two expressions can be simplified to

$$\zeta = \zeta_0(1 - 2R + 2R\cos 2\delta_\phi)^{1/2} \tag{5.8}$$

and

$$\tan\eta = (1 - 2R)\tan\delta_\phi \tag{5.9}$$

The contrast calculation shows that secondary-line contamination will always decrease the measured contrast. The contamination will result in an oscillation in the contrast with an amplitude of $\sqrt{1-4R}$ occurring when $\delta_\phi = (2n+1)\pi/2$ for $n$ in $\{0, 1, 2, 3...\}$.

The mean phase can be re-written as $\eta = \delta_\phi + \epsilon_\phi$, where $\epsilon_\phi$ describes a small phase distortion in the interferogram. A first order expansion gives $\tan(\delta_\phi + \epsilon_\phi) = \tan\delta_\phi + \epsilon_\phi \sec^2\delta_\phi$ and substitution into 5.9 therefore gives

$$\epsilon_\phi = -R\sin 2\delta_\phi \tag{5.10}$$

The $\epsilon_\phi$ phase distortion acts directly on the measured drift phase and will manifest as an oscillation with an amplitude of $R$ radians.

Using equations 5.8 and 5.10 it is possible to model the phase and contrast expected where a secondary spectral line is present in the measurements. The spectral line ratios calculated in figure 5.11 show that the spectral contamination can be as high as 11% for either secondary line. Table 5.1 shows the plasma parameters considered for this model and spectral contamination from the 486.5 nm line is considered.

Figure 5.12 (a) shows the expected (i) contrast and (ii) phase measurements with 10% spectral contamination over the delay range $0 - 200$ mm of BBO crystal. The red plots show the modeled contrast and phase when there is no spectral contamination and the black points show the modeled values for measurements sampled at every 20 cm of $\alpha-$BBO delay crystal. The grey dashed lines show the maximum modulation amplitude for the degree of contamination. The temperature and flow have also been calculated from these quantities and are shown in (iii) and (iv) respectively. The same quantities are modeled

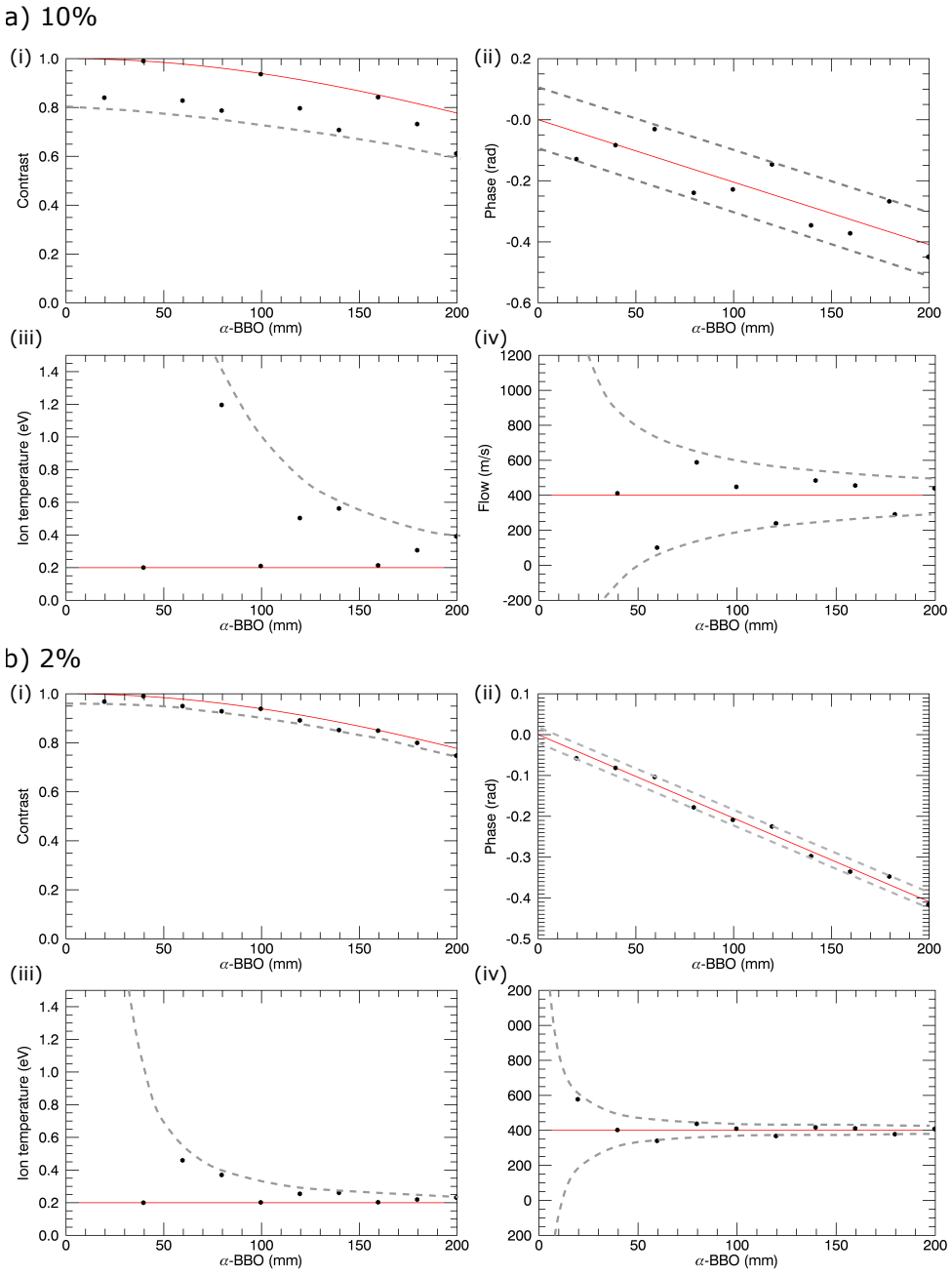


**Figure 5.12:** Effects of spectral contamination are shown for (a) 10% and (b) 2% spectral contamination in (i) contrast, (ii) phase, (iii) ion temperature and (iv) the flow. The grey plots show the maximum extent of the contamination and the red plot shows the quantities with no contamination effects. The black points (•) show a sample of measurements (with contamination effects included) taken at 20 mm $\alpha-$BBO delay intervals.

| model parameter | value chosen |
|---|---|
| $V_D$ | 400 m/s |
| $T_i$ | 0.2 eV |
| $I_1$ | 1 (normalised) |
| $I_2$ | 0.1 or 0.05 |
| $\lambda_1$ | 487.9 nm |
| $\lambda_2$ | 486.5 nm |

**Table 5.1**: Parameters used to model the contamination effects of a secondary spectral line.

in (b) for 2% line contamination.

The spectral contamination can be calculated for a given delay using [42],

$$\delta_\phi = \kappa\phi_0\frac{\delta\lambda}{\lambda_0} \tag{5.11}$$

If the contamination ratio $R$ is known, then equation 5.10 can be used to calculate the phase distortion and equation 5.8 will give the contrast adjustment. For an 80 mm imaging system (where $\phi_0 \sim 20,000$ waves), contamination from the 486.5 nm line will give a $\delta_\phi$ value of $\sim 58$ waves ($\sim 365$ radians). If the instrumental delay is known to within 10 waves then $\delta_\phi$ can be calculated to within 0.2 radians, which is marginal.

The plots in figure 5.11 show that there is only a small amount of spectral contamination ($< 1.5\%$) in the edge region of the 3 mT measurements. Although spectral contamination is found to artificially increase the temperature, the small secondary-line contribution in these measurements is not enough to cause sharp edge-peaked ion temperature profile. The degree of contamination in some cases can be quite high ($\sim 10\%$) depending on the plasma conditions and it is therefore important to consider this effect when drawing insights from measurements made over a scan of plasma conditions.

### 5.2.2 Contamination from stray reflections

Stray reflections in the chamber and also reflection internal to the optical system can cause phase mixing from light from different regions of the plasma which will result in contamination of the temperature measurements.

Reflections in MAGPIE are tricky to quantify as this involves knowing the reflective properties of the chamber. To investigate the extent of these reflections, coherence imaging measurements of the plasma were made with and without blackened view-dump sheeting installed in the chamber. A radial cross-section for the contrast in the high magnetic field region at 3 mT with and without the view-dump sheeting is shown in figure 5.13 (c). The same study at 10 mT is also shown in figure 5.13 (d). The corresponding brightness profiles are shown in (a) and (b).

The 3 mT results show that the apparent edge temperatures decrease and the apparent

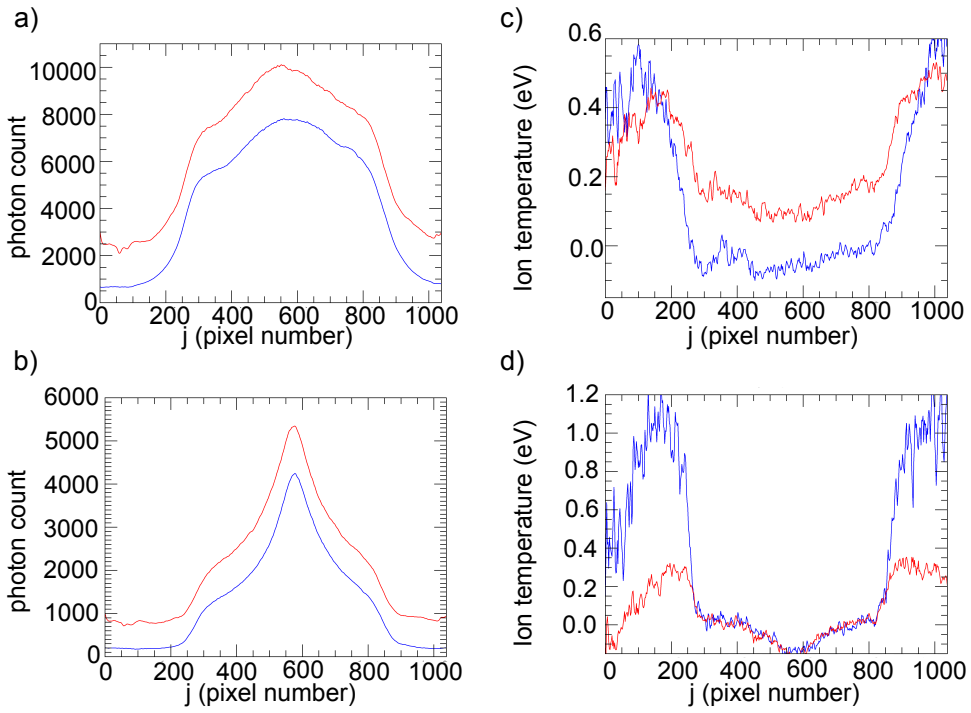


**Figure 5.13:** Figures (a) and (b) are plots of the measured radial brightness in MAGPIE at 3 mT and 10 mT and plots (c) and (d) show the corresponding ion temperature measurements, respectively. The plots are taken with (blue) and without (red) anti-reflective shielding installed.

core temperatures increase in the presence of reflections. This suggests that bright light from the cold plasma center reflects into the edge region and decreases the apparent temperatures at the edge while the low-light high-temperature edge light will reflect into the center region and increase the core apparent temperature. The 10 mT contrast study shows the same decrease in the apparent edge temperatures however no change the apparent central temperatures. From the brightness profile in figure (d) we see that the 10 mT plasma has a beam-like brightness profile and so the bright cold center will to have a much larger effect on temperature contamination on the edge features than vice-versa. These results confirm that reflections within the chamber can affect the apparent temperature profile (high edge-temperatures reduce and low core-temperatures increase) and demonstrate the need to use blackened view-dump sheeting.

Reflections within the optical system also present a concern in this study due to the large optical systems used ($\sim$ 100 mm). Collimated light passing through the crystal cell (even at small angles) can be cut-off and internally scattered by the blackened optical cell walls. The diagram in figure 5.14 shows an example where the rays from two points in the plasma are traced through the imaging system. In this image the blue rays are generated at the edge of the plasma source and red rays are generated at the center of the plasma. The green arrow identify where rays from each of these points hit the internal walls of the crystal cell and become reflected (shown by the dashed rays). These reflected rays are directed into another part of the image on the CCD and have a different path length compared with the collimated rays focused at the same position. The path length difference can result in a phase difference and, once averaged with the unperturbed rays, will result in a decrease

in the contrast at that point. This effect can be minimised by decreasing the aperture of the front lens in order to stop edge vignetting effects in the instrument.

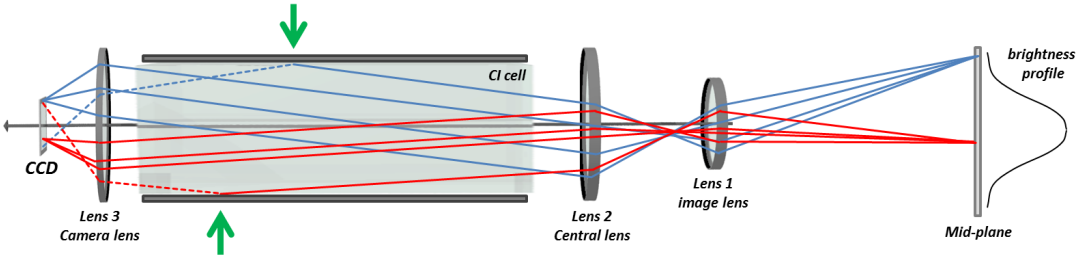


**Figure 5.14:** Diagram shows an illustrative example of how internal reflections within a coherence imaging system can be reflected by the walls of the system (indicated by the green arrows) and result in decreased instrumental contrast. Generally this effect can be minimised by reducing the aperture of the front lens.

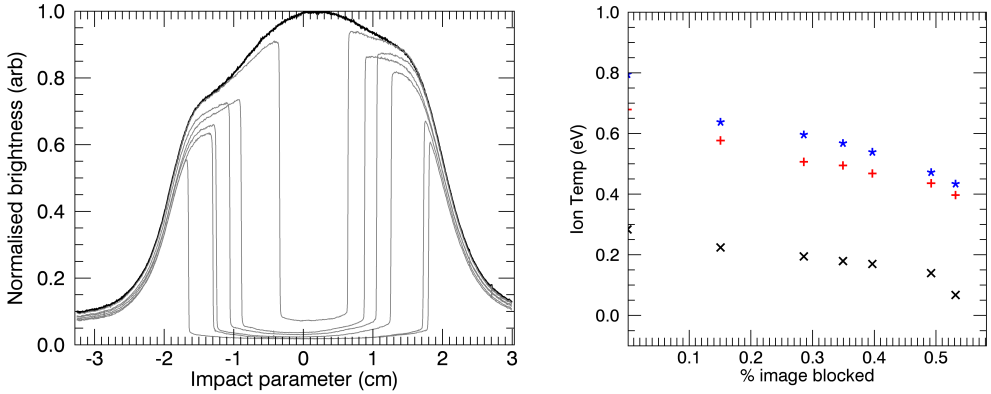


**Figure 5.15:** shows (left) the radial brightness profile taken in the high magnetic field region at the reference condition. For each of these measurements the central segment of the image has blocked by a card (with increasing width). The second image (right) shows the corresponding projected ion temperatures from radial positions of 2 cm ($\times$) 2.5 cm ($+$) and 3 cm ($\star$) shown plotted against the percentage of the image blocked by the card.

An attempt to quantify the effect on the edge temperatures due to internal reflections was made by placing a card in the view of the imaging system so that the central light of the plasma was blocked. This eliminated the source of bright light which could reflect within the imaging system. By varying the card width the dependence on the edge temperature was observed. The brightness profiles measured in the high magnetic field region, with the central segment blocked by different card widths is shown in the left figure of 5.15. The corresponding projected ion temperature at radial positions of 2 cm ($\times$), 2.5 cm ($+$) and 3 cm ($\star$) are shown plotted against the percentage of the image blocked by the card, is shown in the right figure.

It was found that the edge temperatures decreased by blocking the central light ($\sim$ 0.2 eV over the measurement). This suggests that phase-mixing due to internal reflections in the imaging system will result in an instrumental increase in the measured temperature.

Even though this is an instrumental effect, it is a product of the phase information in the plasma light and hence cannot be removed with calibration.

It is important to note that while this measurement blocks the central bright plasma light from reflecting into the edge of the image, it does not completely eliminate all internal reflections within the optical cell. For example light from the plasma edge (the blue rays in image 5.15) can still be internally reflected within the optical cell. This study therefore examines some of the effects of internal reflections but is not able to show the full extent of this contamination. In this study, the effects of reflections have only been examined for measurements of the temperature. It is expected that the phase will be 'washed-out' in presence of reflections due to phase-mixing resulting in an underestimate of the flows.

### 5.2.3 Angular effects of the imaging filter

Narrow-band imaging filters are highly effective in transmitting a single emission line with passband $\sim 1$ nm and with very little contamination from neighboring lines. These filters achieve such clean transmission by using a series of Fabry-Periot cavities with thickness of $n\lambda_0/2$ sandwiched by quarter-wave stacks (made from layers of high and low refractive index dielectric material with thickness $\lambda_0/4$), where $\lambda_0$ is the desired central wavelength of the transmitted line. The quarter-wave stacks reflect light in the vicinity of the line so that the background transmission in clean, while the Fabry-Periot cavities are designed so that the wavelength of interest resonates in the cavity and high transmission is achieved for a very narrow wavelength range. Such transmission efficiency is usually limited to rays at normal incidence and narrow-band filters are known to exhibit significant shifts in passbands for rays that have angular incidence.

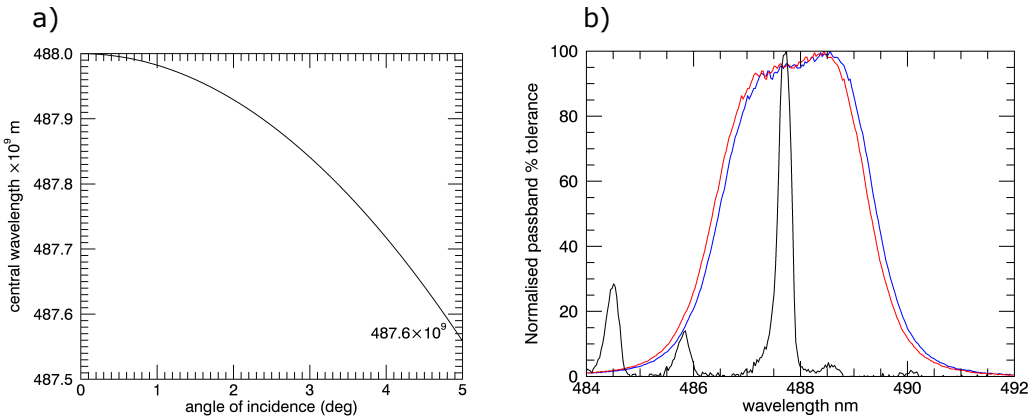


**Figure 5.16:** (a) central wavelength by incident-angle for a 488 nm imaging filter (b) (Black) spectral scene for the high-magnetic field core region for the MAGPIE plasma and (Blue) is the filter passband for normal incidence and (Red) is the filter passband for normal incidence at 2.5° angle of incidence.

The wavelength shift for a passband filter in air is well known and given by [103, 104]

$$\lambda = \lambda_0 \Big(1 - \frac{\sin^2 \alpha}{n_{eff}^2}\Big)^{1/2} \tag{5.12}$$

where $\lambda$ is the expected shift in wavelength for the incident angle $\alpha$. The effective refractive index of the filter, $n_{eff}$, is determined by the material characteristics of the filter which include the individual materials of the quarter-wave stack and that of the refractive index of the Fabry-Periot cavity substrate. For 488 nm imaging filters the effective refractive index has been quoted as $\sim 2.05$ [103, 104].

The angular effects of the imaging filter have been modeled using equation 5.12 along with the quoted values for the 488 nm filter refractive index. As the filter is located in front of the 75 mm camera lens, the transmission will be confined to a small range of viewing angles ($\sim 3.7°$ in the direction aligned with the machine axis and $\sim 2.5°$ in the direction aligned with the radial cross-section). Figure 5.16 (a) shows the expected shift in the central transmission wavelength for a 488 nm filter with incident angle. Figure (b) shows the filter pass-band for normal incidence (blue) and at a transmission angle of 2.5° (red).

These plots show that, for a maximum angle of 2.5°, the filter shifts the pass-band towards the red (lower wavelengths) by only $\sim 0.1$ nm. Considering the results obtained in section 5.2.1, the pass-band shift will enhance the contributions from the 486.5 nm line and reduce the contributions from the 488.9 nm line for views of the plasma-edge.

### 5.2.4 Laser broadening

In this study, the contrast measured at small radii in the high magnetic field region is observed to deliver values above 1.0 (and hence returning apparent negative temperatures). This effect becomes more apparent with increased interferometric delay. 'Negative' temperatures arise in these measurements when the fringe contrast of the calibration image is less than the contrast from the plasma measurement.

In order to investigate the cause of these negative temperatures, plasma measurements (contrast and phase) were made over varying interferometric delay. These measurements were made over 29 different delays, which were varied by manually changing the length of the birefringent crystal cell. Figure 5.17 (a) shows an example of the measured contrast for the calibration, $\zeta_0$ and the plasma, $\zeta = \zeta_0 \zeta_D$ measured over a range of delays. The plasma measurement has been taken at the reference condition, for coordinates $z = 47.8$ cm and $p \sim 0$ cm. Here, both contrast values decrease with instrumental delay due to the deterioration of the instrumental contrast which becomes more apparent with larger instrument size.

Plot (a) shows that for small delays the plasma contrast is less than the calibration contrast ($\zeta < \zeta_0$) and therefore the Doppler contrast, $\zeta_D$, is less than 1 - which is as expected. However, at large delays the contrast values reverse so that the plasma contrast is larger than the instrumental contrast ($\zeta > \zeta_0$) and therefore the Doppler contrast is greater than 1. The Doppler contrast plotted against instrumental delay is shown in (b). This plot

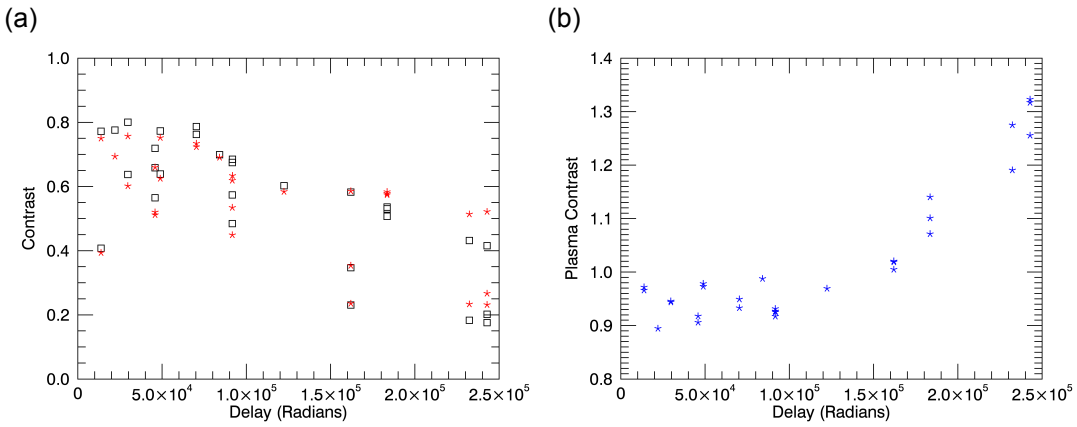


**Figure 5.17:** The (a) raw instrumental contrast for the calibration laser $\zeta_0$ (□) and the inferred plasma contrast $\zeta = \zeta_0\zeta_D$ (⋆), and (b) the measured Doppler contrast $\zeta_D$ against delay.

shows the Doppler contrast $\zeta_D$ increasing above 1 for large delays and the clear trend suggests that this is caused by some real effect rather than natural variability in the measurement.

A possible explanation for this is that the broadening of the calibration laser is greater than the broadening of the plasma spectral line in the core of the plasma. Argon ion lasers are typically generated from the positive column region of a high density discharge. There are 13 visible wavelengths from transitions emitted by the excited states of $Ar^+$, the strongest lines emitting at 488 nm and 514 nm. The typical parameters for an argon ion laser have been summarised from literature [84, 105–107] and presented in the table 5.2. Argon gas lasers with effective parallel ion temperatures of up to 6000 K have also been reported [108].

| Laser property | |
|---|---|
| Input voltage | 240 V-DC, 16 A |
| Tube diameter | typically $\sim 3$ mm (range: $1-10$) mm |
| Output power | laser used:160 mW (typical range $1-10$ W) |
| Gas pressure | $0.1-1$ Torr |
| Electron temperature | $2-4$ eV |
| Ion temperature (Doppler width) | $2000-3000$ Kelvin |
| Axial magnetic field | $0.1-1$ Tesla ($100-1000$ Gauss) |
| typical cavity lengths | $10-180$ cm |
| typical coherence lengths | $3-6$ cm |

**Table 5.2**: Typical parameters for argon gas lasers. [84, 105–107]

Lasers operate by reflecting standing waves at resonant frequencies within an optical cavity. On repeat reflections the light is amplified and then finally, with enough gain, the light is liberated through one of the cavity mirrors forming a directed beam. Just like standard plasmas, gas laser lines can undergo broadening due to thermal movement of the ions. Unlike standard discharges, laser amplification means only selective ion velocities will contribute to Doppler broadening, namely, thermal velocity shifts which accelerate or decelerate the ions within the resonance of the cavity. Doppler broadening in lasers is therefore called an inhomogeneous broadening mechanism. The discrete frequencies at

which the Doppler broadening is observed are resonant and given as

$$\nu = \frac{cn}{2L} + \nu_0 \qquad \text{where} \qquad n = \pm 1, 2, 3...N \tag{5.13}$$

and $\Delta\nu = c/2L$ is the frequency difference between the shifted frequencies, $\nu_0$ is the central frequency, and $L$ is the length of the optical cavity. Small cavities $\Delta\nu$ will support less discrete Doppler frequencies compared to larger cavities. In the case where there are only two resonances, the contrast will be modulated due to the interference between the modes. For larger cavities there will be multiple Doppler resonances supported and these will sit within the laser gain envelope. An example laser lineshape for this case is shown in figure 5.18 where multiple Doppler resonances are supported.

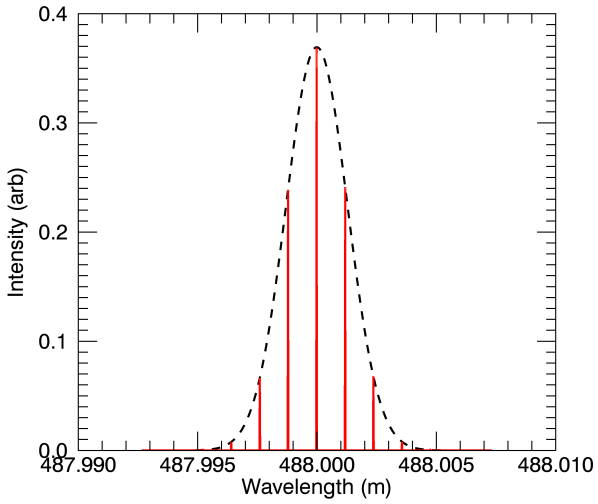


**Figure 5.18:** Model spectral lineshape of a laser assuming an ion temperature of 3000 K and 10 cm cavity length. The laser gain envelope is indicated by the grey dashed line.

Considering broadening of the laser line, the measured plasma contrast is $\zeta_0\zeta_D$ and the measured calibration contrast is $\zeta_0\zeta_L$ where $\zeta_L$ is the contrast contribution from the laser. If the plasma ion temperatures are assumed to be cold in the core ($\zeta_D = 1.0$) then the exponential growth observed in the contrast in figure 5.17 (b) can be attributed to laser broadening only. The data plotted in 5.17 (b) is effectively $1/\zeta_L$ where $\zeta_L = \exp(-T_L/T_C)$, assuming multiple Doppler modes are supported and therefore the gain envelope is Gaussian ($T_L$ is the temperature of the laser). The coherence length (where $\zeta_L = 1/e$) is therefore $\hat{\phi}_0 \sim 535,000$ rads (or $85,000$ waves).

As the characteristic temperature of the instrument is known from equation 2.20 the temperature of the laser can be calculated using

$$T_L = \frac{2m_s}{k_B}\left(\frac{c}{\hat{\phi}_0}\right)^2 \tag{5.14}$$

which gives a laser temperature of $\sim 3000$ K which is in the range reported by literature

[84, 105].

## 5.3 Features of the distribution function

It is clear that without proper characterisation of the laser lineshape information about the velocity distribution function from the contrast measurements is very uncertain. However, the correction does not affect the phase and hence insight regarding the velocity distribution function can still be obtained by looking for a non-linear dependence on delay in the phase measurements. The contrast measurements are still useful as the variability in the contrast due to contamination effects can indicate the magnitude of the modulations expected in the phase. For this study all measurements were made at the reference plasma condition.

Firstly, the IVDF in the azimuthal direction is considered. The phase was measured over a range of impact parameters ($p = 0$ cm, 1 cm, 2 cm and 2.5 cm) in the high magnetic field region ($z = 47.8$ cm) and was tracked over interferometric delay. The central columns of the phase measurement, where the line-of-sight is near vertical, was considered so that the measurement was only sensitive to the asymmetric phase component corresponding to the effects of the rotational flows. The phase measured at each position has been averaged over a $40 \times 40$ pixel area and these points are plotted in figure 5.19. A linear fit of $\phi_D$ verses $\phi_0$ has been applied to the measurements taken at each impact parameter.

There is a clear linear dependence with the delay suggesting that in the case of the azimuthal component of the IVDF is Maxwellian. The variability in the results is consistent with what was predicted in the case of a $< 2\%$ secondary line contamination (see section 5.2.1). The contour plot shown in figure 5.19 shows that the measured phase with delay is linear for all radii including the flow shear region ($r > 2$ cm).

The challenge is now to determine if the IVDF in the axial direction is also Maxwellian. The axial flows will be obscured by the uncertainty in the laser phase. A linear ramp in axial angle must be fitted to each phase image in order to extract the axial flow (see discussion around equation 5.1). Only measurements where there is a clear ramp in the phase have been considered. The phase was considered along the image axis of symmetry ($z$ axis) so that the measurement was only sensitive to the symmetric component of the phase (corresponding to the axial flows). This measurement is shown in figure 5.20 for positions (a) $z = 52$ cm and (b) 32 cm which correspond to the locations either side of the observed axial flow reversal. The red lines here have been added as a reference only so that the images may be compared easily. Figure 5.20 (c) shows a contour plot for the symmetric component of the phase (corrected for $\sin\chi$ viewing angle) for all axial positions.

The variability in these measurements is larger than what was found in the symmetric component. It is unclear why the variability is so high in these measurements however this may simply just reflect large variability in the axial flows which is also suggested by the larger error bars in figure 5.8. Unfortunately the variability in these measurements is too high to draw conclusions regarding whether the phase has a linear dependence with delay.

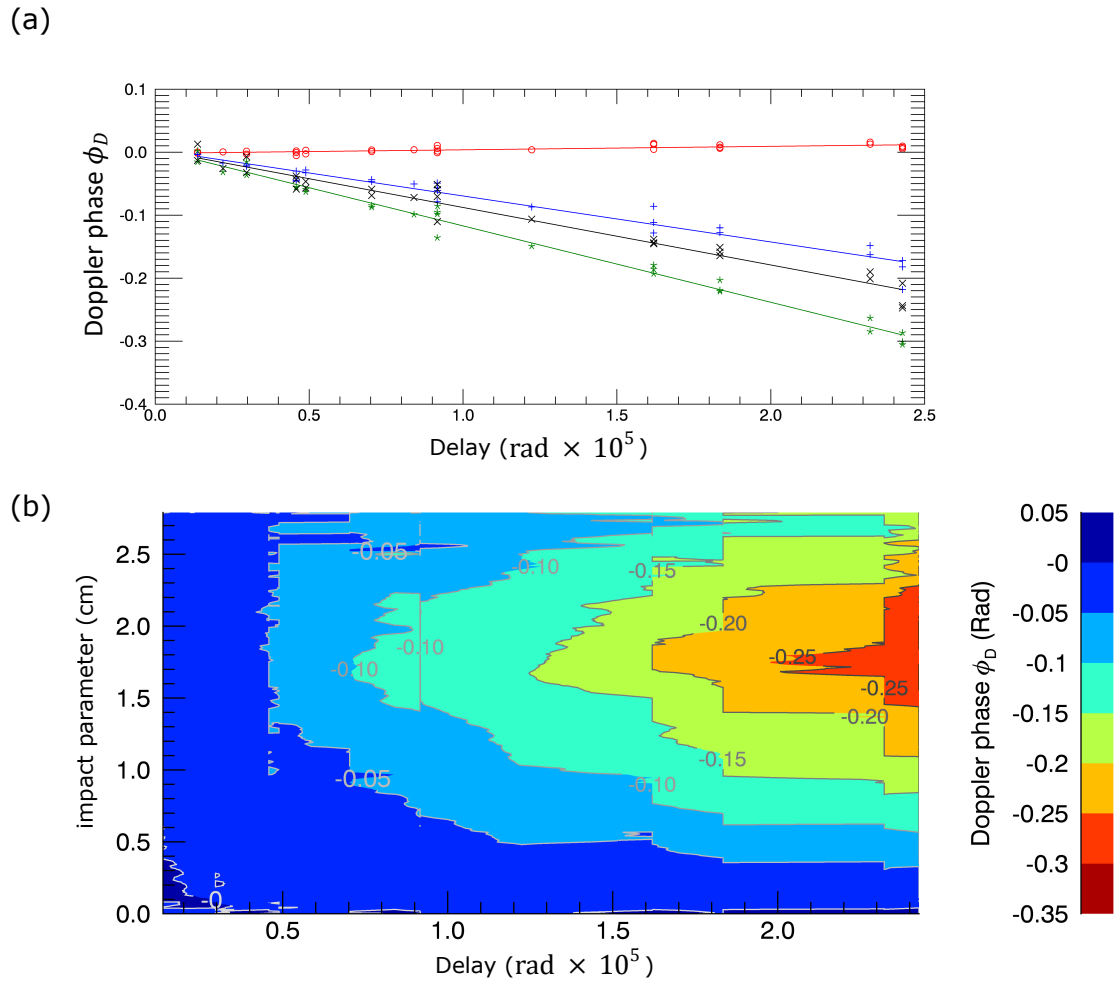


**Figure 5.19:** The measured Doppler phase (asymmetric component only) at (a) $p = 0$ cm (○), 1 cm (+), 2 cm (⋆) and 2.5 cm (×) taken at axial position, $z = 47.8$ cm. The solid lines are linear fits made at each position. Figure (b) shows a contour plot of the Doppler phase over each impact parameter at $z = 47.8$ cm.

Nevertheless, there are trends within each measurement that supports the insights drawn from single delay results (figure 5.8). The positive phase increase with delay at 52 cm and the negative decrease in phase with delay at 32 cm are suggestive of an axial flow reversal around 48 cm. The contour plot in figure 5.8 (c) shows that the delay measurements change smoothly with axial coordinate and delay.

These measurements illustrate that with a monochromatic and known calibration source and in the absence of spectral contamination it is be possible to determine if the phase and contrast exhibit the expected spectral characteristics associated with a non-Maxwellian velocity distribution function. Under such conditions it is possible to tomographically reconstruct the 3D velocity distribution function.

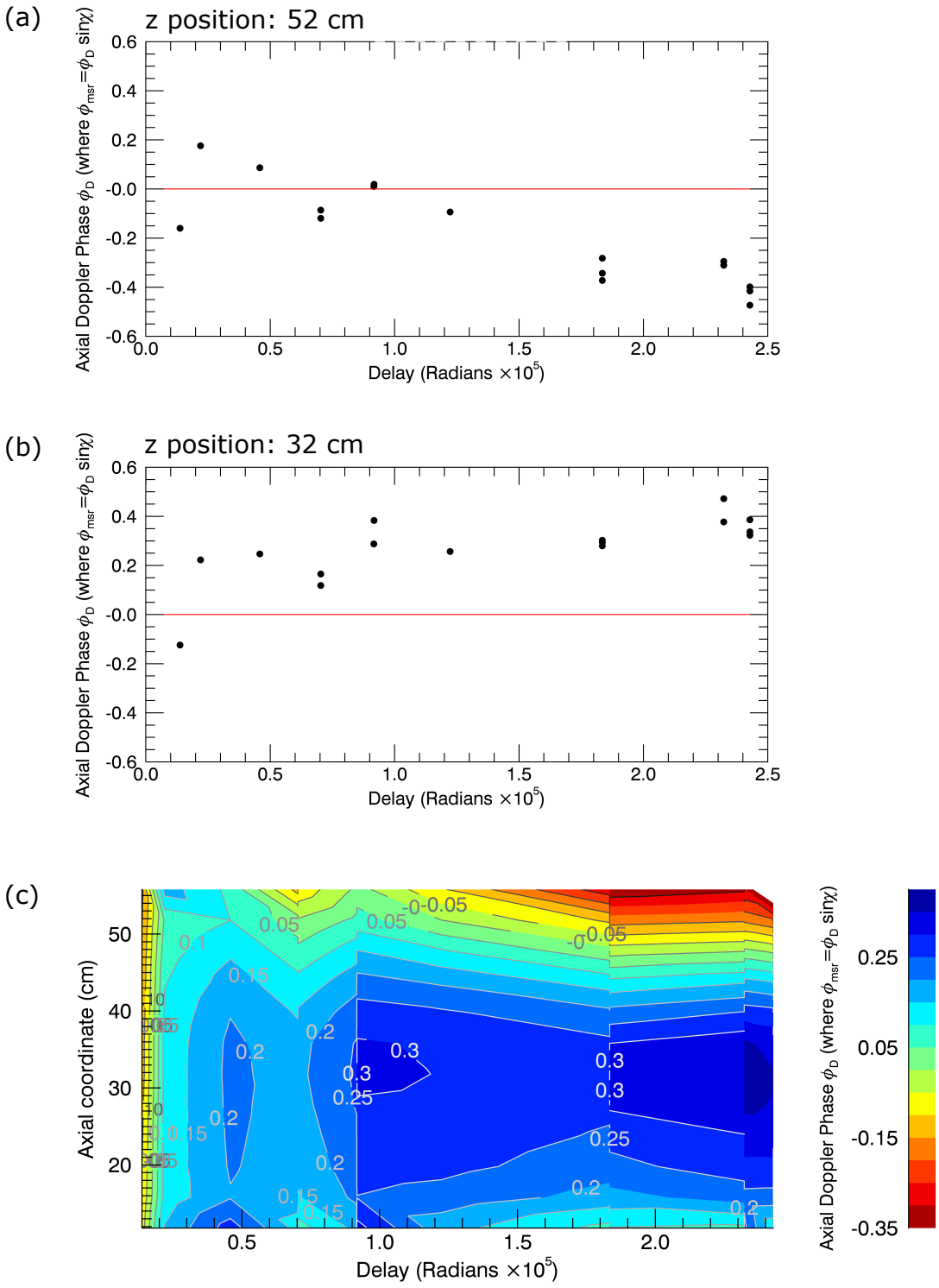


**Figure 5.20:** Symmetric phase component (corrected for $\sin\chi$ viewing angle) measured over delay for axial positions (a) 52 cm and (b) 32 cm. The red reference lines are used to aid comparison of data. Figure (c) shows a contour plot of the symmetric component of the phase (corrected for $\sin\chi$ viewing angle) over axial coordinate and delay.

Chapter 6

# Tomography of plasmas

2D coherence imaging measurements represent planar-integration of the distribution function in velocity space which is then integrated along the line of sight. The interpretation so far has assumed that the ion velocity distribution function is Maxwellian and the line-integration effects are ignored. We consider here the central row of the coherence imaging measurement and apply tomographic reconstruction techniques to determine the radial profiles for the local emissivity, ion temperature and flow. The reconstructions are then compared to the line integrated approximations, which were found by applying equations 4.25, 4.27 and 4.28 to the projected brightness, contrast and phase. The comparison between the reconstructed quantities and the approximations is used to identify the extent of the line-integration effects.

## 6.1 Tomography and the Radon transform

Tomographic reconstruction is an imaging technique used to reconstruct the internal structure of an object when only line- or planar-integrated features of the object can be measured. Tomographic reconstruction techniques have been used in conjunction with interferometric measurements to find the 3D spatial distributions of the electron density [109,110]. The 3D refractive index fields have also been reconstructed from holographic interferometry [111]. Tomographic reconstruction been applied to camera images on the TORPEX plasma to find the 3D spatial distribution of the plasma emissivity [112], Doppler coherence imaging measurements taken on the DIII-D Tokamak of the doubly ionised carbon emission (465 nm) have been inverted to yield radial distributions of the parallel ion flow and emissivity [52] and reconstruction of X-ray measurements have aided studies of sawtooth oscillations on the TFTR Tokomak [113]. These forms of measurements use tomography to construct a 3D spatial distribution from line-integrated measurements.

Laser Induced Fluorescence (LIF) is a technique commonly employed in plasma studies to measure features of the velocity distribution function such as bulk ion or neutral temperatures, flows and densities. In this technique a narrow-band laser is used to excite the plasma species over a small range of wavelengths. For a thermally broadened distribution the ions and atoms will be excited when the laser frequency matches the excitation energy at their respective rest-frames. The emission intensity is measured over the fre-

quency scan to indicate the population of excited particles. Standard LIF measurements target a local position in the plasma and therefore do not require spatial tomography, however, tomography over velocity-space is required to determine the 3D velocity distribution function [31].

The Radon transform, first used by Johann Radon in 1917, is a mathematical way of relating a function to its projection along a line. His work was further extended to the 3D transform where the projection is determined from the integral over a series of planes. Both types of Radon transform are relevant in this work and have already been encountered in chapter 2.1 sections 2.1.6 and 2.1.7.

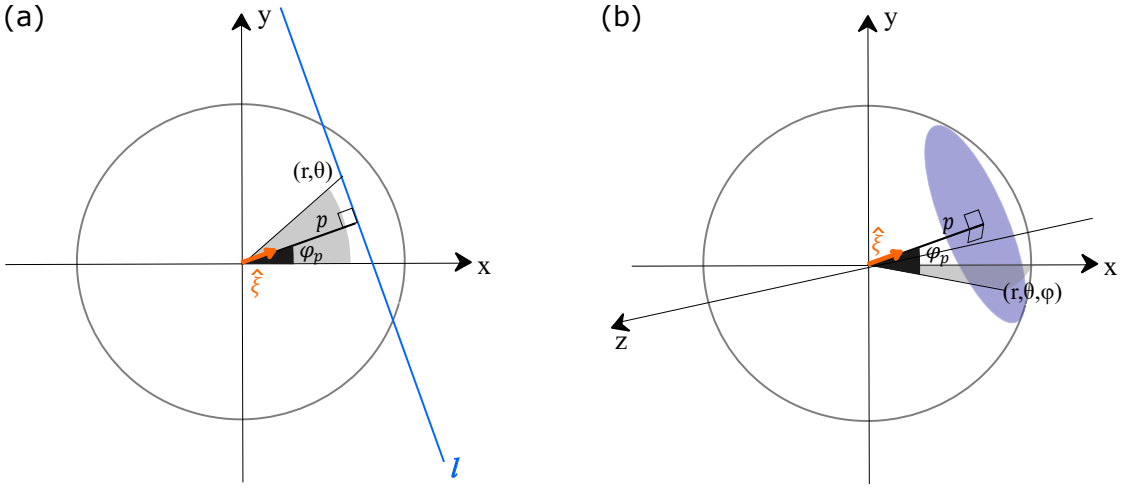


**Figure 6.1:** Geometry showing (a) the 2D Radon transform where the function is integrated along the line-of-sight, $\boldsymbol{l}$ to give the projection and (b) the 3D Radon transform where the function is integrated over the 2D plane.

A 2D function $\mathrm{f}(\boldsymbol{x})$ viewed along a line $\boldsymbol{l}$, where $\boldsymbol{x} = (x, y)$, is related to the 1D projection $\check{\mathrm{f}}(p, \varphi_p)$ through,

$$\begin{aligned}
\check{\mathrm{f}}(p, \varphi_p) &= \int_{\mathrm{L}} \mathrm{f}(x, y)\ dl \\
&= \iint_{\mathbb{R}^2} \mathrm{f}(x, y)\ \delta(p - \boldsymbol{\xi} \cdot \boldsymbol{x})\ d\boldsymbol{x} \\
&= \iint_{\mathbb{R}^2} \mathrm{f}(x, y)\ \delta(p - x\cos\varphi_p - y\sin\ \varphi_p)\ dx\ dy
\end{aligned} \tag{6.1}$$

where $p$ and $\varphi_p$ are the impact parameter and impact angle, respectively, and $\boldsymbol{\xi} = (\cos\varphi_p, \sin\varphi_p)$ is a unit vector describing the direction of the impact parameter such that $p = \boldsymbol{\xi} \cdot \boldsymbol{x}$. The function $\mathrm{f}(x, y)$ is integrated along the line of sight and the geometry is shown in figure 6.1(a).

A 3D function $\mathrm{f}(\boldsymbol{x})$, where now $\boldsymbol{x} = (x, y, z)$, is viewed along the line $\boldsymbol{l}$ and related to its 1D projection through

$$\begin{aligned}\check{\mathrm{f}}(p,\xi) &= \int_{\mathrm{L}} \mathrm{f}(\boldsymbol{x})\ dl \\ &= \iiint_{\mathbb{R}^3} \mathrm{f}(\boldsymbol{x})\ \delta(p-\boldsymbol{\xi}\cdot\boldsymbol{x})\ d\boldsymbol{x}\end{aligned} \tag{6.2}$$

Where $\boldsymbol{\xi} = (\xi_1, \xi_2, \xi_3)$ is the unit vector which describes the direction of $p$. In this case the 3D function is integrated over a plane normal to the line-of-sight $\boldsymbol{l}$ (See geometry given in 6.1(b)). Both figures (a) and (b) can be compared back to the case of the line-integral (figure 2.11) and the velocity space integral (figure 2.9), respectively, described in chapter 2.1.

Equations 6.1 and 6.2 can also be written as

$$\check{\mathrm{f}} = \mathcal{R}\ \mathrm{f} \tag{6.3}$$

where $\mathcal{R}$ indicates the 2D or 3D Radon transform. Equation 6.3 implies that by finding the inversion of $\mathcal{R}$ the projected image can be used to reconstruct the 2D or 3D function.

## 6.2 Tomography techniques for reconstruction of the local plasma

While the Radon transform is analytically invertible, approximate inversion methods are required in the case of a finite number of measurements. Real-world applications include Magnetic Resonance Imaging (MRI) or Computed Tomography scan (CT scan) which are medical imaging tools to examine internal anatomy. Another application can be found in seismology where the tomography of the seismic waves of earthquakes or explosions can be used to determine the various composition of layers in the Earth.

Various reconstruction methods exist to handle discrete inversion problems. One such method for the reconstruction of 2D images is filtered-back-projection (FBP) where high-pass filtered projections, obtained for a large number of viewing angles, are 'smeared' over the reconstruction area and added together to reveal the underlying reconstructed image. Other reconstruction methods take large numbers of projections across many viewing angles and iterate a backprojection algorithm until a stable solution is found. [114].

The circular symmetry of the MAGPIE plasma means that only a single projection is required to reconstruct scalar fields. For this study, the central row of the measured brightness, contrast and phase projections can be tomographically inverted to find the local radial profiles of the emissivity, temperature and flow. In this work the Radon transform was inverted using a pixel-method, where the plasma region is modeled as a series of radial shells which are related to the projection using a discrete linear transformation.

Tomographic inversion techniques are highly sensitive to noise. For this reason, a second

reconstruction method based on the expansion of orthogonal polynomials [114,115], which are analytically linked through the Radon transform, was developed to compare to the pixel based results.

### 6.2.1 Tomography of the 2D Radon transform using the pixel-method

A central column of pixels, normal to the machine axis spanning the impact parameter, are selected for reconstruction. The viewing chords from each of these pixels pass through a circular cross section of the plasma which is the region for reconstruction (see figure 2.11). The cylindrical symmetry of MAGPIE eliminates any dependence on the impact angle, allowing the projection, $\check{\mathrm{f}}(p)$, to be written in terms of only the impact parameter, $p$. In the discrete case, a finite number $M$ of samples of the projection $\check{\mathrm{F}}(i)$ are available. Here, $i$ is an index denoting the ith impact parameter, $p_i$.

The plasma may be modeled as a set of $N$ discrete radial shells identified by index $j$ and the unknown source function, written as $\mathrm{F}(j)$ for discrete radii $r_j$. The function $\mathrm{F}(j)$ is related to the projection $\check{\mathrm{F}}(i)$ through a sum with the weight function $W(i,j)$

$$\check{\mathrm{F}}(i) = \sum_{r=1}^{N} W(i,j)\ \mathrm{F}(j) \tag{6.4}$$

or in matrix notation,

$$\check{\mathbf{F}} = \boldsymbol{W}\mathbf{F} \tag{6.5}$$

where $\boldsymbol{W}$ is an $M \times N$ weight matrix. The values of the weight matrix can be determined in various ways, for example, the length of the viewing segment for the line $\hat{\boldsymbol{l}}_i$ which passes through each $r_j$ shell can be used as the value for $W(i,j)$. In the absence of smoothness or other a priori constraints, the number of projections must be significantly higher than the number of radial shells ($N >> M$) so that the problem is over-determined.

To obtain the reconstruction it is necessary to invert the response matrix. As the response matrix is not square, a reconstruction can be obtained using by finding a pseudoinverse obtained using single value decomposition (SVD). This decomposes the $M \times N$ response matrix into three sub matrices

$$\boldsymbol{W} = \boldsymbol{U_M}\ \boldsymbol{\Sigma}\ \boldsymbol{U_N}^T \tag{6.6}$$

where $\boldsymbol{U_M}$ is a unitary matrix of dimension $M \times M$ containing the eigenvectors of $\boldsymbol{W}\boldsymbol{W}^T$ and $\boldsymbol{U_N}$ is an $N \times N$ unitary matrix constructed from the eigenvectors of $\boldsymbol{W}^T\boldsymbol{W}$. The subscript $T$ denotes the transpose. The matrix $\boldsymbol{\Sigma}$ is a rectangular diagonal ($M \times N$) matrix where diagonal entries are the singular values of $\boldsymbol{W}$ (square-root of the non-zero

and non-negative eigenvalues of $\boldsymbol{U_M}$ and $\boldsymbol{U_N}$).

The pseudoinverse of the response matrix is given by

$$\boldsymbol{W}^{-1} = \boldsymbol{U_N}\ \boldsymbol{\Sigma}^{-1}\ \boldsymbol{U_M}^T \tag{6.7}$$

The reconstruction is found by matrix multiplication of the pseudoinverse with the projection

$$\mathbf{F} = (\boldsymbol{U_N}\boldsymbol{\Sigma}^{-1}\ \boldsymbol{U_M}^T)\check{\boldsymbol{F}} \tag{6.8}$$

A regularisation can be applied by selecting a minimum threshold on the singular values in $\boldsymbol{\Sigma}$. This effectively reduces the rank of the reconstruction in order to suppress noise produced by small singular values. The rank of the reconstruction is given by the number of radial shells and so alternatively noise can be suppressed by reducing $N$. This therefore sets some limits on the number of radial shells used in the model. $N$ must not be chosen so small that spatial features of the reconstructions are lost, but not so big that the reconstructions become noisy.

In this model the radial shells are chosen so that each shell spans a $\approx 1$ mm radial width, $N = 29$, where the plasma radius is taken to be 2.9 cm. For this choice of $N$ a minimum threshold on the singular values is not applied. The weight matrix $\boldsymbol{W}$ is calculated by modeling 5000 evenly spaced points along each viewing line and counting the number of points which fall within each radial shell. The geometry of the model is shown in figure 6.2, showing the trajectory of every 40th viewing line (black) and the boundary of each radial shell (red). The position of the viewing lines includes an offset that accounts for a misalignment between the camera and the plasma axis which was determined from the center of mass of the brightness projection.

This model assumes that each line-of-sight is infinitely thin with no overlap from the adjacent pixels. In actuality, each line will collect light from the plasma contained within a narrow viewing cone and there will be some contribution from adjacent pixels however it is anticipated that this effect will be small and will not significantly change the reconstruction.

A central slice, $20 \times 1040$ pixels, was selected from each of the projected measurements. This slice spanned the full range of impact parameters and 10 pixels either side of the central point in the axial direction. The slice was averaged over all 20 columns in axial direction to give the single row of pixels as a projection for the inversion. The projection was re-binned to only half the number of pixels in the direction of the impact parameter to reduce noise while reserving 520 pixels, as independent lines-of-sight through the plasma.

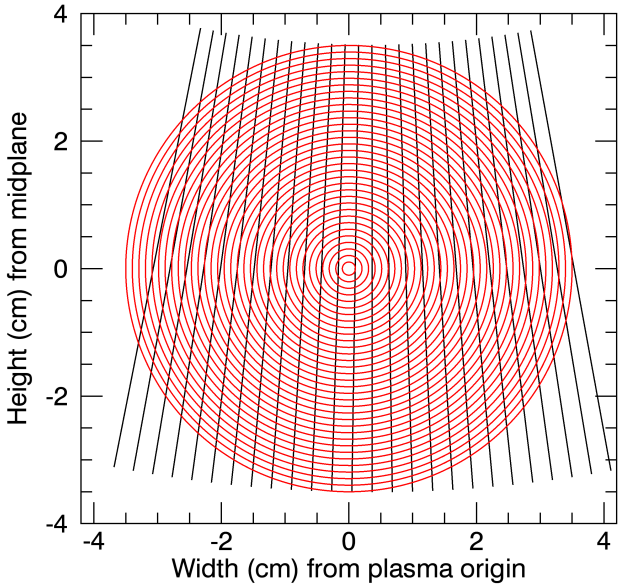


**Figure 6.2:** Model of optical view through plasma for the pixel method. The view (along each camera pixel) is shown by the black lines, and the radial pixels spanning the plasma region are shown by the red circles.

### 6.2.2 Tomography of the 2D Radon transform using expansion of orthogonal functions

A second way of approaching the reconstruction problem is to approximate the projection in terms of orthogonal functions. There are orthogonal function pairs which represent analytic solutions to the Radon transform. One such combination is the Chebyshev polynomials of the second kind which analytically transform under the inverse Radon transform into the orthogonal Zernike polynomials. The Hermite-Laguerre transformation pair is another example [114].

The Zernike-Chebyshev transformation pair is a natural choice for the reconstruction of the circular plasma in MAGPIE. The key equations governing this transformation are given below and further details can be found in the works of [114, 115].

A two dimensional function $\mathrm{f}(x, y)$ defined on the unit circle can be represented by an infinite set of harmonic polynomials, $R^{\ell}_{|\ell|+2s}(r)\ e^{i\ell\theta}$, using the expansion

$$\mathrm{f}(x, y) = \mathrm{f}(r\cos\theta, r\sin\theta) = \sum_{s=0}^{\infty}\sum_{\ell=-\infty}^{\infty} A_{\ell,s}\ R^{\ell}_{|\ell|+2s}(r)\ e^{i\ell\theta} \tag{6.9}$$

Where $(r, \theta)$ are polar coordinates and $Z^{\ell}_{|\ell|+2s}(r, \theta) = R^{\ell}_{|\ell|+2s}(r)\ e^{i\ell\theta}$ are the Zernike polynomials defined on the unit circle ($0 \leq r \leq 1$). These functions are dependent on the

radial order $n$ and azimuthal frequency $\ell$ where the substitution $n = |\ell| + 2s$, is often made and $s$ takes the values $\{0, 1, 2, 3 \ldots\}$ [115].

The radial polynomial is given by

$$R^{|\ell|}_{|\ell|+2s}(r) = \sum_{k=0}^{s} (-1)^k \frac{(|\ell| + 2s - k)!}{k!\big[|\ell| + s - k\big]!\big[(s-k)\big]!} r^{|\ell|+2s-2k} \tag{6.10}$$

The expansion coefficients $A_{\ell,s}$ can be calculated using the well known orthogonality relation [114, 115].

The Radon transform of the Zernike polynomials gives rise to the Chebyshev polynomials of the second kind [114]

$$R^{|\ell|}_{|\ell|+2s}(r) \exp \pm i\ell\theta \xrightarrow{\mathcal{R}} \frac{1}{|\ell| + 2s + 1} \sqrt{1 - p^2}\; U_{|\ell|+2s}(p) \exp \pm i\ell\psi \tag{6.11}$$

where, $U_{|\ell|+2s}(p)$, defined along the unit line ($-1 \leq p \leq 1$) are given by

$$U_{|\ell|+2s}(p) = \frac{(p + \sqrt{(p^2-1)})^{|\ell|+2s+1} - (p - \sqrt{p^2-1})^{|\ell|+2s+1}}{2\sqrt{p^2-1}} \tag{6.12}$$

and the angle $\psi$ is the viewing angle.

In the case of the MAGPIE geometry, azimuthal symmetry eliminates the dependence on the azimuthal index ($\ell = 0$) and the coefficients $A_{0,s}$ are found by forming the inner product

$$A_{0,s} = \frac{(2s+1)}{\pi} \int_{-1}^{1} \check{\mathrm{f}}(p)\; U_{2s}(p)\; dp \tag{6.13}$$

so that

$$\mathrm{f}(r) = \sum_{s=0}^{\infty} A_{0,s}\; R^{0}_{2s}(r) \tag{6.14}$$

For this analysis, $\check{\mathrm{f}}(p)$ is the same as the central projection used for the pixel method described in the previous section. The same averaging has also been applied to reduce noise. Once again it is important to keep as many pixels as possible so that high frequency features of the Chebyshev polynomials are captured. The degrees of freedom in this analysis are set by the polynomial degree $s$. We note here, that the Zernike-Chebyshev transformation across the inverse Radon transform only exists for even orders, and so for $s$ polynomial expansion terms, the highest polynomial degree will be $2s$. Ideally the number of Chebyshev polynomials should be comparable to the number of radial zones used in the

pixel method. For this reason the degrees of freedom was set to 20 polynomial expansion terms. As the degrees of freedom for the orthogonal expansion method does not rely on the number of radial coordinates, it is possible to sample the Zernike polynomials over a large number of radial coordinates. The number of radial coordinates chosen here was 40.

## 6.3 2D vector tomography of the azimuthal flows

The above inversion methods are suited to handling scalar fields however reconstruction of the vector flow field is more challenging as the flows have both a direction and magnitude. Given that the interferometric phase measurement is sensitive to the parallel velocity component, and assuming the emission intensity is constant along streamlines, it is possible under the right conditions to reconstruct the solenoidal component of the velocity field. Here we discuss three possible methods for extracting the azimuthal flow component from the phase projection.

### 6.3.1 Flow reconstruction using the vorticity and potential

The component of the plasma flow directed along the viewing chord $\hat{\boldsymbol{l}}$ is related to the measured phase (assuming a Maxwellian velocity distribution function) through the line integral

$$\phi_D \frac{I_0 \zeta}{\phi_0} = \int_{\mathrm{L}} \epsilon(r) \exp\left(-T_S(r)/T_C\right) \boldsymbol{v_D}(r) \cdot \hat{\boldsymbol{l}}\, dl \tag{6.15}$$

We assume the flows are azimuthal so $\boldsymbol{v_D}$ is only a function of the coordinate $r$. The axial flows are invisible for views normal to the plasma axis. The measured projected quantity is denoted here as $\check{\mathrm{f}}(p) = (\phi_D I_0 \zeta)/\phi_0$ where $p$ is the impact parameter. Tomographic reconstruction of a vector field has been examined in [116] where it has been shown that for 2D flows it is possible to reconstruct the $z$ component of the vorticity

$$\boldsymbol{\Omega} = \boldsymbol{\nabla} \times \mathbf{v} \tag{6.16}$$

where $\mathbf{v} = \epsilon(r)\boldsymbol{v}_D(r)$ and the contrast is assumed to be unity. Using Stokes theorem it can be shown that [116]

$$\frac{\partial \check{\mathrm{f}}(p)}{\partial p} = -\int_{\mathrm{L}_1}^{\mathrm{L}_2} \Omega_z\, dl \tag{6.17}$$

This result says that by taking the derivative of the projection a reconstruction of the vorticity component $\Omega_z$ can be obtained using standard reconstruction techniques. Integration of the vorticity then yields the azimuthal component of the flow field

$$\Omega_z = \frac{1}{r}\left(\frac{\partial(r\mathrm{v})}{\partial r}\right) \tag{6.18}$$

With the same assumption of a 2D flow field, it is also possible to invert the flows via the vector potential [116, 117]. A smooth rapidly-decaying flow field $\mathbf{v}$ can be written as a sum of a solenoidal component and an irrotational component, according to the Helmholtz theorem 6.19.

$$\mathbf{v} = \nabla\Phi + \boldsymbol{\nabla} \times \boldsymbol{A} \tag{6.19}$$

Where $\boldsymbol{A}$ is the vector potential for the solenoidal component of the flow and $\Phi$ is the scalar potential for the irrotational component. The vector potential is related to the vorticity through

$$\Omega_z = -(\nabla^2 \boldsymbol{A})_z \tag{6.20}$$

allowing the projection to be expressed as [116]

$$\check{\mathrm{f}}(p) = -\frac{\partial}{\partial p}\int_{\mathrm{L}_1}^{\mathrm{L}_2} A_z(x,y)\ dl \tag{6.21}$$

In this form, the projection can be numerically integrated with respect to the impact parameter and standard inversion techniques can then be used to reconstruct the scalar $A_z$ component of the vector potential. Numerical differentiation of $A_z$ then yields v and hence the azimuthal flow $v_D(r) = \mathrm{v}/\epsilon(r)$.

We note here that inversion using the vector potential performed well at small radii however deteriorated for large radii where low brightness levels caused noise to be amplified through the $\epsilon(r)$ inverse term. This was not apparent in the inversion of the vorticity which performed well for all radial values. The vorticity must be integrated in order to calculate the flows. Integration will smooth out noise and so it is expected that this quantity is less effected by noise amplification from the $\epsilon(r)$ inverse term. For this reason the vorticity was chosen to reconstruct the azimuthal flows.

### 6.3.2 Flow reconstruction using cosine symmetry

The pixel method, as described in section 6.2.1, is suitable for the reconstruction of scalar fields. If however we consider a 2D solenoidal flow field written in terms of the line-of-sight,

$$\boldsymbol{v_D}(r) \cdot \hat{\boldsymbol{l}} = v_D(r)\cos\Theta \tag{6.22}$$

The projected quantity in equation 6.15 can be written as,

$$\phi_D \frac{I_0 \zeta}{\phi_0} = \int_{\mathrm{L}} v_D(r) \cos\Theta \; dl \tag{6.23}$$

Where $\Theta = \psi - \theta$ is the angle between the azimuthal flow component and the line-of-sight (see geometry in 4.28). Here the temperature term is taken as $\exp -T_S(r)/T_C \approx 1$. In this form we see the azimuthal flow component becomes a scalar field, dependent on the radial coordinate only and weighted by the $\cos\Theta$ term. Importantly, we notice that the cosine term is symmetric with angle $\Theta$ for the range $(-\pi/2, \pi/2)$ and so all measured $v_D(r)$ contributions will add along the line-of-sight. It is possible to reconstruct the scalar flow component $v_D(r)$ by building in the $\cos\Theta$ dependency to each $W(i,j)$ weight term.

Here we note that this method requires that the $\cos\Theta$ dependency does not change significantly along the line-of-sight as it passes through a given radial shell. This can be achieved by ensuring the radial shells are narrow.

## 6.4 Noise in the reconstruction

With enough degrees of freedom, the inversion methods described above can provide a perfect reconstruction of the source function. However the addition of noise to the projection can greatly reduce the accuracy of the reconstruction.

There are various types of noise present in the CCD measurements. This includes photon shot noise, detector read noise which arises due to various components in the camera such as analog to digital conversion, and, dark noise which arises due to statistical thermal processes within the silicon structure of the CCD and is related to the device temperature. These forms of noise can often be reduced by averaging over multiple exposures or increasing exposure time. Spatial noise can also be present due to non-uniformity in pixel response. The noise level was estimated from the standard deviation in the signal at each pixel over time. The SNR was then easily calculated using $SNR = \langle S \rangle / \sigma_S$ (where $\langle S \rangle$ is time-averaged interferometric signal) and was found to be 66. We see here that, unlike standard Poisson noise from a emitting source, the noise in the CCD measurement is not proportional to the square-root of the signal $\sigma = \sqrt{S}$ which would, for these measurements, give a SNR of 113. Dark noise here acts to reduce the SNR below what is expected for standard shot noise.

In order to minimise the noise, the raw measurements are firstly averaged over 5 exposures so that the level of temporal noise is reduced. A black shot is also subtracted to account for dark noise and large exposure times are used so that readout noise is relatively low. Averaging over columns of pixels in the axial direction and re-binning the projections in the direction along the impact parameter reduces noise (both spatial and temporal) so that the projected quantities are smooth.

We therefore expect that the largest source of error in the local reconstructed quantities

for these studies will arise from natural departures from circular symmetry. The point of symmetry has been determined from the center of mass (COM) of the brightness projection. However, we note that the difference in the COM between the brightness, contrast and phase projections can have up-to a 10 pixel variation. In order to quantify this, the measured brightness, contrast and phase were reconstructed 10 times each, with each iteration stepping the point of symmetry by one pixel in the vicinity on the brightness COM. The average and standard deviation were then calculated using this set of reconstructions at each radial coordinate. The standard deviation has been used to provide error bars to the reconstructed quantities.

## 6.5 Reconstruction of MAGPIE local emissivity

Inversion of equation 2.23 will yield the local emissivity, $\epsilon(r)$. Measurements of the line-integrated brightness have been presented in chapter 5 and the region near $z = 35.8$ cm was chosen for the reconstruction. The brightness projection used for the reconstruction is shown in figure 6.3 (a).

To account for error in the reconstruction, the inversion is repeated 10 times whilst shifting the centre-of-mass of the projection. The average of these trials is calculated and shown as the solid plots in figure 6.3 (b) where red corresponds to the reconstruction using pixel-methods and blue corresponds to the reconstruction using orthogonal expansion. The error bars are found from the standard deviation in the values obtained across repeat trials. The inversion using orthogonal expansion has been plotted over 40 radial coordinates.

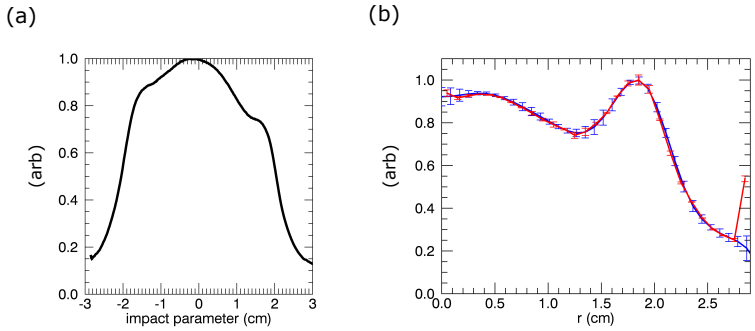


**Figure 6.3:** Figure (a) the projection (black) of the MAGPIE line-integrated brightness. Figure (b) brightness reconstructions via (red) the pixel method and (blue) orthogonal expansion with error bars indicating the standard deviation.

The reconstructions for the local emissivity agree within error for both inversion methods and show a double-peaked profile, where there is a broad peak at the plasma core and a secondary narrow peak of near equal magnitude appearing at the radial edge around 2 cm. This profile is similar to the electron temperature profile presented in figure 5.3.

## 6.6 Reconstruction of MAGPIE local ion temperature

Inversion of equation 2.27 yields the reconstruction of the local ion temperature $T_S(r)$. Here, the projected value comes from the measured contrast in the region centered at $z = 35.8$ cm (see contrast measurements presented in chapter 5). The contrast projection for the tomography is shown in 6.4 (a) and the resulting reconstructions of the radial ion-temperature are shown in figure (b), where the red and blue plots correspond to reconstructions via the pixel method and orthogonal expansion, respectively. As discussed previously (section 6.4), the solid line is the average over 10 independent inversions, where the centre-of-mass has been shifted by one pixel for each trial. The error bars are the standard deviation calculated over these trials.

The black plot in (c) shows the approximate ion-temperature derived in equation 4.27 where line-integration effects have been ignored. Here, we will refer to this as the line-integrated temperature. This is overlaid on the two reconstruction plots from (b) (shown here in grey) for comparison.

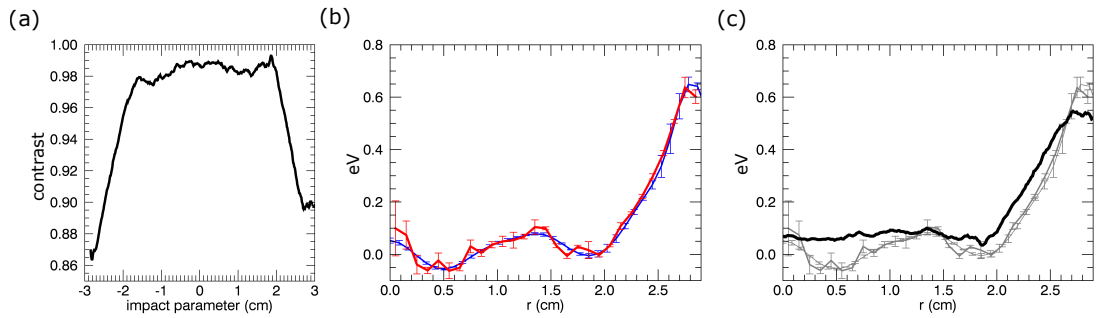


**Figure 6.4:** Figure (a) the projection (black) of the MAGPIE plasma contrast. Figure (b) shows the temperature reconstructions via (red) the pixel method and (blue) orthogonal expansion with error bars indicating the standard deviation. Figure (c) is the temperature derived using the approximation in equation 4.27.

Both reconstructions shown in (b) agree within error across all radii and we note that both reconstructions suggests that there is structure in the plasma core which may be the result of second order contributions from the radial flow. However, as both the temperatures reconstructions in the core fall below zero - this structure is not trustworthy. It would be possible to apply a minimum constraint to the temperature inversion which would remove any negative temperatures from being returned in the reconstruction. This has not been attempted here. The line-integrated temperature follows the same trend as the reconstructions and is of near-equal magnitude. This indicates the line integration effects are small because of the centrally bright intensity weighting of the line integral. It is therefore enough to calculate the ion-temperature using equation 4.27 for the purpose of this study.

## 6.7 Reconstruction of MAGPIE local azimuthal ion flow

Inversion of equation 6.15 yields reconstruction of the local azimuthal flow from the phase projection. The measured phase (presented in chapter 5) in the vicinity of $z = 35.8$ cm is used here as the projected quantity and is shown in figure 6.5 (a). At this position, the camera has a direct vertical view of the plasma so that only the azimuthal component of the flow is detected (not sensitive to $v_z$). Reconstructions via the vorticity are plotted in 6.5 (b) for the pixel method (red) and orthogonal expansion (blue). Reconstruction via the $\cos\Theta$ weight term using the pixel method is also shown by the dark red plot in (b). The error bars indicate the standard deviation over 10 independent inversions (see section 6.4). The black plot in figure (c) is the azimuthal flow calculated using the approximation (equation 4.28) where line-integration effects have been ignored. This quantity will be referred to here as the line-integrated flow. The reconstructions are overlaid in figure (c) (grey) so that they may be compared to the line-integrated azimuthal flow.

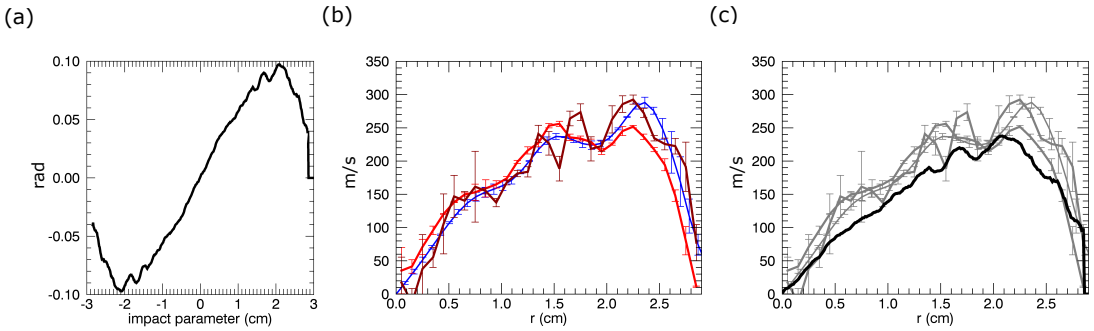


**Figure 6.5:** Figure (a) the projection (black) of the MAGPIE plasma phase. Figure (b) shows the flow reconstructions for (red) the pixel method (via the vorticity), (dark red) the pixel method (via cosine symmetry) and (blue) orthogonal expansion (via the vorticity) with error bars indicating the standard deviation. Figure (c) is the flow derived using the approximation in equation 4.28.

All reconstructions follow the same trend and have the correct magnitude when compared with the line-integrated azimuthal flow. This indicates that line-integration effects are small and the flows can be implied directly from the phase using equation 4.28.

# Coherence imaging of the MAGPIE argon plasma: parameter study

This chapter presents coherence imaging results across a range of magnetic field and gas pressure conditions in MAGPIE. These results are used to demonstrate that coherence imaging can be used for Doppler studies in cold temperature plasmas. Measurements made using a Mach probe are also presented here to validate the coherence imaging flow results. The previous chapter demonstrated that line integration effects are small in the contrast and phase as long as the MAGPIE plasma is centrally bright. We therefore proceed by analysing the brightness, phase and contrast data over parameter space by applying the approximations given in equations 4.25, 4.27 and 4.28.

## 7.1 Magnetic field scan

In this study the brightness, ion-temperature and ion-flow is examined at 3 mT pressure and $\sim 1$ kW forward power for different magnetic field configurations. We have already observed that the brightness, ion temperature and ion flows all show features which compress with the magnetic field (see results presented in 5.1).

The MAGPIE magnetic field can be controlled by changing the current in either the source or mirror coils. For this study both the source and mirror currents were changed. The magnetic field configurations reported in this study are shown in figure 7.1 with the mirror ratio (MR) specified. The mirror ratio has been calculated as the ratio of the highest and lowest magnetic field values in the region highlighted in red - corresponding to the axial region accessible using coherence imaging measurements.

The coherence imaging data was obtained for each configuration by taking an axial scan of the plasma. These scans were not repeated, but were performed using the same exposure times and method as the results shown in section 5.1. We therefore assume the same level of error as found in the reference condition study.

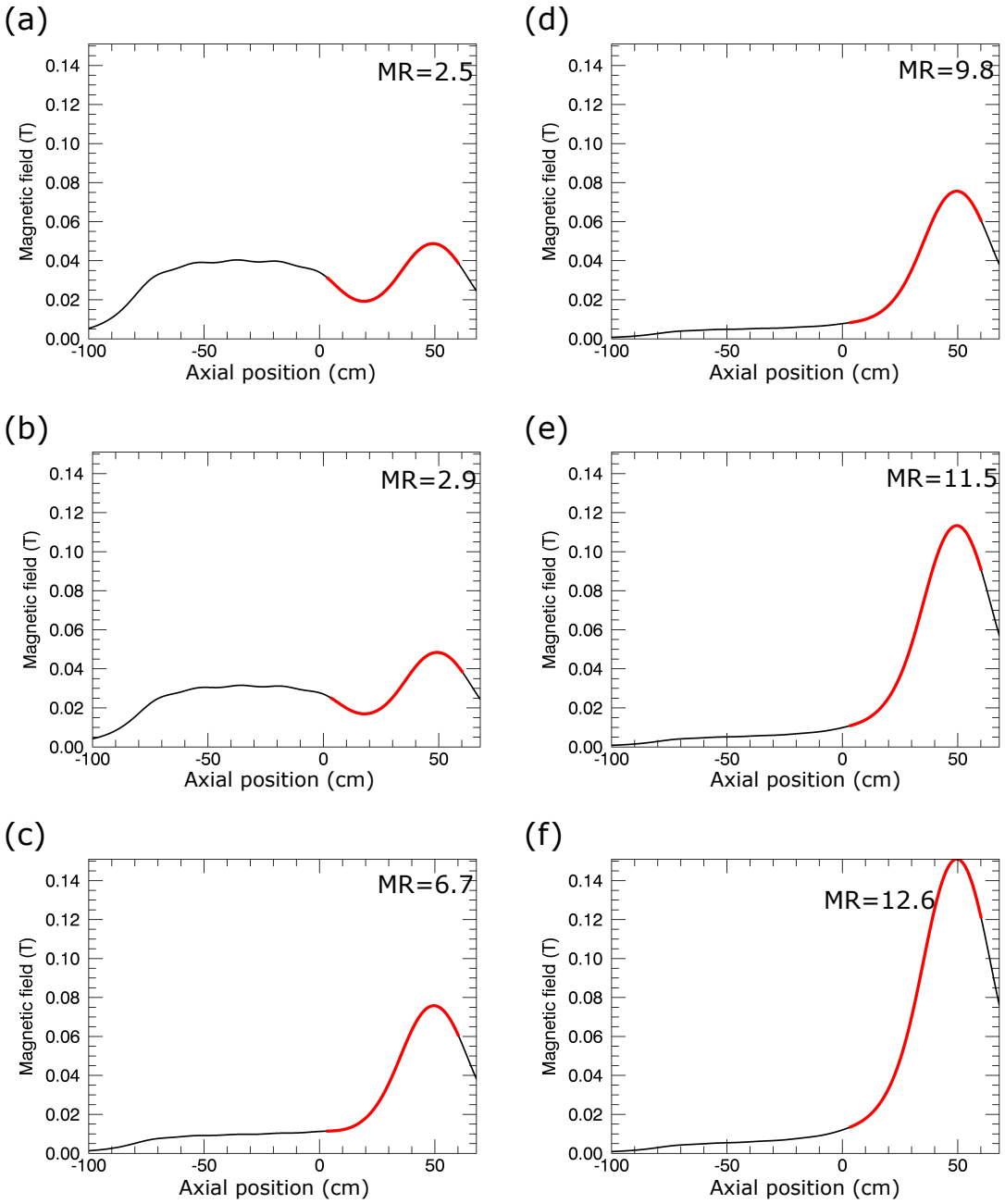


**Figure 7.1:** The axial magnetic field profiles used for magnetic field study. The MR value is the mirror ratio for the given profile. The region highlighted in red shows the axial length visible by the coherence imaging system.

### 7.1.1 Brightness and the magnetic field

The reference condition study has shown that the brightness is strongest in the high magnetic field region (along the central axis of the chamber) and has a double-peaked profile in the radial direction.

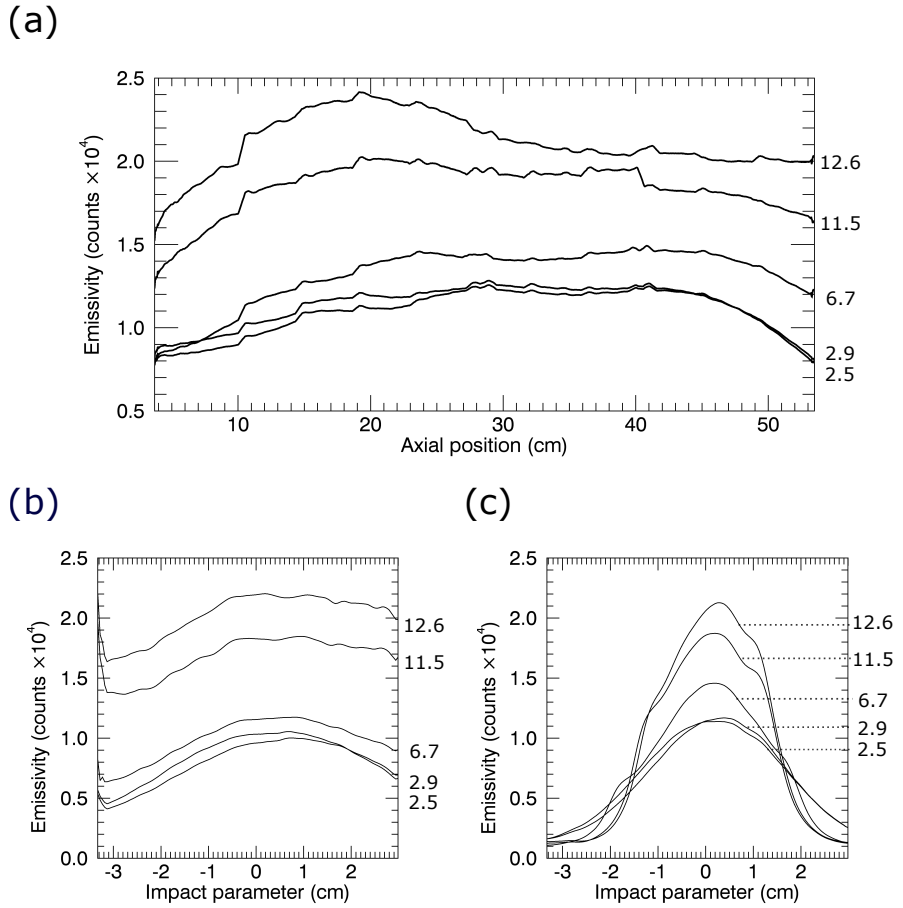


**Figure 7.2:** The brightness profiles plotted for the magnetic field conditions shown in figure 7.1 corresponding to the mirror ratios (MR) 2.5, 2.9, 6.7, 11.5 and 12.6 (annotated). Figure (a) shows the brightness profile along the central machine axis ($\boldsymbol{z}$ axis). Figures (b) and (c) show the radial brightness profiles taken at axial positions 11 cm (near-source region) and 47.8 cm (magnetic pinch region), respectively.

Figure 7.2 (a) shows the emission along the central axis of MAGPIE with axial coordinate $z$. The bumpiness of the profiles is caused by marks on the base plate of the chamber. This data has been smoothed using a rectangular window function with width of 10 pixels ($\sim$ 1 mm). Each of the profiles, shown in the order of increasing peak brightness value, correspond to magnetic field configurations shown in figure 7.1(a), (b), (c), (e) and (f) respectively.

Considering the brightness along the central axis, figure 7.2 (a), the downstream peak in the emission is located in the magnetic pinch for magnetic field configurations with smaller mirror ratios, MR$\leqslant$ 6.7, however this peak appears to shift back towards the antenna for

the configurations with the largest mirror fields.

The radial cross sections of the brightness are shown for the near-antenna and magnetic pinch regions in figure 7.2 (b) and (c) respectively. The profiles near the antenna, figure (b), are broad and the brightness increases with magnetic field. For the magnetic pinch region, the emission profiles follow the compression of the magnetic field lines and the secondary wing-like feature becomes more pronounced with larger mirror ratios ($> 2.9$).

The profiles in 7.2 show that the magnitude of the brightness increases with the strength of the mirror magnetic field. It is expected that the coupling efficiency between the helicon wave and the plasma will increase with magnetic field and also there will be a higher density and electron temperature, both of which will result in a global increase in the ion emission. Similar results for helicon generated plasmas have been reported elsewhere [57, 118].

This study has already identified, from the probe measurements shown in section 5.1, that (in the radial direction) the secondary peaks in the brightness profile are also observed in the electron temperature. It has been shown in the works of Kinder et al. [21] that the electron temperature is expected to peak where the electric field of the RF wave is maximum. In their HPEM-3D model this occurred at around half the radius of the chamber.

### 7.1.2 Ion temperature and the magnetic field

In this study, the ion temperature is examined over the range of magnetic field configurations shown in figure 7.1. Radial plots of the ion temperature in the near-source and the magnetic pinch regions are shown in figure 7.3 (a) and (b) respectively. The red plot indicates the measurement taken at the reference condition. The ion temperature results

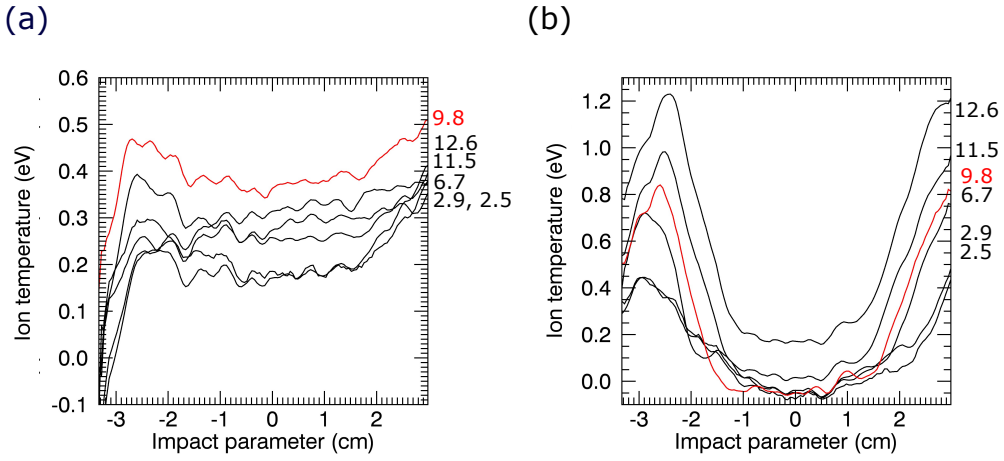


**Figure 7.3:** Ion temperature profiles in (a) the near-source region, $z = 11$ cm and (b) the magnetic pinch region, $z = 47.8$ cm. The mirror ratios for each measurement are annotated and correspond to the magnetic field configurations shown in figure 7.1.

presented for the reference condition (section 5.1.2) showed that there is ion heating near the antenna and the ions are cold in the core of the magnetic pinch region. There is also ion heating at the radial edge of the plasma which is possibly a consequence of a resonance between the Trivelpiece-Gould mode and the lower hybrid frequency. Such edge heating effects have been observed in other helicon devices [29].

The ion temperature near the source, shown in 7.3 (a), is relatively flat and, with the exception of the reference condition (MR 9.8), the ion temperature increases with mirror ratio. An asymmetry is observed in the edge temperatures which is most likely an effect of the antenna. The ion temperature profiles for the magnetic pinch region, shown in 7.3 (b), all exhibit the edge-peaked temperatures. The core temperatures are flat and cold and are mostly insensitive to the change in magnetic field. This data suggests the magnetic field does not have an effect on the ion core temperature, but the edge temperature will increase with stronger magnetic field. The peak values for these edge temperatures are plotted against the magnetic field in figure 7.4. This plot suggests there is a linear dependence between peak ion-temperature and magnetic field.

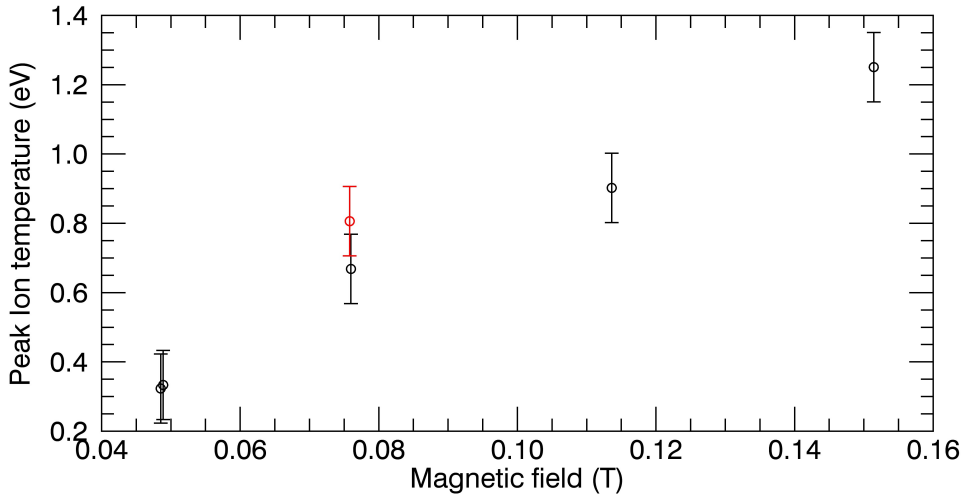


**Figure 7.4:** Plot of the peak ion temperature measured in the magnetic pinch region (at $z = 47.8$ cm) against the magnetic field at that position. The error bars are the same as those given in section 5.1.

A radial edge-peaked ion temperature profile has been observed in HELIX for the perpendicular component. This was also found to scale linearly with magnetic field. For these HELIX measurements, the parallel temperature component was observed to be unaffected by the magnetic field [28].

The axial variation in the ion temperature is now considered on axis and is shown in figure 7.5. These measurements show a smaller set of ion temperature values compared with figure 5.5. For independent images of the temperature a residual 'ramp' feature manifested axially in the measurements. Initially it was thought that this might arise due to non-Maxwellian features in the IVDF (which prompted investigation) however due to the inconsistent appearance of this 'ramp' (taken over the same plasma conditions) it was determined that this feature was instrumental in origin. In figure 5.5 this 'ramp' feature is smoothed out due to the averaging over multiple measurements at the same condition

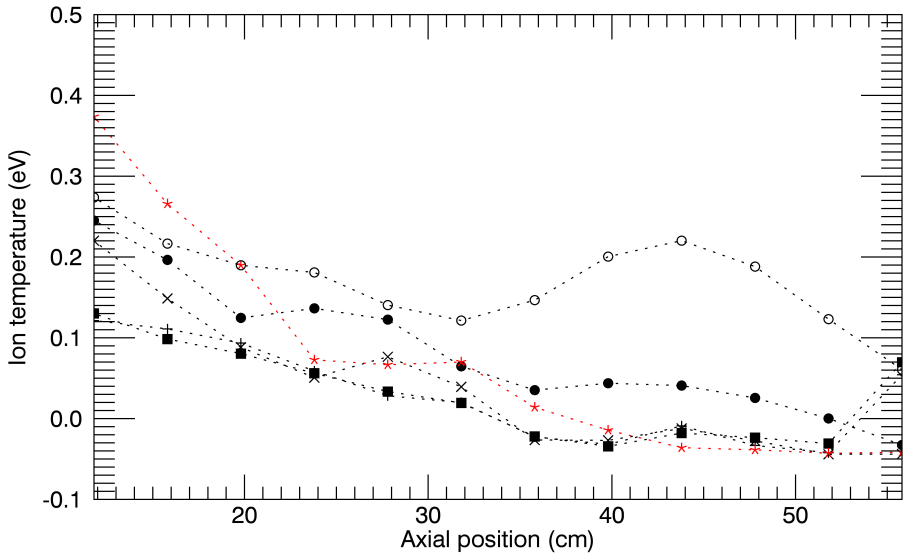


**Figure 7.5:** Ion temperature measured at $r = 0$ cm along the axial coordinate, $z$. The ion temperature plots correspond to mirror ratios $MR$ : 2.5 (■), $MR$ : 2.5 (+), $MR$ : 6.7 (×), $MR$ : 9.8 (*), $MR$ : 11.5 (•) and $MR$ : 12.6 (○).

and hence the ion temperature can be plotted across all pixels in the image. Multiple measurements were not taken for the data presented in figure 7.5 and and so in order to remove the effects of the 'ramp' the centre point of each temperature measurement (where the 'ramp' was zero) is shown instead.

For all magnetic field configurations the plot shows that the ion temperature decrease from the near-source to the magnetic pinch region. In the source (as shown in figure 7.3 (a)) the ion temperatures increase with mirror ratio.

The temperature results presented here are consistent with the dual ion heating mechanism as reported by Kline and Scime in the HELIX device [26–29]. Kline has reported that, firstly, electrons are heated near the antenna by electron Landau damping with the helicon wave and collisional equilibration with these hot electrons results in ion heating localised to the antenna region. Secondly, resonance between the Trivelpiece-Gould mode and the lower hybrid frequency result in ion Landau damping of the slow wave and ion heating at the periphery of the plasma. Kline found there was also a strong dependency on the RF driving frequency with edge ion heating.

In this work the lower hybrid frequency was calculated (on axis at peak magnetic field) to be 6.8 MHz at the reference magnetic field condition (MR=9.8) and 12.3 MHz for the high magnetic field condition (MR = 12.6). The driving frequency for all of these measurements was kept constant at 13.56 MHz. This suggests that a resonance would only begin to appear in the high-magnetic field case, where the lower hybrid frequency is near the RF driving frequency. As such, even though the edge ion heating increases with magnetic field, it is expected that the lower hybrid frequency is too low for these conditions to be the driving mechanism for edge heating via a resonance. Studies over RF

frequency would be useful to confirm this and as such, would be a good avenue for further investigation.

### 7.1.3 Ion flow and the magnetic field

Results from the reference condition study have shown a large rigid body rotational ion flow which is sheared at the plasma periphery. There also appears to be a reversal in the axial flows in the magnetic pinch region where the ions flow away from this point either towards the antenna or towards the target end plate. This study reports on the dependence of the ion flow profile with magnetic field.

#### Azimuthal ion flow - magnetic field study

Radial cross sections of the azimuthal ion flow are shown in figure 7.6 (a) and (b) for the magnetic pinch ($z$ = 47.8 cm) and near-source ($z$ = 11.8 cm) regions respectively. The expected errors (estimated in section 5.1.3 based on the reproducibility in plasma conditions) are on the order of 30 m/s. The flows in figures (a) and (b) have been measured for the magnetic field conditions shown in 7.1 and follow the trend by which the peak flow value increases with the mirror ratio. The correlated small amplitude bumps in the flow profile are a consequence of residual hyperbolic patterns in the interferogram and are not treated as features of the plasma flow. These features persist even when passive stabilisation and high quality optical components have been used (see discussion in section 4.3.4).

Figure 7.6 (a) shows that the maximum flow in the magnetic pinch region increases with magnetic field and the peak in the azimuthal flows shifts inwards as a consequence of the magnetic field compression. This trend is shown again in figure (c) where the peak flow value has been plotted against the associated magnetic field value. The rotational flows extend into the near-source region but are considerably smaller here as shown by figure (b). In all cases the core of the plasma appears to rotate as a rigid body, while the edges are sheared.

The azimuthal flows can be plotted against the magnetic flux coordinate which will remove any magnetic field compression effects. Plotting the azimuthal flows as a function of magnetic flux, see figure 7.7, the flow maximum appears to not change position and remains at the same flux level in all cases. The rate of shearing is not constant with magnetic flux suggesting that the flow shear is a consequence of a necessary zero boundary condition. The same trend has been observed by Scime [31] for the rotational flows in HELIX where the flow shear moves inwards as the magnetic field compresses and it appears that the shearing acts to reduce the rotational flow to zero at the plasma periphery.

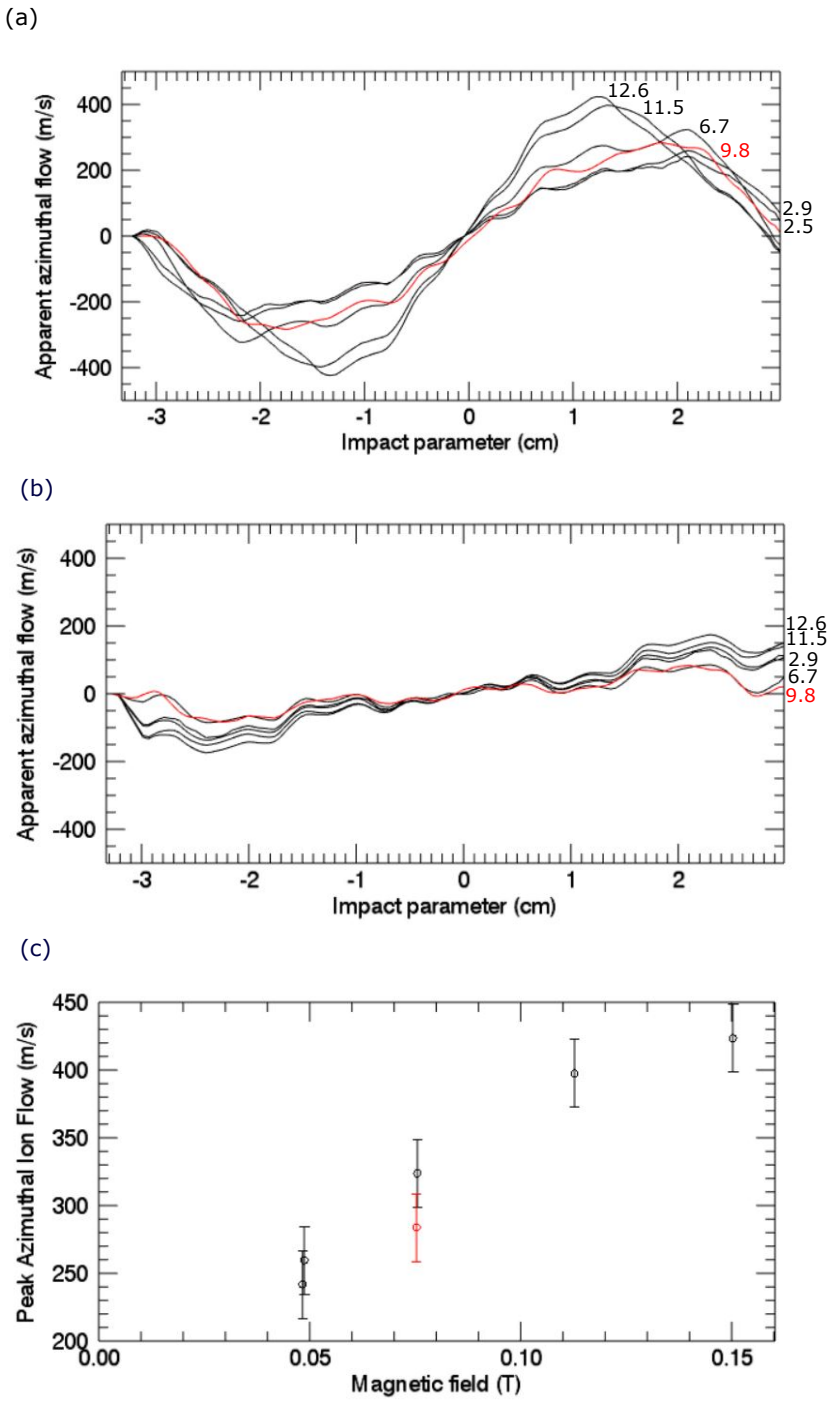


**Figure 7.6:** Azimuthal flow at different magnetic field configurations are plotted as a radial cross section in (a) the magnetic pinch region ($z = 47.8$ cm) and (b) the near-source region ($z = 11.8$ cm). Plot (c) shows the value of the peak rotational flow against magnetic field. The mirror ratio is annotated and correspond to the magnetic field configurations shown in 7.1.

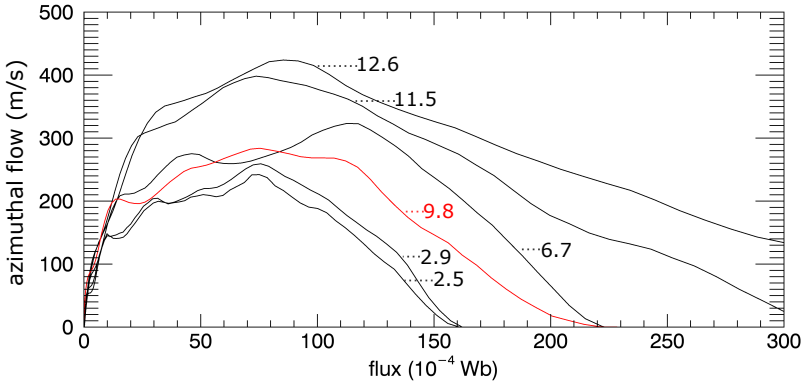


**Figure 7.7:** Azimuthal flow in the magnetic pinch region plotted as a function of magnetic flux coordinate. Here each plot corresponds to the magnetic configurations shown in figure 7.1 where the peak flow value increases with mirror ratio (annotated).

### Axial ion flow - magnetic field study

The axial flows (measured along $z$ at $r = 0$ cm) also vary with magnetic field and are shown in figure 7.8. The overall trend in the flow profiles exceed the expected error ($\pm 20$ m/s) determined by the reference condition study for measurements made in the same experimental set (see red error bars in figure 5.8). It should be noted that the the apparent union of the flow profiles immediately before the end plate, at $z = 58$ cm, have large associated errors $\sim 100$ m/s and therefore this feature is not considered significant.

There are three regions of interest in the axial flow which are observed for all magnetic field configurations. Firstly, the region between the antenna and $z = 32$ cm, appears to have near constant flow. The regions between $z = 32$ cm and the flow stagnation point at $z \sim 45$ cm and then to the end-plate both show flow acceleration. If its assumed that the flows are accelerated into a diverging magnetic field (with conservation of magnetic moment), then the stagnation point is a source and flow is accelerated away from this point towards the antenna and the end plate. The directionality of the flows is confirmed later in this chapter using a Mach probe.

The scans over magnetic field suggest that the position of the first transition point, $z = 32$ cm appears to be unchanged with magnetic field. The position of the source point at $z \sim 45$ cm shifts towards the end plate with increasing mirror field strength. It has been suggested [101, 102] that the MAGPIE ion axial flows are driven by gradients in the electron pressure. Considering the electron temperature for the 3 mT data (see figure 5.3) it is observed that the transition point at ($z = 32$ cm) coincides with the maximum of the electron temperature.

The flows measured here are all below the sound speed and on the order of the ion thermal speed $\sim 800$ m/s. The axial flows in HELIX have been reported within the same range [28]. Measurements of the neutrals and the electrons are needed in order to fully understand the mechanism behind the axial flows. This would be an area for further research.

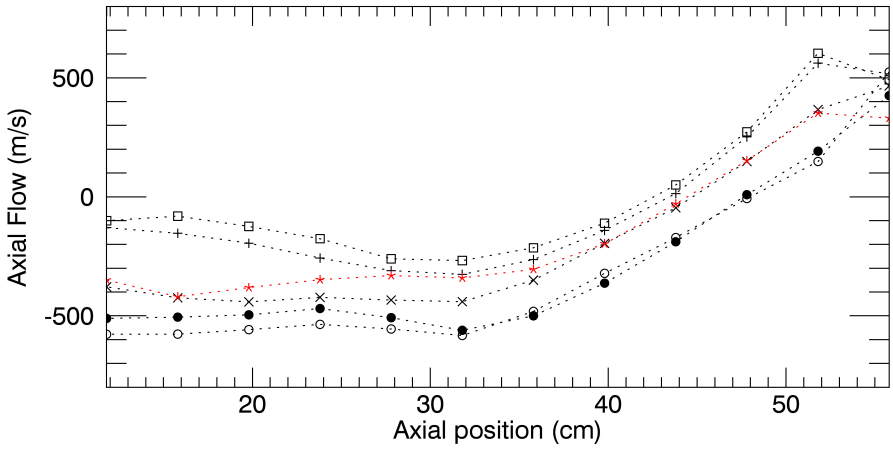


**Figure 7.8:** Axial ion flows measured at $r = 0$ cm along the axial coordinate, $z$. The axial flow plots correspond to magnetic ratios $MR : 2.5$ (□), $MR : 2.5$ (+), $MR : 6.7$ (×), $MR : 9.8$ (*), $MR : 11.5$ (•) and $MR : 12.6$ (○).

## 7.2 Pressure scans

For this investigation, the effects of gas pressure on the ion emission brightness, temperature and flows is studied over the range of 0.4 mT to 10 mT. The results presented here were acquired using the 80 mm compensated imaging system with fixed magnetic field at the reference condition (see figure 7.1 (d)) and an input power of $\sim 1$ kW.

### 7.2.1 Brightness and the gas pressure

The brightness was found to significantly change as the gas pressure was increased. Figure 7.9 (a) shows plots of radial the cross sections of the brightness taken at axial coordinate 47.8 cm (magnetic pinch region). The brightness is always centrally peaked and observed to, in most cases, increase with pressure. At lower pressures the profile is smooth and rounded and the secondary wing peaks only become present for pressure of 3 mT and higher. At high pressures the central peak becomes focused along the axis with the maximum brightness occurring at 7 mT. Figure 7.9 (b) shows a plot of the brightness near the antenna (11 cm). The brightness for pressures 4.5 mT and below are low and flat in the near-source region and increase with pressure. For the high pressure conditions, $7 - 10$ mT, the profiles become focused and centrally peaked with near equal amplitude.

For the measurements in the magnetic pinch region, the decrease in peak amplitude between $7-10$ mT (figures 7.9 a) is the result of an axial shift in the peak brightness towards the antenna. This is better understood by plotting the brightness along the axis of the MAGPIE chamber, as shown in figure 7.10.

The downstream brightness peak in the 3 mT data is small here compared to the brightness

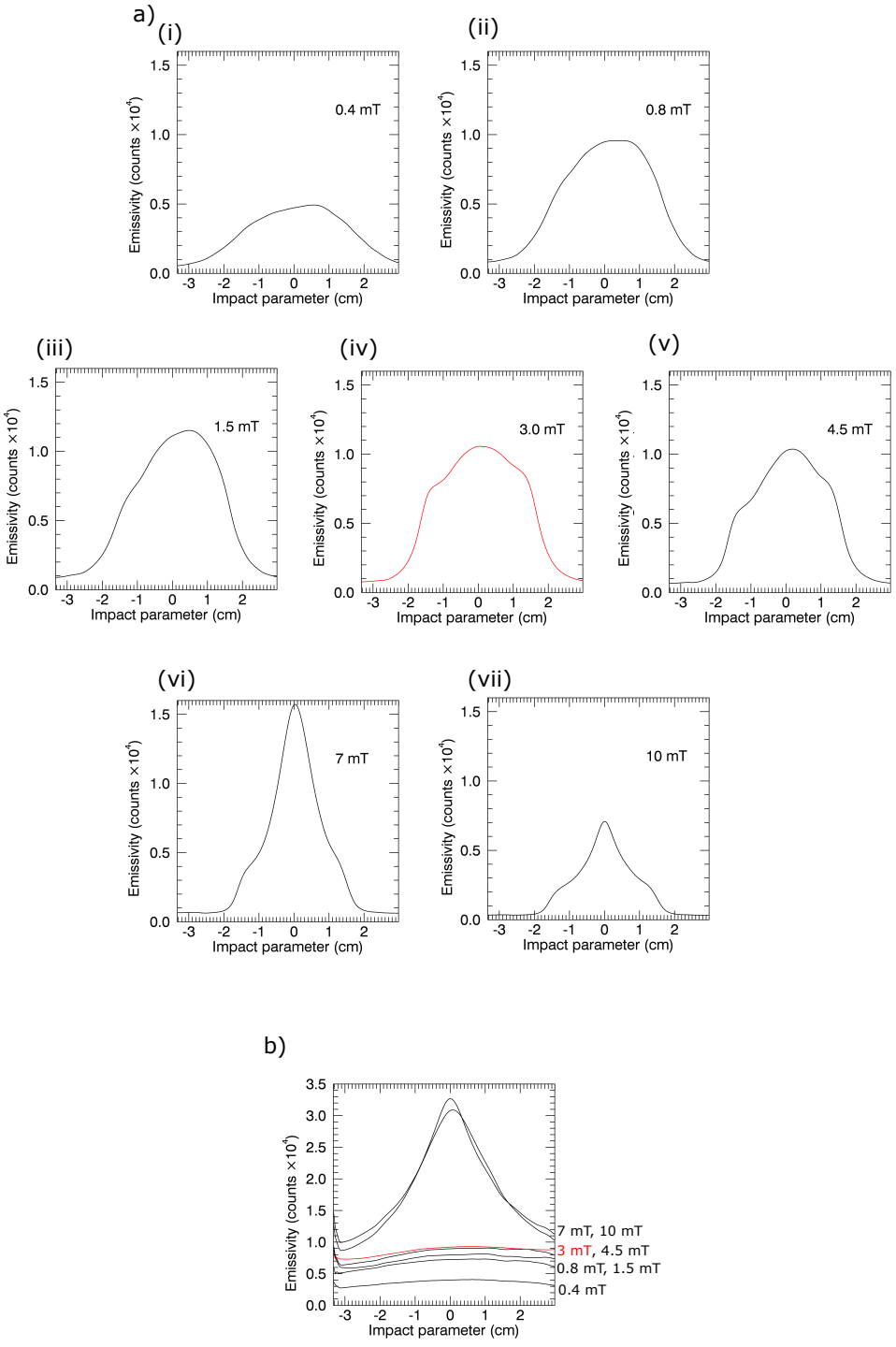


**Figure 7.9:** The brightness measured at (a) 47.8 cm (magnetic pinch region) for pressures (i) 0.4 mT (ii) 0.8 mT (iii) 1.5 mT (iv) 3 mT (v) 4.5 mT (vi) 7 mT and (vii) 10 mT. The plots in (b) show the emissivity at $z = 11$ cm (near antenna region) for the same pressure conditions.

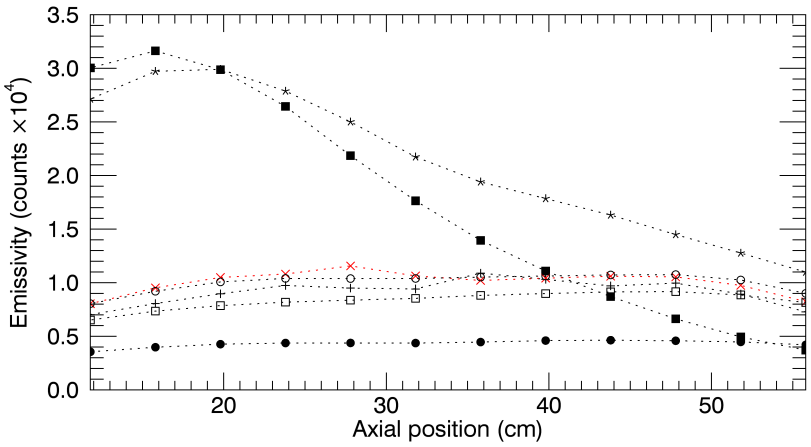


**Figure 7.10:** Brightness plotted along the central axis for pressure conditions 10 mT (■), 7 mT (∗), 4.5 mT (+), 3 mT (×), 1.5 mT (○), 0.8 mT (□) and 0.4 mT (•).

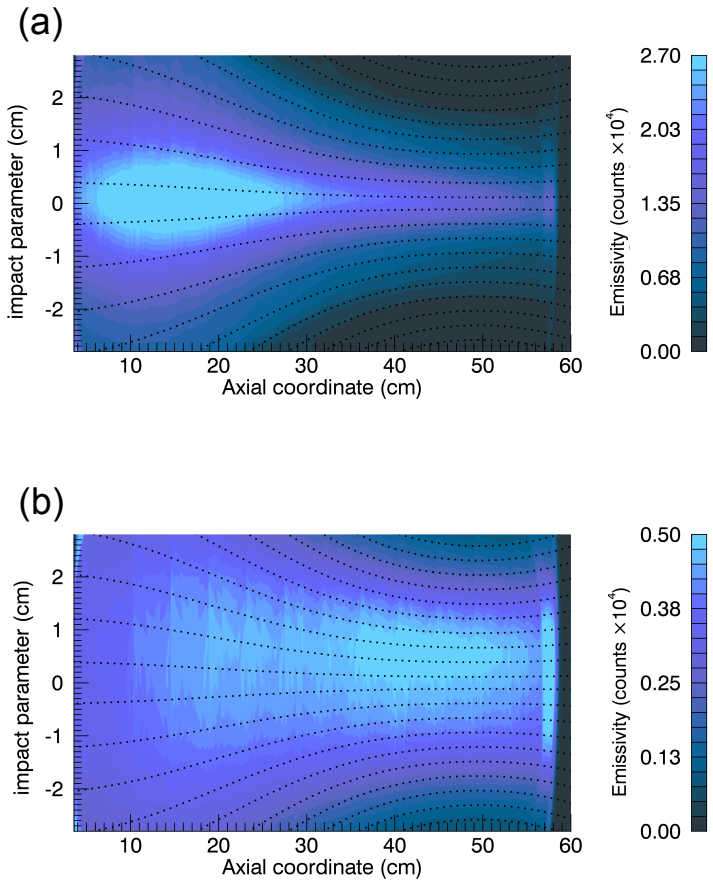


**Figure 7.11:** Brightness scans taken at (a) high pressure of 10 mT and (b) reference pressure of 3 mT.

increase at the high pressure conditions and so brightness profile appears flat along the entire length of the chamber at pressures at and below 4.5 mT. For for pressures 7 mT and above, the brightness peak has shifted towards the antenna and is almost beam like along the central axis.

Full scans of the brightness along the MAGPIE chamber for the reference condition (3 mT) and high pressure (10 mT) conditions are shown for comparison in figure 7.11 (a) and (b) respectively.

### 7.2.2 Ion temperature and the gas pressure

The ion temperature was studied over the same pressure conditions presented in the previous section. The ion temperatures are shown plotted over the impact parameter and pressure. Figures 7.12 (a) and (b) show the ion temperature at $z = 47.8$ cm (magnetic pinch region) and $z = 11$ cm (near-source region), respectively.

The ion temperature in the near-source region was found to decreases with pressure. The ion heating in this region is likely caused by collisional equilibration with the electrons heated by the antenna. Higher pressure indicates more collisions which enhances transport and cools the plasma.

The axial measurements of the ion temperature for each pressure condition, taken along the central axis (r=0), is plotted in figure 7.13 (a). This shows that at lower pressures the ion temperature is hotter and extends along the plasma chamber away from the antenna. At higher pressures the ion temperature is low throughout the chamber.

These trends agree with the results measured in the HELIX-LEIA system [32]. Under low pressure conditions the plasma is considered collisionless and hence the ions are also free to move along the magnetic lines of force. At high pressures collisional effects will be higher and hence the ion energy is quickly lost in the near source region. Collisionality is considered in the following section.

Measurements of the electron temperature were made using a double probe (courtesy of Dr Juan Caneses) for 3 mT and 10 mT in order to compare the electron and ion temperature profiles. The axial scan of the electron temperatures for 3 mT (red) and 10 mT (black) are plotted in figure 7.13 (b). The electron temperature is found to also decreases with pressure. The electron and ion temperature profiles are quite different at 3 mT, where the electron temperature peaks at some distance away from the antenna while the ion temperature exhibits a monotonic decrease along the axis. At higher pressures (10 mT) both profiles follow the same trend.

The ion temperatures in the magnetic pinch region ($z = 47.8$ cm) are shown as radial plots in figure 7.12 (i)-(vii) for increasing pressure. The edge-temperatures remain fairly constant over the pressure scan suggesting that neutral pressure plays little role in the localised edge-ion heating. The gradient between the edge and central temperatures becomes steep in the high pressure, 7 mT -10 mT, measurements. This occurs in conjunction with

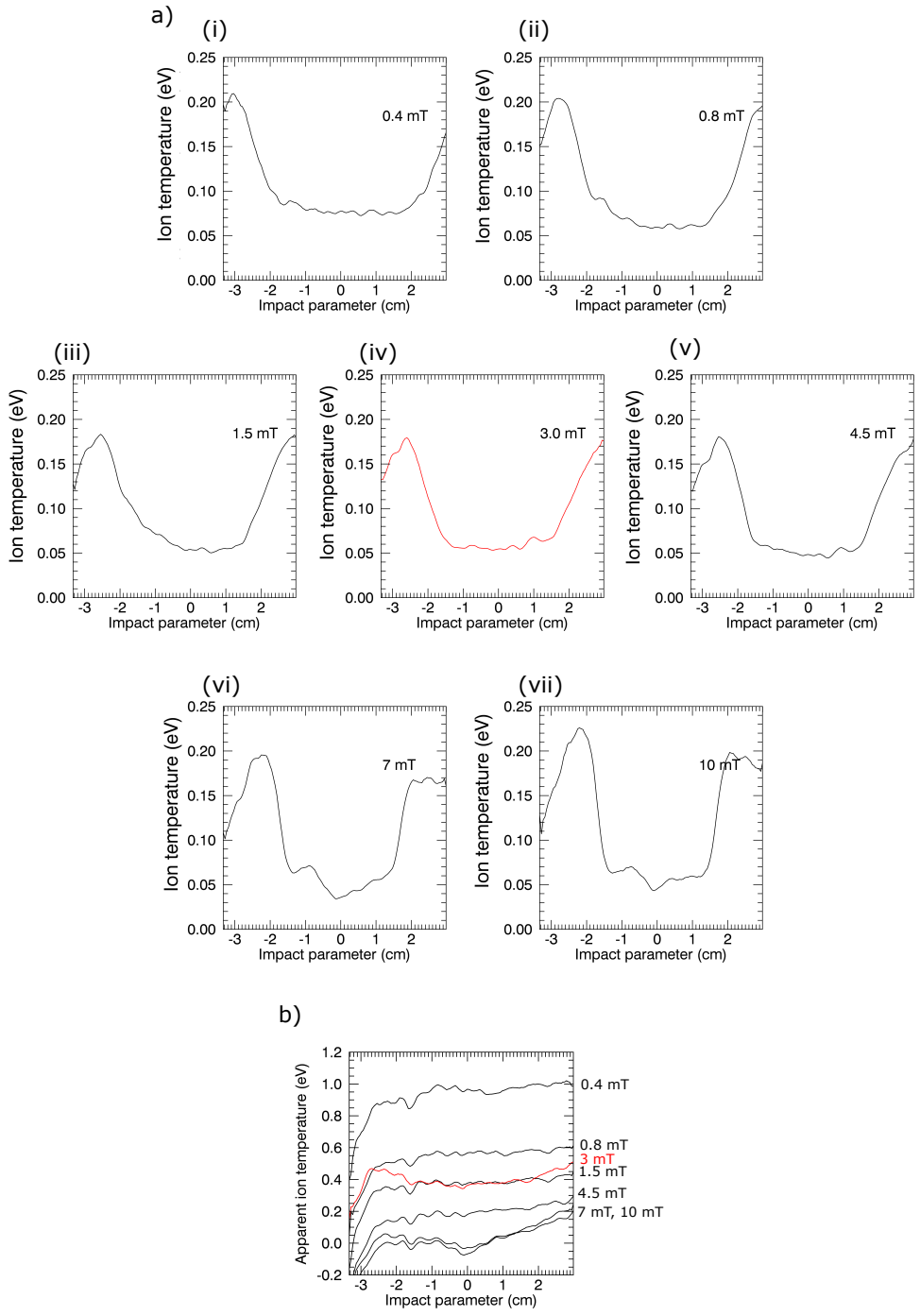


**Figure 7.12:** The ion temperature measured at (a) 48 cm (magnetic pinch region) for pressures (i) 0.4 mT (ii) 0.8 mT (iii) 1.5 mT (iv) 3 mT (v) 4.5 mT (vi) 7 mT and (vii) 10 mT. The plots in (b) show the ion temperatures at $z = 11$ cm (near antenna region) for the same pressure conditions.

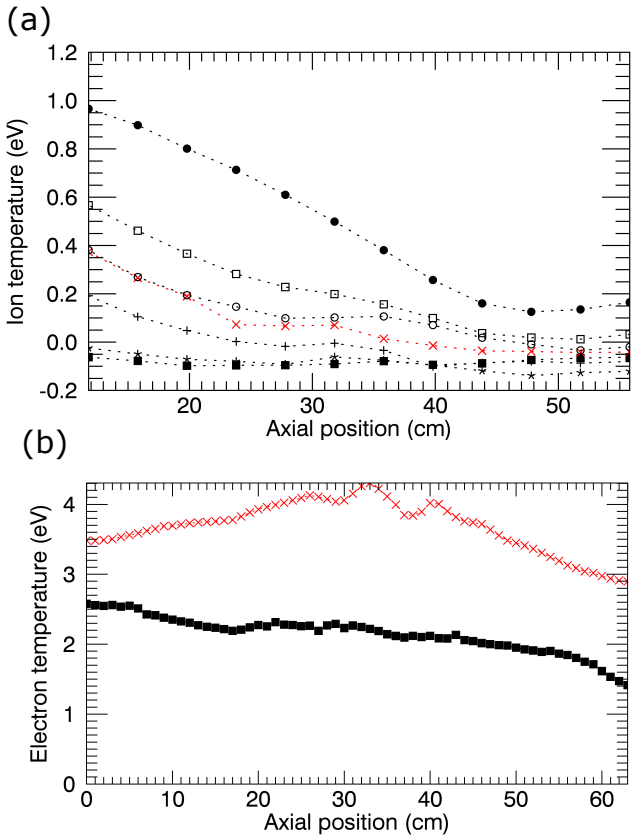


**Figure 7.13:** (a) Ion temperature along the central axis ($r = 0$ cm) for pressure conditions 10 mT (■), 7 mT (∗), 4.5 mT (+), 3 mT (×), 1.5 mT (○), 0.8 mT (□) and 0.4 mT (•). Figure (b) shows the electron temperature plotted along the central axis ($r = 0$ cm) for 3 mT (×) and 10 mT (■).

the beam like brightness profile measured at high pressures (see figure 7.9). The increased collisionality in the high pressure case has an important implication on the edge-peaked temperatures. This is discussed in the following section. It should be noted that at high pressures the spectral contamination from the 486.5 nm ion line in the magnetic pinch region was around 10% (see discussion in section 5.2.1), however, this is not responsible for the steep gradients in the temperature as the spectral contamination was equal in both the core and the edge plasma regions.

### 7.2.3 Ion flow and the gas pressure

The azimuthal and axial flows are studied over a range of gas pressures. It is expected that as pressure increases, collisionality should act to suppress flows.

#### Azimuthal flow - pressure study

Radial cross sections of the azimuthal flow for the magnetic pinch is shown in figure 7.14 (a). The flows are a maximum at low pressure in the magnetic pinch region, reaching

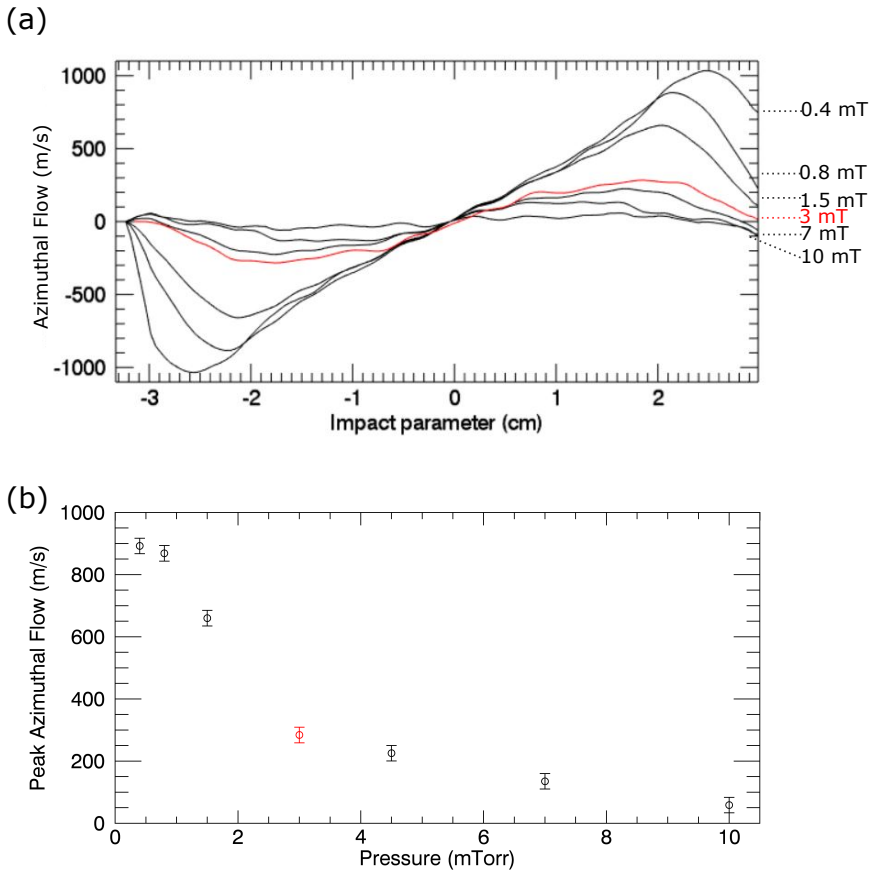


**Figure 7.14:** Radial cross sections of the azimuthal flow for (a) the magnetic pinch region ($z = 47.8$ cm). Figure (b) show the maximum flow value (for plots in a) against pressure.

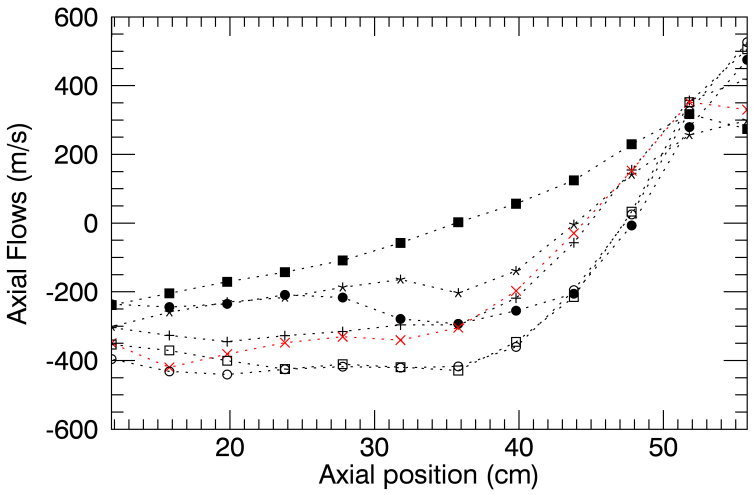


**Figure 7.15:** (a) Axial flows along the central axis ($r = 0$ cm) for pressure conditions 10 mT (■), 7 mT (∗), 4.5 mT (+), 3 mT (×), 1.5 mT (○), 0.8 mT (□) and 0.4 mT (●).

velocities up to 1000 m/s. This is lower than the expected sound speed, $\sim$ 3000 m/s, and is on the order of the thermal speed $\sim$ 800 m/s. The plasma maintains rigid-body rotation between the core and the peak flows before the flow shear region. As expected the flows are damped as the neutral pressure increases. At high pressures $\sim$ 10 mT, the azimuthal flow is virtually zero. Flows near the source are small and follow the same trend as observed in the magnetic pinch region.

Figure 7.14 (b) shows the dependency of the peak azimuthal flow (in the magnetic pinch region) with pressure. The trend appears to be non-linear with no azimuthal flows expected for pressures greater than 10 mT.

#### Axial flow - pressure study

The axial flows near the source are observed to decrease and the identified 'transition point' at $z = 32$ cm becomes less evident with increased gas pressure. Kline [28] has also observed a decrease in the axial flows with increasing neutral pressure on the HELIX device. For the study presented here on MAGPIE, there are observed changes in the axial flow with neutral pressure as shown in figure 7.15. For the region $z > 32$ cm the flows are near linear with axial coordinate however the acceleration appears to decrease, and therefore suggest a reduction in the driving force, as the pressure increases.

For most pressure conditions ($0.4 - 7$ mT) there are clearly two distinct regions. That is for $0 < z < 32$ cm, there is a constant flow towards the antenna, and for $z > 32$ cm the flow is accelerated away from some source point in the high magnetic field region. For the high pressure case (10 mT) the transition point vanishes and the flow varies near linearly with axial coordinate. The source point in the high magnetic field region is observed to shift towards the antenna as the pressure increases. It is possible that these axial flows are driven by changes in the electron pressure as has been already found in the case of hydrogen [101]. Measurements of the electron pressure over the same range of conditions would be useful to confirm this.

## 7.3 Plasma confinement study

The results so far have demonstrated significant features in the ion temperature and flows which change according to pressure and magnetic field conditions. It is expected then that ions confined by a high magnetic field and low fill pressure will show different transport and heating properties to those in a low magnetic field and high pressure regime. Here the ion temperatures and flows are considered over a combination of magnetic field and pressure conditions to study the effects of plasma confinement.

### 7.3.1 Magnetic field and collisionality

For a plasma that is exposed to a strong magnetic field and has low neutral gas pressure, it is expected that the collisionality will be low and the plasma will be well confined. For high pressures the ion-neutral mean-free-path will shorten and collisions are expected to wash out plasma flows. The Hall field, $\mathbf{E_H}$, is a potential difference that arises between charge carriers when a magnetic field is applied perpendicular to a particles drift velocity. It is given by the magnetic part of the Lorentz force where $q\mathbf{E_H} = q(\boldsymbol{V} \times \mathbf{B})$. The Hall parameter, can be used to quantify the extent of which a plasma responds to an external magnetic field. In terms of ions, the Hall parameter is defined as [119],

$$\beta_H = \omega_{c,i}/\nu_{i,n} \tag{7.1}$$

where $\omega_{c,i}$ is the ion cyclotron frequency and $\nu_{i,n}$ is the ion-neutral collision frequency given by,

$$\nu_{i,n} = V_{th,i}/\lambda_{mfp} \tag{7.2}$$

where $V_{th,i}$ is the ion thermal speed and $\lambda_{mfp} = 1/330\mathrm{P}$ is an approximation for the ion-neutral mean-free-path in argon (in cm) with pressure dependence P (in Torr) [120]. Ion temperature measurements over different magnetic field configurations have been used here to approximate the Hall parameter for ion-neutral collisions. Here the measured ion temperatures have been scaled up by 0.3 eV to account for the effects of the laser broadening. Figure 7.16 shows the Hall parameter calculated for (a) the reference magnetic field configuration and high pressure (10 mT), (b) the reference magnetic field and moderate pressure (3 mT) and (c) the high magnetic field (peak magnetic field $\sim 0.2$ Tesla) and low pressure (0.4 mT).

When the Hall parameter is low ($< 1$) the plasma will not be responsive to the magnetic field. It is expected that at these conditions flows will be washed out due to collisions between ions and neutrals. Large Hall parameters ($>> 1$) indicate that the plasma is magnetised. The contour plot in 7.16 (a) shows that for high pressure-low magnetic field the Hall factor is $< 1$ and therefore collisionality will washout magnetic field effects. In case (b) for the reference magnetic field and pressure, the core plasma in the magnetic pinch region is magnetised $\beta_H > 1$ while the plasma edge and the source regions are dominated by collisions. In the edge region the Hall parameter drops lower than the core due to the high edge ion temperatures. The Hall parameter also drops near the source as the magnetic field is not as strong in this region. For the high magnetic field and low pressure case (see figure 7.16 (c)) the plasma is highly magnetised with a peak $\beta_H$ value of $\sim 12$. It is important to remember that these calculations are based on the measured ion temperatures and rely on an appropriate correction for the laser broadening.

The following measurements of the ion temperatures and flows are made considering these various regimes of confinement.

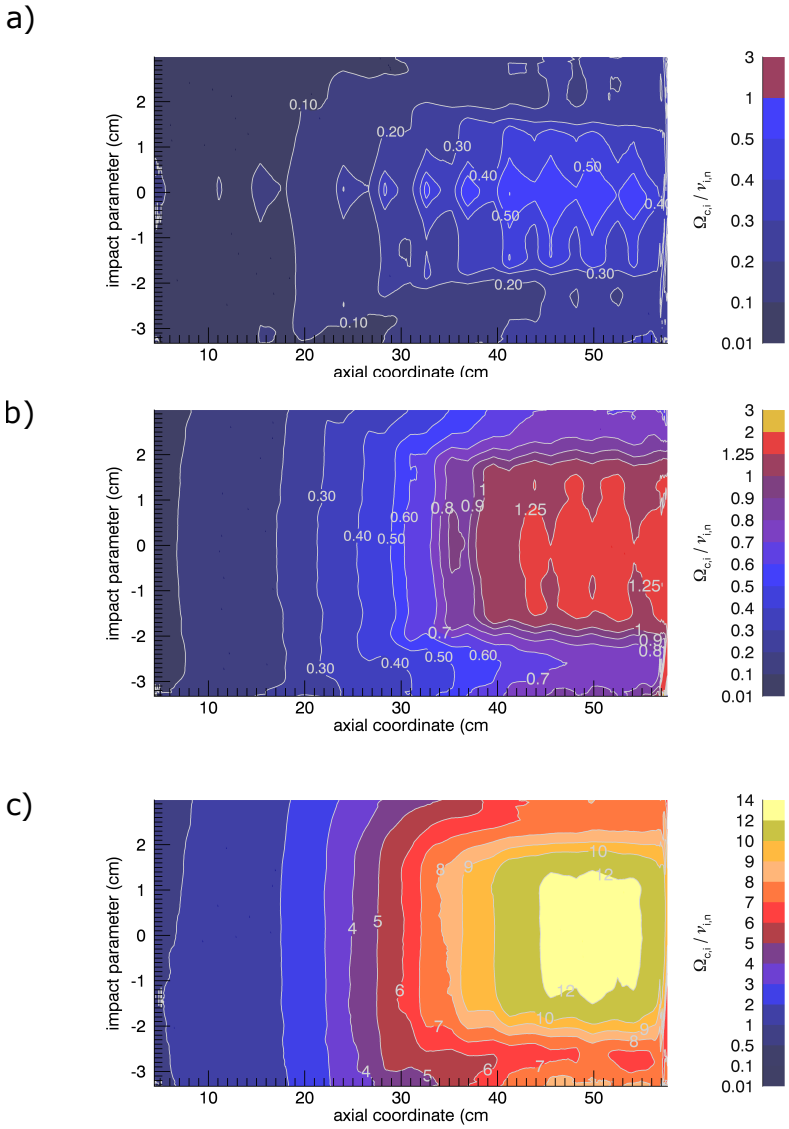


**Figure 7.16:** The Hall parameter calculated for ion-neutral collisions for (a) the reference magnetic field and high pressure (10 mT) (b) the reference magnetic field and moderate pressure (3 mT) and (c) the high magnetic field (peak magnetic field $\sim 0.2$ Tesla) and low pressure (0.4 mT).

### 7.3.2 Ion temperature and plasma confinement

A study of the ion temperatures was conducted over a combination of pressure and magnetic field conditions. The ion temperatures in the magnetic pinch region ($z = 47.8$ cm) for the edge and center are shown in figure 7.17 (a) and (b) respectively. Here, the x-axis is the neutral gas pressure (0.4 mT, 3 mT and 10 mT) and the y-axis specifies the magnetic mirror ratio (MR: 12.8, 11.5 and 9.8).

Figure 7.17 (a) shows the peak ion temperature in the plasma edge in the magnetic pinch region (47.8 cm). It is clear from the data that the highest ion temperatures occur in the region of highest plasma confinement where there is a strong magnetic field and low pressure. Figure 7.17 (b) shows the ion temperatures in the center of the magnetic pinch region ($r = 0$ cm and $z = 47.8$ cm). Here the temperatures are far lower than in the edge and do not appear responsive to either the pressure or the magnetic field changes. Plot 7.17 (c) shows the ion temperatures in the center of the plasma near the source ($r = 0$

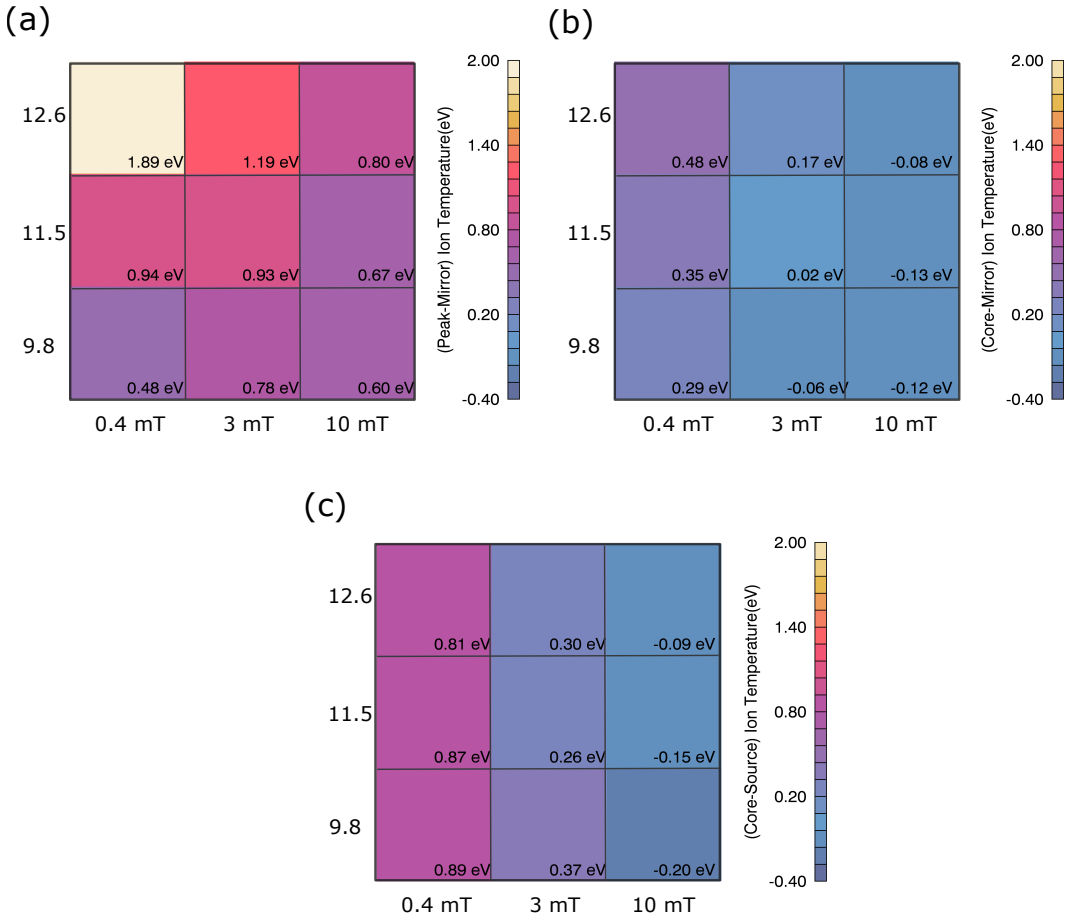


**Figure 7.17:** Ion temperature for (a) the peak edge temperature value in magnetic pinch region where $z = 47.8$ cm and (b) the core temperature in the magnetic pinch region where $r = 0$ cm and $z = 47.8$ cm. Figure c) shows the core ion temperature value near the source where $r = 0$ cm and $z = 11$ cm. Here the ion temperature values are been plotted over pressure (x axis) and magnetic mirror ratio (y axis). The expected error is on the order of 0.2 eV.

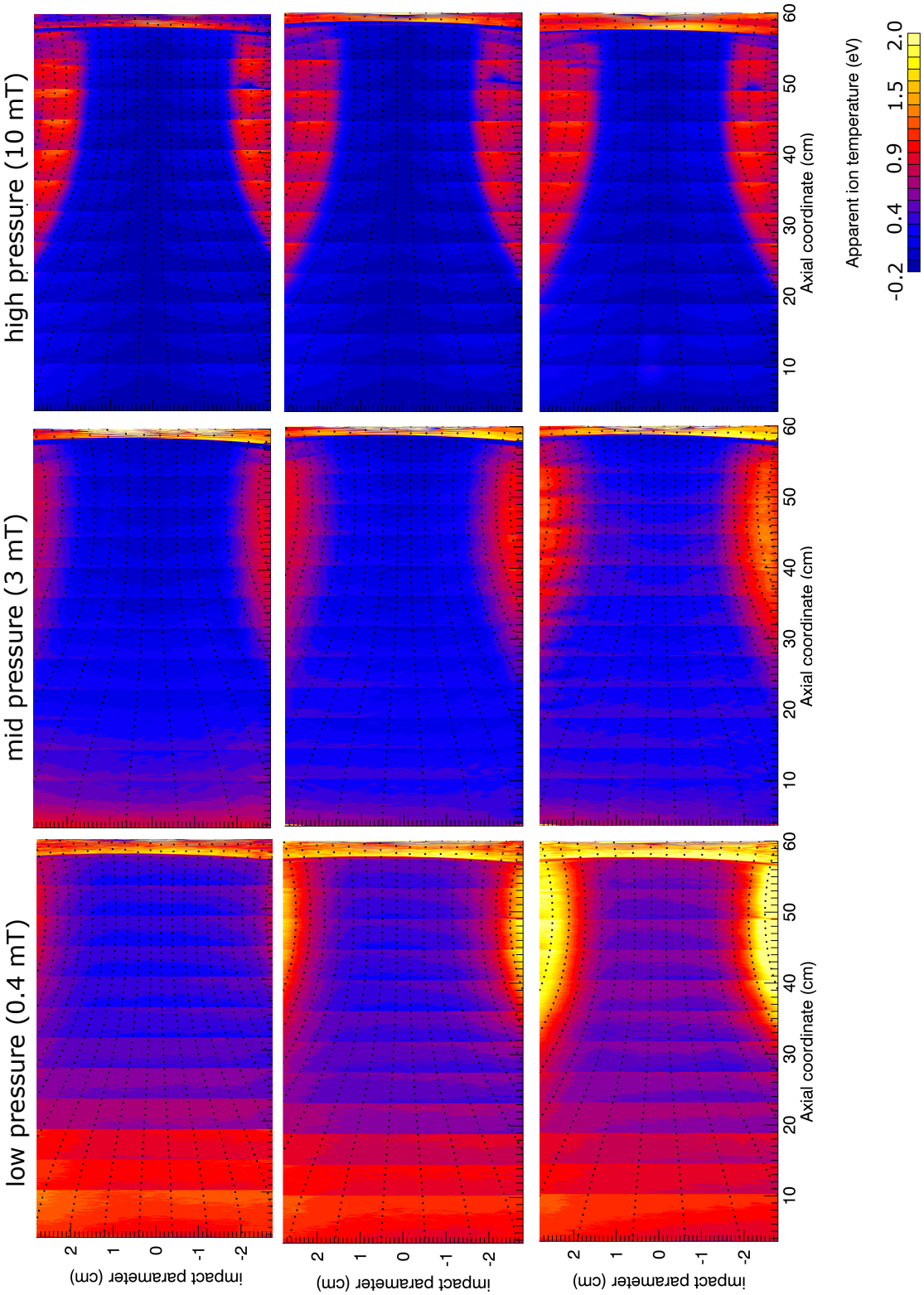


**Figure 7.18**: Scans of the apparent ion temperature for a range of magnetic field configurations and pressures.

cm and $z = 11$ cm). The trend here shows that the ion temperatures are responsive to changes in the pressure. It is likely that the minimal variation with mirror ratio is simply a result of the near constant in the magnetic field ($\sim 0.01$ T) at this position.

A distinctive change occurs in the ion temperatures between the high confinement (high magnetic field and low pressure) and low confinement (low magnetic field and high pressure) regimes. Figure 7.18 shows scans of the ion temperature over various pressures and mirror ratios. These scans show that at low pressure the plasma core is hot near the source and for lower mirror ratios the edge temperatures are not as apparent. As the magnetic field increases, so does the peak ion temperatures and for high magnetic fields there is a steep ion temperature gradient separating the cold core plasma and the hot edge plasma.

For the high-pressure low magnetic field case, collisionality is expected to wash out the effects of the magnetic field. Instead, the measurements of the ion temperatures presented in figure 7.18 show that the temperature is well confined to the magnetic lines of force. This would suggest that the heating is generated through the electrons, which are well magnetised due to their smaller mass and therefore are still tied to the magnetic field lines. The ion are then heated by the electrons through collisions. The secondary wing-like feature in the brightness profile (which was attributed to the electron temperature) is present at these conditions however it is difficult to determine the extent of edge-electron heating at this position using the brightness alone. Radial measurements of the electron temperature at these conditions would be necessary to investigate this.

### 7.3.3 Azimuthal ion flow and plasma confinement

The peak azimuthal flows are shown in figure 7.19 for the same pressure and magnetic field study. The peak flows are greatest for high plasma confinement regime (high magnetic field and low pressure). The drop in rotational flow as the magnetic field decreases and the pressure increases is most likely due to the decreased penetration of the external magnetic field.

Radial plots of the flow maximum are shown for pressure conditions 0.4 mT, 3 mT and 10 mT in figures 7.20 (a), (b) and (c), respectively. Here the flows have been plotted against the magnetic flux coordinate to remove the compression effects of the magnetic field so that differences in the flow profile (such as a shift in maximum) and change in peak magnitude can be directly compared. The text label provides the axial location of the flow maximum. In each plot the flows increase with magnetic field according to magnetic configurations given by the mirror ratios $9.8, 11.5$ and $12.6$.

The flows in the high pressure case, figure 7.20 (c), appears flatter than the other conditions most likely because the mean-free-path is shorter at high pressures and therefore there is less diffusion. For the high pressure case the peak flows shift towards the antenna with increased magnetic field. For low pressures (0.4 mT) the peak in the flows occurs at exactly $z = 48$ cm for all magnetic field conditions. At 3 mT the position of the peak flow is unstable and lies between $41 - 51$ cm. For this case the azimuthal flows are not confined to the high magnetic field region but are more spread out along the field lines.

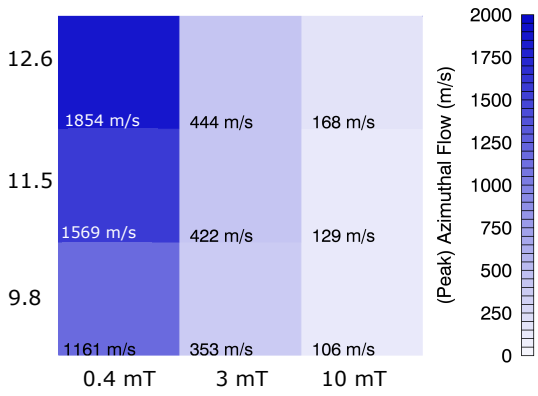


**Figure 7.19:** Peak azimuthal ion flow plotted over for pressure (x axis) and magnetic mirror ratio (y axis)

Axial scans of the azimuthal flows are shown at low and high collisionality in figure 7.21 (a) and (b), respectively.

### 7.3.4 Axial ion flow and plasma confinement

The axial flows are shown in figure 7.22 for pressures 0.4 mT, 3 mT and 10 mT, (plot (a), (b) and (c), respectively). The individual plots correspond to the mirror ratios 9.8 (solid), 11.5 (○) and 12.6 (×).

There is a clear transition in the flow profile between the low confinement and high confinement regimes. It appears that the acceleration from the source point in the magnetic pinch region is highest for the high confinement regime. The flows approaching the antenna appear to decelerate between the transition point at $z = 30$ cm and $z = 0$ cm. As pressure increases and magnetic field decreases this transition point disappears and the flow profile becomes near linear along the plasma chamber for the high confinement regime. The flows near the antenna tend towards zero for the low confinement regime.

## 7.4 Confirmation of ion flows using the Mach probe

The following section presents the ion flow measurements taken using the Mach probe in the MAGPIE argon plasma over a variable pressure. A pressure study was performed here as the coherence imaging results have suggested a distinct change in both the axial and azimuthal flow profiles between low and high pressure. Coherence imaging results determined in section 7.2.3 at the same plasma conditions are included for comparison.

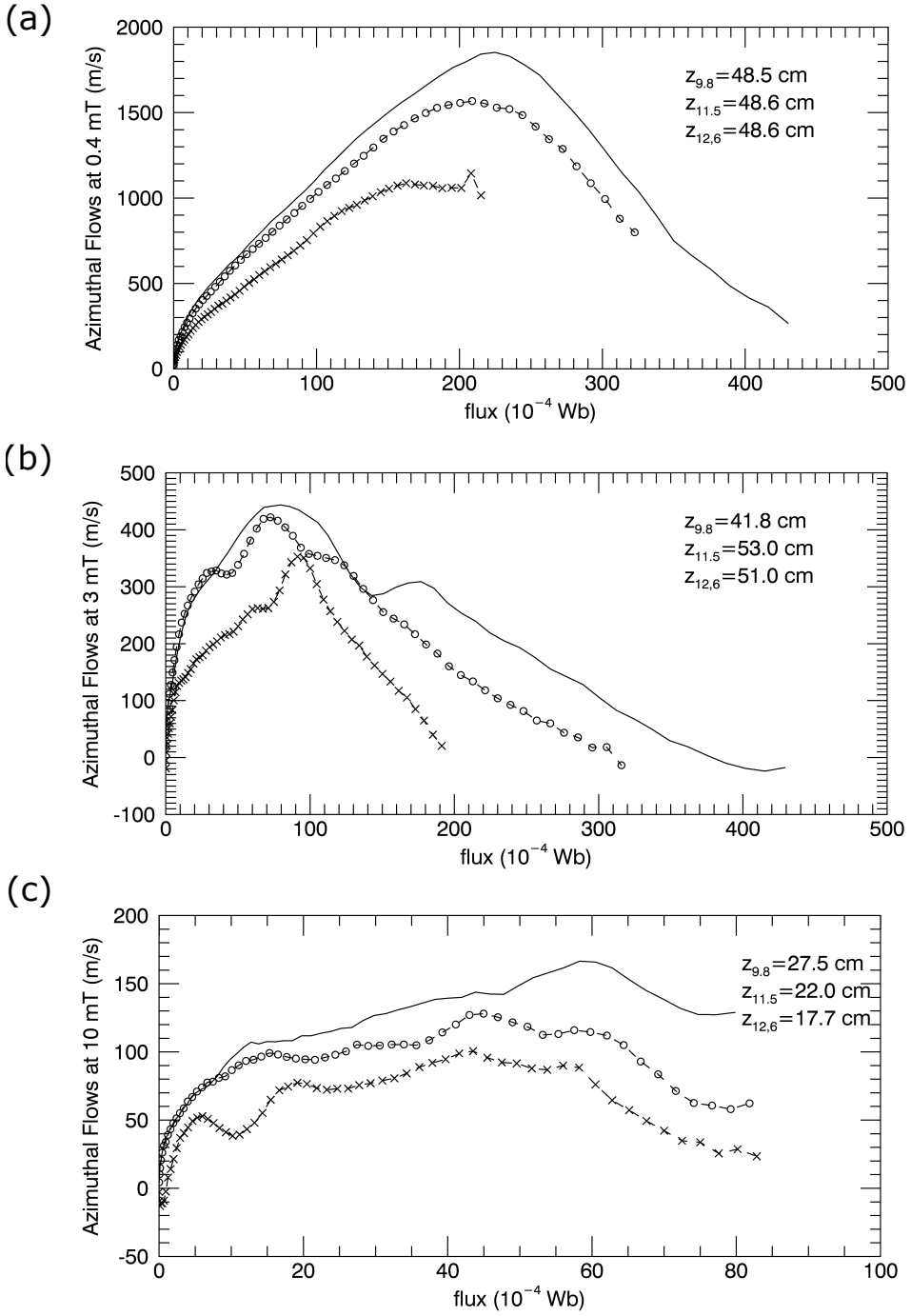


**Figure 7.20:** Azimuthal ion flow plotted over the magnetic flux coordinate at (a) low pressure (0.4 mT) (b) mid pressure (3 mT) and (c) high pressure (10 mT); where the each plot is given for the mirror ratios 12.8 (solid), 11.5 (∘) and 9.8 (×).

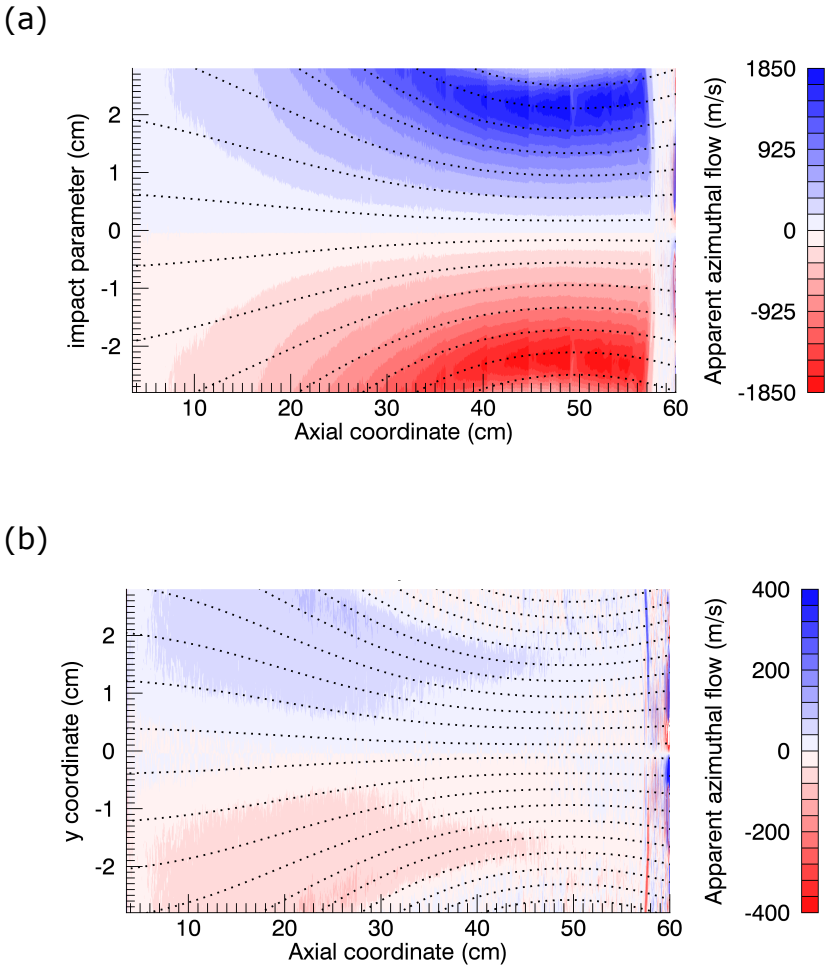


**Figure 7.21:** Axial scans of the azimuthal flow at (a) 0.4 mT and mirror ratio $M = 12.6$ and power $\sim 1$ kW and (b) 10 mT and mirror ratio $M = 9.8$ and power $\sim 1$ kW.

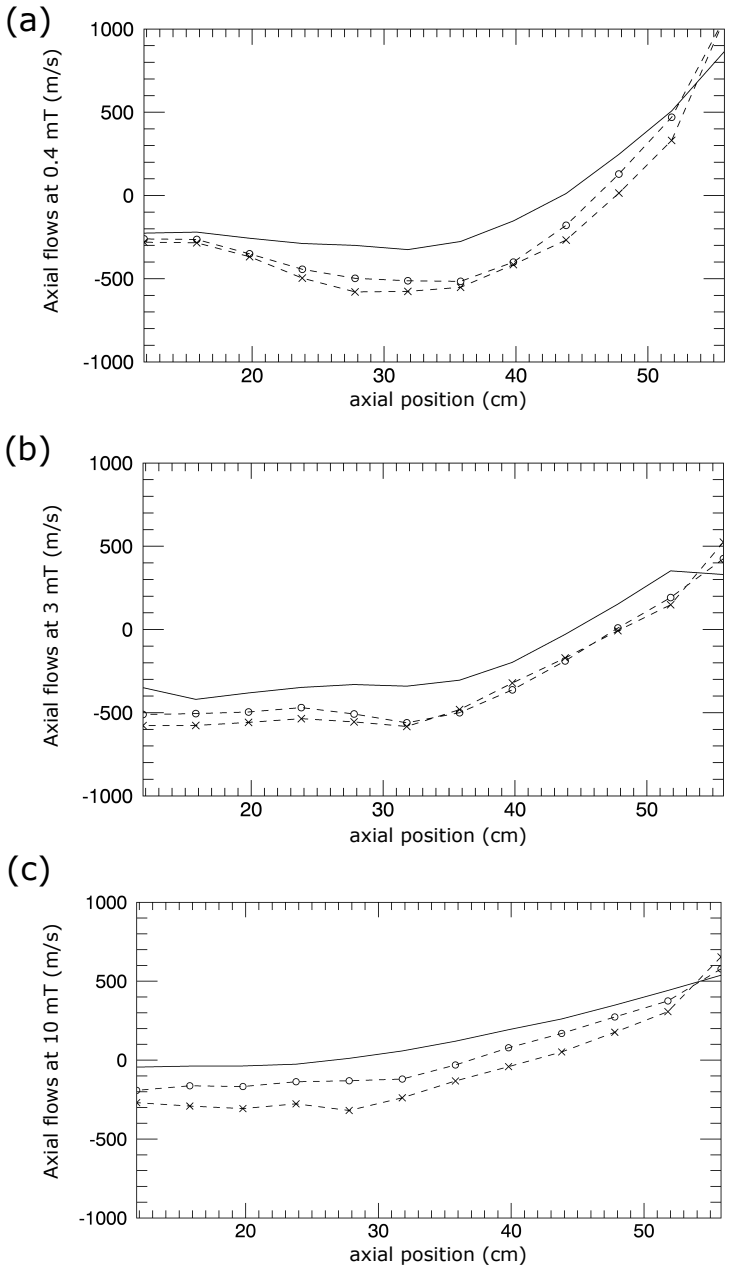


**Figure 7.22:** The axial flows along the core of the plasma ($r = 0$ cm) for (a) Low pressure, 0.4 mT (b) mid pressure 0.3 mT and (c) high pressure, 10 mT. Each plot corresponds to the magnetic field with mirror ratios 12.6 (solid), 11.5 (∘) and 9.8 (×).

### 7.4.1 Axial ion flows

The thick-tip Mach probe was used to confirm the profile and directionality of the axial flows for the argon ions at a low and high pressure condition. The results are presented in figure 7.23 where (a) shows the flows at low pressure, 3 mT, and (b) shows the flows at high pressure, 10 mT. These scans were taken at the reference magnetic field and power conditions where the peak magnetic field in mirror was 0.08 T and the power was set to 1 kW.

The ion flows measured by the Mach probe are shown by the black points and the error bars are calculated from the standard deviation (see discussion 4.4.2). The results from the coherence imaging measurements at the same conditions are shown in red and the error bars are assumed to be the same as those reported for the reference study presented in chapter 5 and account for reproducibility between measurements not taken consecutively.

For both measurements the probe data agrees within error of the flows measured using the coherence imaging system. The ion flows are on the order of the ion thermal speed ($V_{th} =$ 800 m/s) which compliments axial flow measurements measured in HELIX [28]. The probe data confirms that for both pressure conditions the flows are accelerating towards the end plate of the target chamber.

Both the probe data and the coherence imaging data suggest that, for the 3 mT case, there is a reversal in the axial flow at $z = 45$ cm and for $z < 45$ cm the ions appear to flow towards the antenna. It is interesting to note the bump in the probe data at 20 cm which is not captured in the coherence imaging data. This feature is well resolved by the probe given the error bars for this position. It is likely that this is some kind of effect due to the probe interacting with the plasma.

For the high pressure case (10 mT) both the probe and the coherence imaging measurements agree that there is a flow reversal point at $z \sim 30$ cm. Both measurements also agree that ions flow away from this reversal point, however they are not accelerated to the extent that is found in the 3 mT measurements.

### 7.4.2 Azimuthal ion flows

The results of the azimuthal flows measured using the thin probe tip are shown in figure 7.24 over variable neutral gas pressures. For these measurements the magnetic field and coupled power were kept constant. The azimuthal flow dependence has already been presented for coherence imaging data in section 7.2.3 and shows the azimuthal flows increase with decreasing pressure and reaching $\sim 1000$ m/s for pressures of 0.4 mT.

The probe measurements of the azimuthal flows are shown in figure 7.24 (black) for pressures (a) 4.5 mT, (b) 3 mT and (c) 1.5 mT. With the correction factor applied for the thin probe tip measurements (see discussion on shadowing in section 4.4.2) the probe data for all the pressure measurements generally fit well (within error) and show the same trends as the data obtained using coherence imaging (shown in red).

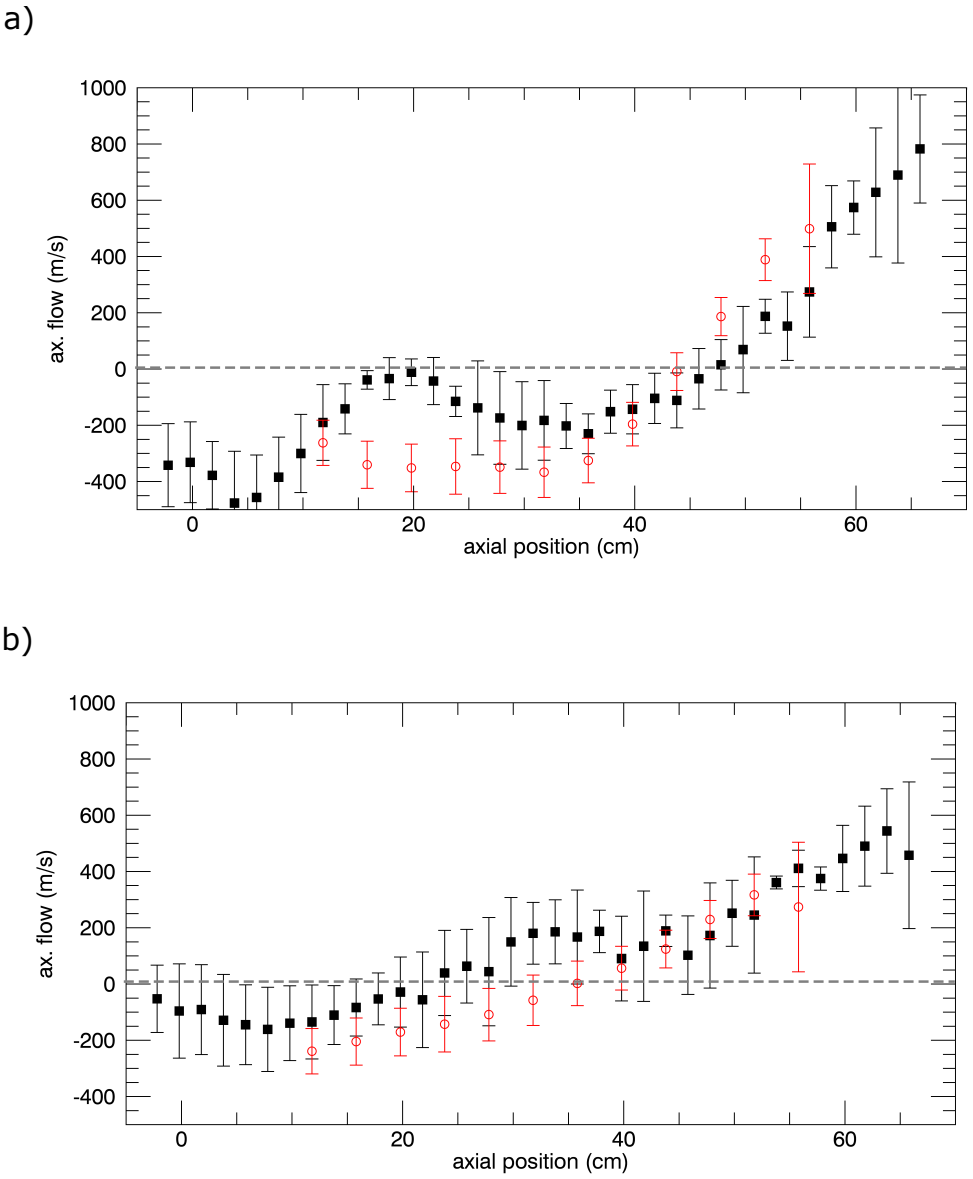


**Figure 7.23:** The ion velocity calculated using the thick-tip Mach probe (■) and coherence imaging (○) for variable pressures at (a) 3 mT and (b) 10 mT. The horizontal dashed line is used to indicate zero flow.

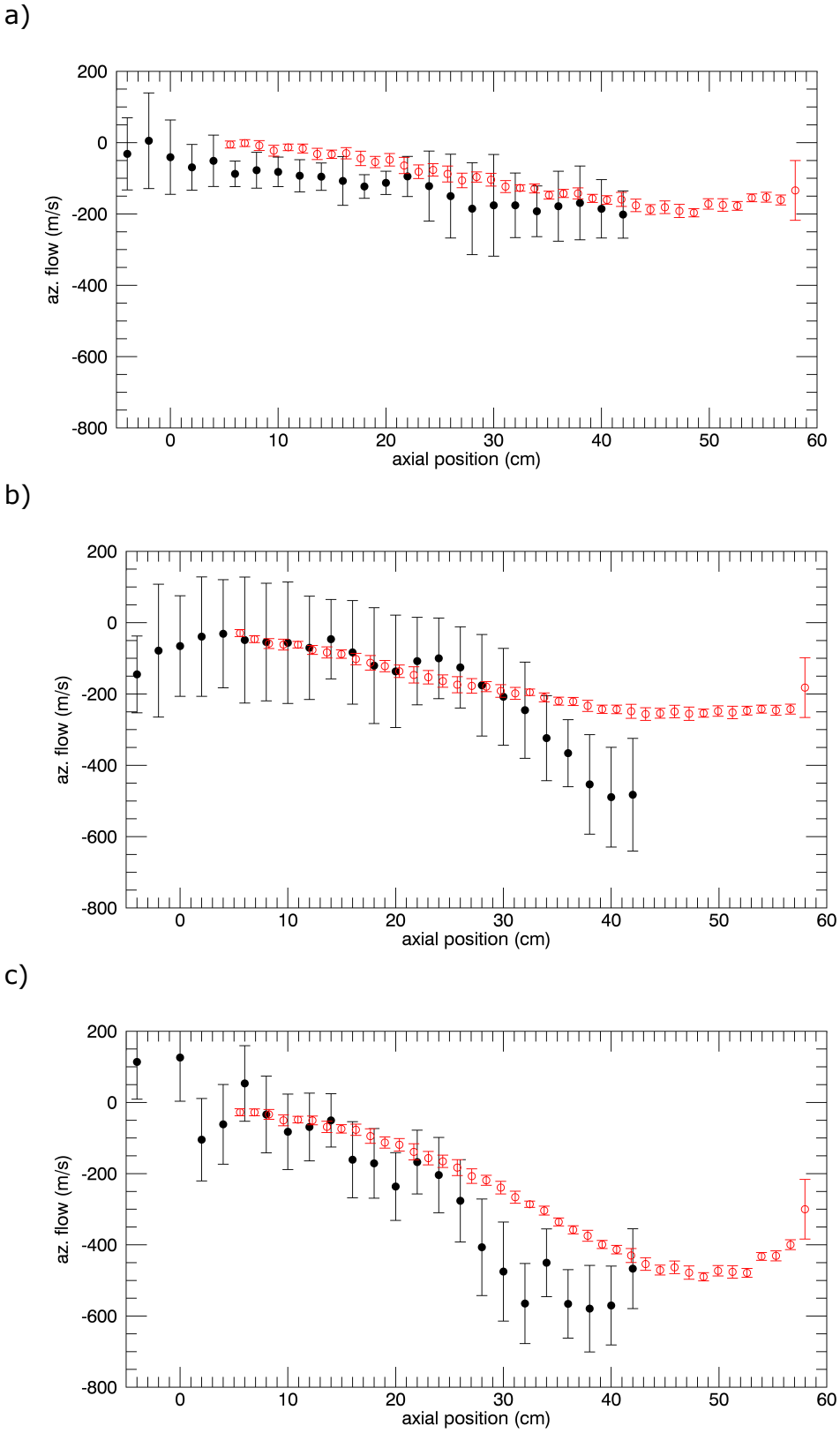


**Figure 7.24:** Azimuthal ion flow measured at 3 different pressure conditions (a) 4.5 mT, (b) 3 mT and (c) 1.5 mT. The Mach probe measurements are plotted in black (•) and the coherence imaging results are shown in red ○.

The density data obtained from the double probe (see figure 5.3) along with the coherence imaging ion temperature results, sets the expectation that the ions in the core are cold and suggests there is an inward-pointing radial ion-pressure gradient. This allows us to characterise the ion diamagnetic drift direction. Using this definition, the Mach probe confirms that the azimuthal flows are in the ion diamagnetic direction. This is in agreement with azimuthal ion flows in argon measured in the HELIX [28,31] and VINETA [39] linear helicon devices, which share similarities in chamber geometry, source, gas species and pressure to MAGPIE.

# Concluding Remarks

Snapshot coherence imaging has been used to examine an argon helicon plasma at equilibrium in the MAGPIE device thereby demonstrating that this technique can be used to measure ion features on cold temperature plasmas. There were three main aims of this project which included,

- the design of a coherence imaging instrument suitable for low temperature ion studies
- an investigation of the line-integration effects in measurements of inhomogeneous plasmas
- demonstration of Doppler coherence imaging as a diagnostic tool for low temperature measurements

The findings of this study are now summarised for each of these aims.

## 8.1 Design - coherence imaging for low temperature ion studies

Large lengths of birefringent crystal ($\sim$ 100 mm) are required to provide adequate interferometric delay for coherence imaging measurements of low temperature ($\sim$ 1 eV) ions. Measurements using such large crystal lengths are susceptible to drifts in the phase and contrast due to small changes in the temperature and mechanical stress across the optical elements. As such passive temperature stabilisation was necessary to alleviate such effects. It was found that a system built using $\alpha-$barium borate as the main delay crystal and lithium niobate for thermal compensation was the best option for this study due to the high compensation ratio and material properties (see discussion in section 4.3). On top of this, an online calibration system was built in order to minimise the time (for the phase to drift) and mechanical stress (due to the movement of the motorised stage) between the calibration and plasma measurements. Field-widening was implemented using a modified Savart plate so that the interferometric fringes remained uniform under such large delays which aided the demodulation of the interferogram. Spectral studies of the

argon ions in MAGPIE showed that there was a small contribution from the neighboring 486.5 nm spectral line which would result in oscillations within the ion temperature and flow measurements over delay. Such effects could be minimised in future measurements by selecting a imaging filter with $< 1$ nm passband. The major challenge in these measurements was identified as the calibration measurement. For such large crystal lengths, a bright intensity source (such as a laser) was necessary for adequate uniform illumination of the interferometric fringes, however, the large delays also meant that broadening of the calibration source could also contaminate the measurement. The temperature of the ions in the core of the plasma was found to be on the order of the argon calibration laser and it is believed this resulted in measurements of negative temperatures. For future studies with such large delays it is recommended that the line-shape of the calibration source is also measured (perhaps using a Fabry-Perot interferometer) so that correct scaling of the temperature can be applied.

## 8.2 Line-integration effects in measurements of inhomogeneous plasmas

Tomography of the 2D Radon transform was used to examine the effects of line-integration in the brightness, temperature and flow measurements (see chapter 6). Two methods of inversion were investigated, a pixel-method and an expansion using orthogonal functions. Straight forward application of these methods yielded the local emissivity (from the projected brightness) and the temperature (from the projected contrast). Inversion of the phase was more challenging as this required reconstruction of the vector flow field. Inversion of the phase using the vorticity was shown to be successful in reconstructing the local azimuthal flow. An inversion method based on the cosine symmetry of the line-of-sight directed azimuthal flow was also examined.

The tomographic results indicated that the line-integrated contrast and phase can give a good approximation of the local ion temperature and flow, and that the effects of line-integration are only small. Line-integration effects were found to suppress the secondary wing-like peaks in the brightness. The similarity between the tomographic results and the line-integrated approximation is fairly expected as the line-integrated measurements are weighted by the emissivity. As the emissivity for the MAGPIE plasma is greatest in the center of the plasma, features across the plasma mid-plane will dominate the projection and edge contributions are only small. A plasma which has the emissivity peak at the periphery of the plasma column will have the edge effects dominate the projection and line-integration effects, in such a case, cannot be ignored.

## 8.3 Demonstration of Doppler coherence imaging as a diagnostic tool for low temperature ion measurements

Doppler coherence imaging was applied to measure the ion brightness, temperature and flows in the MAGPIE chamber to demonstrate the capabilities of this instrument for

measuring low temperature ion features.

The ion brightness, ion temperature and ion flow results have been presented along the length of the MAGPIE plasma chamber at the reference plasma condition (see chapter 5). The ion brightness exhibits a double-peaked profile in the radial direction and an on axis maximum which peaks downstream of the antenna, near the position of the peak magnetic field. The ion temperature profile is very low at the core of the plasma but has high edge peaked temperatures at the boundary of the plasma. Rotational flows are very small near the antenna region but increase to peak in the high magnetic field region. These flows increase linearly with radius for $0 < r < 2.5$ cm (for the mirror region) suggesting bulk rotational flow, however, at larger radii the flows are sheared to zero. The axial flows appears to have a flow reversal at the point $z \approx 48$ cm which is the same position as the peak downstream brightness and magnetic field maximum. In the mirror region the flows appear to change linearly with $z$ however in the near-antenna region they were measured as flat.

The parameter scan (see the results in chapter 7) revealed that the brightness increased with both mirror ratio and pressure which may be a consequence of increased coupling of the helicon wave with the plasma and a greater number of collisions due to a reduced mean-free-path. The edge-peaked ion temperatures were found to be maximum where the plasma had highest confinement (high magnetic field and low pressure). Calculations of the lower hybrid frequency were found to be lower than the driving frequency (13.56) MHz suggesting that it is unlikely this heating is due to the resonance between the Trivelpiece-Gould mode and the lower hybrid frequency which has been reported in other helicon devices [29]. The ion temperatures were observed to follow the magnetic compression even at high pressures where collisionality is expected to wash out the magnetic field effects. This suggests that the edge heating may be generated through the electrons which are well magnetised and the ions are heated through collisions. The core source temperatures only showed a dependency on the pressure and were shown to be a maximum at low pressures. This is expected as high pressures result in collisions which acts to reduce the temperature. The core mirror temperatures in all cases appeared to be near constant showing no dependency on the magnetic field or gas pressure.

The azimuthal flows were also dependent both on the pressure and the magnetic field, and were a maximum for low pressures and high mirror fields where collisionality was lowest. At these conditions the peak azimuthal flow occurred downstream of the antenna near the magnetic field maximum. For high pressures and high magnetic fields the azimuthal flows were small and located closer to the antenna. At high pressure and reduced magnetic confinement there was a reduction in the rotational flows. The axial flows exhibit a dependency on both magnetic field and gas pressure. For high magnetic fields and low pressures there are two distinct regions of flow, a relatively flat (non-accelerating) component between the antenna and the $z = 35$ cm. From this point to the end plate the flows had a linear profile along $z$. At high pressure and low magnetic field the axial flow profile appeared to be linear with $z$ between the antenna and end-plate.

The Mach probe study has been able to confirm ion flows less than or on the order of the ion thermal speed in both the azimuthal and axial directions which support the flow results measured by the coherence imaging system. It was found that along the axis,

there is a flow reversal point at $z \approx 48$ cm where the ions are accelerated from the mirror towards the end-plate and also from the mirror towards the antenna. The azimuthal flows were also measured using the Mach probe and were found to rotate in the ion diamagnetic drift direction if an inward-pointing radial ion-pressure gradient is assumed.

The Doppler coherence imaging measurements presented in this study have reported on a series of plasma features consistent with those observed in other helicon devices. These results have been able to show that this technique is able to deliver a rich set of results and can be used as new tool for the study of ion flows and ion temperatures in cold plasmas.

## 8.4 Future work

Doppler coherence imaging of cold-temperature plasmas gives the opportunity to measure brightness, ion temperature and ion flows simultaneously over a large array of spatial positions. As the spatial data is encoded into a single measurement it is possible to also track changes in ion dynamics over time. With consideration made to thermal stability, spectral contamination and appropriate calibration, this technique presents an opportunity to study the ion behavior across events such as plasma ignition, in complex geometries such as thrusters and in the vicinity of targets and also; to investigate the role of ions within various turbulent structures. Only the ion features in argon have been studied here, however studies using krypton and neon (if a suitable calibration source is available) could be used to extend this study to investigate how ion dynamics change according to mass and possibly in the presence of gas composites. Measurements of neutral light could be used to reveal information on neutral heating and flow. The measurements presented here open opportunities to further understand mechanisms behind secondary ion heating, sheared flows and axial flows in the MAGPIE helicon device. Measurements of the electron density and neutral temperatures and flows could be the next step in understanding these features. In this study it was also shown that coherence imaging systems built using large interferometric delays are on the order of sensitivity required to measure coherence in gas lasers which perhaps offers an alternative avenue of investigation.

# Appendices

# Sellmeier equations for calculation of the refractive index

The following section lists the coefficients and equations used in the calculation of the refractive index $n$ as well as the formula used to calculate the change in the refractive index with wavelength, $\frac{dn}{d\lambda}$, which is required when calculating the dispersion factor $\kappa$, see equation 2.8. Values for $\frac{dn}{d\lambda}$ and $\kappa$ are quoted for each material.

## A.1 Calcite ($CaCO_3$) and yttrium orthovanadate ($YVO_4$)

The refractive indices for calcite and yttrium orthovanadate can be calculated using the five parameter Sellmeier equation [78, 87]

$$n^2_{\mathrm{O,E}} = A_{0_{\mathrm{O,E}}} + \frac{A_{1_{\mathrm{O,E}}}\,\lambda^2}{\lambda^2 - A_{2_{\mathrm{O,E}}}} + \frac{A_{3_{\mathrm{O,E}}}\,\lambda^2}{\lambda^2 - A_{4_{\mathrm{O,E}}}} \tag{A.1}$$

The wavelength is specified in $\mu$m and the coefficients for the ordinary and extraordinary refractive indices $(n_{\mathrm{E}}, n_{\mathrm{O}})$ of each material listed in the table below.

| material | | $A_0$ | $A_1$ | $A_2 \times 10^{-2}$ ($\nu$m$^2$) | $A_3$ | $A_4$ ($\nu$m$^2$) |
|---|---|---|---|---|---|---|
| $CaCO_3$ | $n_{\mathrm{O}}$ | 1.73358749 | 0.96464345 | 1.94325203 | 1.82832454 | 120.0 |
| | $n_{\mathrm{E}}$ | 1.35859695 | 0.82427830 | 1.06689543 | 0.14429128 | 120.0 |
| $YVO_4$ | $n_{\mathrm{O}}$ | 2.3409 | 1.4402 | 4.825 | 1.8698 | 171.27 |
| | $n_{\mathrm{E}}$ | 2.7582 | 1.853 | 5.6986 | 3.0749 | 195.06 |

**Table A.1**: The Sellmeier constants for equation A.1 for $CaCO_3$ and $YVO_4$

The temperature dependence on the refractive index for yttrium orthovanadate can be approximated by the second order polynomial fit

$$n_{\mathrm{O,E}} = n_{23_{\mathrm{O,E}}} + A_{T_{\mathrm{O,E}}}(T - 23) + B_{T_{\mathrm{O,E}}}(T - 23)^2 \tag{A.2}$$

where T is given in centigrade and $n_{23_{\mathrm{O,E}}}$ is the refractive index at 23 °C given by the $YVO_4$ coefficients presented in table A.1. The temperature constants for YVO4 are $A_{T_{\mathrm{O}}} = 2.38 \times 10^{-5}$ and $A_{T_{\mathrm{O}}} = 2.48 \times 10^{-8}$ and; $A_{T_{\mathrm{E}}} = 2.17 \times 10^{-5}$ and $A_{T_{\mathrm{E}}} = 2.80 \times 10^{-5}$, determined for the wavelength 0.45 $\mu$m.

The coefficients for $YVO_4$ were taken for a sample doped with 5% Neodymium rather than the pure crystal. however, the study suggests that the doping will only have subtle effects on the data and that the large spectral range investigated, should yield higher accuracy in the refractive indices compared with values presented in older work [87].

The change in the refractive index with wavelength is found by taking the derivative of equation A.1

$$\frac{dn_{\mathrm{O,E}}}{d\lambda} = -\frac{\lambda}{n_{\mathrm{O,E}}}\left(\frac{A_{1_{\mathrm{O,E}}}\ A_{2_{\mathrm{O,E}}}}{\lambda^2 - A_{2_{\mathrm{O,E}}}} + \frac{A_{3_{\mathrm{O,E}}}\ A_{4_{\mathrm{O,E}}}}{\lambda^2 - A_{4_{\mathrm{O,E}}}}\right) \tag{A.3}$$

For $CaCO_3$, the change in the birefringence with respect to wavelength is $\frac{dB}{d\lambda} = -6.3 \times 10^4$ m giving $\kappa = 1.18$. For $YVO_4$, the change in the birefringence with respect to wavelength is $\frac{dB}{d\lambda} = 22.8 \times 10^4$ m giving $\kappa = 1.46$.

## A.2 Lithium niobate ($LiNbO_3$)

The refractive indices for lithium niobate can be calculated using the temperature dependent Sellmeier equation [75]

$$n^2_{\mathrm{O,E}} = A_{0_{\mathrm{O,E}}} + \frac{A_{1_{\mathrm{O,E}}} + B_{0_{\mathrm{O,E}}}\ F}{\lambda^2 - (A_{2_{\mathrm{O,E}}} + B_{1_{\mathrm{O,E}}}F)^2} + B_{2_{\mathrm{O,E}}}\ F - A_{3_{\mathrm{O,E}}}\ \lambda^2 \tag{A.4}$$

Where $F = (T - 24.5)(T + 570.5)$ with $T$ in °C and the wavelength values specified in nm. The coefficients for the ordinary and extraordinary refractive indices give by

| | $A_0$ | $A_1$ | $A_2$ | $A_3$ | $B_0$ | $B_1$ | $B_2$ |
|---|---|---|---|---|---|---|---|
| $n_{\mathrm{O}}$ | 4.9048 | 0.11775 | 0.021802 | 0.027153 | $2.2314 \times 10^{-8}$ | $-2.9671 \times 10^{-8}$ | $2.1429 \times 10^{-8}$ |
| $n_{\mathrm{E}}$ | 4.5820 | 0.09921 | 0.21090 | 0.021940 | $5.2716 \times 10^{-8}$ | $-4.9143 \times 10^{-8}$ | $2.2971 \times 10^{-7}$ |

**Table A.2**: The Sellemier constants for equation A.4 for $LiNbO_3$

These parameters were quoted without units in the original work.

The change in the refractive index with wavelength is found by taking the derivative of equation A.4

$$\frac{dn_{\mathrm{O,E}}}{d\lambda} = -\frac{\lambda}{n_{\mathrm{O,E}}}\left(\frac{B_{0_{\mathrm{O,E}}}F - A_{1_{\mathrm{O,E}}}}{\left(\lambda^2 - (A_{2_{\mathrm{O,E}}} + B_{1_{\mathrm{O,E}}}F)^2\right)^2} - A_{3_{\mathrm{O,E}}}\right) \tag{A.5}$$

For $LiNbO_3$, the change in the birefringence with respect to wavelength is $\frac{dB}{d\lambda} = -10.21 \times 10^4$ m giving $\kappa = 1.54$.

## A.3 $\alpha-$barium borate ($\alpha-$BBO)

The refractive indices for $\alpha-$barium borate can be calculated using the the four parameter Sellmeier equation [76]

$$n^2_{\mathrm{O,E}} = A_{0_{\mathrm{O,E}}} + \frac{A_{1_{\mathrm{O,E}}}}{\lambda^2 + A_{2_{\mathrm{O,E}}}} + A_{3_{\mathrm{O,E}}}\ \lambda^2 \tag{A.6}$$

with the coefficients for the ordinary and extraordinary refractive indices $(n_{\mathrm{E}}, n_{\mathrm{O}})$ of $\alpha-$BBO listed in the table below.

| material | | $A_0$ | $A_1$ ($\mu$m$^2$) | $A_2$ ($\mu$m$^2$) | $A_3$ ($\mu$m$^{-2}$) |
|---|---|---|---|---|---|
| $\alpha-$BBO | $n_{\mathrm{O}}$ | 2.7405 | 0.0184 | −0.0179 | −0.0155 |
| | $n_{\mathrm{E}}$ | 2.3730 | 0.0128 | −0.0156 | −0.0044 |

**Table A.3**: The Sellmeier constants for equation A.6 for $\alpha$-BBO

The change in the refractive index with wavelength is found by taking the derivative of equation A.6

$$\frac{dn_{\mathrm{O,E}}}{d\lambda} = -\frac{\lambda}{n_{\mathrm{O,E}}}\left(\frac{A_{1_{\mathrm{O,E}}}}{(\lambda^2 + A_{2_{\mathrm{O,E}}})^2} - A_{3_{\mathrm{O,E}}}\right) \tag{A.7}$$

For $\alpha-$BBO, the change in the birefringence with respect to wavelength is $\frac{dB}{d\lambda} = -3.24\times10^4$ m giving $\kappa = 1.13$.

# Interpretation of the interferogram for the case where $v_D \sim v_{th}$

Coherence imaging systems have so far only been applied to plasma where $v_D << v_{th}$. This limit ensures that the phase and contrast are uniquely determined by the flow and temperature respectively (see expressions given by 4.27 and 4.28).

In MAGPIE, the drift velocity of the argon plasma is expected to be on the same order of magnitude as the thermal velocity $v_D \sim v_{th}$. In this case, second order terms can cause cross-contamination of the measured phase and contrast. The following work shows that in this limit second order contributions from the radial flow can manifest as elevated ion temperatures at small impact parameters. An upshot of this cross-contamination is that radial diffusive flows, which have so far been invisible to this technique, can be estimated.

The complex-coherence, sampled by the interferometer, for a general Maxwellian velocity distribution function takes the form

$$\gamma(\hat{\phi}_0;\hat{l}) = \frac{1}{I_0}\int_L \epsilon(\boldsymbol{r}) \exp\left(i\hat{\phi}_0 \boldsymbol{v_D}\cdot\hat{\boldsymbol{l}}\right)\ \exp\left(-\frac{\hat{\phi}_0^2\xi_{th}^2}{4}\right) dl \tag{B.1}$$

Where the complex phasor term carries information about the Doppler-shifted flow and the real exponent describes the thermal broadening. The normalised frequency coordinate is equivalent to the normalised thermal speed, $\xi_{th} \equiv V_{th}/c$.

Denoting the terms under the integral as $f(\phi)g(\phi)$ the Taylor series expansion can be applied, where the derivatives for the first terms of the Taylor series expansion are given as

$$\begin{aligned} f(\hat{\phi}_0) &= \exp\left(i\hat{\phi}_0 \boldsymbol{v_D}\cdot\hat{\boldsymbol{l}}\right) \\ f'(\hat{\phi}_0) &= i(\boldsymbol{v_D}\cdot\hat{\boldsymbol{l}}) \exp\left(i\hat{\phi}_0 \boldsymbol{v_D}\cdot\hat{\boldsymbol{l}}\right) \\ f''(\hat{\phi}_0) &= -(\boldsymbol{v_D}\cdot\hat{\boldsymbol{l}})^2 \exp\left(i\hat{\phi}_0 \boldsymbol{v_D}\cdot\hat{\boldsymbol{l}}\right) \end{aligned} \tag{B.2}$$

and the derivatives for the second terms are given as

$$\begin{aligned} g(\hat{\phi}_0) &= \exp\Big(-\frac{\hat{\phi}_0^2\xi_{th}^2}{4}\Big) \\ g'(\hat{\phi}_0) &= -\Big(\frac{\hat{\phi}_0\xi_{th}^2}{2}\Big)\exp\Big(-\frac{\hat{\phi}_0^2\xi_{th}^2}{4}\Big) \\ g''(\hat{\phi}_0) &= -\Big(\frac{\xi_{th}^2}{2}\Big)\exp\Big(-\frac{\hat{\phi}_0^2\xi_{th}^2}{4}\Big) + \Big(\frac{\hat{\phi}_0\xi_{th}^2}{2}\Big)^2\exp\Big(-\frac{\hat{\phi}_0^2\xi_{th}^2}{4}\Big) \end{aligned} \tag{B.3}$$

The integral in equation B.1 can therefore be re-written as

$$\gamma(\hat{\phi}_0;\hat{l}) = \frac{1}{I_0}\int_L \epsilon(\boldsymbol{r})\left(1 + i(\boldsymbol{v_D}\cdot\hat{\boldsymbol{l}})\hat{\phi}_0 - \frac{(\boldsymbol{v_D}\cdot\hat{\boldsymbol{l}})^2\hat{\phi}_0^2}{2}\right)\left(1 - \Big(\frac{\hat{\phi}_0^2\xi_{th}^2}{4}\Big)\right)\,dl \tag{B.4}$$

For convenience, we define $w^2 = \hat{\phi}_0^2\ \xi_{th}^2/4$ and $v = \boldsymbol{v_D}\cdot\hat{\boldsymbol{l}}\hat{\phi}_0$ which are small ($\sim 0.2$ rad) and are on the same order of magnitude. Expanding the bracket terms and collecting the real and imaginary parts, the integral can be rewritten as

$$\gamma(\hat{\phi}_0;\hat{l}) = \frac{1}{I_0}\int_L \epsilon(\boldsymbol{r})\left(1 - w^2 - \frac{v^2}{2}\right)\,dl + \frac{i}{I_0}\int_L \epsilon(\boldsymbol{r})v\left(1 - w^2\right)\,dl \tag{B.5}$$

Where $v^2w$ terms have been neglected as their contribution is too small. The phase is extracted by taking the arctangent of the complex coherence

$$\phi_D = \arctan\gamma(\hat{\phi}_0;\hat{l}) = \frac{\frac{1}{I_0}\int_L \epsilon(\boldsymbol{r})v\ dl - \frac{1}{I_0}\int_L \epsilon(\boldsymbol{r})v\ w^2\ dl}{1 - \frac{1}{I_0}\int_L \epsilon(\boldsymbol{r})w^2\ dl - \frac{1}{I_0}\int_L \epsilon(\boldsymbol{r})\frac{v^2}{2}\ dl} \tag{B.6}$$

The dominating term is the first term in the numerator, which is an order of magnitude higher than the second order terms. Using the definition of $v$, the expression for the phase is simply

$$\phi_D = \frac{\hat{\phi}_0}{I_0}\int_L \epsilon(\boldsymbol{r})\boldsymbol{v_D}\cdot\hat{\boldsymbol{l}}\ dl \tag{B.7}$$

which (ignoring line-integration effects) is the same expression given in equation 4.28 and shows that the measured phase is is directly related to the projection of the Doppler-shifted flow.

The fringe contrast is calculated by taking the complex modulus of the coherence. Using the expression for the coherence in equation B.5, the contrast can be calculated

$$|\gamma(\hat{\phi}_0;\hat{l})|^2 = \left(1 - \frac{1}{I_0}\int_L \epsilon(\boldsymbol{r})w^2 dl - \frac{1}{I_0}\int_L \epsilon(\boldsymbol{r})\frac{v^2}{2}\, dl\right)^2 + \left(\frac{1}{I_0}\int_L \epsilon(\boldsymbol{r})v dl - \frac{1}{I_0}\int_L \epsilon(\boldsymbol{r})v\ w dl\right)^2 \tag{B.8}$$

Expanding the bracket terms, eliminating third and forth order terms, and noting that the Taylor series of $(1-\varepsilon)^{1/2}$ is just $1-\varepsilon/2$, the expression can be expanded to first order to remove the square root. Substituting the values for $w$ and $v$ this becomes

$$\zeta_D = 1 - \frac{1}{I_0 T_C}\int_L \epsilon(\boldsymbol{r})T_S\ dl - \frac{\hat{\phi}_0^2}{2}\left\{\left(\frac{1}{I_0}\int_L \epsilon(\boldsymbol{r})\boldsymbol{v_D}\cdot\hat{\boldsymbol{l}}\ dl\right)^2 - \frac{1}{I_0}\int_L \epsilon(\boldsymbol{r})(\boldsymbol{v_D}\cdot\hat{\boldsymbol{l}})^2\ dl\right\} \tag{B.9}$$

The first and second terms combine to give the Taylor series expansion of equation 4.27. the final bracketed terms are a correction to the temperature due to contributions from the Doppler flow. These terms are equivalent for azimuthal and axial flow contributions where a uniform brightness profile is assumed and hence this correction term will vanish. Under other brightness conditions the contributions are generally negligible.

On the other hand, for the radial diffusive flows, the first integral term will vanish due to cancellation of terms using a circular-symmetry argument, however, it is clear that for the second integral term there is no cancellation. Simple geometric argument says that the radial components will be maximum at small impact parameters which would result in elevated ion temperatures recorded along the central viewing chords.

This derivation shows that in the $v_D \sim v_{th}$ then coherence imaging offers the opportunity to extract information about the radially diffusive flows.

# Bibliography


[1] Peratt A. *Physics of the Plasma Universe*. New York/Springer Verlag, 1992.

[2] Hollweg J and Isenberg P. Generation of the fast solar wind: A review with emphasis on the resonant cyclotron interaction. *Journal of Geophysical Research*, 107(A7), 2001.

[3] Marsch E, Tian H, Sun J, Curdt W, and Wiegelmann T. Plasma flows guided by strong magnetic fields in the solar corona. *The Astrophysical Journal*, 685(2), 2008.

[4] Erukhimov L and Genkin L. The ionosphere as a space plasma laboratory (review). *Radiophys Quantum Electron*, 35:555–568, 1992.

[5] Charles C. The terrestrial plasma source: A new perspective in solar-terrestrial processes from dynamics explorer. *Reviews of Geophysics*, 26(2):229–248, 1988.

[6] Chapman S. *Solar Plasma, geomagnetism and aurora*. New York, Gordon and Breach, 1964.

[7] Xue S, Yuan P, Cen J, Liu J, and Li Y. Study on physical characteristics of a bipolar cloud-to-ground lightning discharge plasma. *IEEE Transactions on Plasma Science*, 43(3), 2015.

[8] Salvermoser M and Murnick D. High efficiency, high-power, stable 172 nm xenon excimer light source. *Appl. Phys. Lett.*, 83(10):1932–1934, 2003.

[9] Helliwell R. *Whistlers and Related Ionospheric Phenomena*. Stanford University Press, 1965.

[10] Graves D and Gottscho R. Computer applications in plasma materials processing. *MRS bulletin*, 16(2):16–22, 1991.

[11] Malka V. Laser plasma accelerators. *Physics of Plasmas*, 19(055501), 2012.

[12] Greig A, Charles R, Hawkins, and Boswell R. Direct measurements of neutral gas heating in a radio-frequency electrothermal plasma micro-thruster. *Optics Communications*, 103(074101), 2013.

[13] Lee I, Park J, and Lee Y. Imaging turbulent structures and tomographic reconstruction of TORPEX plasma emissivity. *Surface and Coatings Technology*, 171(1–3):252–256, 2003.

[14] Verberck B and Taroni Andrea. Nuclear fusion. *Nature Physics*, 12(5):383, 2016.

[15] Credit ©ITER Organisation. https://www.iter.org/. downloaded on 12/11/2018.

[16] Shimomura Y, Aymar R, Chuyanov V, Huguet M, Matsumoto H, Mizoguchi T, Murakami Y, Polevoi A, and Shimada M. ITER-FEAT operation. *Nucl. Fusion*, 41(3):309–316, 2001.

[17] Rehbut P, Bickerton R, and Keen B. The Joint European Torus: installation, first results and prospects. *Nucl. Fusion*, 25(9):1011–1022, 1985.

[18] Norajitra P, Abdel-Khalik S, Giancarli L, Ihli T, Janeschitz G, Malang S, Mazul I, and Sardain P. Divertor conceptual designs for a fusion power plant. *Fusion Engineering and Design*, 83(7):893–902, 2008.

[19] Blackwell B, Caneses J, Samuell C, Wach J, Howard J, and Corr C. Design and characterization of the magnetized plasma interaction experiment (MAGPIE): A new source for plasma-material interaction studies. *Plasma Sources Sci. Technol.*, 21:1–7, 2012.

[20] Hasegawa A. *Plasma Instabilities and non-linear Effects*. Springer-Verlag, 1975.

[21] Kinder R, Ellingboe A, and Kushner M. H- to W-mode transitions and properties of a multimode helicon plasma reactor. *Plasma Sources Sci. Technol.*, 12:561–575, 2003.

[22] Lieberman M and Lichtenberg A. *Principles of Plasma Discharges and Materials Processing*. Wiley-Interscience, 2005.

[23] Ellingboe A and Boswell R. Capacitive, inductive and helicon-wave modes of operation of a helicon plasma source. *Phys. Plasmas*, 3(7):2797–2804, 1996.

[24] Scime E, Keesee A, and Boswell R. Mini-conference on helicon plasma sources. *Phys. Plasmas*, 15(058301), 2008.

[25] Boswell R. Very efficient plasma generation by whistler waves near the lower hybrid frequency. *Plasma Physics and Controlled Fusion*, 26(10):1147–1162, 1984.

[26] Scime E, Keiter P, Zintl W, Balkey M, Kline J, and Koepke M. Control of ion temperature anisotropy in a helicon plasma. *Plasma Sources Sci. and Tech.*, 7:186–191, 1998.

[27] Kline J, Scime E, Keiter P, Balkey M, and Boivin R. Ion heating in the HELIX helicon plasma source. *Physics of Plasmas*, 6(12):4767–4772, 1999.

[28] Kline J et al. Ion dynamics in helicon sources. *Physics of Plasmas*, 10(5):2127–2135, 2003.

[29] Kline J, Scime E, Boivin R Keesee A, and Sun X. RF absorption and ion heating in helicon sources. *Physical Review Letters*, 88(19):1–4, 2002.

[30] Scime E, Carr J, Galante M, Magee R, and Hardin R. Ion heating and short wavelength fluctuations in a helicon plasma source. *Phys. Plasmas*, 20(032103), 2013.

[31] Scime E, Hardin R, Biloiu C, Keesee M, and Sun X. Flow, flow shear and related profiles in helicon plasmas. *Phys. Plasmas*, 14(043505):1–11, 2007.

[32] Sun X, Biloiu C, Hardin R, and Scime E. Parallel velocity and temperature of argon ion in an expanding, helicon source driven plasma. *Plasma Sources Sci. and Tech.*, 13:359–370, 2004.

[33] Biloiu I, Scime E, and Biloiu C. One and two-dimensional laser induced fluorescence at oblique incidence. *Plasma Sources Sci. Tenchnol.*, 18(025012), 2009.

[34] Carr J, Cassak P, Galante M, Keesee A, Lusk G, Magee R, McCarren D, Sears S Scime E, Vandervort R, Gulbrandsen N, Goldman M, Newman D, and Eastwood J. Spontaneous ion beam formation in the laboratory, space, and simulation. *Phys. Plasmas*, 20(072118), 2013.

[35] Thakur C, McCarren D, Fedorczak N Lee T, Manz P, Scime E, Tynan G, Xu M, and Yu J. Comparison of azimuthal ion velocity profiles using Mach probes, time delay estimation, and laser induced fluorescence in a linear plasma device. *Rev. Sci. Instrum.*, 83(10D708), 2012.

[36] Tynan G, Burin M, Holland C, Antar G, Crocker N, and Diamond P. Radially sheared azimuthal flows and turbulent transport in a cylindrical plasma. *Phys. Plasmas*, 11(4), 2004.

[37] Tynan G, Holland C, Yu J, James A, Nishijima D, Shiada M, and M Taheri. Observations of turbulent-driven shear flow in a cylindrical laboratory plasma device. *Plasma Phys. Control. Fusion*, 48, 2006.

[38] Thakur C, McCarren D, Lee T, Fedorczak N, Manz P, and Scime E. Laser induced fluorescence measurements of the ion velocity and temperature of drift turbulence driven sheared plasma flow in a linear helicon plasma device. *Physics of Plasmas*, 19, 2012.

[39] Schroder C, Grulke O, Klinger T, and Volker N. Drift waves in a high-density cylindrical helicon discharge. *Physics of Plasmas*, 12(042103), 2005.

[40] Howard J, Michael C, Glass F, and Cheetham A D. Optical coherence techniques for plasma spectroscopy. *Rev. Sci. Instrum.*, 72:888–897, 2001.

[41] Howard J. Electro-optically modulated polarizing Fourier-Transform spectrometer for plasma spectroscopy applications. *Appl. Opt.*, 41:197–208, 2002.

[42] Howard J, Michael C, Glass F, and Danielsson A. Time-resolved two-dimensional plasma spectroscopy using coherence-imaging techniques. *Plasma Phys. Control. Fusion*, 45:1143–1166, 2003.

[43] Chung J, König R, Howard J, Otte M, and Klinger T. Time resolved coherence imaging spectrometer on the WEGA stellorator. *Plasma Phys. control. Fusion*, 47:919–940, 2005.

[44] Howard J. High-speed high-resolution plasma spectroscopy using spatial-multiplex coherence imaging techniques. *Rev. Sci. Instrum.*, 77:1–8, 2006.

[45] Howard J, Jaspers R, Lischtschenko O, Delabie E, and Chung J. Imaging charge exchange recombination spectroscopy on the TEXTOR tokamak. *Plasma Phys. Control. Fusion*, 52:1–10, 2010.

[46] Howard J. Coherence imaging spectro-polarimetry for magnetic fusion diagnostics. *J. Phys. B: At. Mol. Opt. Phys.*, 43:1–10, 2010.

[47] Howard J et al. Coherence imaging of flows in the DIII-D divertor. *Contrib. Plasma Phys.*, 51:194–200, 2011.

[48] Steel W H. *Interferometry.* Cambridge University Press, 1983.

[49] Hutchinson I H. *Principles of Plasma Diagnostics.* Cambridge University Press, 2002.

[50] Chung J, König R, Howard J, Otte M, and Klinger T. Time resolved coherence imaging spectrometer on the wega stellarator. *Plasma Phys. Control. Fusion*, 47:919–940, 2005.

[51] Michael C A. *Doppler spectroscopy of Argon Plasma in H-1NF using a coherence imaging camera.* PhD thesis, Research School of Physics and Engineering, Australian National University, 2003.

[52] Howard J et al. Doppler coherence imaging and tomography of flows in tokamak plasmas (invited). *Rev. Sci. Instrum.*, 81:1–6, 2010.

[53] Howard J. Snap-shot imaging motional Stark effect polarimetry. *Plasma phys. Control. Fusion*, 50, 2008.

[54] Howard J and Chung Jinil. Spatial hetrodyne Stokes vector imaging of the motional Stark-Zeeman multiplet. *Rev. Sci. Instrum.*, 83, 2012.

[55] Ford O, Howard J, Reich M, Hobirk J, Svensson J, and Wolf R. First results from the imaging motional Stark effect diagnostic on ASDEX upgrade. *Proceedings of the 40th Eurpean Physical Society Conference on Plasma Physics*, 02.110, 2013.

[56] Thoman A, Michael C, and Howard J. A high spatial resolution Stokes polarimeter for motional Stark effect imaging. *Rev. Sci. Instrum.*, 84, 2013.

[57] Sudit I and Chen F. Discharge equilibrium of a helicon plasma. *Plasma Sources Science and technology*, 5:43–53, 1996.

[58] Howard J, Glass F, and Michael C. Doppler spectroscopy and tomography of plasmas. *Plasma and Fusion Research*, 2:1–7, 2007.

[59] Nakano T, Giapis K, Gottscho R, Lee T, and Sadeghi N. Ion velocity distributions in helicon wave plasmas: Magnetic field and pressure effects. *J. Vac. Sci. Technol. B*, 11(6):2046–2056, 1993.

[60] Merlino R. Understanding Langmuir probe current-voltage characteristics. *Am. J. Phys.*, 75(12), 2007.

[61] Cherrington B. The use of electrostatic probes for plasma diagnostics-a review. *Plasma Chemistry and Plasma Processing*, 2(2):113–140, 1982.

[62] Chung K. Mach probes. *Plasma Sources Sci. Technol.*, 21:1–47, 2012.

[63] Solomon W and Shats M. Fluctuation studies using combined Mach/triple probe. *Rev. sci. Instrum.*, 72(1):449–452, 2001.

[64] Gonclaves B, Hidalgo C, Pedrosa M, Silva C, Balbin R, Erents K, Hron M, Loarte A, and Matthews G. Edge localized modes and fluctuations in the JET SOL region. *Plasma Phys. and control. Fusion*, 45:1627–1635, 2003.

[65] Gonclaves B, Hidalgo C, Pedrosa M, Orozco R, Sanchez E, and Silva C. Role of turbulence on edge momentum re-distribution in the TJ-II stellarator. *PRL*, 96, 2006.

[66] Fasoli A et. al. Electrostatic instabilities, turbulence and fast ion interactions in the TORPEX device. *Plasma Phys. Control. Fusion*, 52, 2010.

[67] Kado S, Shikama T, Kajita S, Oishi T, and Tanaka S. Plasma flow measurements in linear divertor simulator MAP-II using Mach probe and directional Langmuir probe. *Contrib. Plasma Phys.*, 44(7–8):656–661, 2004.

[68] Deline C, Bengtson R, Breizman B, Tushentsov M, Jones J, Chavers D, Dobson C, and Schuettplez B. Plume detachment from a magnetic nozzle. *Physics of Plasmas*, 16, 2009.

[69] Hudis M and Lidsky L. Directional Langmuir probe. *Journal of applied physics*, 41(12), 1970.

[70] Chung K S and Hutchinson I H. Kinetic theory of ion collection by probing objection in flowing strongly magnetized plasma. *Physical Review A*, 38:4721–4731, 1988.

[71] Hutchinson I H. Ion collection by a sphere in a flowing plasma:i quasineutral. *Plasma Phys. Control. Fusion*, 44:1953–1977, 2002.

[72] Hutchinson I H. Ion collection by a sphere in a flowing plasma:ii non-zero debye length. *Plasma Phys. Control. Fusion*, 45:1477–1500, 2003.

[73] Hutchinson I H. Ion collection by a sphere in a flowing plasma:iii floating potential and drag force. *Plasma Phys. Control. Fusion*, 47:71–87, 2005.

[74] Ko E and Hershkowitz N. Asymmetry reversal of ion collection by Mach probes in flowing unmagnetised plasma. *Plasma Phys. Control. Fusion*, 48:621–634, 2006.

[75] Edwards G and Lawrence M. A temperature dependent dispersion equation for congruently grown lithium niobate. *Opt. Quant. electron.*, 16:373–375, 1984.

[76] Eimerl D, Davis L, Graham E, and Zalkin A. Optical, mechanical, and thermal properties of barium borate. *J Appl. Phys*, 62:1968–1983, 1987.

[77] Ter-Gabrielyan N, Fromzel V, and Dubinskii M. Linear thermal expansion and thermo-optic coefficients of YVO4 crystals the 80-320K temperature range. *Optical Materials Express*, 2:1624–1631, 2012.

[78] Ghosh G. Dispersion-equation coefficients for the refractive index and birefringence of calcite and quartz crystals. *Optics Communications*, 163:95–102, 1999.

[79] Veiras F E, Perez L I, and Garea M T. Phase shift formulas in unaxial media: an application to waveplates. *Applied Optics*, 49(15):2769–2777, 2010.

[80] Francon M and Mallick S. *Polarization Interferometry*. Wiley-Interscience, 1971.

[81] Bass M. *Handbook of Optics-Devices, Measurements and Properties*, volume II. McGraw-Hill Inc, 1995.

[82] Samuell C, Blackwell B, Howard J, and Corr C. Plasma parameters and electron energy distributions functions in magnetically focused plasma. *Phys. Plasmas*, 20(034502):1–4, 2013.

[83] Sansonetti J and Martin W. *Handbook of basic atomic and spectroscopic data*. National Institute for Standards and Technology (NIST), 2005.

[84] Corney A. *Atomic and Laser Spectroscopy*. Clarendon Press, 1977.

[85] Candler C. *Atomic Spectra and the Vector Model*. Hilger and Watts LTD, 1964.

[86] Sobelman I. *Introduction to the theory of atomic spectra*. Pergamon Press, 1972.

[87] Zelmon D, Lee J, Currin K, Northridge J, and Perlov D. Revisiting the optical properties of nd doped yttrium orthovanadate. *Applied Optics*, 49(4):644–647, 2010.

[88] Browder J and Ballard S. Thermal expansion data for eight optical materials from 60K to 300K. *Appl. Opt.*, 16(12):3214–3217, 1977.

[89] Jundt D, Fejer M, and Byer R. Optical properties of lithium-rich lithium niobate fabricated by vapor transport equilibrium. *IEEE Journal of Quantum Electronics*, 26(1):135–138, 1990.

[90] Bass M. *Handbook of Optics-Fiber Optics and Nonlinear Optics*, volume IV. McGraw-Hill Inc, 2000.

[91] Moretti L, Iodice M, Della-Corte F, and Rendina I. Temperature dependence of the thermo-optic coefficient of lithium niobate from 300 to 515 K in the visible and infra-red regions. *J. Appl. Phys.*, 98, 2005.

[92] Cohen A, Siefert N, Stange S, Boivin R, Scime E, and Levinton F. Ion acceleration in plasmas emerging from a helicon-heated magnetic mirror device. *Physics of Plasmas*, 10(6):2593–2598, 2003.

[93] Oksuz L and Hershkowitz N. Understanding Mach probes and Langmuir probes in a drifting, unmagnetised, non-uniform plasma. *Plasma Sources Sci. Technol.*, 13:263–271, 2004.

[94] Shikama T, Kado S, Okamoto A, Kajita S, and Tanaka S. Investigation of Mach probe geometry effects in weakly magnetized plasmas. *Journal of Nuclear Materials*, 337–339:1077–1081, 2005.

[95] Gosselin J, Thakur S, Sears S, McKee J, Scime E, and Tynan G. Overestimation of Mach number due to probe shadow. *Phys. Plasmas*, 23(073519), 2016.

[96] Gosselin J, Thakur S, Sears S, McKee J, Scime E, and Tynan G. Mach probe wakes are important in weakly magnetized, collisional plasmas. *57th Annual Meeting of the APS Division of Plasma Physics*, 57(19), 2015.

[97] Yan Z, Tynan G, Holland C, Xu M, Muller S, and Yu J. Shear flow and drift wave turbulence dynamics in a cyindrical plasma device. *Phys. Plasmas*, 17(032302), 2010.

[98] Holland C, Yu J, James A, Nishijima D, Shimada M, Taheri N, and Tynan G. Observations of turbulent-driven shear flow in a cylindrical laboratory plasma device. *Phys. Rev. lett.*, 96(195002), 2006.

[99] Horton W. Drift waves and transport. *Reviews of Modern Physics*, 71(3), 1999.

[100] Howard J, Michael C, Chen H, Lester R, Thorman A, and Chung J. Spectropolarimetric optical systems for imaging plasma internal fields, structures and flows. *Jinst*, 10, 2015.

[101] Caneses Marin J. *Helicon wave propagation and plasma equilibrium in high-density hydrogen plasma in converging magnetic fields.* PhD thesis, Research School of Physics and Engineering, Australian National University, 2015.

[102] Wright A, Qu Z, Caneses J, and Hole M. An experimentally constrained MHD model for a collisional, rotating plasma column. *Plasma Phys. Control. Fusion*, 59(025003), 2017.

[103] Andover Cooperation. 2017 andover catalog. Downloaded from company website Sep/2017, 4 Commercial Drive, Salem, New Hampshire, 03079-2800, Nov 2016. https://www.andovercorp.com/static/pdf/catalog.pdf.

[104] Spectrofilm optical filter guide. Downloaded from company website Sep/2017, 34 Dunham Rd, Billerica MA 01821. http://www.spectrofilm.com/optical-filter-guide-spectrofilm.pdf.

[105] Bridges W, Chester A, Halsted A, and Parker K. Ion laser plasmas. *Proceedings of the IEEE*, 59(5), 1971.

[106] Yin J, Zhu S, Sun H, and Gao W. Relationship between coherence length and output power of a multi-longitudindal-mode $Ar^+$ laser. *App'. Phys. B*, 61:111–115, 1994.

[107] Lexel Lasers. How gas-ion lasers work. Technical report, Cambridge Lasers Laboratories, Inc. Lexel Lasers, http://www.lexellaser.com/PF/techinfo_gas-ion.pdf, 2010. downloaded: 04/01/2017.

[108] Kitaeva V, Odintsov A, and Sobelov N. Continuously operating argon ion lasers. *Usp. Fiz. Nauk/AIP*, Russian Volume 99(3–4):361–416, 1969/1970.

[109] Baker K. Tomographic reconstruction of high-energy-density plasmas with picosecond temporal resolution. *Optics Letters*, 31(6):730–732, 2006.

[110] Warr G, Tarrant R, Bilek M, and McKenzie D. Tomographic interferometry of a filtered high-current vacuum arc plasma. *J. Appl. Phys*, 101(073302), 2007.

[111] Sweeney D and Vest C. Reconstruction of three-dimensional refractive index fields by holographic interferometry. *Applied Optics*, 11(1):205–207, 1971.

[112] Iraji D, Furno I, Fasoli A, and Theiler C. Imaging turbulent structures and tomographic reconstruction of TORPEX plasma emissivity. *Physics of Plasmas*, 17(122304):1–8, 2010.

[113] Nagayama Y et. al. Analysis of sawtooth oscillations using simultaneous measurements of electron cyclotron emission imaging and x-ray tomography on TFTR. *Physical Review Letters*, 67(25):3527–3530, 1991.

[114] Deans S R. *The Radon Transform and some of its applications.* Wiley-Interscience, 1983.

[115] Born M and Wolf E. *Principles of Optics.* Pergamon Press, 1959.

[116] Howard J. Vector tomography application in plasma diagnostics. *Plasma Phys. Control. Fusion*, 38:489–503, 1996.

[117] Norton S. Tomographic reconstruction of 2D vector fields: application to flow imaging. *Geophysical Journal*, 97:161–168, 1988.

[118] Boswell R. Plasma production using a standing helicon wave. *Physics Letters A*, 33(7):457–458, 1970.

[119] Kunkel W. The Hall effect in a plasma. *Am. J. Phys.*, 49(8):733–738, 1981.

[120] Lieberman M. A mini-course on the principles of plasma discharges. Department of Electrical Engineering and Computer Science University of California, Berkeley, CA 94720, 2003.